Western boundary dynamics and overturning circulation in the Subpolar North Atlantic

Yingjie Liu

DOCTORAT SCIENCES BRETAGNE DE LA MER LOIRE ET DU LITTORAL

UBO Université de Bretagne Occidentale

THESE DE DOCTORAT DE

L'UNIVERSITE
DE BRETAGNE OCCIDENTALE

ECOLE DOCTORALE N° 598
Sciences de la Mer et du littoral
Spécialité : *Océanographie Physique et Environnement*

Par

Yingjie LIU

Western boundary dynamics and overturning circulation in the Subpolar North Atlantic

Thèse présentée et soutenue à Plouzané, le 19 Décembre 2022
Unité de recherche : Laboratoire d'Océanographie Physique et Spatiale (LOPS, UMR 6523)

Rapporteurs avant soutenance :

Léon CHAFIK — Professeur de Université, Stockholm University, MISU
Gilles REVERDIN — Directeur de Recherche, CNRS, LOCEAN

Composition du Jury :

Président :	Anne-Marie TREGUIER	Directeur de recherche, CNRS, LOPS
Examinateurs :	Léon CHAFIK	Professeur de Université, Stockholm University, MISU
	Gilles REVERDIN	Directeur de Recherche, CNRS, LOCEAN
	Thierry PENDUFF	Directeur de Recherche, CNRS, IGE
	Virginie THIERRY	Chercheur, IFREMER, LOPS
Dir. de thèse :	Herlé MERCIER	Directeur de recherche, CNRS, LOPS
Co-dir. de thèse :	Damien DESBRUYERES	Chercheur, IFREMER, LOPS

Le vent se lève !… Il faut tenter de vivre !
L'air immense ouvre et referme mon livre,
La vague en poudre ose jaillir des rocs !
Envolez-vous, pages tout éblouies !
Rompez, vagues ! Rompez d'eaux réjouies
Ce toit tranquille où picoraient des focs !

Paul Valéry

Acknowledgements

Prior to anything else, I would to express my appreciation to my supervisors, Dr Herlé Mercier and Dr Damien Desbruyères. I am grateful for the generosity of their time, wisdom, encouragement, and financial assistance in making my PhD life stimulating and fruitful. They allowed me to explore my own thoughts at my own pace, guided me with thought-provoking questions, and were always available for discussions. The knowledge I have gained from them exceeds what is required to be an oceanographer.

I'd like to thank Dr Michael Spall and Dr Alan Fox for their insightful comments and fruitful collaborations on my work. I also thank my CSI committee, including Dr Camille Lique, Dr Christophe Herbaut, and Dr Jean-Baptiste Sallée for their involvement, support and helpful discussions during committee meetings. In addition, I appreciate Dr Anne-Marie Tréguier, Dr Gilles Reverdin, Dr Léon Chafik, Dr Thierry Penduff, and Dr Virginie Thierry for serving on my dissertation committee and willingness to share their knowledge and time.

To my former and current LOPS lab mates in Freycinet Building, thank you for the scientific conversations, encouragement, and laughs. This includes Adam Ayouche, Adele Moncuquet, Ashwita Chouksey, Etienne Pauthenet, Ivane Salaün, Kenneth Lee, Lénaïg Brun, Odilon Joël Houndegnonto, Rémy Asselot, Soumaïa Tajouri and Xiaolong Yu. I would like to give special thanks to Coline Poppeschi and Zoé Caspar-Cohen for being there for me during my PhD program and, more significantly, for being my friends. Thanks are also extended to the supporting staff of LOPS and BOCATS2 2021 cruise for facilitating the logistics of my study.

I am fortunate to be in Brest with wonderful friends. I owe special thanks to Yue Cheng and our kitty Yuwan Cheng, my 3-year roommates and who have become my family and

made me smile everyday. I am also thankful for my Brestoise friends, including Anna Li, Fangping Ye, Heng Zhang, Hong Chin Ng, Lu Wang, Xiaoyu Wang, and Yutong Yan, as well as my Parisien-Rennais friends, including Gen Lu, Jiaxin Liu, Matthieu Breger, Xin Wen, Yifeng Jiang, Yingxue Han, and Zixin Li. Thanks are also extended to my two Spanish cuties, Juanma Leyva and Sofía Ortín. Thank you for the hugs, laughter, and love. Cheers, for our friendship!

My special gratitude goes to Yi Zhou, my best friend in China, who supplies me with continuous encouragement from a distance. Thank you for always being there and inspiring me to pursue a career in science.

Last but not least, I will always be grateful to my parents, Rongtang Liu and Guiying Yu, for their unconditional love and support. You made this possible; this dissertation is as much as yours and mine.

Abstract

The Atlantic Meridional Overturning Circulation (AMOC) is comprised of a northward upper limb that transports warm near-surface waters from southern latitudes to the subpolar North Atlantic and Nordic Seas and a southward lower limb that transports cold deep waters back to the southern latitudes. The AMOC is an essential component of the climate system due to its vital role in the global distribution of heat, carbon, and water masses. The downwelling of North Atlantic surface waters connecting the upper and lower AMOC limbs is an essential yet vulnerable part of this global circulation. This downwelling partly occurs along continental boundaries due to complex interactions between the atmosphere, the mean ocean circulation, and the turbulent mesoscale field. Boundary downwelling has been investigated extensively through idealized and realistic numerical models but focused observational studies are still fairly limited. This dissertation presents an extended observational quantification of Eulerian-mean downwelling along the continental slopes of the North Atlantic subpolar gyre (SPG) and an examination of the underlying mechanisms, with an emphasis on the role of mesoscale eddies.

Using observational data, a first quantification of the vertical mass transport along the boundary of SPG is presented. The 2002–2019 long-term mean along-boundary density and velocity fields were reconstructed using Argo and shipboard hydrography data. A volume budget of the SPG boundary reveals a total Eulerian-mean downwelling of -4.00$\pm$0.96 Sv at 1200 m depth between Denmark Strait and Flemish Cap, with the barotropic transport (BT) contributing 2.00$\pm$0.61 Sv and the baroclinic transport (BC) contributing 2.00$\pm$0.43 Sv. The BT downwelling is produced by the interaction between the meandering of the deep western boundary current and the bottom topography, while the BC downwelling is produced by the

large-scale along-shore density gradient. A recognizable regional pattern of the boundary vertical transport emerges, with BT (BC) upwelling (downwelling) in the Irminger Sea and western Labrador Sea and downwelling (upwelling) in western Greenland. Comparisons with independent cross-basin estimates confirm that the majority of vertical overturning transport in the subpolar North Atlantic marginal seas occurs along the continental slopes.

To investigate the processes that cause the BC boundary downwelling, i.e., the boundary heat loss and associated along-boundary density gradient, the long-term mean (2002-2019) heat budget of the boundary current system is studied using various types of in-situ data (Argo, OSNAP moorings) in conjunction with atmospheric reanalysis and remote sensing data products. Both lateral heat fluxes, driven by the mean advection and the eddy field, and air-sea heat flux play significant roles in the boundary heat loss. In a semi-Lagrangian framework based on surface eddy tracking and collocated Argo-derived temperature anomalies, it is found that cross-shore eddy propagation generally cools the SPG boundary. Similar to previous studies, a significant number of eddies (especially anticyclones) are generated downstream of Cape Farewell along the western Greenland boundary and transport warm Irminger Current water into the convective interior. In the western Labrador Sea and Irminger Sea, however, eddies form offshore of the boundary and transport cold interior water into the boundary current.

Taken together, this dissertation provides a first comprehensive observational study of the long-term Eulerian mean vertical transport and the associated thermaldynamical processes along the western boundary of SPG that must be accounted for in future ocean and climate modeling.

Résumé

La circulation méridienne de retournement de l'Atlantique (AMOC) est composée d'une branche supérieure orientée vers le nord qui transporte les eaux chaudes des régions subtropicales vers les latitudes subpolaires, et d'une branche profonde orientée vers le sud qui transporte les eaux froides vers les latitudes méridionales. L'AMOC est une composante essentielle du système climatique en raison de son rôle vital dans la distribution globale de la chaleur, du carbone et des masses d'eau. La descente des eaux de surface de l'Atlantique Nord reliant les branches supérieure et inférieure de l'AMOC est une composante essentielle mais vulnérable de cette circulation globale. Le transport vertical associé se produit en partie le long des frontières continentales en raison des interactions complexes entre l'atmosphère, la circulation océanique moyenne et le champ turbulent de méso-échelle. Ce « downwelling » de bord a été largement étudié à l'aide de modèles numériques idéalisés et réalistes, mais des études observationnelles ciblées sont encore assez limitées. Cette thèse présente une étude observationnelle étendue sur la quantification du « downwelling » moyen eulérien le long des pentes continentales du gyre subpolaire de l'Atlantique Nord (SPG) et un examen des mécanismes sous-jacents, en mettant l'accent sur le rôle des tourbillons de méso-échelle.

En utilisant des données d'observation, une première quantification du transport vertical de masse le long des bords du gyre SPG est présentée. Les champs moyens (2002-2019) de densité et de vitesse le long des bords ont été reconstruits à l'aide des données hydrographiques et de données Argo. Un bilan de volume révèle un « downwelling » total moyen de 4.30 ± 0.67 Sv à 1200 m de profondeur entre le détroit du Danemark et le Cap de Flemish, le transport barotrope (BT) contribuant pour 2.46 ± 0.52 Sv et le transport barocline (BC) pour 1.84 ± 0.44 Sv. Le BT downwelling est produit par l'interaction des méandres du courant

profond de bord ouest avec la bathymétrie, tandis que le BC downwelling est produit par le gradient de densité à grande échelle le long de la pente continentale. Une distribution spatiale particulière du transport vertical de et de ses composantes émerge, avec une remontée (downwelling) associée au BT (BC) dans la mer d'Irminger et la mer du Labrador occidentale et une descente (upwelling) dans l'ouest du Groenland. Des comparaisons avec des estimations indépendantes trans-bassins confirment que la majorité du transport vertical dans les mers marginales subpolaires de l'Atlantique Nord se produit le long des pentes continentales.

Afin d'étudier les processus à l'origine de la plongée BC le long des bords du gyre SPG, i.e. la perte de chaleur et le gradient de densité associé, le bilan de chaleur moyen (2002-2019) du courant de bords est étudié à l'aide de diverses sources de données in situ (Argo, mouillages OSNAP), de réanalyses atmosphériques et de produits satellitaires. A la fois les flux de chaleur latéraux, induits par les courants de bord et les tourbillons à méso-échelle, et les flux de chaleur air-mer jouent un rôle important dans la perte de chaleur du courant de bord. Dans un cadre lagrangien basé sur le suivi des tourbillons de surface et les anomalies de température colocalisées dérivées d'Argo, on constate que la propagation des tourbillons contribue à refroidir la région de bord du gyre SPG. Comme dans les études précédentes, de nombreux tourbillons (en particulier des anticyclones) sont générés en aval du cap Farewell le long de la frontière ouest du Groenland et transportent l'eau chaude du courant d'Irminger vers l'intérieur convectif. Dans l'ouest de la mer du Labrador et la mer d'Irminger, cependant, les tourbillons se forment principalement au large et transportent les eaux intérieures froides vers le courant de bord.

Cette thèse fournit une première étude observationnelle complète du transport vertical eulérien moyen et des processus dynamiques et thermiques associés le long des bords du gyre SPG qui devront être pris en compte dans les modélisations futures.

Table of contents

List of figures

List of tables

Nomenclature

Commonly used abbreviations in this dissertation:

AMOC Atlantic Meridional Overturning Circulation

AMV Atlantic Multidecadal Variability

BC baroclinic

BCEs Boundary current eddies

BT barotropic

CEs Convective Eddies

CF Cape Farewell

DKS Denmark Strait

DSOWC Denmark Strait Overflow Water Cyclones

DSOW Denmark Strait Overflow Water

DVS Davis Strait

DWBC Deep Western Boundary Current

EGCC East Greenland Coastal Current

EGC East Greenland Current

EG East Greenland

EKE eddy kinetic energy

FC Flemish Cap

IC Irminger Current

IRs Irminger rings

ISOW Iceland-Scotland Overflow Water

LSW Labrador Sea Water

MAR Mid-Atlantic Ridge

NAC North Atlantic Current

NACW North Atlantic Central Waters

NADW North Atlantic Deep Water

NAO North Atlantic Oscillation

OHC ocean heat content

OW Nordic Seas Overflow Water

RR Reykjanes Ridge

SAF Sub-Arctic Front

SLA sea-level anomaly

SPG North Atlantic subpolar gyre

SST surface temperature

Sv Sverdrup

WGCC West Greenland Coastal Current

WGC West Greenland Current

WG West Greenland

WL western Labrador Sea

Chapter 1

Introduction

1.1 The Atlantic Meridional Overturning Circulation

As an essential component of the climate system, the Atlantic Meridional Overturning Circulation (AMOC) is the zonally integrated component of surface and deep currents in the Atlantic Ocean. As depicted in Figures 1.1 and 1.4, in the North Atlantic, the warm northward surface flow carried by the Gulf Stream merges with the cold southward Labrador Current to form the North Atlantic Current (NAC) (e.g., Rossby, 1999). The NAC flows eastward and then northeastward as a surface-intensified baroclinic flow and then splits into multiple branches while crossing the Mid-Atlantic Ridge to reach the eastern subpolar gyre (Rossby, 1996). Intense surface buoyancy loss and diapycnal mixing in the subpolar North Atlantic and in the Nordic Seas densify the surface waters that eventually sink to great depth (Marshall and Schott, 1999; Spall and Pickart, 2001). The water mass thus formed is the North Atlantic Deep Water (NADW), which flows equatorward and largely upwells in the Southern Ocean through Ekman pumping (Marshall and Speer, 2012), but also in thin bottom boundary layers over steep bathymetry where diapycnal mixing is bottom-intensified (Lumpkin and Speer, 2007; Ferrari et al., 2016). The AMOC-related northward heat transport and associated heat exchanges with the atmosphere significantly influence the global climate system. It has been shown that the variability of AMOC controls the Atlantic Multidecadal Variability (AMV; Zhang, 2017; Sutton et al., 2018), a multidecadal cycle of North Atlantic sea surface

temperature. It is also related to regional and hemisphere-scale climate phenomena such as the North Atlantic Oscillation (NAO; Enfield et al., 2001) and the position of ITCZ (Vellinga and Wood, 2002). Therefore, it is essential to comprehend how the AMOC works and how it has changed on decadal and millennial timescales in order to predict how it may evolve in the future.

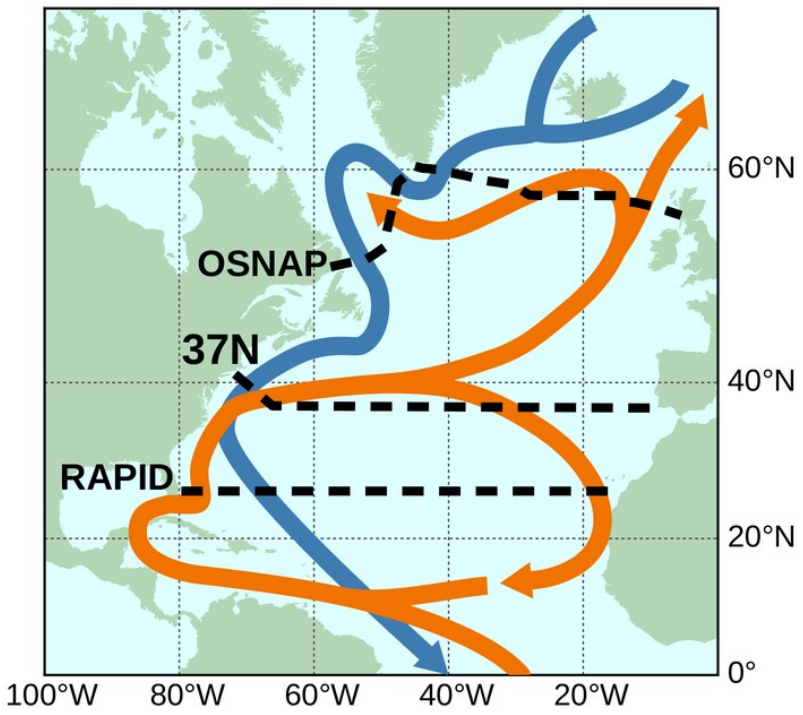

Fig. 1.1 Schematic circulation of the Atlantic Meridional Overturning Circulation (AMOC), where warm, light waters are advected northwards at the surface, and cold, dense waters are advected southward at depth. The RAPID-MOCHA and OSNAP hydrographic arrays are indicated by the black dashed lines. Image Credit: WHOI.

According to climate model forecasts, anthropogenic climate change is "extremely likely" to result in a reduced AMOC's strength during the 21st century (IPCC,2021). Paleoclimate reconstructions, which provide information on AMOC's past and current strength, also raise the possibility of an AMOC collapse (e.g., Rahmstorf, 2002; Caesar et al., 2018). Modern continuous AMOC measurements are notably supported by the U.K.-U.S. Rapid Climate Change-Meridional Overturning Circulation and Heat flux Array at 26.5N (RAPID-MOCHA) and the Subpolar North Atlantic Program (OSNAP) in the subpolar North Atlantic. Their

respective mooring arrays enable direct measurement of the AMOC's overturning strength on daily to decadal timescales (e.g., Cunningham et al., 2007; Lozier et al., 2017). Even though the RAPID-MOCHA and OSNAP time series are not yet long enough to provide a conclusive answer about the proposed AMOC slowdown, continuing to gather these data will be crucial for future comprehension of both short-term and long-term trends.

The Subpolar Gyre (SPG), a crucial part of the AMOC in high latitude regions of the North Atlantic Ocean, is marked by significant decadal-scale variability (Chen and Tung, 2014; Drijfhout et al., 2014; Robson et al., 2018) that contribute to set the properties of the water masses that constitute the AMOC's lower limb (Delworth et al., 1993; Zhang, 2010; Yeager and Danabasoglu, 2014). In the SPG, the vertical sinking of dense waters feeding the lower limb of the AMOC occurs near continental boundaries, while water mass transformation primarily takes place within the basin interiors (Spall and Pickart, 2001; Spall, 2003; Straneo, 2006; Katsman et al., 2018; Georgiou et al., 2019; Liu et al., 2022). The scientific community puts therefore a lot of effort by describing with observations the Eulerian mean vertical transport along the SPG boundary a and its underlying mechanisms. In this dissertation, I join this effort by studying the quantification and underlying mechanisms of Eulerian mean vertical transport in the SPG boundary with observations. In section 1.2, we provide a general description of the three-dimensional circulation of the subpolar North Atlantic Ocean. Section 1.3 discusses the dynamics of the SPG boundary downwelling that connects the upper and lower limbs of the AMOC. In section 1.4, we emphasize the lack of observational studies on boundary downwelling and introduce the central questions of the dissertation.

1.2 The mean forcing and circulation of the northern North-Atlantic Ocean

1.2.1 The climatological atmospheric forcing and the North Atlantic Oscillation

The large-scale wind drives the basin-scale horizontal circulation in the North Atlantic. Figure 1.2(c) shows the climatological pattern of the wind-stress curl. In the subtropics (20°N-45°N), the wind-stress curl is negative, which drives an Ekman pumping and an anticyclonic ocean circulation (the subtropical gyre). A positive wind-stress curl drives Ekman suction and cyclonic ocean circulation (the subpolar gyre) at midlatitudes (45°N-65°N). The line of zero wind-stress curl is frequently regarded as the climatological boundary separating the subtropical and subpolar gyre circulations.

Air-sea buoyancy (heat and freshwater) fluxes significantly impact the state of the large-scale current systems such as the circulation intensity and water properties. Figure 1.2(ab) shows the climatological pattern of the air-sea heat flux and freshwater flux in the North Atlantic. Heat fluxes are predominantly directed from the ocean to the atmosphere (Figure 1.2a). Therefore, on average, the atmosphere cools the ocean in the subtropics and at mid-high-latitude. The most substantial negative fluxes (-150 W/m^2) are found in the Gulf Stream region, a significant winter cyclonic storm region (Brayshaw et al., 2011). Intense negative fluxes are also observed in the western Labrador Sea and eastern SPG (aboutt 50 to 100 W/m^2), where dense and deep water masses are formed by deep convection and feed the AMOC lower branch. The ocean gains heat from the atmosphere in shallow areas around Newfoundland as well as in the subtropical eastern Atlantic. The regional distribution of air-sea freshwater fluxes exhibits a shift from net evaporation (negative flux) to net precipitation (positive flux) north of 40°N-45°N (Figure 1.2b). The substantial evaporation regions are found off Cape Hatteras and in the eastern subtropical zone, whereas substantial precipitation occurs along the east Greenland boundary and near Flemish Cap (FC).

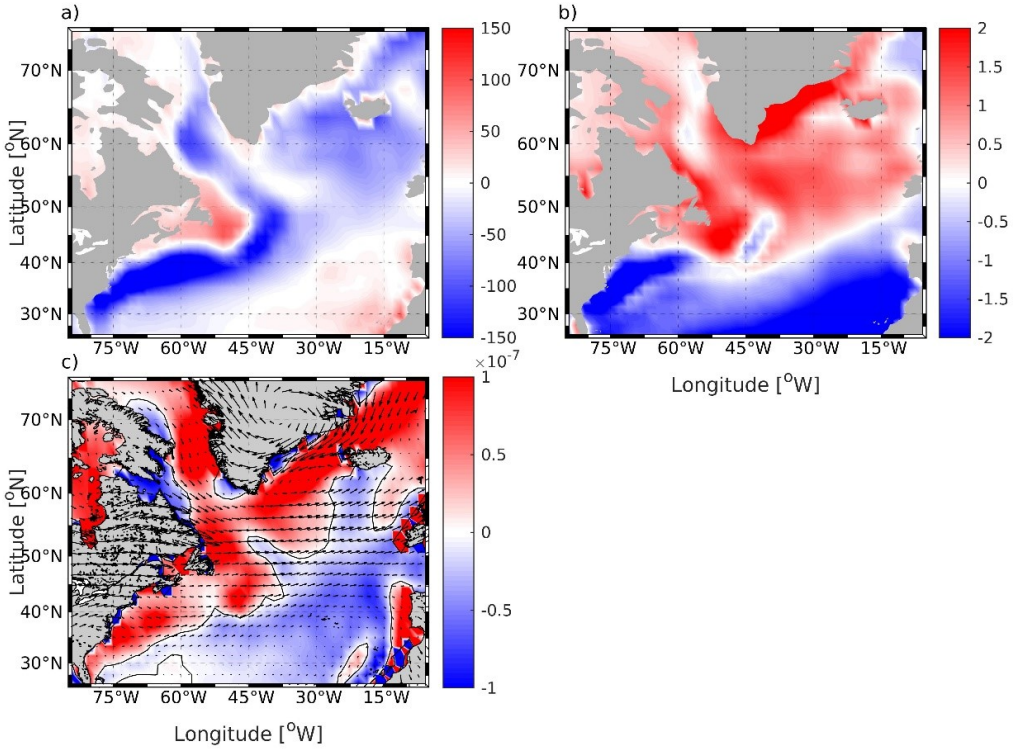

Fig. 1.2 Climatological field of (a) air-sea heat flux (W/m^2, positive downward), (b) air-sea freshwater flux ($kg/(m^2 \cdot day)$), positive upward), and (c) windstress curl (N/m^3) from the NCEP climatology (1981-2018). The black line in (c) indicates the zero windstress curl line.

The North Atlantic Oscillation (NAO) is a weather phenomenon described by an index derived from the differential in surface pressure between the centers of the Icelandic Low and the Azores High (Figure 1.3). It is the predominant mode of variability in the northern North Atlantic sector (e.g., Hurrell, 1995). A positive (negative) phase of the NAO is characterized by a strengthening (weakening) of the westerlies and a northward (southward) shift of storm tracks toward Europe. Variations in the wind field across the basin suggest significant changes in air-sea buoyancy fluxes that affect the ocean locally (mixed-layer response) and on broad regional scales (SPG response). For instance, during 1989-1995, substantial buoyancy loss paired with a persistently positive NAO phase led to the formation of dense and deep LSW, commonly referred to as the "classical" LSW (e.g., Kieke et al., 2006; Rhein et al., 2007). High (low) NAO conditions are frequently accompanied by a northerly (southerly) NAC position (e.g., Curry and McCartney, 2001; Bower and von Appen, 2017). A sharp slowdown

of the circulation after the NAO dropped in the winter of 1995/96 was demonstrated by Curry and McCartney (2001) and Kieke et al., (2007).

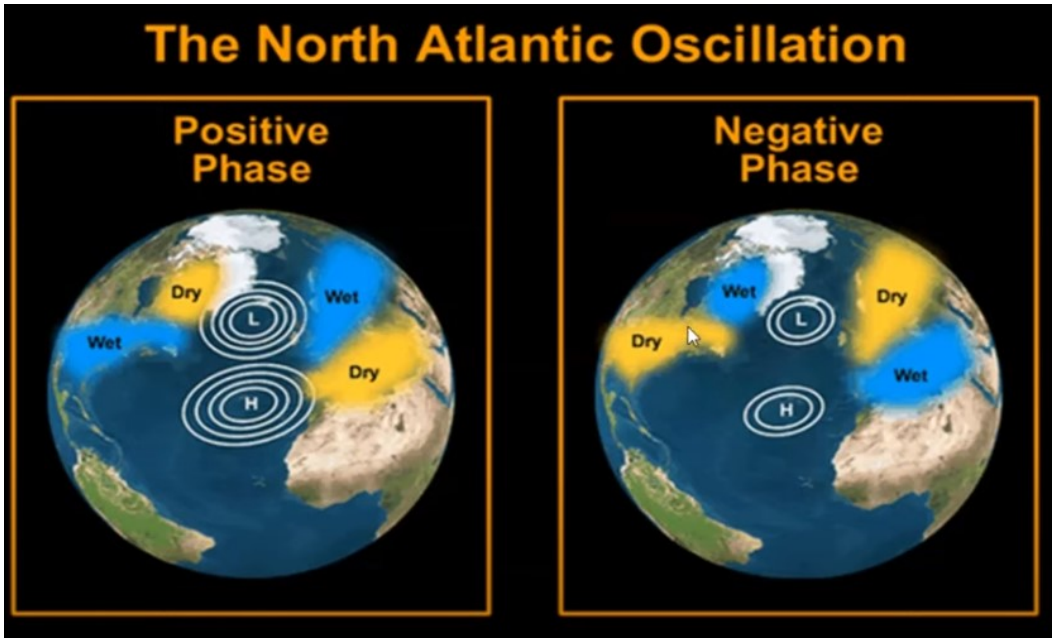

Fig. 1.3 Schematic illustration of a positive (left) and negative (right) North Atlantic Oscillation phase. The positive (negative) phase indicates a substantial (weak) meridional pressure differential between Iceland and the Azores. As a result, the subsequent westerlies are stronger (weaker) than usual, and the storm track is moved northward (southward), resulting in a wet and mild (dry and cold) winter across northern Europe. Source: UCAR.

As mentioned above, the three-dimensional circulation in the SPG can be decomposed into three components: a northward transport of surface waters within the 0-1000m layer, a relatively confined downwelling north of ∼50°N, and a deep southward flow between 2000m and 3000m depth. Those three components are described separately below.

1.2.2 The surface circulation and EKE of the SPG

By integrating repeated ship-based measurements along the Greenland-Portugal OVIDE line with satellite altimetry and from previously reported observations such as CPIES array (Roessler et al., 2015) and drifter data (Flatau et al., 2003), Figure 1.4 illustrates the mean circulation in the northern North Atlantic Ocean (Daniault et al., 2016). In the subtropical

zone (south of ∼45°N), the Gulf Stream flows northeastward into the northern North Atlantic, transporting warm and salty water masses as the upper limb of the AMOC (red lines in Figure 1.4). Approaching Flemish Cap in the Newfoundland Basin, the northward flow meets the southward Labrador Current (green lines in Figure 1.4), carrying the fresh/cold waters to form the NAC. The NAC flows northeastward as a more diffuse flow, with several branches crossing the Mid-Atlantic Ridge (MAR) through distinct fracture zones. Further downstream, the northern NAC branch flows cyclonically around the Iceland basin; the central NAC branch corresponding to the Sub-Arctic Front (SAF) flows around the Rockall Plateau; and the southern NAC branch crosses MAR and splits into two branches, with the northern branch joining the central NAC and the southern branch transporting southward to the Western European Basin.

After crossing the Reykjanes Ridge (RR), the branch of the NAC flowing northward in the Irminger Current recirculates southward to flow along the coast of East Greenland (EG) as the East Greenland Current/Irminger Current (EGC/IC, Lherminier et al., 2007). On the inner shelf, the East Greenland Coastal Current (EGCC) transports cold and fresh Arctic waters (green lines in Figure 1.4). Near Cape Farewell (CF), the EGC/IC partly recirculates to form the Irminger Gyre, a narrow cyclonic recirculation (Våge et al., 2011, orange lines in Figure 1.4). The boundary currents flow northward along the coast of West Greenland (WG) in the eastern Labrador Sea after passing around CF. After passing WG, a portion of the West Greenland Coastal Current (WGCC) flows north along the coast into the Davis Strait (DVS). The remainder of the WGCC and the West Greenland Current (WGC) flow cyclonically around the rim of the Labrador Sea (Cuny et al., 2002). The WGCC combines with the cold and fresh Labrador Current from DVS and continues southward over the western Labrador Sea margin until Flemish Cap.

Figure 1.5(a) shows the time-mean distribution of sea surface geostrophic currents derived from the AVISO-CMEMS altimetry dataset. It depicts the coherent boundary current flowing parallel to the topography (red line). The fastest boundary currents travel at roughly 0.20–0.35 $\mathrm{m/s}$ along the Greenland and Labrador coasts. The southerly flow along the east Greenland shelf can exceed 0.35 $\mathrm{m/s}$. Along western Greenland, the circulation is cyclonic with a

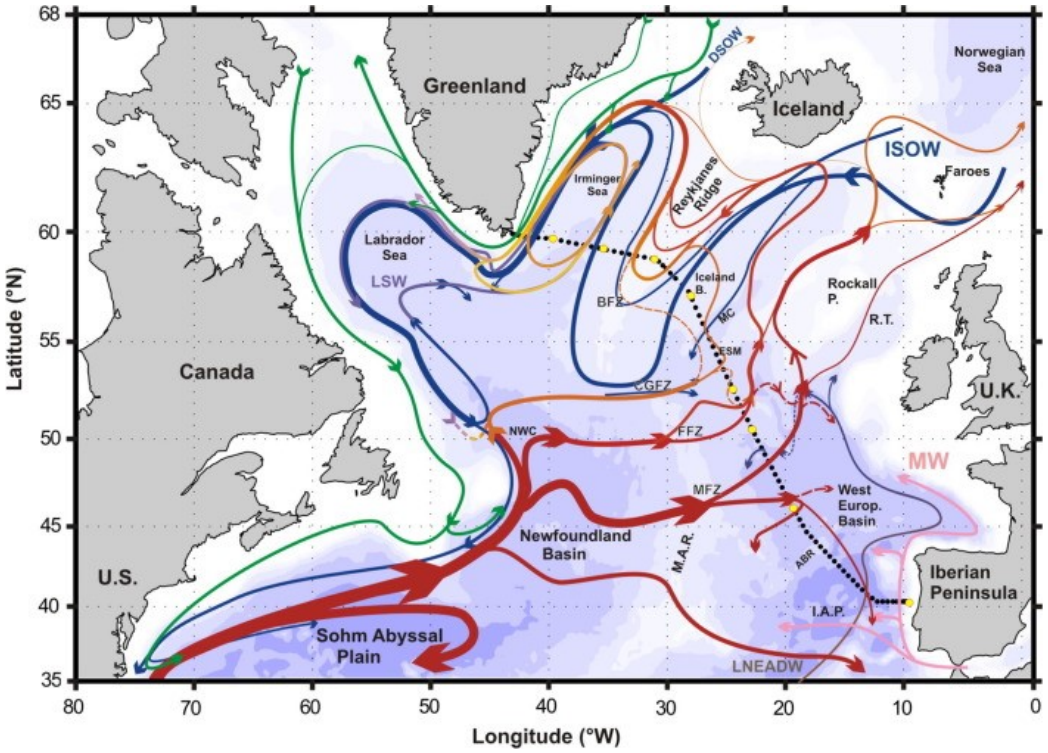

Fig. 1.4 Schematic of the large-scale circulation in the Subpolar North Atlantic with OVIDE hydrographic station locations (black dots). Bathymetry is depicted in color, ranging from 100 m, 1000 m, and every 1000 m below 1000 m. Azores-Biscay Rise (ABR), Bight Fracture Zone (BFZ), Charlie-Gibbs Fracture Zone (CGFZ), Faraday Fracture Zone (FFZ), Iberian Abyssal Plain (IAP), Maury Channel (MC), Maxwell Fracture Zone (MFZ), Mid-Atlantic Ridge (MAR), Northwest Corner (NWC), Rockall Plateau (Rockall P.), and Rockall Trough (RT) are the topographical features. The major related water masses are indicated: Denmark Strait Overflow Water (DSOW), Iceland-Scotland Overflow Water (ISOW), Labrador Sea Water (LSW), Mediterranean Water (MW), and Lower North East Atlantic Deep Water (LNEADW), or Lower Deep Water (LDW). Image Credit: Daniault et al., (2016).

boundary current that becomes increasingly narrow because of the steep topography. The boundary current widens significantly in the northern part of the Labrador Sea, where the slope is gentler. Along the rim of the Labrador Sea (isobath 3000 m), the flow recirculates cyclonically (orange line). The averaged SST map displays warm subtropical surface waters in the eastern SPG and cold subpolar and Arctic surface waters along the western boundary.

Observational and modeling studies have highlighted the high levels of eddy kinetic energy (EKE) at some specific sites of the SPG (e.g., Gascard and Clarke, 1983; Lilly et al.,

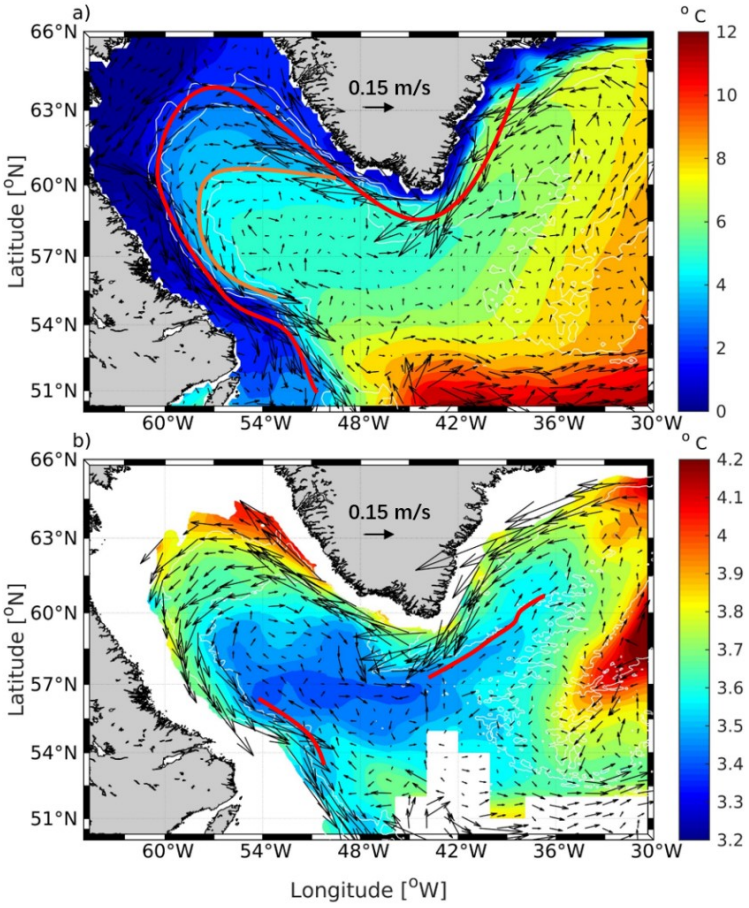

Fig. 1.5 (a) The mean velocity vectors at the sea surface (2002-2019) computed from the AVISO-CMEMS dataset and (b) at 1000 m depth computed from the ANDRO dataset. The color map illustrates the mean SST and 1000m temperature field during 2002-2019, respectively derived from the SST CCI dataset and an Argo-based dataset produced from a specific optimal interpolation method (see more details in Chapter 2), respectively. Some of the circulation paths are denoted by colored lines. The region indicated by the blank field in panel (b) is not the area of our interest and is therefore not interpolated.

1999; Chanut et al., 2008; Fischer et al., 2018). The altimetry-based surface EKE provides valuable information about the spatial distribution of intense turbulent activity over the upper water column (Figure 1.6). There are several EKE hot spots along the continental slope of the western Greenland boundary, along the western flank of RR, and along the path of the NAC south of 53°N. The latter shows the highest EKE values, exceeding 200 cm^2/s^2. The second strongest EKE is located at the downstream end of steep topographic slope along

west Greenland, where Irminger Current and West Greenland Current instabilities and eddy formation are known to occur (Lilly et al., 2003; Katsman et al., 2004). This EKE maximum exhibits relatively substantial values exceeding 60 cm^2/s^2 and encompasses a significant portion of the Labrador Sea's interior due to the Irminger rings propagation. Farther away from the coast, the eddy activity decays rapidly. There is also a mid-basin EKE maximum in the Irminger basin, with values around 50 cm^2/s^2, and smaller but non-negligible mesoscale activities along the boundary current of the Irminger Sea, around CF, and at the Labrador Sea exit ($\sim$30 cm^2/s^2).

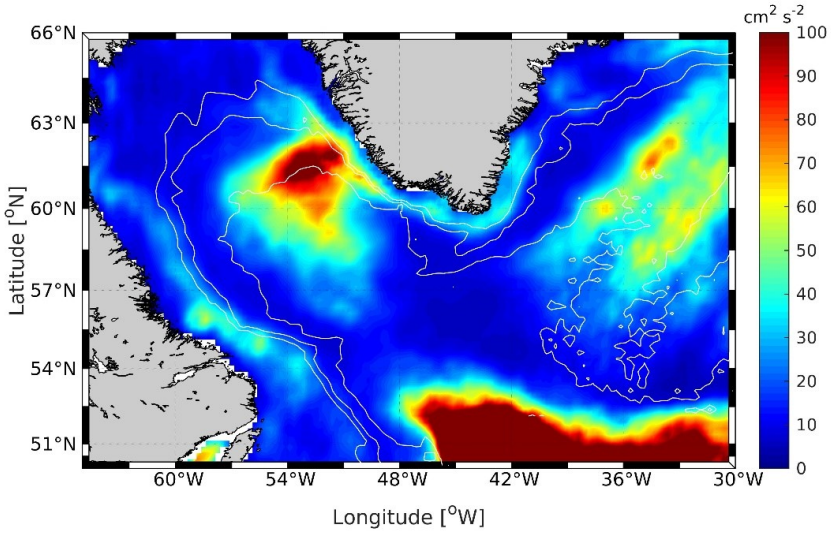

Fig. 1.6 The sea surface eddy kinetic energy field (EKE) computed from the AVISO-CMEMS altimetry dataset during 2002-2019.

1.2.3 Water mass transformation and deep convection in the SPG

During their cyclonic routes within the SPG circulation, the upper North Atlantic Central Waters (NACW) transported by the NAC are converted to denser classes throughout both surface buoyancy fluxes and interior diapycnal mixing, and feed the lower limb of AMOC. This produces NADW which is thought to be composed of two primary components: the Labrador Sea Water (LSW) and the deeper Nordic Seas Overflow Water (OW).

The cyclonic circulation in the Labrador Sea undergoes substantial buoyancy loss to the atmosphere during winter that generates deep convective events that produce relatively cold and fresh LSW down to roughly 1500 m, but some winters down to 2000 m (Talley and McCartney, 1982; Pickart et al., 2002; Stramma et al., 2004; Yashayaev, 2007). It has been suggested that the air-sea buoyancy flux and the horizontal advection of buoyancy into the basin via boundary currents are the two most important elements influencing the variability in LSW volume and properties (Stramma et al., 2004). In the North Atlantic, the western Irminger Sea has been suggested as a second LSW formation site (Piron et al., 2016; de Jong et al., 2018). The LSW is observed to have a density (σ_1) of roughly 32.15 (kg/m³), a salinity of 34.8–34.9 and a temperature of 3–4°C in the intermediate layer (hundreds to 2000 m depth) of the OVIDE line (Daniault et al., 2016). The NAO index variations have been linked to the interannual and interdecadal variability of LSW properties, as measured by hydrographic data spanning up to 60 years (Curry et al., 1998; Stramma et al., 2004; Yashayaev, 2007; Kieke and Yashayaev, 2015).

The densest component of NADW waters is OW. These dense waters are formed in the Nordic Seas through the transformation of Atlantic water along the rim of the Nordic Seas, open-ocean convection in the Greenland Sea, and dense water production along the Arctic shelf (Rudels et al., 1999; Eldevik et al., 2009). Two main classes of overflow waters can be distinguished: the cold and saline Iceland-Scotland Overflow Water (ISOW), which enters the SPG through Iceland-Scotland ridge, recirculates around Reykjanes Ridge through Charlie-Gibbs Fracture Zone and enters the Irminger basin, and the denser (colder but fresher) Denmark Strait Overflow Water (DSOW), which constitutes the bottom layer of the Western Boundary Current through Denmark Strait (Smethie and Swift, 1989). The ISOW is observed to have a density $\sigma_0 > 27.8$ (kg/m³), a salinity > 34.94 and a temperature of 2–3 (°C) in the deep layer (below 2000 m) of the OVIDE line, whereas the DSOW has a density (σ_0) larger than 27.88 (kg/m³), a salinity of 34.8–34.9 and a temperature less than 1 (°C) (Daniault et al., 2016).

Figure 1.7 depicts a time-averaged picture of summer temperature and salinity sections obtained from the merge of AR7W and A25-OVIDE lines. The light and dense waters

respectively occupying the upper and lower AMOC branches are evident, with the steeply sloping isopycnals from Greenland to Portugal illustrating the substantial densification of surface and subsurface waters within the cyclonic circulation in the Iceland Basin and Irminger Sea. The warm and saline NACW in the upper layer (above 1000 m) is observed in the eastern SPG. In the Labrador Sea intermediate layers (above 2000 m), the patch of cold and fresh LSW water is observed to be vertically homogeneous. The LSW is also observed in the intermediate layers (1000-2000 m) of the Irminger Sea and Iceland Basin. Beneath the LSW, the cold, saline ISOW and the deep, cold DSOW waters are depicted.

1.2.4 The intermediate and deep circulation of the SPG

The above-mentioned dense water masses constitute the NADW and it is traditionally considered that. NADW leaves the formation region transported by the Deep Western Boundary Current (DWBC, blue lines in Figure 1.4). Observations at the western boundary of the North Atlantic have uncovered southward transport cores of shallower LSW and deeper OW (Talley and McCartney, 1982; Pickart, 1992; Smethie et al., 2000; Toole et al., 2017). In the eastern North Atlantic, the ISOW transport core is observed in the DWBC along the eastern flank of the RR (Saunders, 1996; Kanzow and Zenk., 2014). In the Irminger Sea, for example, the DWBC at OVIDE shows a southward transport of 9.7 ± 0.9 Sv of water denser than σ_0 = 27.8 kg/m³, which consists of downward transport of LSW (1.7±1.3 Sv) from the intermediate layer and cascading of east Greenland shelf water (2 Sv, Falina et al., 2012), northward entrainment of ISOW (2.6 Sv), and southward entrainment the DSOW (3.4 Sv, Jochumsen et al., 2012) (Daniault et al., 2016).

Recent studies, however, have demonstrated that the NADW is also exported to the subtropical gyre via interior pathways driven by eddies, suggesting that the DWBC is not the only export pathway of NADW. From 2003 to 2006, only 8% of RAFOS floats released at LSW depths in the DWBC off the coast of Labrador were able to reach the subtropical basin via the DWBC (Bower et al., 2009). Instead, the majority of RAFOS floats traveled from subpolar latitudes to the subtropical basin via internal pathways (Bower et al., 2009; Lozier, 2012).

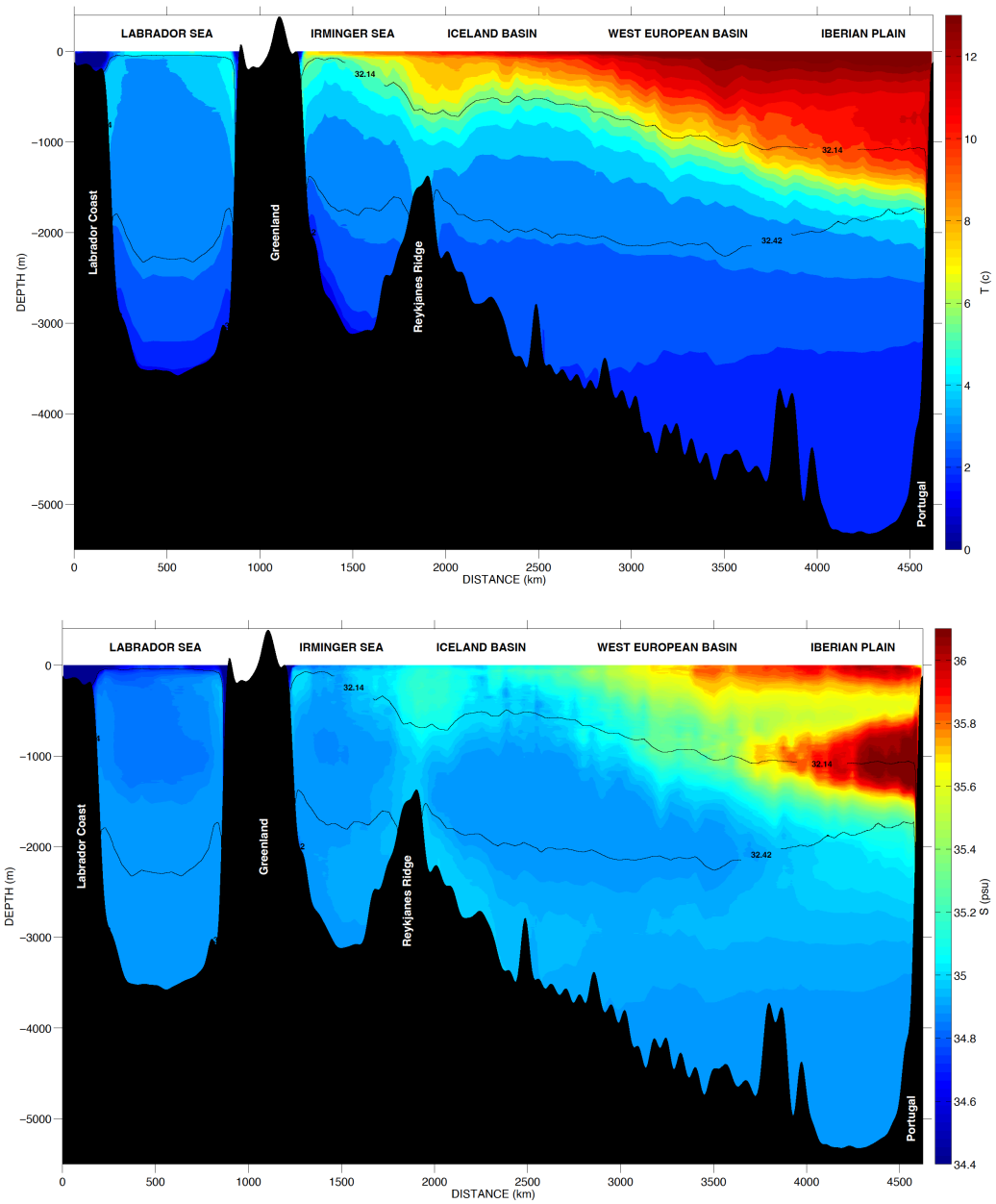

Fig. 1.7 Mean summer sections of (top) temperature and (bottom) salinity along the merged AR7W/A25-Ovide for the 2002-2010 period. The isopycnal layer σ_1 = 32.14, σ_1 = 32.42 and σ_1 = 32.54 are shown (source: Desbruyères 2013).

The 1000 m-depth circulation derived from ANDRO deep-displacement dataset (Figure 1.5b) is similar in many aspects to the surface circulation. The warm boundary current confined inshore of isobath 3000 m is observed in the Argo-based temperature field at 1000

m depth. The center of the Labrador Sea contains the coldest water, known as the cold and weakly stratified LSW. Following the mean circulation, part of the LSW in the interior of the Labrador Sea is exported southward toward Flemish Cap and northeastward towards the Irminger Sea (red lines). This is consistent with previous observations, which show that the LSW is advected at intermediate depth from the forming site not only towards the subtropics, but also eastward towards the Irminger and Iceland basins (e.g., Talley and McCartney, 1982; Yashayaev et al., 2007).

1.3 The dynamics of boundary downwelling

Considerable effort has been devoted to determining where and how diapycnal transports (i.e., in density space) occur in the SPG. Large buoyancy losses within the interior of marginal seas at high latitudes promote water mass transformation. Nevertheless, observations, theoretical investigations, and modeling indicate that the net downwelling (i.e., in depth space) within the deep convection area is insignificant (Schott et al., 1993; Marshall and Schott, 1999; Send and Marshall, 1995; Spall, 2010; Katsman et al., 2018). The locations where most sinking occurs therefore do not correlate with the regions where convection reaches its greatest depth. For the purpose of understanding the ocean's circulation and its role in climate, a better understanding of where the vertical mass fluxes occur in SPG and what physical processes control the location and amplitude of the vertical exchange is essential. This is the driving force behind my PhD research.

In recent years, interest in the processes by which upper ocean waters sink within the SPG has increased (e.g., Spall, 2003; Pickart and Spall, 2007; Holte and Straneo, 2017). In the past, it was thought that the dense waters formed through deep convection would sink in their main formation areas before spreading away within the lower limb of the AMOC (Broecker, 1987). In reality, widespread sinking in the open ocean is unlikely to occur because upwelling balances off downwelling in convective plumes (Send and Marshall, 1995). Additionally, the horizontal gradient of planetary vorticity in these extremely localized (500 km or less) deep convection regions is insufficient to counteract the vorticity changes brought on by

sinking (Spall and Pickart 2001), which must therefore occur elsewhere. Recent studies have demonstrated that at high latitudes, most of the net downwelling in the SPG that feeds the lower branch of the AMOC mainly takes place near the continental boundaries (Marotzke and Scott, 1999; Spall 2003, 2004; Pedlosky, 2003; Straneo, 2006; Cenedese et al., 2012; Katsman et al., 2018). Overflows also considerably contribute to the net sinking, reaching about 2.2 Sv through Denmark strait and 2.6 Sv through Iceland-Scotland Ridge (Katsman et al., 2018), and distinct dynamics govern them (e.g., Shapiro and Hill, 1997; Yankovsky and Legg, 2019). In this dissertation, I will focus on boundary downwelling.

1.3.1 Theoretical and experimental knowledge

Theoretical and modelling studies have demonstrated that sinking happens near continental boundaries. Spall and Pickart (2001) discussed the possible mechanisms for such a downwelling from a thermodynamic perspective. They assumed a flow along a continental boundary with a deep mixed layer subject to atmospheric cooling. In the absence of horizontal diffusion, the thermodynamic balance within this mixed layer is between the horizontal advection of boudnary density and atmospheric cooling. The former is achieved via a cross-isopycnal (i.e., along-shore) barotropic flow that balances the buoyancy loss to the atmosphere. The ensuing along-shore density gradient is the signature of a vertically-sheared cross-shore baroclinic flow in thermal wind balance. As a result, the sum of the along-shore barotropic and cross-shore baroclinic flows rotates counterclockwise with depth. The cross-shore flow impinging on the boundary causes vertical motions because of mass conservation. Therefore, net downwelling may occur near a boundary with increasing flow density, and can be approximated by the total meridional overturning $M_B = (g\Delta\rho_B h^2)/(8\rho_o f)$ as a function of the alongshore density change (Spall and Pickart, 2001). Here, g is the gravitational acceleration, $\Delta\rho_B$ is the alongshore density gradient, h is the depth at which the maximum downward mass transport, ρ_o is a reference density, and f is the Coriolis parameter. This equation highlights that the amount of sinking adjacent to continental boundary largely depends on the density change (atmosphere cooling, diffusion, and lateral eddy fluxes, for

example). This thermal wind-induced downwelling will be referred to in this dissertation as the 'baroclinic downwelling'.

As shown schematically in Figure 1.8, the along-boundary density increase due to buoyancy loss requires a vertically sheared cross-shore baroclinic flow in thermal wind balance (V_{in}) fed by the boundary current itself (U_{in}; there is no exchange with the basin interior). Therefore, the flow rotates counterclockwise with depth along the boundary within a so-called "cooling spiral". To maintain local mass conservation, a net downwelling (W) is required to balance the mass flux towards the boundary. This causes a barotropization of the boundary current, with the upper part decelerating and the lower part accelerating (Spall 2004, 2008; Straneo 2006). Without any mean mass flux between the boundary region and the basin interior, the sinking water joins the lower part of the boundary current (V_{out}) and is rapidly exported within the lower limb of AMOC (U_{out}). Thus, the along-boundary pressure (or density) gradient and associated cross-shore geostrophic flow are vital for sinking to occur.

Using an idealized model, Spall (2010) further established that downwelling within the boundary current occurs in both a diffusive boundary layer at the topographic slopes subject to buoyancy loss. The downward flow near boundaries must satisfy the ageostrophic vorticity balance in the temperature and vorticity equations. The temperature conservation equation can be written as $w\overline{T_z} = A_T \bigtriangledown^2 T$, where w is the vertical velocity, $\overline{T_z}$ is the vertical mean temperature, A_T is the vertical viscosity, and T is the temperature. This means vertical advection of the mean stratification is balanced by horizontal diffusion of density. The vorticity equation in the thin boundary layer can be written as $f\frac{\partial w}{\partial z} = -A_h \bigtriangledown^2 \xi$, where f is the Coriolis parameter, w is the vertical velocity, A_h is the lateral viscosity, and $\xi = \partial v/\partial x - \partial u/\partial y$ is the vertical component of the relative vorticity (Barcilon and Pedlosky 1967). Hence, the stretching of planetary vorticity resulting from downwelling is compensated by the dissipation of relative vorticity in a thin viscous boundary layer (Spall and Pickart, 2001; Spall, 2004, 2008).

Straneo (2006) developed a two-layer model to simulate the Labrador Sea boundary current. In this model, the boundary current exhibits a baroclinic structure as the thickness of

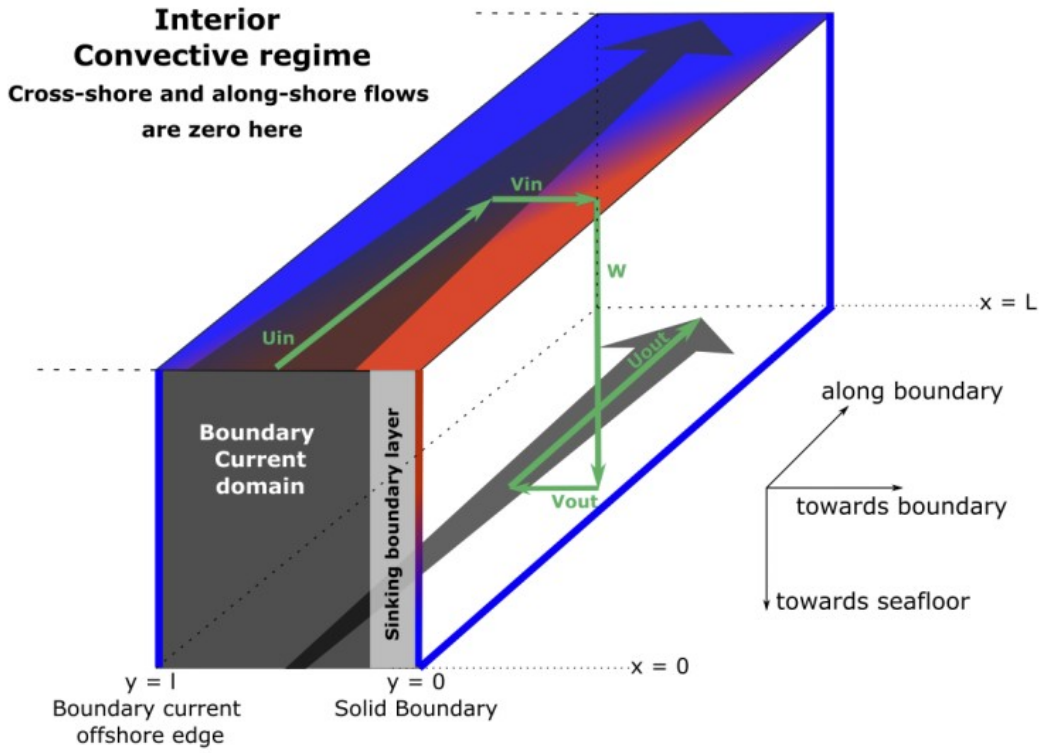

Fig. 1.8 The cooling spiral and associated boundary baroclinic downwelling. Gray arrows represent the background boundary current. The blue-red shading depicts the horizontal density fields, with the distribution of light waters in red and dense waters in blue giving rise to a cross-shore baroclinic flow in thermal wind balance (V_{in}) fed by the boundary current (U_{in}). Local mass conservation leads to a downward flow at the wall (W), a deep entrainment in the boundary current (V_{out}), and a rapid along-boundary export (U_{out}). The overall effect is a net downwelling within and a barotropization of the boundary current.

the denser water layer varies between the boundary and interior currents. Mesoscale eddies shed by the unstable boundary current remove buoyancy from the boundary and deposit it in the interior (to balance open-ocean heat loss and convection). As a result, along-shore densification of the boundary current develops. When the boundary current becomes denser along its route, an inshore flow grows, and downward transport is required to conserve mass. Tank experiments conducted by Cenedese (2012) led to the same conclusion, assuming equilibrium between interior heat loss and lateral eddy fluxes. The eddies remove heat from the boundary current, and the boundary current cools as it flows downstream. Baroclinic

downwelling occurs inside a boundary layer thickness that scales with the baroclinic Rossby radius of deformation as the upper baroclinic flow moves toward the vertical tank wall.

1.3.2 Regional patterns and seasonality

Building upon those idealized and experimental studies, recent works used more realistic or finer-resolution hindcast simulations to study the distribution, variability and mechanism of the net downwelling in the entire SPG (Katsman et al., 2018, Sayol et al., 2019) and in the Labrador Sea where strong convection occurs (Brüggemann and Katsman, 2019; Georgiou et al., 2019).

Katsman et al., (2018) estimated the net downwelling in the North Atlantic in two global ocean models: an eddy-permitting model at $1/4^o$ resolution (ORCA025) and its coarser 1^o counterpart (ORCA1). As expected, both simulations show that a strong net downwelling occurs along the boundary rather than within the convective interior (an example of ORCA025 is shown in Figure 1.9). The total net downwelling along the SPG boundary is notably stronger in the finer-resolution simulation because of the representation of part of the mesoscale activity near the boundary. The regional distribution of the sinking is significantly correlated with variations in density along the SPG boundary, except for the overflow regions.

To investigate how the net sinking in the North Atlantic changes seasonally and regionally, Sayol et al., (2019) used a high-resolution model (0.1^o at the Equator) to analyze the monthly mean fields of the net downwelling. In the whole domain, the maximum vertical transport is reasonably around -14 Sv, matching the magnitude of the meridional transport of the AMOC at 45°N. There is a seasonal variation of 10 Sv in the vertical transport, with the greatest transport occurring during the summer. The regional variability shows a more complex picture than the entire SPG: the depths at which the most considerable sinking occurs (ranging from 450 to 2000 m), the distinct spatial distribution, and the asynchronous seasonal variations of the net downwelling vary in different regions of the SPG. The authors found that 90 % of the downwelling occurs in the regions at a distance of nearly 250 km to the coast, whereas the largest seasonal variability occurs in the interior. In their study, the

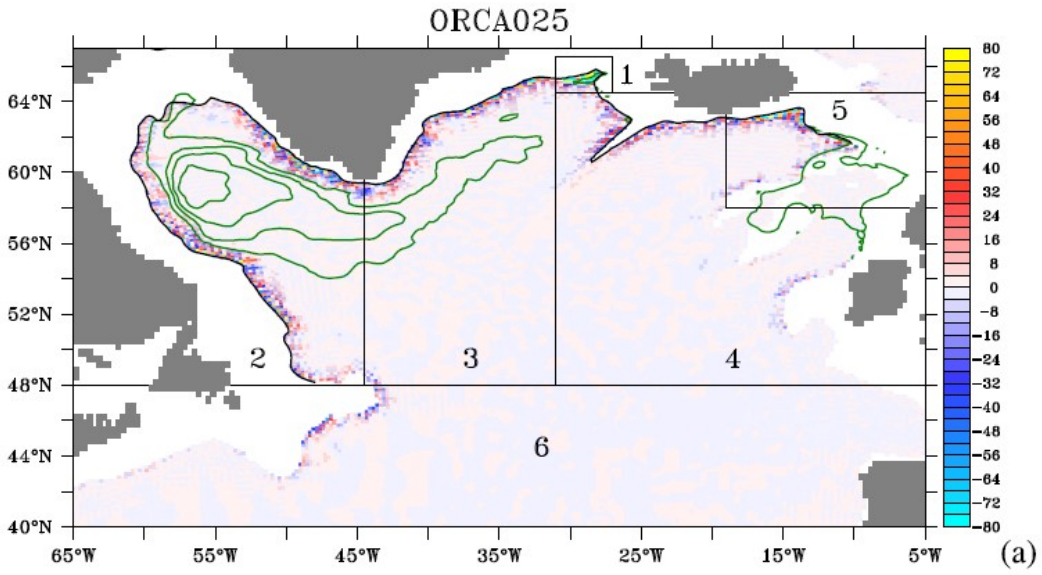

Fig. 1.9 Vertical velocity per grid box at a depth of 1061m in ORCA025 (in m/d). Blue colors denote sinking; red colors denote upwelling. Vertical motions in grid boxes containing overflows (regions 1 and 5) exceed the chosen color scale. Green contours outline the time average of the maximum mixed layer depth (contour interval is 500 m; maximum is 2,255 m), and the thick black solid line is the 1061-m isobath (source: Katsman et al., 2018).

downwelling mainly occurs within the Labrador Sea, Newfoundland basin, and across the Greenland-Iceland-Scotland Sills.

Taking the Labrador Sea as an example, Brüggemann and Katsman (2019) and Georgiou et al., (2019) looked into the impact of mesoscale eddies on boundary sinking. Brüggemann and Katsman (2019) utilized an idealized model with fine horizontal resolution (3 km) to better understand how eddies connect downwelling, overturning, and dense water pathways. They discovered two sites for the diapycnal transport. One occurs within the boundary current, where the upper water masses are transformed into denser water masses as the boundary current cools along the perimeter of the basin. The other happens in the convective interior, with the export of dense water mass to the boundary along the downward-sloping isopycnal by eddy flow. From another perspective, Georgiou et al., (2019) developed an idealized eddy-resolving model that emphasizes the significance of eddies in balancing the heat loss across the Labrador Sea and restratifying the basin's interior. The near-coast eddies shed from the boundary and carry the warm boundary water into the interior. The strongest

downwelling occurs at the lateral boundaries where the eddies form, and this downwelling is sensitive to changes in the eddy pathways.

1.4 Research questions

Previous studies have shown that most of the Eulerian downwelling connecting the upper and the lower limbs of the AMOC occurs near the subpolar North Atlantic boundaries. This downwelling is generated by the complex interactions between the atmosphere, the mean ocean circulation, and the turbulent mesoscale field. So far, theoretical and numerical works have provided insight into the spatiotemporal variability of downwelling and understanding the physical processes of those interactions. However, observational analyses are significantly lacking as of now.

This dissertation aims to increase our understanding of downwelling dynamics along the SPG western boundary (from Denmark Strait to Flemish Cap) through observational analysis of its mean pattern, seasonal variability, and driving mechanisms. In addition to evaluating the baroclinic boundary downwelling, the barotropic boundary downwelling associated with the convergence/divergence of the barotropic mean flows will also be assessed. To do so, I will take advantage of several global and regional ocean observation networks (including Argo, GO-SHIP, altimetry, mooring, and atmospheric reanalysis). This dissertation's final aim is to contribute to a better understanding of the vertical dynamics that underlines the depth-space and (part of) the density-space AMOC. In addition, understanding the downwelling processes will also be helpful in understanding how the ocean transports and sequestrates physical and biogeochemical properties (heat, freshwater, carbon, oxygen) into the deep layer over long spatial and temporal scales. Specifically, we will address three primary questions in this manuscript, as detailed below.

1.4.1 Question 1

Can we estimate the magnitude and regional distribution of the Eulerian-mean downwelling near the boundary of the subpolar North Atlantic with observations?

Using observations, this study will quantify the long-term mean SPG boundary horizontal transport and the vertical sinking. The vertical sinking will then be decomposed into barotropic and baroclinic components. A description of the regional and seasonal patterns of boundary baroclinic vertical transport will be presented. The total vertical transport will be compared to the estimates of the meridional overturning circulation in the SPG.

1.4.2 Question 2

What are the driving mechanisms for the boundary heat budget and their relative contributions?

The amount of sinking adjacent to continental boundaries is partially determined by the along-shore density (temperature) change (Spall and Pickart, 2001; Spall, 2004; Straneo, 2006). Both idealized models and observations indicate that the air-sea heat flux, lateral heat flux contributed by eddy flows, and mean flows play a significant role in regulating the temperature change of boundary currents (Spall, 2004; Palter et al., 2008). We will use observations (remote sensing measurements, hydrographic observations, and atmospheric reanalysis) to estimate the long-term mean full-depth heat budget of the SPG boundary to establish how various mechanisms affect this along-shore temperature change and, consequently, the boundary downwelling.

1.4.3 Question 3

What is the contribution of mesoscale eddies' propagation to boundary heat budget?

Eddies are extremely important for the boundary downwelling, interior convection, and heat budget in the Labrador Sea because they transport heat between the boundary and the interior (e.g., Spall, 2004; Palter et al., 2008; Saenko et al., 2014; Georgiou et al., 2019). For instance, the existence of Irminger rings can contribute to the boundary cooling in the Labrador Sea by trapping warm Irminger current water from the boundary and depositing it within the interior. In this study, we analyze the contribution of eddy heat transport through eddy propagation in a Lagrangian framework using remote sensing measurements and Argo

float observations. The thermohaline properties of the cross-shore eddies will be described. This study, in conjunction with the analysis in Question 2, will form a comprehensive basis to explain how the propagation of eddies leads to boundary cooling in various marginal seas from both the Eulerian and Lagrangian perspectives.

1.4.4 Outline of the dissertation

Chapter 2 describes the reconstruction of a boundary density field using a dedicated optimal interpolation of observational data. The observational datasets used for the volume and heat budgets of the SPG boundary are then listed. The algorithm and dataset required to detect and track coherent mesoscale eddies to study heat transport by eddy propagation are also provided. Chapter 3 answers Question 1, with a description of the long-term mean volume budget of the SPG western boundary and the associated downwelling. Chapter 4 answers Question 2, with a description of the long-term mean heat budget of the SPG boundary that controls (part of) the boundary downwelling. Chapter 5 answers Question 3, with a description of the specific role of the eddy "trapping" heat transport across the SPG boundary. Chapter 6 summarizes the key findings and presents future axes of research.

Chapter 2

Data and tools

2.1 A boundary-focused mapping of the SPG hydrographic properties

2.1.1 Input datasets

We use three datasets of temperature and salinity profiles to map the long-term mean (2002-2019) and seasonal cycle of hydrographic properties in the SPG (52–66°N; 30°W–66°W): the In Situ Analysis System-ISAS19 (Gaillard et al., 2016; Kolodziejczyk et al., 2021), the Coriolis data set for ReAnalysis-CORA (Cabanes et al., 2013; Szekely et al., 2019), and EN.4.2.2 (Good et al., 2013).

The delayed-mode ISAS19 dataset is derived from the Argo array from 2002 to 2019. The dataset provides temperature and salinity in the upper 2000 m with an accuracy of 0.01 °C and 0.01, respectively. Only the "good" and the "probably good" profiles (QC flag 1 and 2) data are used in the estimation. The Argo profiles have 152 vertical levels, with a vertical spacing of 5 m down to 100 m, 10 m down to 800 m, and 20 m below. Note that the Argo profiles display irregular and uneven distribution in the study region (Figure 2.1): the density distribution decreases close to the shelf, and few profiles are distributed inshore of the 1000-m isobath. The missing values inshore of the 1000-m isobath will have a negligible effect on the estimations of maximum vertical transport (see more details in Chapter 3).

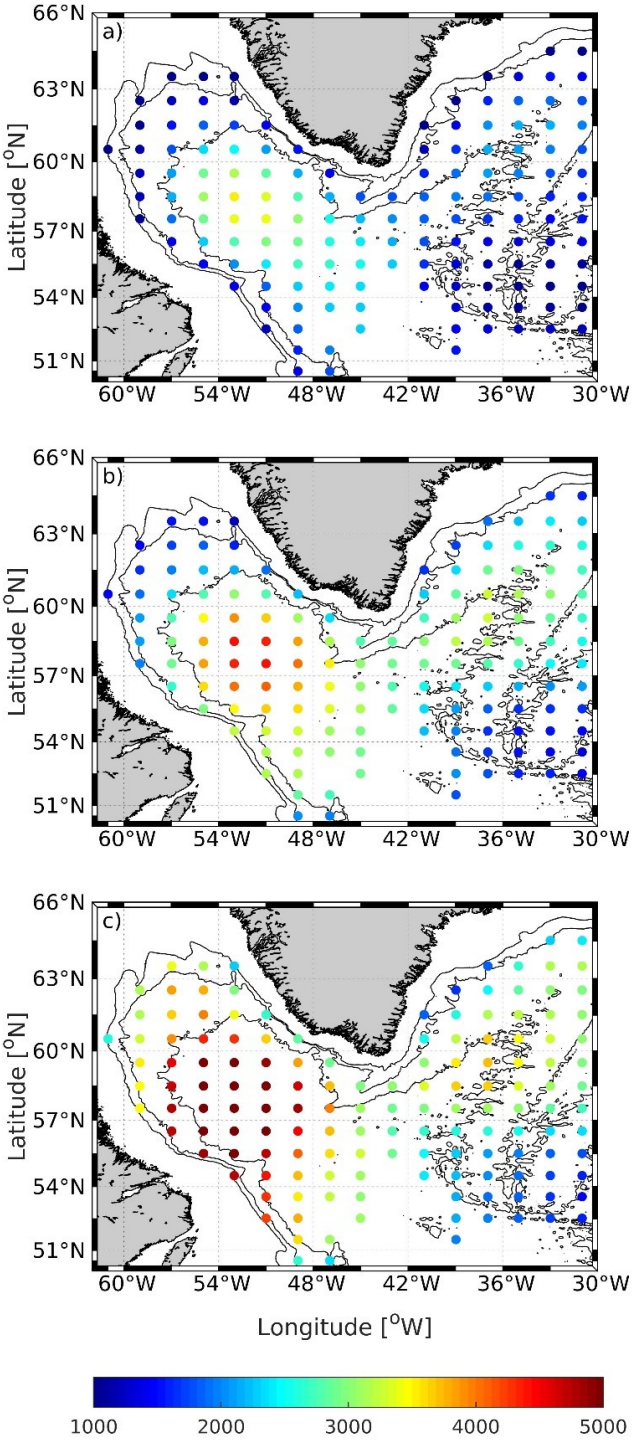

Fig. 2.1 The number of profiles in each computational box ($7.2^o \times 3.6^o$) derived from ISAS/CORA/EN4 (a/b/c) datasets between 2002 and 2019. Contours indicate isobaths 1000 m, 2000 m and 3000 m. All three datasets have an irregular and uneven distribution of profiles: the density distribution is the largest in the region with a depth of more than 3000 m and decreases toward the shelf. The ISAS dataset contains 600-3000 profiles in each bin. The CORA dataset contains 1000–4000 profiles and the EN4 dataset contains 1000–6000 profiles in each bin.

The EN4 and CORA datasets consist of temperature and salinity profiles from the Argo array and include data from moorings and shipboard full-depth CTD profiles. In particular, the EN4 dataset covers the period 1900 to 2019, and includes the World Ocean Database 2018 (WO18), Arctic Synoptic Basin Wide Oceanography (ASBO), and the Global Temperature and Salinity Profile Program (GTSPP). The CORA dataset includes all types of in-situ temperature and salinity measurements from 1990 to 2017, i.e., profilers (ARGO, CTD, etc...), surface and sub-surface time series (Thermosalinographs and surface drifters, etc...) from French projects (such as SO ARGO, SO PIRATA), European partners (such as SeaDataNet, EuroGOOS) and international projects (such as ARGO, WOD13). All the profiles of EN4/CORA will be interpolated into the same vertical resolution as that of the ISAS database. Accompanying Argo profiles, the other data types fill in the data-poor areas. The description of the three datasets is summarized in Table 2.1.

Table 2.1 Description of the datasets

Dataset	**Data sources**	**Period**
ISAS19	Argo temperature and salinity data	2002-2019
EN4 quality controlled ocean data (EN.4.2.2)	World Ocean Database 2018 (WO18), Arctic Synoptic Basin Wide Oceanography (ASBO), and Global Temperature and Salinity Profile Program (GTSPP)	1900-2019
CORA: Coriolis Ocean database for ReAnalysis	French projects (such as SO ARGO, SO PIRATA), European partners (such as SeaDataNet, EuroGOOS) and international projects (such as ARGO, WOD13)	1990-2017

2.2 Optimal Interpolation

Optimal interpolation (OI) is a widely-used tool to produce global monthly gridded temperature and salinity fields from Argo profiles (Gaillard et al., 2009). It estimates the field being

observed at a given location and time through a linear combination of the available data, as presented in Bretherton et al., (1976).

The interpolated field is the sum of a reference field (or first guess) and a linear weighted sum of the observations (such as Argo profiles):

$$X = X_{ref} + K^{OI}(Y - Y_{ref}) \tag{2.1}$$

where X and Y are the vectors of the estimated field values at grid points and observation points and X_{ref} and Y_{ref} are the vectors of the reference field values at grid points and observation points. In our estimation, we use the global climatological ISAS product as the reference field, with a $0.5^{o} \times 0.5^{o}$ grid. The OI grid horizontal resolution is set as 4 km, which enables us to refine the properties along boundaries and topographic features (such as the sharpest portions of the continental slope). The properties will remain unchanged by increasing the resolution from 4 km. For most of the domain, there are at least 10 observations by a 15 km×15 km grid box, indicating that the mapping can resolve the horizontal scale to at least 15 km. Consistent with the vertical spacing of Argo profiles, interpolation is conducted at 152 levels independently between 0 and 2000 m; the vertical spacing is 5 m down to 100 m, 10 m down to 800 m, and 20 m below. The density below 2000 m is obtained by linear extrapolation from the above 2000 m. The spatial resolution of the reference field has to be interpolated to be consistent with the resolution selected for the mapping fields. In case a value of the reference field is missing because of the land mask, we used the spatial average in the computational domain. The estimation remains close to the reference in poorly sampled areas, with the weights given by the gain matrix:

$$K^{OI} = C_{ao}(C_{oo} + R)^{-1} \tag{2.2}$$

C_{ao} is the covariance matrix between the analyzed field at grid points and observations; C_{oo} is the covariance matrix of the analyzed field at different observation points. The covariance matrices Coo and Cao are built based on the function C (dx, dy, dt), modeled as a Gaussian

function:

$$C(dx,dy) = \sigma_L^2 e^{-(\frac{dx^2}{2a^2} - \frac{dy^2}{2b^2})} \tag{2.3}$$

where σ_L is the field variance, dx and dy observation points in the meridional and zonal direction, respectively, and a, b the corresponding e folding scales. The variation in time will not be considered because we only seek to build climatological estimates.

The total variance σ for the observations is considered as the sum of three terms:

$$\sigma^2 = \sigma_L^2 + \sigma_{UR}^2 + \sigma_{ME}^2 \tag{2.4}$$

Here σ_L is computed as the variance of the anomaly relative to the monthly reference field, i.e., the variations of the annual climatic cycle. σ_{ME} is the measurement error and σ_{UR} is the unresolved small-scale processes considered as noise (also called representativeness error). The measurement error is assumed to be constant (0.01° and 0.01 psu). For C_{ao} the σ_{UR} and σ_{ME} are assumed to be zero.

The normalized weights give the other two variances as a function of the total ocean variance:

$$\begin{aligned} \sigma_L^2 &= W_1 \sigma_{ocean}^2 \\ \sigma_{UR}^2 &= W_2 \sigma_{ocean}^2 \end{aligned} \tag{2.5}$$

Since a large part of the oceanic variability cannot be resolved by Argo profiles with a limited resolution, for this analysis, the weights are set to W_1=0.7, W_2=0.3 over the computation domain.

The R error matrix combines the representativeness (unresolved) error σ_{UR} and the measurement error σ_{ME} which are assumed diagonal:

$$R_i i = \sigma_{UR_i}^2 + \sigma_{ME_i}^2 \tag{2.6}$$

The conventional OI algorithms for climatological mapping use circle-shaped Gaussian correlation functions (see Gaillard et al., 2016 for additional details). Here, we employ an elliptic Gaussian correlation function parallel to isobaths, with length scales of 67 km (cross-

shore axis) and 145 km (along-shore axis) to account for the larger (smaller) correlation length scales in the along-shore (cross-shore) directions (Figure 2.2). The ellipse's major axis (b) should be parallel to the boundary, providing profiles placed along the boundary current's primary path with larger weights in the estimation, whereas the minor axis (a) should be perpendicular to it. The rotation is implemented by modifying the dx and dy in the rotating coordinates (Figure 2.2):

$$\begin{aligned} dx' &= dL \times cos(\alpha - \beta) \\ dy' &= dL \times sin(\alpha - \beta) \end{aligned} \tag{2.7}$$

where $dL = \sqrt{(dx^2 + dy^2)}$,$\alpha = arctan(\frac{dx}{dy})$ and β the rotation angle clockwise to the y axis. In each computational box, the rotation angle β is obtained from the slope of the polynomial function evaluated from the nearest isobath.

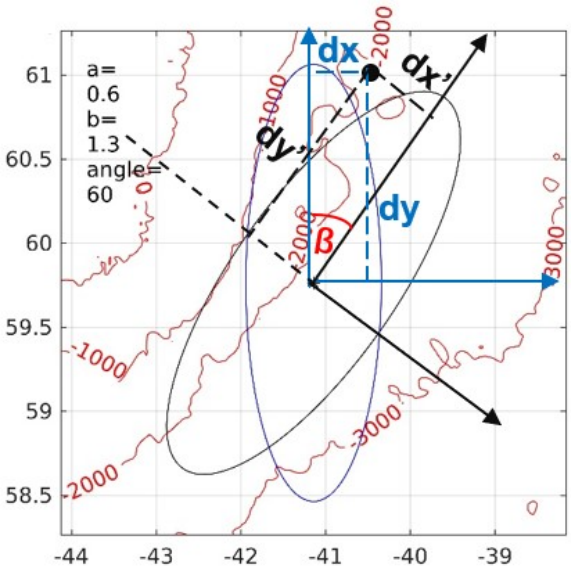

Fig. 2.2 The schematic diagram of the rotating ellipse applied in the covariance function of OI: the ellipse rotates by β, parallel to the 2000 m isobath; dx and dy are the distances in the original coordinates, whereas dx' and dy' are the distances in the rotating coordinates. The characteristic ellipse is given by an example with a = 0.6 (67km), b = 1.3 (167km) and β = 60°. Contour lines are isobaths of 0, -1000 m, -2000 m, -3000 m.

The overall mapping methodology was eventually validated against independent properties along the OVIDE and AR7W hydrographic lines (see Appendix Figure S2–S5 in Supporting Information). The final multiproduct mappings of temperature and salinity

Winter (January–March), Spring (April–June), Summer (July–September), and Autumn (October–December) are the average of the fields derived independently from the three datasets. The climatological OI-based full-depth density field based on ISAS19 is used in Chapter 3 to estimate the vertical transport of the SPG boundary and in Chapter 4 to evaluate the boundary's heat budget. The density fields derived from the other two datasets (EN.4.2.2 and CORA) will be used for the uncertainty estimates.

2.3 Other observational datasets

2.3.1 ANDRO

The ANDRO dataset used in this study is an Argo-based deep displacement dataset (Ollitrault et al., 2021). It includes pressure, temperature, salinity, and deep and surface velocities. The ANDRO dataset provides the current velocity at the float's parking pressure (typically 1000 dbar) with the two surface location estimates (the first fix during the current cycle and the last spot during the previous cycle). It spans the period 2002 – 2019. In Chapter 3, the ANDRO dataset is used to map the mean velocity at 1000 m depth in the subpolar North Atlantic region. In Chapter 4, it is used to compute the eddy heat flux at 1000 m for a heat budget purpose. The mean velocity and eddy heat flux at 1000 m depth are then used as the reference level for the full-depth velocity or flux calculation along the boundary of SPG. The ANDRO dataset is freely available at http://wwz.ifremer.fr/lpo/.

2.3.2 CMEMS

The AVISO team provided along-track and gridded products of the global ocean's anomalous sea level and surface geostrophic velocities. The Copernicus Marine and Environment Monitoring Service (CMEMS) are now in charge of the processing and distribution of these products. We use daily altimetry-derived (mean dynamic topography-MDT) sea surface geostrophic velocity and sea level anomaly (SLA) data from the CMEMS altimetry dataset from 2002 to 2019, with a resolution of 0.25°×0.25°. The daily geostrophic velocity field

produced from altimetry is used to depict the mean and variability of the subpolar North Atlantic surface circulation in Chapter 1. The eddy heat flux at the sea surface used in Chapter 4 is computed by merging the sea surface velocity field from the CMEMES dataset with the altimetry-based SST dataset (2.2.3). The daily SLA maps are also utilized to detect and track mesoscale eddies in Chapter 5. The data can be downloaded at https://climate.copernicus.eu/.

2.3.3 SST CCI

This dataset is a daily L4 sea surface temperature (SST) product of the Climate Change Initiative (CCI) project built from data collected by a variety of instruments (such as Advanced Very High Resolution Radiometer and Along Track Scanning Radiometer SST) during 2002-2019 with a spatial resolution of $0.05° \times 0.05°$. We use this SST dataset in conjunction with altimetry data to determine surface mean and eddy heat fluxes in Chapter 4. We also match the SST of each detected eddy on a given day using daily SST in Chapter 5. The data is available in Copernicus Climate Change Service Climate Data Store (CDS), https://cds.climate.copernicus.eu/cdsapp!/home.

2.3.4 OSNAP

The moorings of the Overturning in the Subpolar North Atlantic Program (OSNAP) that were deployed across the western Greenland boundary in the Labrador Sea (OSNAP WG) and eastern Greenland boundary in Irminger Sea (OSNAP EG) from August 2014 to September 2018 are utilized to obtain a typical vertical structure of the eddy heat flux along the SPG boundary. Each mooring is equipped with several MicroCATs-Aquadopps (CM) pairs that measure temperature and salinity, and horizontal velocity at depths ranging from 100 m -250 m to the bottom with a 250 m interval. The velocity in the layer above the shallowest CM is measured using an upward-looking ADCP. The temperature and current velocity measurements from OSNAP moorings are processed to obtain a typical vertical profile of the cross-shore eddy heat flux in Chapter 4. The OSNAP mooring dataset can be downloaded at https://research.repository.duke.edu/collections/1z40kt318?locale=en.

2.3.5 ERA 5

The hourly reanalysis estimates of air-sea heat flux from ERA 5 between 2002 and 2019 with a resolution of $0.5° \times 0.5°$are used in the heat budget calculation in Chapter 4. The Ekman transport included in the volume budget (Chapter 3) and heat budget (Chapter 4) is estimated using the 10-m wind velocity from ERA 5. The data is available from Copernicus Climate Change Service Climate Data Store (CDS), https://cds.climate.copernicus.eu/cdsapp#!/home.

2.4 Eddy tracking dataset and algorithm

We use a global daily mesoscale ocean eddy dataset that covers 2002-2014 (Faghmous et al., 2015) to detect and track eddies in the subpolar North Atlantic that have a lifetime greater than 5 days. This dataset contains mesoscale eddy properties (such as eddy central location, time, polarity, size, and amplitude) and eddy trajectories that persist for at least two days with a radius larger than 20 km, as identified in the CMEMS SLA dataset from 1993 to 2014. We then use the provided eddy tracking algorithm to identify and track eddies in the CMEMS daily SLA map from 2015 to 2019. Instead of using the closest eddy strategy to detect the eddy (e.g., Chelton et al. (2011)), this algorithm defines eddies as the outermost closed-contour SLA with a single SLA extreme (maximum/minimum) inside. It then builds up the exact contour, which guarantees only one extreme point in the eddy. For each eddy at time step k, it identifies the closest eddy with similar features (such as size and amplitude) at time step k+1 as part of the trajectory of the same eddy. To reduce the searching area, an estimate of an eddy's anticipated propagation speed—the phase speed of nondispersive baroclinic Rossby waves is used (Faghmous et al., 2015).

Chapter 3

Observation-based Eulerian mean downwelling in the western Subpolar North Atlantic

In this Chapter, we first reconstruct the long-term (2002-2019) full-depth boundary current velocities using the Argo-based ANDRO deep displacement records at 1000 dbar and the OI-based boundary density field presented in Chapter 2. Then, we estimate the associated Eulerian mean boundary downwelling from a volume budget and discuss the regional variations of the boundary downwelling. We finally compare our results to independent cross-basin meridional transport estimations.

3.1 Introduction

Through its role in redistributing heat, freshwater, and chemical properties between low and high latitudes, the Atlantic Meridional Overturning Circulation (AMOC) is a critical component of Earth climate system. Warm and saline waters flow from low latitudes toward the poles in the AMOC upper limb. Following significant mixing-driven and surface-forced water mass transformation, colder and fresher waters are returned southward as intermediate and deep-water masses within the AMOC lower limb. Climate model studies indicate that the AMOC could weaken significantly over the next century (IPCC, 2021), and significant efforts have been consequently made over the last decades to understand the processes maintaining

the AMOC and the drivers of its variability (e.g., Lozier et al., 2012; Buckley and Marshall, 2016; Johnson et al., 2019).

The vertical connection between the upper and lower limb of the AMOC and the underlying mechanisms are still under investigation (e.g., Spall and Pickart, 2001; Pedlosky, 2003; Straneo, 2006; Spall, 2010; Brüggemann and Katsman, 2019). The location of this downwelling has long been associated with regions of intense open-ocean convection, such as the Labrador and Irminger seas, where dense and deep waters form because of convective mixing. However, deep convection regions have large vertical heat and salt transports but negligible vertical mass transport (in depth space) (Marshall and Schott 1999; Send and Marshall 1995; Spall 2003, 2004). Instead, the Eulerian-mean downwelling connecting the AMOC upper and lower limbs should occur near continental boundaries, where geostrophy breaks down and a new balance between vertical stretching of planetary vorticity and dissipation of relative vorticity in a thin boundary layer emerges (Spall, 2010). Notably, the dynamics of Eulerian-mean downwelling are primarily governed by the large-scale geostrophic flow, so the details of the thin boundary layer where vorticity is ultimately dissipated do not need to be resolved for capturing the overall impact of downwelling (Spall, 2008).

One widely known mechanism that contributes to the boundary downwelling is the onshore baroclinic transport on the top of the ocean. Previous research has established that the onshore baroclinic transport and the associated downwelling occur through modification of the boundary current properties in a region is undergoing buoyancy loss (e.g., Spall and Pickart, 2001; Straneo, 2006; Spall, 2010; Cenedese, 2012; Katsman et al., 2018). Several processes, including surface buoyancy flux or mean and eddy-driven heat advection, likely contribute to boundary buoyancy loss. While the respective contribution of these processes is regionally unknown, lateral eddy-driven heat exchanges – generated by the lateral density gradients and baroclinic instability – are widely acknowledged as important in densifying the boundary region, as seen for instance, in the Labrador Sea (Lilly et al., 2003; Katsman et al., 2004). Eddies contribute to interior downwelling and boundary current barotropization through along-isopycnal water masses stirring and exchange between the boundary current and the interior (Khatiwala and Visbeck, 2000; Brüggemann and Katsman, 2019).

The convergence/divergence of horizontal barotropic flows within the boundary based on the mass balance is an additional potential mechanism for driving the boundary vertical transport that has not previously been studied. In the SPG boundary, the interaction between cross-shore flow and the sloped bottom is the most possible driver to the convergence or divergence of horizontal flows, as a result of the observed strong lateral barotropic mean flow between the boundary currents and the interior of SPG. One example is the recirculation of southward Irminger Gyre along the western Greenland current (6.8$\pm$1.9 Sv, Våge et al., 2021). The other example is the offshore transport of western Greenland Current over the Eirik Ridge (10.9$\pm$5.9 Sv, Holliday et al., 2009). When such near-barotropic inshore/offshore transport encounters/leaves the bottom slope, significant upward/downward transport above the slope may arise.

Recent studies have used realistic and high-resolution model simulations to investigate the net downwelling in the entire Subpolar Gyre (SPG) (Katsman et al., 2018, Sayol et al., 2019) or in marginal seas characterized by high convective activity, such as the Labrador Sea (Brüggemann and Katsman 2019; Georgiou et al., 2019). Katsman et al. (2018) and Sayol et al. (2019) confirmed that the bulk of the vertical volume flux occurs along the boundary and that its spatial integral in the SPG is close to the magnitude of the AMOC – the zonally-integrated meridional flow – at the southern exit of the SPG (i.e., near 45°N). Katsman et al. (2018) further demonstrated that the amount of boundary sinking is correlated to along-shore density changes, except in those regions with deep overflows. The vertical transport in Labrador Sea was particularly studied by Brüggemann and Katsman (2019) and Georgiou et al. (2019), who showed the importance of atmospheric forcing and mesoscale eddies in balancing heat loss over the Labrador Sea and in triggering boundary downwelling along steepened isopycnal surfaces.

Estimates of boundary-focused sinking and its associated mechanisms from *in situ* observations are still lacking. Here we estimate for the first time the long-term (2002-2019) Eulerian-mean along-boundary downwelling and its spatial and seasonal distribution within the western SPG, from Denmark Strait (DKS) to Flemish Cap (FC), based on the vertical structure of the volume budget in SPG boundary. The long-term mean density field is firstly

derived from global ocean monitoring programs (such as Argo and Go-Ship; see Chapter 2). In combination with surface Ekman transport, we then construct the full-depth boundary current velocities by referencing the hydrography-derived mean baroclinic profiles to the mean absolute geostrophic velocity at 1000 m derived from Argo float displacements. The relative contribution of baroclinic and barotropic flows to regional vertical transport is then examined. Section 3.2 explains the computation of the full-depth mean velocities and the configuration of SPG boundary volume budget. Section 3.3 discusses the volume budget and the associated vertical transport estimations in the SPG boundary. We summarize our findings in section 3.4.

3.2 Methodology

3.2.1 Calculation of absolute geostrophic velocity at 1000 m

The Argo-based ANDRO deep displacement datasets between 2002 and 2019 are used to quantify the long-term mean velocity at 1000 m. ANDRO provides the current velocity at the float's parking pressure ($\sim$1000 dbar) and at locations determined from the preceding two surface location estimates. We utilize simple Eulerian averages of velocity within a 0.5° latitude by 1° longitude grid ($\sim$50 km square bins) to derive the mean (Figure 3.1). For most of the domains, each grid box contains more than ten float displacements. We then project the velocities perpendicular and parallel to the isobaths to obtain along-shore and cross-shore velocities. The sign convention is: in the along-shore direction (x), a positive sign is oriented downstream of the mean boundary current; in the cross-shore direction (y), a positive sign represents flow entering the interior, and a negative sign represents flow entering the boundary region; in the vertical direction (z), upward flow is positive. After processing the ANDRO dataset, two-dimensional 0.5°×1° gridded fields of mean along-shore and cross-shore velocities at 1000 m depth in SPG are obtained.

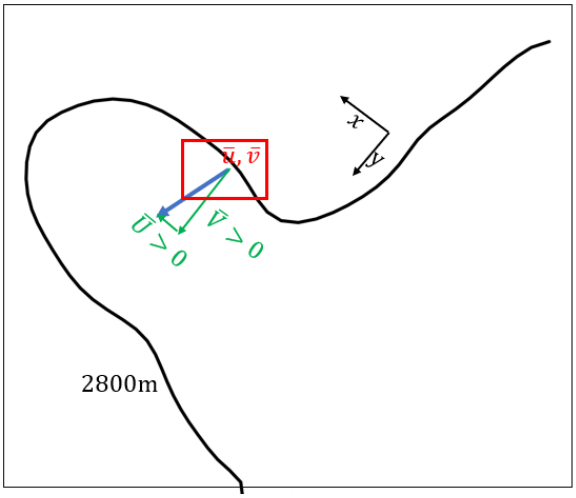

Fig. 3.1 Schematics describing the projection. The mean flows $\overline{u}$(eastward velocity) and $\overline{v}$ (northward velocity) are obtained from the average of the floats in the red grid. The velocity is decomposed into its along-isobath ($\overline{U}$) and cross-isobath ($\overline{V}$) components (green arrows).

3.2.2 Volume budget of SPG boundary

The box configuration used for the volume budget is shown in Figure 3.2. The limits are between DKS and FC in the x-direction, between isobath 1000 and 2800 m in the y-direction, and between the bottom and surface in the z-direction. We will refer to this region as the SPG boundary hereafter. Several smoothed isobaths are selected between 1000 and 2800 m with a 100-m spacing. Each isobath consists of 67 points (gray points in Figure 3.2) that are spaced $\sim$50 km apart to correspond to the resolution of the gridded ANDRO dataset. This defines 66 small boxes (Figure 3.2). The velocities at 1000 m depth of the given points along the isobaths are then linearly interpolated from the two-dimensional gridded fields. The missing values of some points close to the coast will be interpolated linearly from the values of the nearby points at the same isobath.

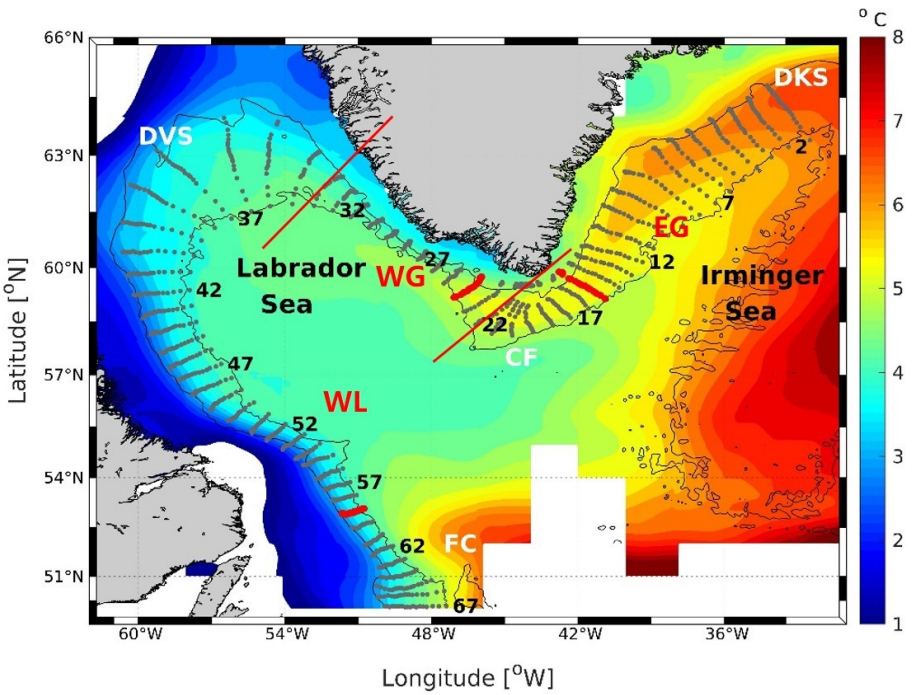

Fig. 3.2 The horizontal plane configuration of the boxes. The gray dots extracted from each isobath between 1000 and 2800 m with a spacing of 100 m define 66 boxes with a width of nearly 50 km. The color map is the Argo-observed time-mean (2002–2019) temperature field averaged in the upper 300 m as obtained from an optimal interpolation tool specifically designed for the boundary region (see Chapter 2). Key locations are noted: Denmark Strait (DKS), Cape Farewell (CF), Davis Strait (DVS), and Flemish Cap (FC). The red lines delimit three distinct regions: the eastern Greenland region (EG) from DKS to CF, the western Greenland region (WG) from CF to DVS and the western Labrador Sea region (WL). The red dots represent the transects across which we compare the along-shore transport to earlier publications.

The full-depth absolute along-shore/cross-shore velocities of the SPG boundary $\overline{U}/\overline{V}(x,y,z)$ (unit: m/s) are calculated using a reference level of 1000 m at each point:

$$\begin{aligned}\overline{U}(x,y,z) &= \overline{U}(x,y,1000m) - \overline{U}_{baroclinic}(x,y,1000m)\\ &\overline{U}_{baroclinic}(x,y,z) + \overline{U}_{ek}(x,y,z_{surf})\\ \overline{V}(x,y,z) &= \overline{V}(x,y,1000m) - \overline{V}_{baroclinic}(x,y,1000m)\\ &\overline{V}_{baroclinic}(x,y,z) + \overline{V}_{ek}(x,y,z_{surf})\end{aligned} \tag{3.1}$$

where $\overline{U}/\overline{V}(x,y,1000m)$ are the mean along-shore/cross-shore velocities at 1000 m depth interpolated from the ANDRO gridded maps. The baroclinic component of the along-shore (cross-shore) velocity relative to the sea surface ($U_{baroclinic}$ and $V_{baroclinic}$) is obtained from the density gradient across (along) the boundary using the OI-based full-depth density fields described in Chapter 2.

$$\begin{aligned}\frac{\partial \overline{U}_{baroclinic}(x,y,z)}{\partial z} &= \frac{g}{\rho_0 f}\frac{\partial \rho(x,y,z)}{\partial y} \\ \frac{\partial \overline{V}_{baroclinic}(x,y,z)}{\partial z} &= -\frac{g}{\rho_0 f}\frac{\partial \rho(x,y,z)}{\partial x}\end{aligned} \tag{3.2}$$

where g is 9.8 $\mathrm{m/s^2}$, *rho* is the in-situ density field derived from OI, ρ_0 is 1024 $\mathrm{kg/m^3}$, and f is the Coriolis coefficient ($1.26 \times 10^{-4} s^{-1}$). In this case, the density ρ at the center between the two adjacent points (in order to determine the gradient) in SPG is linearly interpolated from the 4 km gridded density field.

$\overline{U}_{ek}/\overline{V}_{ek}(x,y,z_{surf})$ indicate the Ekman velocity at the sea surface (0-30 m) derived from estimates of the Ekman transport:

$$\begin{aligned}\overline{U}_{ek}(x,y,z_{surf}) &= \frac{M_x}{30} = \frac{\tau_y}{30\rho_{surf} f} \\ \overline{V}_{ek}(x,y,z_{surf}) &= \frac{M_y}{30} = -\frac{\tau_x}{30\rho_{surf} f}\end{aligned} \tag{3.3}$$

where M_x,M_y indicate the Ekman transport in the along-shore and cross-shore direction, which is assumed to be evenly distributed within the first 30 m of the water column. The along-shore wind stress τ_x is calculated as $\tau_x = \rho_a C_D \overline{U}_{wind}|\overline{U}_{wind}|$, where ρ_a is the air density (1.2 $\mathrm{kg/m^3}$), C_D is the drag coefficient (1.2×10^{-3}) and $\overline{U}_{wind}$ is the along-shore 10-m wind velocity averaged from 2002-2019 ERA5 field. ρ_{surf} is the surface water density averaged from the upper 30 m OI-based density field.

For each region, volume conservation requires that the divergence of the along-shore barotropic flow balances the divergence of the cross-shore barotropic flow (unit: Sv):

$$\sum_{i=1}^{max-1} \int_0^h \int_0^w \Delta \overline{U}_i dy dz = -\sum_{i=1}^{max-1} \int_0^h \int_0^l \Delta \overline{V}_i dx dz \tag{3.4}$$

where dx, dy represent the integral widths in the x, y directions (l, w) of each box, and dz indicates the integral thickness of the full water column (h). The i denotes the locations

of the transects with a total number of *max*, and a total number of boxes equal to $max-1$. $\iint \Delta\overline{U}dydz$ indicates the divergence of the along-shore transport of each box (the transects along the boundary), whereas $\iint \Delta\overline{V}dxdz$ is the divergence of the cross-shore transport of each box between the deepest and shallowest isobaths, i.e., isobaths 2800 m and 1000 m. The sum over all boxes of the two divergence terms is then used to evaluate the closure of the volume budget of each of the SPG boundary region. If the budget does not close, an adjustment to the cross-shore velocity $\overline{V}$ along the deepest isobath (such as isobath 2800 m) will be made (details will be provided in Section 3.2.1).

Under the rigid-lid assumption, volume conservation between the surface and a particular depth h_c implies:

$$\sum_{i=1}^{max-1}\int_0^{h_c}\int_0^{w}\Delta\overline{U}_i dydz+\sum_{i=1}^{max-1}\int_0^{h_c}\int_0^{l}\Delta\overline{V}_i dxdz=\sum_{i=1}^{max-1}\int_0^{w}\int_0^{l}\Delta\overline{W}_{hc}dxdy \tag{3.5}$$

Here, dz indicates the integral depth with the limit of h_c. The term on the rhs corresponds to the vertical transport across h_c. When the lhs is positive (negative), it indicates that the divergence (convergence) of the horizontal transport in the upper layer above h_c is compensated by upwelling (downwelling), with $W_{hc}>0$ ($W_{hc}<0$). In this study, the depth limit h_c will range from 0 m to 2400 m with an interval of 100 m (the reason will be provided later).

For each point of the SPG boundary, the horizontal velocities $\overline{U}$ and $\overline{V}$ can be decomposed as follows:

$$\overline{U}(x,y,z)=\overline{\overline{U}(x,y)^z}+U(x,y,z) \tag{3.6}$$

where $\overline{\overline{U}^z}$ represents a depth average. The first term on the rhs is the depth-independent barotropic velocity, and the residual $U(x,y,z)$ is the depth-dependent baroclinic velocity. The contribution of barotropic (BT) and baroclinic (BC) flows to the vertical transport of SPG can subsequently be determined by substituting the terms in Equation 3.5.

The error estimates for the vertical transport are:

$$\varepsilon=\sqrt{\varepsilon_{bt}^2+\varepsilon_{bc}^2} \tag{3.7}$$

The uncertainties for the barotropic transport ε_{bt} and baroclinic transport are ε_{bc} computed using a Monte Carlo approach. For ε_{bt}, we use the eastward and northward velocity errors in the ANDRO deep displacement dataset to randomly disturb the velocity of each float and recompute the gridded fields of mean velocities at 1000 m depth. 1000 bootstrap estimates of the velocity fields at 1000 m depth are then produced using 1000 iterations. The uncertainties for the BC transport ε_{bc} are obtained from the disturbed OI-based density field. We use the errors estimated from the OI calculation, which depend on the distribution density and variability of adjacent profiles, to randomly perturb the four-season temperature and salinity fields and recompute baroclinic velocity fields. 12000 bootstrap estimates of the density in four seasons are calculated for the three datasets. Both the BT and BC transport errors are considered two times the standard deviation of the bootstrap estimates.

3.2.3 The decomposition of the along-boundary density field

Since the amount of BC downwelling is expected to be controlled by the along-shore density gradient, we decomposed the density change using a linear equation of state to extract the relative importance of temperature and salinity changes:

$$\rho - \rho_{DKS} = -\alpha(T - T_{DKS})\rho_{DKS} + \beta(S - S_{DKS})\rho_{DKS} \tag{3.8}$$

The α and β are the thermal expansion and saline contraction coefficients, respectively, determined by temperature and salinity. To investigate the downstream density variation starting from DKS (Transect 1), ρ_{DKS}, T_{DKS} and S_{DKS} are assumed to be the Transect 1 values for the isobath with the largest along-shore density gradient. The terms in the rhs of the equation $-\alpha(T - T_{DKS})\rho_{DKS}$, $\beta(S - S_{DKS})\rho_{DKS}$ then indicate the relative importance of temperature and salinity in determining the density change $\rho - \rho_{DKS}$ along the boundary.

3.3 Results

3.3.1 The full-depth volume budget

Figure 3.3(ab) shows the mean along-shore/cross-shore velocity $\overline{U}/\overline{V}$ averaged along 100-m-spaced isobaths between 1000 and 2800 m from DKS to FC. Note that the velocity profiles presented here exclude the Ekman component in order to emphasize the thermal-wind baroclinic velocity. Due to the large cross-shore density gradient generally pointing offshore, the flow on the onshore side of the boundary is considerably sheared, with velocity decreasing from surface to bottom. The flow becomes significantly more barotropic as well as weaker towards the offshore side of the boundary current. The mean cross-shore flow exhibits strong shear due to downstream densification (see Figure 3.2), resulting from the gradual cooling of the warm boundary current in the upper layer as it flows from DKS to FC. The maximum shear is found at isobath around 2400 m, where the maximum along-shore density gradient occurs. This implies that the cross-shore baroclinic transport and, thus the maximum BC downwelling will reach a maximum at the isobath 2400 m. Onshore of isobath 2300 m, the offshore flow is largely barotropic. Both the averaged along-shore and cross-shore velocities indicate that the boundary current is a surface-intensified flow.

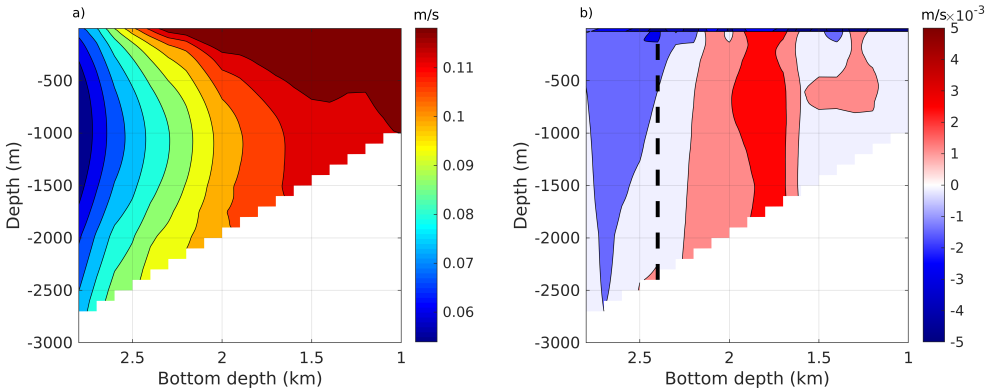

Fig. 3.3 (a) The along-shore velocity (without Ekman component) averaged along 100 m-spaced isobaths between 1000 m and 2800 m from DKS to FC. (b) Same for the cross-shore velocity. The negative values indicate onshore flows. The black dashed line indicates the transect at isobath 2400 m.

We further compare the ANDRO-based velocities to those calculated from altimetry data. Their respective mean velocities along the isobaths of 2800 m and 1000 m are displayed in Figure 3.4, with yellow curves showing CMEMS-derived sea surface velocities (hereinafter, CMEMS-surface) and red and blue curves indicating ANDRO-OI derived sea-surface and 1000-m depth velocities (without Ekman component), respectively (hereinafter, ANDRO-surface and ANDRO-1000). The red dashed curves indicate ANDRO-derived sea-surface velocities with Ekman component (hereinafter, ANDRO-EK-surface). As expected, the along-shore velocity (0.1 m/s, Figure 3.4ab) is one order of magnitude greater than the cross-shore velocity (0.01 m/s, Figure 3.4cd). The ANDRO-based along-shore and cross-shore speeds at the sea surface (ANDRO-surface) are both greater than those at 1000 m, approaching the CMEMS-surface speeds. Along the 2800 m isobath (Figure 3.4a), the along-shore velocities increase from DKS to western Greenland's topographic narrowing region (Transects 22-28), then progressively decline within the DVS topographic broadening region (Transects 29-34), and then remain essentially constant until the end of the SPG boundary (FC). The ANDRO-based along-shore velocities along isobath 1000 m (Figure 3.4b) follow a pattern similar to that of isobath 2800 m, with a maximum in the western Greenland. The magnitude of ANDRO-surface velocity appears generally smaller than that of the CMEMS-surface velocity. The predominantly negative cross-shore velocities along isobath 2800 m in Figure 3.4c indicate interior-to-boundary exchanges over most of the SPG (with the exception of offshore transport in the west of CF), which is consistent with Palter et al., 2008's observations in the Labrador Sea. However, as illustrated in Figure 3.4d, the cross-shore velocities along isobath 1000 m alternate between offshore and inshore directions all along the boundary. Ekman transport carries water inshore (hence the negative change in Andro-surface cross-shore velocities) from DKS to CF and DVS to FC, and offshore (hence the positive change in cross-shore velocities) from CF to DVS. The along-shore Ekman velocities are negligible compared to the along-shore geostrophic Andro-surface velocities.

The along-shore volume transport along the 67 transects of the SPG boundary is presented in Figure 3.5(a). The boundary current transport generally increases from the DKS (18.9 ± 0.3 Sv) to reach a peak around the tip of CF (32.0 ± 0.4 Sv). This significant increase may be

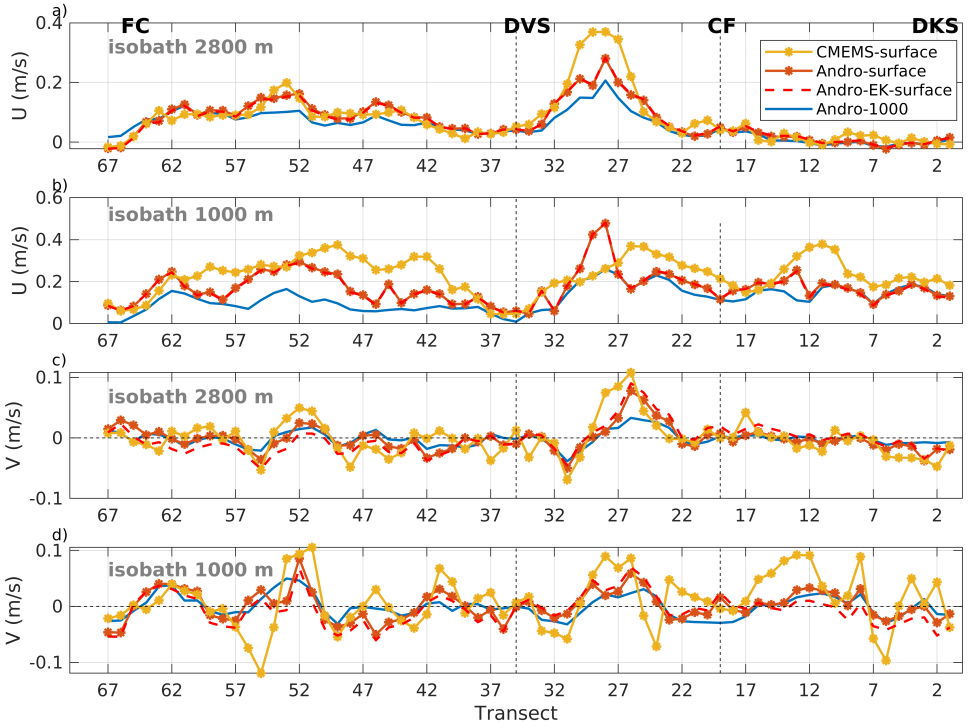

Fig. 3.4 On the estimation of mean velocities along the SPG, with yellow curves representing sea surface velocities from the CMEMS altimetry dataset, red curves representing sea surface velocities from the ANDRO dataset (red solid-without Ekman, red dashed-with Ekman) and OI-based density field, and blue curves showing velocities at 1000m from the ANDRO dataset. The along-shore mean velocities along isobath 2800 m (a) and 1000 m (b). The cross-shore mean velocities along isobath 2800 m (c) and 1000 m (d).

attributed to the Irminger Gyre that intensifies the southward East Greenland Irminger Current (Våge et al., 2011). Further downstream, the along-shore transport decreases substantially as the boundary current is depleted near the Eirik Ridge and then increases slightly due to the recirculation of dense, deep waters in the eastern Labrador Sea (Holliday et al., 2009) before staying relatively constant until FC. According to the boundary extrema of the along-shore transport, we will here divide boundary into three regions: the eastern Greenland (EG), which has a significant net outflow from DKS to CF; the western Greenland (WG), which has a strong net inflow from CF to DVS; the western Labrador Sea (WL), which has rather negligible net flow. We will close the volume budgets in these three regions independently.

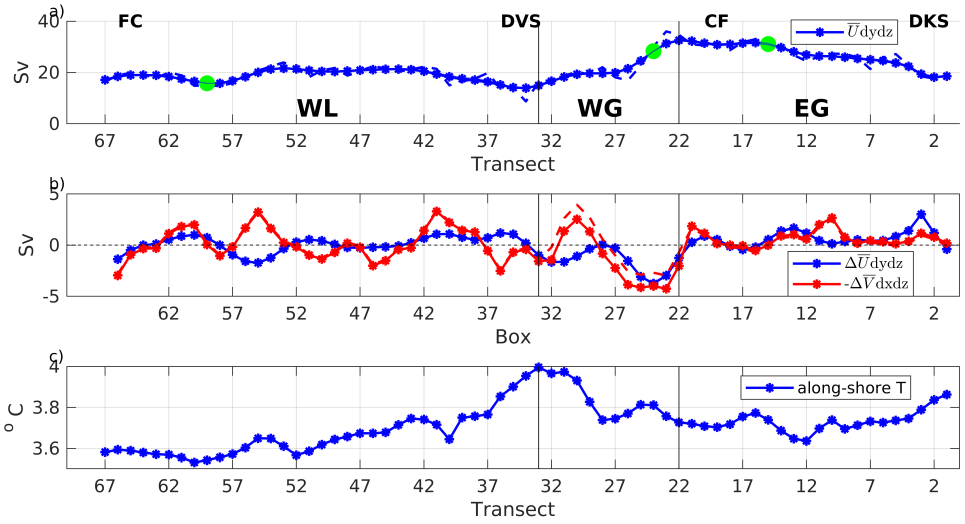

Fig. 3.5 The mean along-boundary transport across the transects of SPG smoothed with a Hanning filter (blue curve in panel a), with selected transect (green dots) compared with some other independent observations (see text). The dashed blue curve indicates the unfiltered along-shore transport. The along-shore convergence (blue curve) and adjusted cross-shore net convergence (solid red curve) across the small boxes of SPG (b). The dashed red curve represents the unadjusted cross-shore net transport. The blue curve in panel (c) presents the full-depth averaged temperature T along the boundary.

We compare the transport to previous observational estimates of the boundary current transport for selected transects in each region (the three red-dotted transects in Figure 3.2). The averaged long-term (2002-2019) surface-to-bottom boundary current transport across transect 59 of the WL region is estimated to be 15.1±0.2 Sv. This is comparable with earlier estimates of 17.9±3.10 Sv at the 53°N observatory from 2002 to 2014 (Zantopp et al., 2017). Across transect 24 in the WG region, which is adjacent to the OSNAP west mooring site, the long-term mean along-boundary transport is estimated to be 30.1±1.2 Sv, which is within the uncertainties of the 2014-2018 observations from Pacini et al., (2020), with 25.6±7.1 Sv. In addition, our along-shore transport estimate across transect 15 at around 59.1°N (32.9±0.8 Sv) is similar to the mean transports determined by combining 2002–2008 yearly hydrographic observations at 59.5°N (32.1±5.9 Sv, Sarafanov et al., 2012). To summarize,

our estimates of the mean transport of boundary current along the SPG are consistent with earlier independent estimates.

Figure 3.5(b) depicts the full-depth net transport of the 66 small boxes, with the blue curve indicating the along-shore convergence ($\iint \Delta\overline{U}dydz$) and the red curves indicating the cross-shore convergence (-$\iint \Delta\overline{V}dydz$). Even though the along-shore and cross-shore flow barely balance locally, it is possible to close the volume budget over relatively large spatial scales. The net residual convergence for the SPG boundary is 13.7 Sv, which consists of 1.4 Sv of along-shore convergence and 12.3 Sv of cross-shore convergence. With a cross-shore transect area of roughly $3 \times 10^9 \mathrm{m}^2$ along the isobath 2800 m, a minor adjustment to the cross-shore velocity (in the order of $10^{-3} \sim 10^{-4}$ m/s, i.e., in line with ANDRO-based velocity errors) must be applied to balance the along-shore and cross-shore transport. In addition, the along-shore velocity is believed to be well-reconstructed, which is supported by the validation of our along-shore transport reconstruction with independent *in situ* estimates, as seen below. Therefore, the adjustment will solely be applied to the cross-shore velocity at the transect of the boundary's outermost isobath. The cross-shore velocity adjustment is 2.3×10^{-4} m/s in the WL region, 4.0×10^{-3} m/s in the WG region, and -3.0×10^{-3} m/s in the EG region. The adjustment is comparable to the measurement error of the cross-shore velocities derived from the ANDRO dataset, which is around 1.0-5.0 10^{-3} m/s.

3.3.2 Vertical transport

The convergence of horizontal transport and associated downwelling is estimated within 100-m thick layers from 0 to 2800 m (Figure 3.6a). The downward vertical volume transport from the surface increases to a maximum of around -4.41$\pm$0.96 Sv at 1300 m. Below 1300 m, the net vertical transport declines gradually until it vanishes at the bottom. We then obtain the BT/BC vertical transport using Equation 3.6, as shown in Figure 3.6(a). Both components contribute equally to the full-SPG boundary downwelling across 1300 m depth, with the BT contributing -2.66$\pm$0.40 Sv and the BC component contributing -1.75$\pm$0.43 Sv. Figure 3.6(bcd) shows the regional decomposition of the total, BT and BC components. Most of the sinking at 1100 m occurs in the WL and WG regions, but those are associated with the same

component of the flow: the WL region contributes -2.07±0.7 Sv due to the BC downwelling, while the WG region contributes to -2.40±0.8 Sv due to the BT downwelling, respectively. The vertical transport of the EG region at 1300 m is negligible (0.05±0.8 Sv) because the BT upwelling and BC downwelling almost compensate for each other. Locally, the maximum transport in the WL region occurs at the same depth (1300 m) as that of the SPG transport, whereas the maximum vertical transport in the WG and EG regions occurs at a depth of 1700 m, with downwelling transport of -3.35±0.72 Sv in the WG region and upwelling transport of 0.84±0.44 Sv in the EG region. Interestingly, the BC/BT vertical transport in all three regions opposes one another.

Figure 3.7 shows the along-shore and cross-shore components of the BT/BC stream-functions. The net BC downwelling in SPG is mostly due to the net onshore baroclinic transport (-2.24 Sv) and only partially offset by a net along-shore baroclinic outflow (0.24 Sv) (Figure 3.7a). This suggests that the majority of the onshore baroclinic flow will sink near the coast, and that only a small portion of the onshore flow recirculates inside the boundary current in the surface layer and drives the net along-shore baroclinic transport. In all regions, the opposite signs of the barotropic along-shore and cross-shore advection indicate meandering; the net along-shore baroclinic transport is insignificant compared to the net cross-shore baroclinic one (Figure 3.7bcd). In the WL regions, the overall downwelling is mainly contributed by the inshore baroclinic transport (Figure 3.7b), whereas in the WG region, substantial downwelling is mainly contributed by the offshore barotropic transport leaving the bottom slope (Figure 3.7c). In the EG region, the deep upwelling is mainly contributed by the deep onshore barotropic transport across the bottom slope.

We observe an opposition between the BT and BC vertical transports in each of the three regions, with the BT transport being induced by the cross-shore transport interacting with the bottom slope and BC transport being driven mainly by the cross-shore baroclinic transport (see schematic Figure 3.8). Positive/negative convergence (Figure 3.5a, corresponding to an onshore/offshore mean flow) always occurs in regions with along-shore cooling/warming (Figure 3.5c). In the region of positive convergence and onshore mean flow ($\overline{V} < 0$, Figure 3.8a), for instance, the boundary may lose heat due to lateral advection, which can be partially

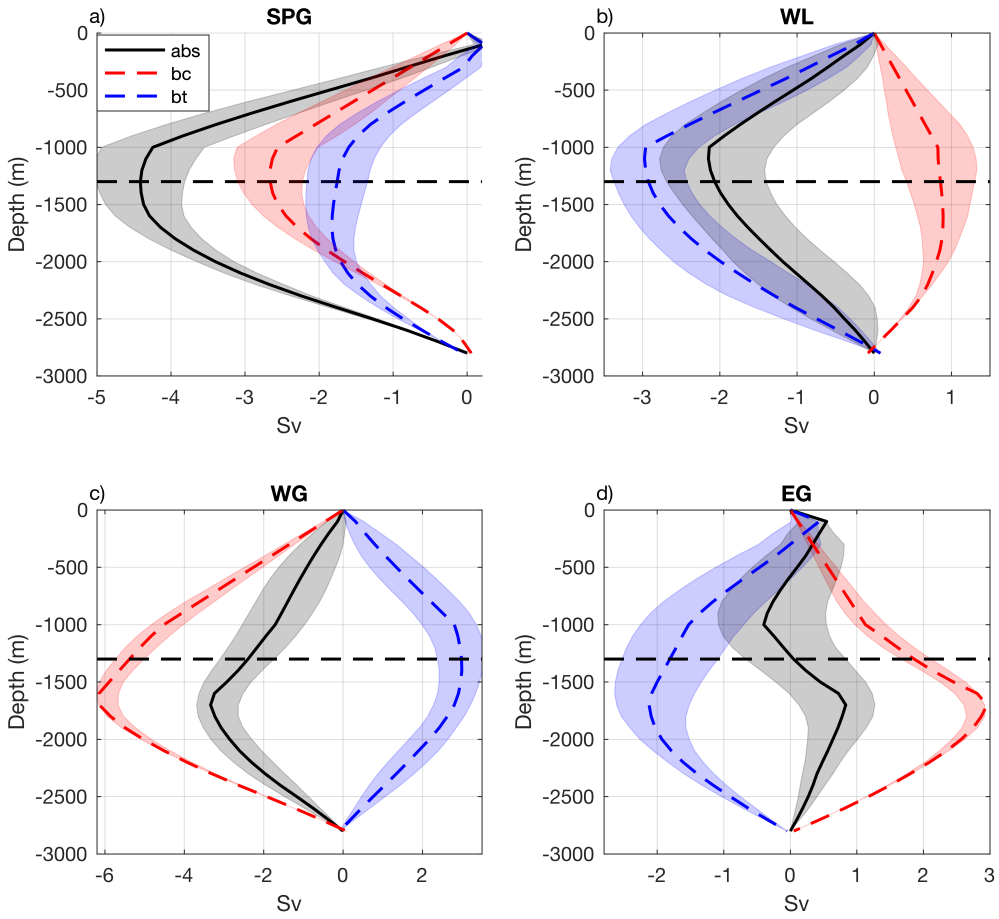

Fig. 3.6 The vertical transport derived from the residual of the horizontal volume budget calculated at 100m-spaced depths ranging from 0 m to 2800 m in SPG boundary (a) and three marginal regions (bcd). The total geostrophic transports are indicated by the black curves. The decomposition of the transports is represented by blue and red curves, representing the baroclinic and barotropic components, respectively. Positive indicates upwelling transport, and negative indicates downwelling transport. The patches indicate the errors (two times the standard deviation) determined from the bootstrap simulations.

explained by the onshore mean heat advection ($\overline{V}\Delta\overline{T}_y < 0$), given that the interior water is colder than the boundary current water ($\Delta\overline{T}_y < 0$). The boundary heat loss results in along-boundary densification ($\partial\rho/\partial x > 0$) and a consequent onshore baroclinic flow (Figure 3.8c), which intensifies the onshore mean flow in the upper layer ($\partial\overline{V}/\overline{z} < 0$). Therefore, in the positive convergence region, the onshore barotropic transport not only contributes to the

BT upwelling but also cools the boundary (as described in Chapter 4), partially producing the BC downwelling, and vice versa in the negative convergence region. This may explain why BC upwelling/downwelling is always partially offset by BT downwelling/upwelling, resulting in less vertical transport in each region.

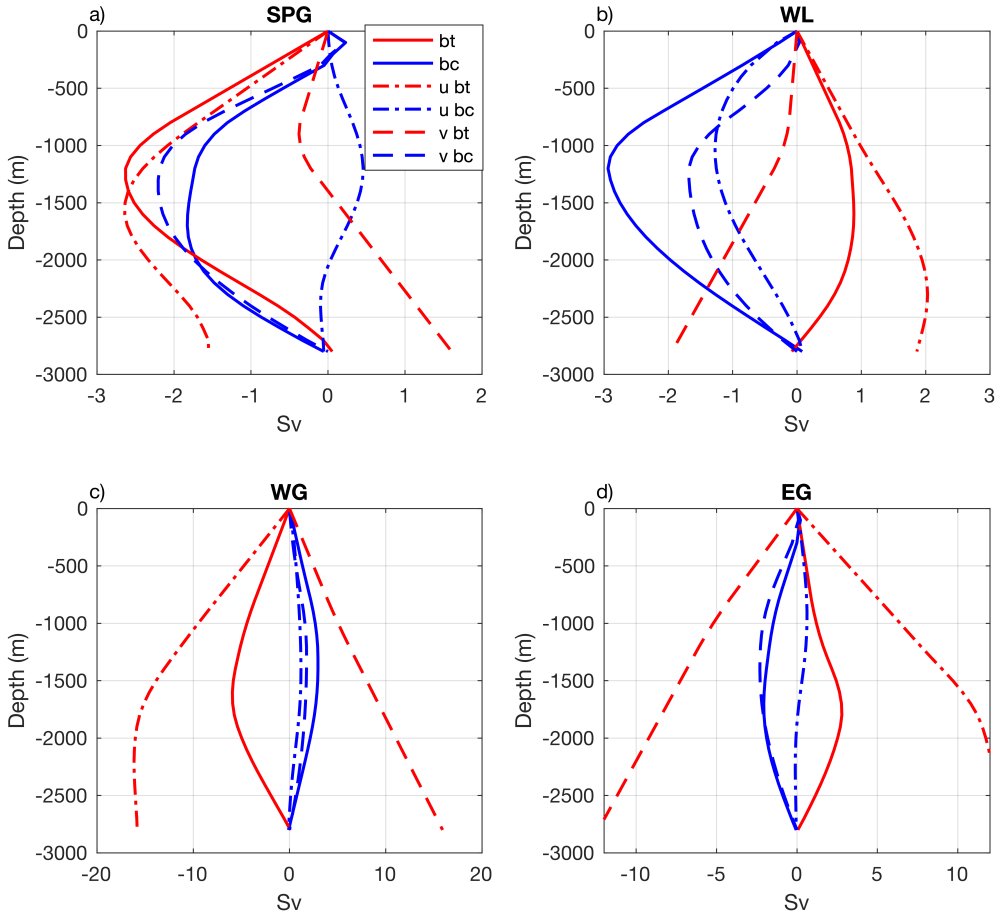

Fig. 3.7 The barotropic (solid red) and baroclinic (solid blue) vertical transport calculated at 100m-spaced depths ranging from 0 m to 2800 m in SPG boundary (a) and three marginal regions (bcd), and the corresponding along-shore (dotted) and cross-shore (dashed) components of each transport.

The vertical sinking in the SPG boundary goes together with -2.88±0.61 Sv diapycnal downwelling across the 27.74 kg/m^3 isopycnal surface, with baroclinic transport accounting for -1.97±0.41 Sv and barotropic transport accounting for -0.91±0.45 Sv (Figure 3.9). The

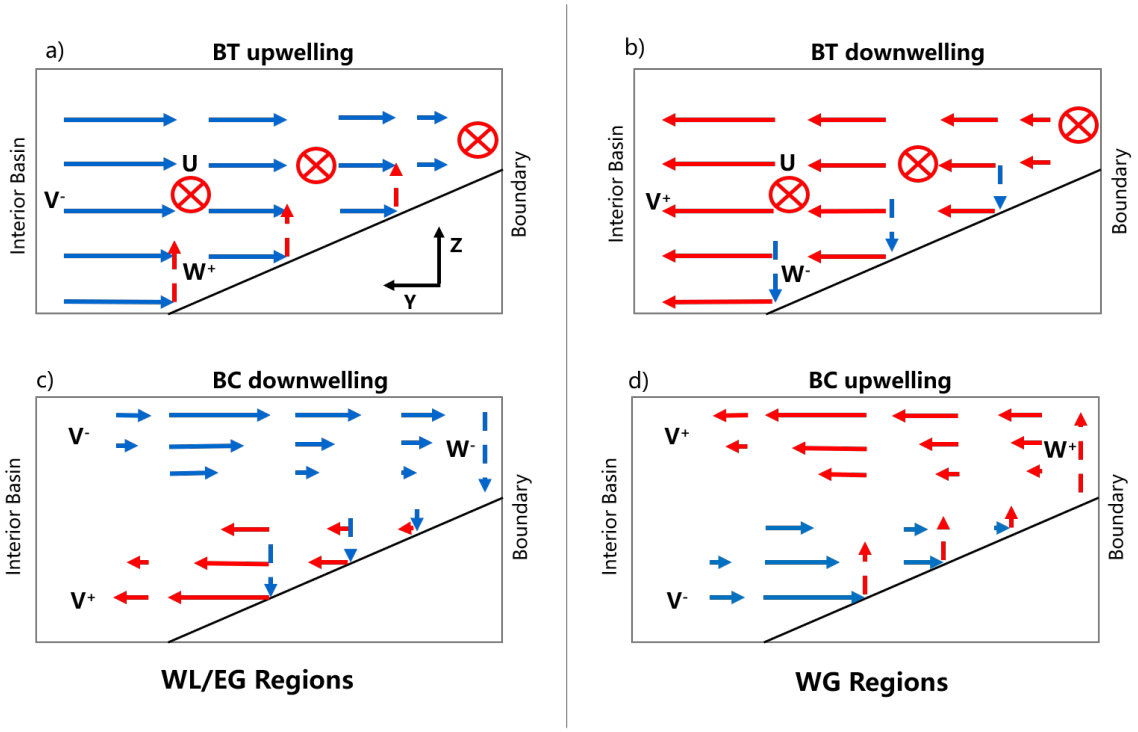

Fig. 3.8 Schematic of the circulation of the barotropic upwelling and baroclinic downwelling near the western Labrador Sea/eastern Greenland boundaries (a,c), the barotropic downwelling and baroclinic upwelling near the western Greenland boundary (b, d). The barotropic vertical transport mainly occurs above the bottom slope, whereas the baroclinic vertical transport mainly occurs near the boundary wall. Solid blue/red arrows indicate the velocity toward/away from the shore (v-/v+). Dashed blue/red arrows indicate the downwelling/upwelling vertical velocity (w-/w+). The red inward arrows indicate the along-shore boundary current (u+).

magnitude of the BC diapycnal downwelling is similar to the BC vertical downwelling (-1.75±0.43 Sv) because the water sinks and crosses the nearly horizontal isopycnal surface of 27.74 kg/m^3 (below 1000 m, see Figure 3.10a). Maximum diapycnal transport for BT downwelling occurs in the lighter layer (27.66 kg/m^3 at depths shallower than 800 m), and the BT diapycnal transport is lower than the BT vertical transport (-2.66±0.40 Sv). This diapycnal flux represents the water mass transformation from the upper layer to the deeper layer within the boundary current, as well as the diapycnal processes at the surface where the horizontal flow crosses the sloping isopycnals. This estimate does not account for the lateral diapycnal flux due to the export of the water mass transformation in the convective interior basin by an isopycnal eddy flow (Brüggemann and Katsman, 2019).

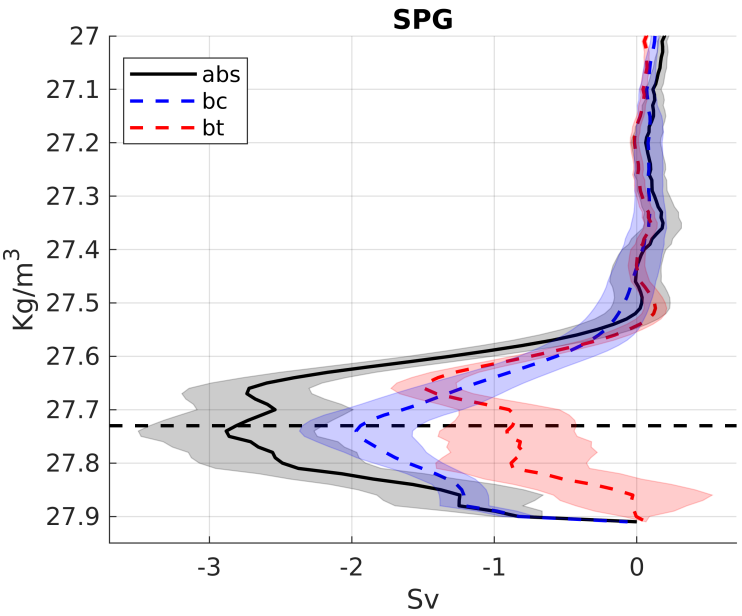

Fig. 3.9 The diapycnal transport derived from the density-space volume budget of the SPG boundary (resolution is 0.01 kg/m^3). The total geostrophic transport is indicated by the black curve. The decomposition of this transport into a (blue) baroclinic and barotropic (red) component is shown. Positive indicates upwelling transport, and negative indicates downwelling transport.

3.3.3 The baroclinic downwelling

Earlier modelling studies have mainly focused on the baroclinic downwelling caused by the along-shore densification (e.g., Spall and Pickart, 2001; Straneo, 2006; Cenedese, 2012; Katsman et al., 2018). We here provide a detailed (observational) description of the regional and seasonal variations of this particular component. Because most of the onshore baroclinic flow will sink and contribute to the total BC downwelling, here we only present the cross-shore baroclinic transport. This work has been published in Geophysical Research Letters (Liu et al., 2022).

Figure 3.10ab depict the density and associated cross-shore baroclinic velocity sections following isobath 2400 m from DKS to FC. The density generally increases downstream (Figure 3.10ac). The full-depth averaged density gradually increases from DKS to CF, decreasing from CF until the east of DVS (Figure 3.10c). Downstream of DVS, the density in increases again. Overall, the increase in density along isobath 2400 m from 27.72 kg/m^3

to 27.74 kg/m^3 expectedly drive an overall BC downwelling. The resulting cross-shore baroclinic velocity (Figure 3.10b) shows the baroclinic flow transport onshore (offshore) and offshore (onshore) in the upper and lower layers, driving downwelling (upwelling). The level of no motion is deeper in the Irminger Sea (EG) than in the Labrador Sea (WL and WG) and ranges from 500 to 1500m depth.

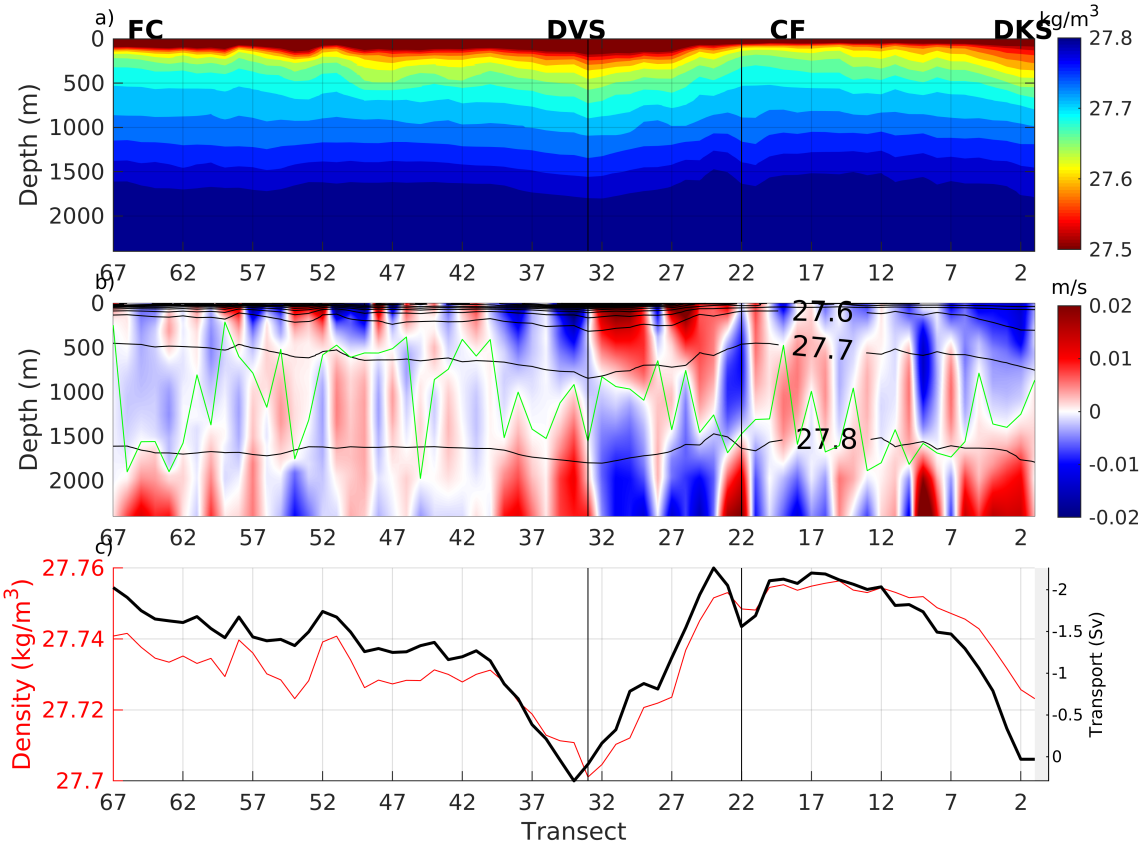

Fig. 3.10 (a) OI-derived multiproduct density (σ_0) field along isobath 2400 m. (b) The cross-shore baroclinic velocity field along isobath 2400 m. The positive (negative) values indicate offshore (onshore) flows. The green line indicates the depth at which the maximum (accumulated) vertical transport is found (i.e., levels of no motion). The σ_0=27.6, 27.7, 27.8 kg/m^3 isopycnals are contoured in black. (c) The density along the boundary from DKS to FC averaged in the full depth (1-2400m, red curve). Black curve indicates the maximum cross-shore baroclinic transport (and thus vertical transport) accumulated along the boundary from DKS to FC. Positive (negative) transport indicates baroclinic upwelling (downwelling). The upward slopes indicate the baroclinic downwelling (EG and WL), and the downward slope indicates baroclinic upwelling (WG).

A vertical section of the DKS-FC along-shore average of the cross-shore velocity crossing different isobaths is shown in Figure 3.11a. It reveals a cell-like structure in the upper and lower layers, with a cell centered at the isobath 2400 m at 100 m depth. In line with theoretical and experimental works (Spall, 2008 and Cenedese, 2012), the cross-shore baroclinic velocity increases from the coast offshore to a maximum near the 2400 m isobath and then decreases offshore until the along-shore density gradient becomes insignificant at circa the 3000 m isobath. The mean maximum cross-shore transport (and thus the rough BC downwelling) along the SPG boundary, consistent with the cross-shore baroclinic transport estimated in Figure 3.7(a), is -2.24 Sv at 1100 m, with an uncertainty of 0.43 Sv. The transport in density space is -2.11$\pm$0.28 Sv by crossing the nearly-horizontal 27.73 kg/m^3 isopycnal surface.

The cumulative transport (Figure 3.10c) along the 2400 m isobath indicates that the BC transport peaks (drops) in the same locations as the extreme value of the along-shore transport occurs (Figure 3.4b). The cross-shore velocities averaged along the isobaths in these three regions are shown in Figure 3.11dgj. They also capture cell-like structures within the boundary current system, with waters flowing onshore (offshore) in the upper layer and offshore (onshore) in the lower layer of the BC downwelling (upwelling) region.

We show in Figure 3.12 the relative contribution of the temperature and salinity to the along-shore density change (Equation 3.9) for the upper layer (above 300m) and the intermediate layer (300-1500m). Temperature and salinity play opposing roles, with the former generally increasing the density and the former generally decreasing the density along the boundary. In the upper layer (Figure 3.12a), the along-boundary density change is significantly driven by temperature in EG and salinity in the Labrador Sea (WG and WL); in the intermediate layer, the density change is overly determined by temperature. As the overall density change in the upper layer is negligible and the significant along-boundary densification due to temperature change occurs in the intermediate layer, the BC boundary downwelling is mostly a result of along-shore cooling in the intermediate layers.

To investigate the seasonal variations of the BC transport, the seasonal cross-shore baroclinic velocity is calculated based on the four-season density field (Chapter 2). Water sinks (upwells) all year in the BC downwelling (upwelling) regions (Figure 3.11). The BC

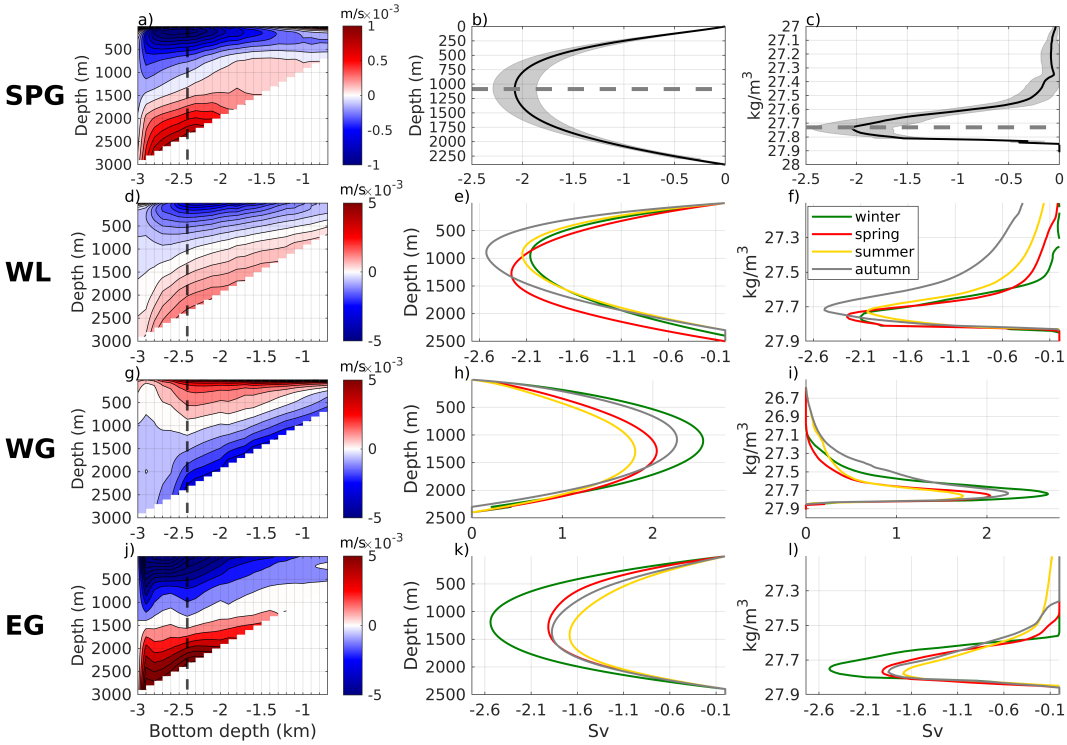

Fig. 3.11 (a) The along-shore average of the cross-shore baroclinic velocity along the SPG averaged at the 100 m-spaced isobaths between 700 m and 3000 m. The x-axis represents distinct isobaths rather than the cross-shore distance. The dashed line indicates the isobath (2400m) where the maximum vertical transport is found. The positive (negative) values indicate offshore (onshore) flows. Positive (negative) transport indicates baroclinic upwelling (downwelling). (b)(c) The corresponding geostrophic streamfunctions obtained by accumulating the cross-shore baroclinic transport (and thus the rough baroclinic vertical transport) from the surface in depth space and density space. The errors in gray patch are one standard deviation derived from the bootstrap simulations. The dashed lines indicate the depth (density) of maximum overturning. Panels (d)-(l) are the same as (a)-(c), but for the three regions defined in Figure 3.2 and Figure 3.7c and for the four seasons: Winter (Jan-Mar), Spring (Apr-Jun), Summer (Jul-Sep), Autumn (Oct-Dec). The uncertainty estimates and maximum overturning depths for each region are represented in Figure 3.1.

downwelling in the WL region is -2.23±0.71 Sv (Figure 3.11e and Table 3.1) at a depth of 986 m. The BC upwelling in the WG region (Figure 3.11h and Table 3.1) is 2.17±0.74 Sv at a depth of 1182 m. The EG has similar BC downwelling of -2.05±0.79 Sv to the WG (Figure 3.11k and Table 3.1) at a depth of 1304 m. The regional density-space transport follows

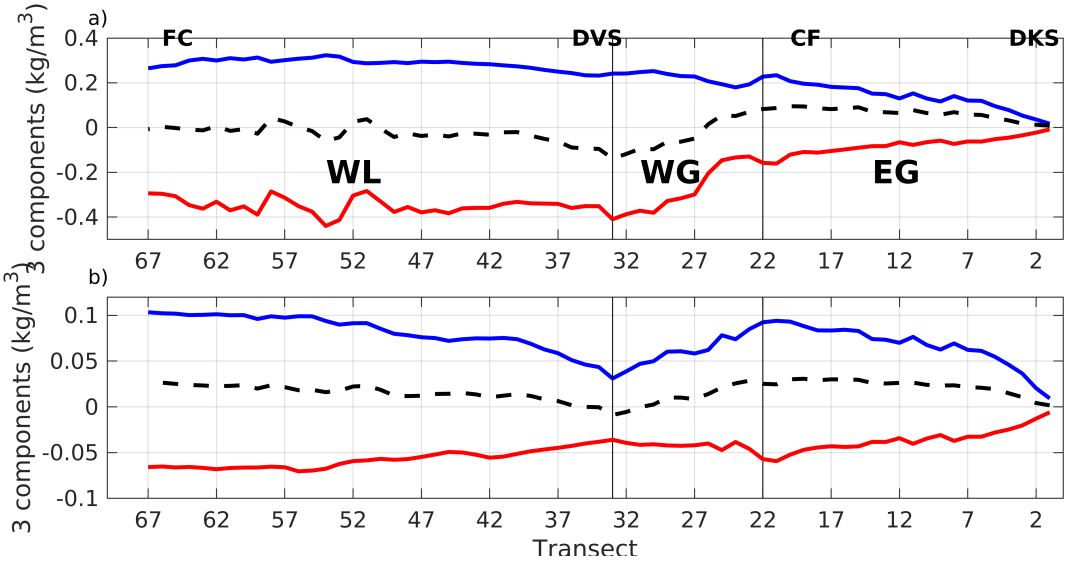

Fig. 3.12 The three terms in Equation 3.9, i.e., density change (dashed black curve), temperature change contribution (solid blue curve), and salinity change contribution (solid red curve) along the boundary from s=0 to s=1 averaged in the upper layer (1-300 m, panel a) and the intermediate layer (301-1500 m, panel b), for the three distinct regions defined in Figure 3.1.

a very similar pattern to that in depth-space, and the density level of maximum transport remains nearly constant at around 27.71 to 27.76 kg^3. The uncertainty estimates in Table 3.1 show the standard deviations calculated from 3000 iterations using the three datasets. Seasonal and regional errors are all between 0.3 and 0.8 Sv. The seasonal variations are of the same magnitude as the uncertainties derived from the bootstrap estimates based on the three datasets, and the present estimates of seasonal changes of the Eulerian-mean BC downwelling are not statistically significant for the whole SPG or individual basins. This is in line with Li et al., (2021), who did not detect a statistically significant signal cycle when estimating the composite monthly mean MOC transport using the 46-month records from OSNAP program. Furthermore, Sayol et al. (2019) used a high-resolution model to find that seasonal variability in boundary sinking is rather insignificant in comparison to interior sinking, and that the variability is thought to be driven by ageostrophic dynamics. Nevertheless, based on our observations, a potential upper bound on the seasonal cycle amplitude has been established. In addition, as more observations of boundary current velocity become available, the seasonal variations of the BT downwelling will be investigated.

Table 3.1 The maximum baroclinic vertical transport (Sv) derived from the multiproduct mean in the WL, WG and EG regions (defined in Figure 3.2) and the whole SPG. A positive (negative) value indicates baroclinic upwelling (downwelling). The errors are two times of standard deviation derived from the bootstrap simulations. The depths (m) of the maximum transport are displayed in parentheses.

Season	**WL**	**WG**	**EG**	**SPG**
Winter	-1.97±0.30 (970)	2.56±0.44 (1108)	-2.57±0.31 (1190)	**-1.99±0.58 (975)**
Spring	-2.27±0.31 (1274)	2.04±0.31 (1288)	-1.92±0.61 (1278)	**-2.14±0.81 (1253)**
Summer	-2.16±0.28 (923)	1.81±0.34 (1301)	-1.84±0.84 (1425)	**-2.19±0.82 (903)**
Autumn	-2.54±0.51 (891)	2.27±0.60 (1084)	-1.88±0.45 (1372)	**-2.14±0.47 (1044)**
Annual	**-2.23±0.71 (986)**	**2.17±0.74 (1182)**	**-2.05±0.79 (1304)**	**-2.12±0.43 (1088)**

3.4 Conclusion and Discussion

By attempting a closure of the volume budget of the western subpolar North Atlantic boundary, we have provided here a first observation-based estimate of the Eulerian-mean downwelling along the boundary of the SPG. Using *in situ* temperature and salinity profiles from sustained global ocean observational networks and the deep-Argo displacement dataset, we mapped the long-term mean density and the full-depth current velocities along the continental slope from the Denmark Strait (DKS) to Flemish Cap (FC). A robust estimate of the along-boundary transport is provided and compares well with independent across various boundary regions, i.e., western Labrador Sea (WL), western Greenland (WG) and eastern Greenland (EG). The volume budget of the SPG boundary shows a convergence of the geostrophic horizontal transport in the upper layer that feeds a downward flow with a maximum vertical transport of -4.41±0.96 Sv reached at 1300 m depth. The barotropic flow (-2.66±0.40 Sv) and baroclinic flow (-1.75±0.43 Sv) contribute equally to the total SPG boundary downwelling. The transport in density space, which is here representative of the boundary water mass formation, is -2.88±0.61 Sv across the 27.74 kg/m^3 isopycnal surface. The region with the largest downwelling transport is western Greenland (-2.40±0.8 Sv at 1300 m), which is mainly controlled by the convergence of barotropic flow, followed by the western Labrador Sea (-2.07±0.7 Sv at 1300 m), where the downwelling is mainly controlled by the cross-shore baroclinic flow. The barotropic (BT) upwelling/downwelling

partially compensates for the baroclinic (BC) upwelling/downwelling along the boundary in WL/WG region. The vertical transport in eastern Greenland is negligible at 1300 m, but it reaches its maximum at 1700 m with an upwelling of 0.84±0.44 Sv. This study acknowledges the fact that the regional patterns of the boundary Eulerian-mean vertical transport are the result of horizontal barotropic flow convergence/divergence as well as cross-shore baroclinic transports. Both the hydrographic properties (i.e., along-shore density gradient) and meandering-topography interaction at the boundary therefore drive the formation of boundary vertical transport. The significance of barotropic flow in the boundary downwelling that we discovered here supplements the estimates of Liu et al., (2022), which only consider the baroclinically-induced boundary downwelling.

The cooling and resulting densification along the boundary region result in a geostrophic cross-shore flow and a BC downwelling above the continental slope, with a maximum value of 1.75 ± 0.43 Sv at 1300 m depth. The BC transport in density space, which is here representative of the cross-shore diapycnal flux, is very similar to the transport in depth space. Cross-shore velocity is found to increase offshore and peak near the 2400 m isobath, before eventually disappearing near the 3,000 m isobath, in good agreement with observation-based descriptions of the distinct circulation of the interior and the boundary current (Pacini et al., 2020), and with theoretical or modelling works suggesting limited mean advective exchanges between those two regimes (Brüggemann and Katsman, 2019; Cenedese, 2012). Our analysis further reveals no strong or statistically significant seasonality in the magnitude of BC downwelling across the entire SPG. The convergence of the horizontal barotropic flow in the layer above 1100 contributes equally to the SPG boundary downwelling (-2.00±0.61 Sv) and reflects the interaction of the flow with the sloping bottom and mass conservation: offshore barotropic flows drive a net downwelling (e.g. in the WG region), while inshore barotropic flows drive a net upwelling (e.g. the WL and EG regions).

The western Greenland boundary is where the largest regional downwelling is found (-3.35±0.72 Sv at 1700 m), which is mainly governed by the BT mechanism. At this site, the boundary current is warming as it flows downstream, which yields a BC upwelling that partially compensates for the BT downwelling. Interestingly, western Greenland is

expected to be a region with strong along-shore densification (and thus cooling) due notably to eddy-driven heat flux, as described in several modelling works (Georgiou et al., 2019; Katsman et al., 2004). However, this pattern of warming has also been evidenced in earlier work. Using subsurface floats, Palter et al. (2008) estimated the temperature field in the Labrador Sea, which shows the along-shore warming along western Greenland (see their Figure 3.10). Using a global ocean model, Katsman et al. (2018) discovered a strong positive correlation between boundary sinking and alongshore densification, with the exception of western Greenland, where boundary sinking occurs despite an alongshore decrease in density (see their Figure 3.11). Even though eddies help to extract heat from the boundary into the interior, the boundary current along western Greenland continues to gain heat due to other processes, such as the offshore mass (and thus temperature) flux (as described in Chapter 4). The significant boundary downwelling observed in western Greenland suggests that the boundary vertical transport depends on the along-shore density change (the baroclinic flow) and the boundary current meandering (the barotropic flow).

The adjustment of cross-slope velocity along the deepest isobath is one of the most important assumptions underlying our volume budget estimates. This adjustment includes not only the uncertainties of the cross-shore velocities derived from ANDRO deep displacement dataset and OI-based density dataset, but also the ageostrophic processes that the displacement of Argo floats cannot capture, such as viscosity, non-linear terms, and bottom Ekman flows. For example, ageostrophic processes may be notably important at the coastal boundary edge, where the viscosity becomes significant above the steep continental slope. Cross-shore bottom Ekman transport induced by along-shore currents in the frictional boundary layer above the slope has been observed in the Amundsen Sea (Wahlin et al., 2012) and East Australian Current (Schaeffer et al., 2014). The bottom Ekman transport could be approximated with a bottom boundary layer parameterization. Further observation and modelling works can be conducted to determine the importance of the ageostrophic processes in the boundary mass balance.

Comparison with independent overturning estimates from cross-basin arrays or realistic modelling provides insights and confidence in the values reported herein. The Eulerian-

mean downwelling from CF to FC is estimated at -4.47 $\pm$ 0.70 Sv. Downwelling in that region was estimated to be -1.4 Sv (Katsman et al., 2018) in a 1/4° hindcast simulation and -4.02$\pm$0.83 (Sayol et al., 2019) in a $\sim$1/12° simulation. Our observational estimations are very close to those of Sayol et al., (2019), who argue that the stronger vertical transport (compared to Katsman et al., 2018) is likely due to the improved ability of higher-resolution models to resolve the eddy activity near the Labrador Sea boundary (Georgiou et al., 2019; Brüggemann and Katsman, 2019). Our observation-based downwelling estimate in the Irminger Sea (-0.05$\pm$0.80 Sv) is in line with the high-resolution modelling estimates of -1.4 Sv from Katsman et al., (2018) and -0.75$\pm$1.13 Sv from Sayol et al., (2019) within uncertainty estimates. Summer downwelling in the Labrador Sea is estimated here to be -1.40 $\pm$ 0.75 Sv at a depth of 1700 m (with BT of -1.84$\pm$1.1 Sv and BC of 0.44$\pm$0.42 Sv) by integrating the transport between the two ends of the AR7W line, which agrees quantitatively with Pickart and Spall's (2007) observation-based meridional transports of about 1 Sv at depth 800 m. The annual mean downwelling rate in the Labrador Sea is estimated here as 0.72 $\pm$ 0.07 Sv, similar to Holte and Straneo's (2017) and Lozier et al. (2019) observations, which amount to 0.9$\pm$0.5 and 0.8$\pm$0.2 Sv, respectively. This also confirms that most sinking occurs near the Labrador Sea boundary, with little vertical mass transport occurring in the convective interior.

We quantify here only the western boundary downwelling downstream of DKS, omitting potential upstream contributions around Reykjanes Ridge or the Rockall Plateau, as demonstrated by modelling studies (Katsman et al., 2018; Sayol et al., 2019). For example, the Iceland Basin can contribute $\sim$2 Sv of downwelling. Additionally, overflows across the DKS or the Iceland-Scotland Ridge contribute significantly to the overall net sinking in the SPG—about 7 Sv (Hansen and Østerhus, 2000)—via hydraulically controlled dynamics not captured by our geostrophic estimate. The boundary sinking calculation refinement is being investigated for these specific areas.

We finally emphasize that novel descriptions of the Eulerian-mean downwelling rooted in observations are critical for understanding AMOC variability in the current context of anthropogenic climate change (IPCC, 2021). Changes in the intensity of the wind-driven and

buoyancy-driven subpolar circulation (including AMOC and horizontal gyre) (Robson et al., 2016) may influence the cross-shore mean flow at the boundary and, consequently the BT downwelling. Furthermore, the accumulation of Greenland meltwater since the 1990s and its dampening effect on deep convection and water mass transformation in the coming years (Böning et al., 2016), could ultimately lead to a decrease in along-boundary densification, and therefore in a reduction of the BC downwelling. A better observation-based understanding of boundary-focused vertical transport may also help us to properly represent or parameterize the details of the underlying boundary dynamics in climate models. It can assist in not only describing the circulation and diagnosing its controls but also in providing valuable insights into how to improve existing ocean circulation theories of overturning.

Chapter 4

The time mean heat budget of the western boundary of the subpolar North Atlantic

In the previous chapter, we showed that the cooling of the boundary current in the intermediate layer was primarily responsible for its downstream densification. This downstream densification generates an inshore baroclinic flow and, consequently, a baroclinic boundary downwelling. In this chapter, we provide an observation-based description of the long-term mean heat budget of the SPG boundary using a combination of Argo-deep displacement data, mooring data, remote sensing data, atmospheric reanalysis, and OI-based temperature field. The respective contribution of mean current, eddy activity, and air-sea flux to boundary cooling is evaluated.

4.1 Introduction

The heat and freshwater carried by the Atlantic Meridional Overturning Circulation (AMOC) are fundamental components of the Earth climate system. At high latitudes, the net downwelling feeding the lower limb of the AMOC occurs above continental slopes as a result of a downstream densification of boundary currents (e.g., Spall and Pickart, 2001; Straneo, 2006; Spall, 2010; Cenedese, 2012; Katsman et al., 2018) and of barotropic current-topography interactions. More interest has been focused on the former, the baroclinic boundary downwelling, driven by the strong surface heat losses and/or boundary-interior heat fluxes (Spall

and Pickart 2001; Spall 2004). Understanding the mechanisms that control the boundary current heat loss is therefore critical for understanding this particular component of the boundary-focused downwelling.

The strongly-barotropic boundary current flowing between Denmark Strait (DKS) and Flemish Cap (FC) in the subpolar gyre (SPG) is a key location where along-stream densification and associated net downwelling have recently been reported (Katsman et al. 2018, Sayol et al. 2019, Liu et al., 2022). Several processes, including surface heat flux and mean or eddy-driven heat advection, are likely involved in the boundary current heat balance and, therefore, in determining the amount of downwelling near the boundary (e.g., Spall and Pickart, 2001). Idealized model studies (e.g., Spall, 2004; Straneo, 2006; Hátún et al., 2007; Georgiou et al., 2019) and experimental studies (Cenedese, 2012) have shown that while atmospheric cooling contributes to this buoyancy loss, it is also significantly controlled by lateral eddy-driven heat fluxes. In deep convection sites such as the Labrador Sea and Irminger Sea, lateral eddy fluxes from boundary currents can balance the interior basins' surface buoyancy fluxes that drive water mass transformation.

The key role of eddies formed along the boundary of the SPG is to exchange properties between the boundary current and basin interiors (Lilly et al., 2003; Katsman et al., 2004; Straneo, 2006; Le Bras et a., 2020; Zou et al., 2021). In the Labrador Sea, these fluxes are thought to be the result of two different sources of instability: baroclinic instability distributed around the basin (convective eddies, Visbeck et al., 1996; Jones and Marshall, 1997) and localized topographic instability of the boundary current (Irminger rings/boundary current eddies, Lilly et al. 2003; Spall, 2004; Hátún et al. 2007; McGeehan and Maslowski, 2011). In the Irminger Sea, energetic cyclones trapping anomalously cold waters can be formed through the cascading of dense Denmark Strait Overflow water (e.g., Bruce 1995; Krauss 1996; von Appen et al. 2014; Zou et al., 2021). A portion of these overflow eddies travel within the boundary current and pass Cape Farewell, reaching the eastern Labrador Sea (Pacini et al., 2021). Overall, eddies appear critical for the heat budget of the boundary region and the basin interiors and, therefore, for determining part of the boundary-confined downwelling of upper waters.

Observations and high-resolution numerical simulations in convective regions such as the Labrador Sea have provided additional insights into the heat exchange between boundary currents and basin interiors. Palter et al. (2008) conducted a scaling analysis utilizing Lagrangian floats operating between 1995 and 2002 and suggested that the cross-shore eddy heat exchange, air-sea heat flux and horizontal mean advective heat flux were potential sources of interannual variability for the temperature of the deep western boundary current (DWBC) and the associated exported Labrador Sea Water (LSW). Chanut et al. (2008) showed that, on the basin scale, the heat required to balance the Labrador Sea heat loss to the atmosphere is supplied by the mean advection of the warm boundary current flowing into the basin, and is then redistributed to the interior almost exclusively by eddies.

Yet, observation-based qualitative and quantitative descriptions of the boundary current heat budget, including the roles of mean flows, eddy flows, and atmospheric forcing, remain largely incomplete. No comprehensive observational study of the broader SPG boundary mean heat budget has been undertaken yet. The objective of this chapter is to contribute to filling this gap. Towards this goal, the long-term (2002-2019) mean heat budget of the western SPG boundary, from DKS to FC, is analyzed using a variety of observational products, including autonomous floats, moorings, remote sensing data, and atmospheric reanalysis. In particular, observations have enabled us to provide a more comprehensive assessment of the long-term cross-shore eddy heat flux across the whole water column of the SPG boundary. The respective contribution of the several processes to boundary cooling is regionally assessed. Section 4.2 presents the method for calculating heat fluxes and the configuration of the heat budget in the western SPG boundary region. Discrete and full-depth estimates of the heat fluxes are presented in section 4.3. Section 4.4 discusses the final heat budget in the SPG boundary. We summarize and discuss our findings in section 4.5.

4.2 Methodology

4.2.1 Calculation of temperature fluxes

4.2.1.1 Calculation of full-depth and sea surface mean temperature fluxes

By combining the full-depth mean velocity fields with the full-depth mean temperature field derived in Chapter 3, the full-depth mean temperature fluxes ($\bar{U}\bar{T}$ and $\bar{V}\bar{T}$) can be obtained. We also use remote sensing products to perform a sea surface analysis. The mean temperature fluxes at the sea surface are computed using CMEMS-based velocity and SST data from 2002 to 2019. The gridded SST field with a resolution of $0.05° \times 0.05°$ is downscaled to the same resolution as the altimetry field, $0.25° \times 0.25°$. The surface mean temperature fluxes are then averaged from the daily fields.

4.2.1.2 Calculation of eddy temperature fluxes at the sea surface and 1000 m

Similarly, eddy temperature fluxes are computed at the sea surface and 1000 m from the CMEMS and ANDRO datasets, respectively. The surface eddy fluxes are calculated as $\overline{U'T'} =$

$overline(U-\overline{U})(T-\overline{T})$ and $\overline{V'T'} = \overline{(V-\overline{V})(T-\overline{T})}$. where the overbars $\overline{U}$, $\overline{V}$ and $\overline{T}$ denote the 100-day average. This averaging period was chosen since the eddy frequency band typically corresponds to frequencies higher than 1 / (100 days), as shown in the two-year series power spectrum of the absolute dynamic topography and sea surface velocities derived from the 18-year CMEMS altimetry dataset (Figure 4.1). The daily '100-day' filtered flux anomalies are then averaged over 18 years. The surface eddy kinetic energy EKE is determined as EKE $=\frac{1}{2}(\overline{U'^2}+\overline{V'^2})$.

To compute the eddy temperature flux at 1000 m, we first interpolate the mean velocity $\overline{U}$,$\overline{V}$ and temperature $\overline{T}$ from the mean gridded field derived on a $\sim$50-km grid in Chapter 3 into the location of each float displacement contained in the ANDRO dataset. By subtracting the mean velocities and temperature from the U_i, V_i, and T_i of the individual float displacement at 1000 m, the anomalies of velocity (U', V') and temperature (T') and thus the eddy

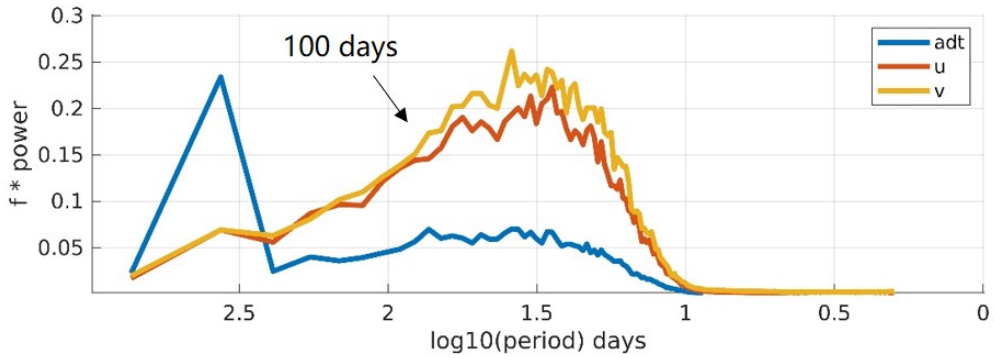

Fig. 4.1 The power spectrum based on absolute dynamic topography (adt) and along-shore/cross-shore velocities derived from CMEMS dataset, averaged over all two-year time segments from 2002 to 2019.

temperature fluxes, $V_i'T_i'$ and $U_i'T_i'$ at the location of each float displacement are then obtained. Individual temperature fluxes are then averaged across the same ∼50-km squares to derive the eddy temperature flux mean fields ($\overline{U'T'}$ and $\overline{V'T'}$).

4.2.1.3 Vertical structure of eddy temperature flux based on OSNAP mooring

To estimate the full-depth eddy temperature fluxes, we derive a typical vertical structure of the eddy temperature flux estimated from two years (2014-2016) of OSNAP mooring data at the continental slopes of the Labrador Sea (OSNAP WG) and the Irminger Sea (OSNAP EG), where water depth exceeds 1000 m (LS5-LS8 and CF5-CF7 labeled in Figure 4.2b). Daily averages of velocity and temperature are computed to filter out high-frequency signals generated by interval waves and tides. As with the fluxes obtained from CMEMS, the eddy temperature flux is computed using a 100-day high-pass average over the two-year period at each measured level of 250-m interval. Note that we have verified that the selection of different average periods results in smaller differences than the uncertainties estimated from a bootstrap analysis. The eddy temperature flux is averaged over all 100-day segments for each instrument. The two vertical profiles are then interpolated from 50 to 3000 m with a 1-m resolution and projected perpendicular to the isobaths. We indeed focus on the full-depth cross-shore eddy temperature flux and neglect the along-shore component for reasons that will be presented in Section 4.3.1. The cross-shore eddy temperature fluxes of each array

(Figure 4.2a) show a similar vertical structure: strong negative fluxes at 50-m depth rapidly declining until about 100m depth and relatively small and homogeneous positive values below 100 m depth. The strong negative fluxes at 50 m depth are of the same order of magnitude as the sea-surface fluxes estimated from the CMEMS dataset at the same OSNAP array sites (blue dot-WG, red dot-EG, Figure 4.2a). The average of the two vertical profiles is here considered as a typical vertical structure of the boundary current's cross-shore eddy temperature flux (black line in Figure 4.2a, and the values in depth are defined as $f(z)$). Below 100 m, the cross-shore eddy temperature flux will be computed using this profile referenced to the flux at 1000 m derived from the ANDRO dataset (as described below). Above 100 m, the flux will be interpolated towards the altimetry-derived sea surface estimates.

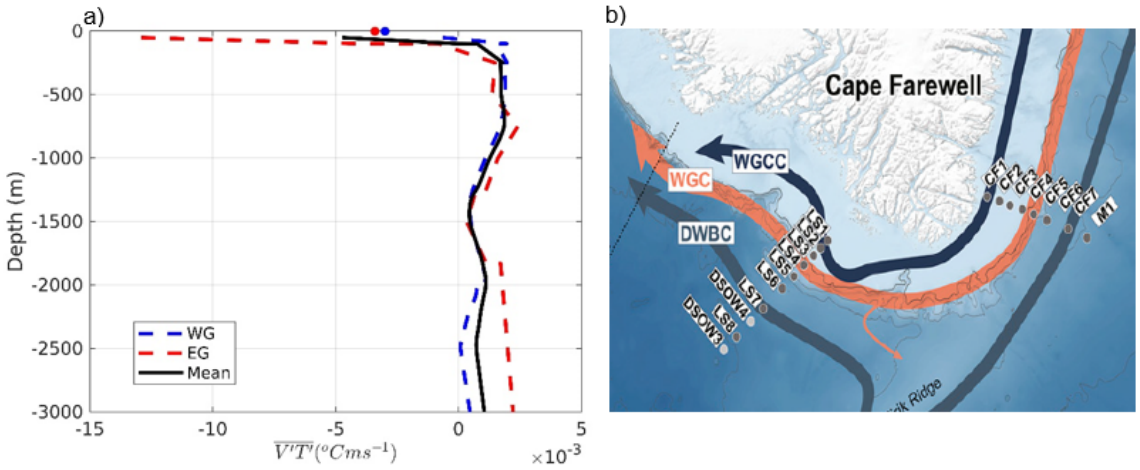

Fig. 4.2 (a) Vertical profiles of cross-shore eddy temperature flux calculated from the LS5-LS8 of OSNAP WG (blue dash) and the CF5-CF7 of OSNAP EG (red dash) mooring arrays. The sea-surface cross-shore eddy temperature fluxes estimated from the CMEMS dataset (2002-2019) at the same sites as the OSNAP array (blue dot-WG, red dot-EG). Positive (negative) values indicate offshore (onshore) fluxes. The black line represents the 'typical' profile obtained by averaging the two profiles. Below the depth of the green dot, the flux changes sign from negative to positive. (b) The labelled OSNAP WG and OSNAP EG arrays (source: Pacini et al., 2021).

4.2.2 Heat budget configuration

Following a similar approach to the volume budget presented in Chapter 3, the boundary current region is divided into 66 boxes between DKS and FC in the along-shore y-direction, between the 2800m isobath and the 1000m isobath in the cross-shore x-direction, and between the surface and the bottom in the vertical z-direction (Figure 4.3). In some analyses, the SPG boundary will be divided into three distinct regions (the western Labrador Sea-WL, the western Greenland-WG, and the eastern Greenland-EG). The primitive potential temperature

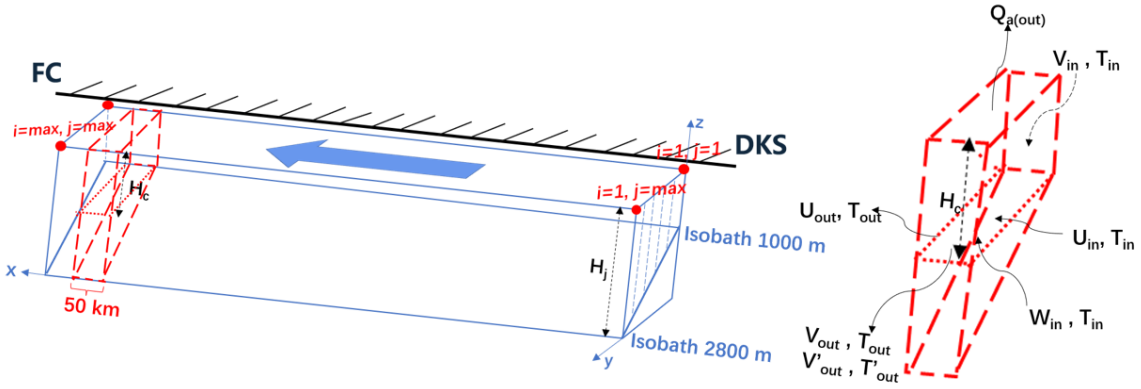

Fig. 4.3 The schematic diagram of the boxes used to compute heat budget. The dashed red lines show one of the 66 small boxes. H_j indicates the thickness of full-depth water, whereas H_c indicates the depth limit of the small box ($H_c \leqslant H_j$). U_{out}, T_{out} (U_{in}, T_{in}) indicate the along-shore mean velocity, and temperature at the transects $i = x_1 (i = x_1 - 1)$ of one small box; V_{out}, T_{out} (V_{in}, T_{in}) indicate the cross-shore mean velocity, and temperature at the transects $j = \max(j = 1)$ of one small box; V'_{out}, T'_{out} indicate the cross-shore velocity anomaly and temperature anomaly at the transect j = max of one small box; Win indicate the mean vertical velocity at the face of $z = H_c$. $Q_{a(out)}$ indicate the surface heat loss to the atmosphere.

equation of the SPG boundary can be written as

$$\frac{\partial T}{\partial t} = -\bigtriangledown \mathbf{v}T - \frac{\partial wT}{\partial z} + (A_T \bigtriangledown^2 T + K_T \frac{\partial^2 T}{\partial z^2}) + f_a \tag{4.1}$$

where $\mathbf{v} = U\mathbf{i} + V\mathbf{j}$ is the horizontal velocity vector. The lhs include the time derivative of temperature, and rhs include horizontal and vertical temperature advection, horizontal and vertical diffusion and air-sea heat flux (f_a). Figure 4.4 depicts the time series of the annual

mean temperature of the SPG boundary from 2002 to 2019 and between the surface and the bottom, as derived from the ISAS dataset. Since the rate of temperature change between 2002 and 2019 is negligible in comparison to the other terms (see Section 4.4), it is reasonable to assume, for our purpose, a steady state heat budget ($\frac{\partial T}{\partial t} = 0$). In this case, the transport of heat into the SPG boundary region must be balanced by the transport of heat out of the boundary region. We then consider the diffusion term as the unresolved term in our study (third and fourth on the rhs of Equation 4.1). The advection terms are further decomposed into mean and eddy components:

$$\bigtriangledown \mathbf{v}T + \frac{\partial wT}{\partial z} = \frac{\partial \bar{U}\bar{T}}{\partial x} + \frac{\partial \bar{V}\bar{T}}{\partial y} + \frac{\partial \overline{U'T'}}{\partial x} + \frac{\partial \overline{V'T'}}{\partial y} + \frac{\partial \bar{W}\bar{T}}{\partial z} + \frac{\partial \overline{W'T'}}{\partial z} + f_a \tag{4.2}$$

Due to the high-frequency variations of the along-shore eddy temperature flux ($\overline{U'T'}$) along the boundary, the along-shore eddy temperature advection calculation is highly sensitive to the end transects (i.e., DKS and CF) of the SPG boundary, which is not the case for the along-shore mean temperature flux ($\bar{U}\bar{T}$) with lower-frequency variations. Therefore, it is difficult to arrive at a robust estimate of the full-depth along-shore eddy temperature advection in our study, which is considered a component of the unresolved term. The inaccessible vertical eddy temperature advection term will also be included in the unresolved term.

Using the box formulation of Equation 4.2 (for the control volume $dxdydz$), the SPG boundary heat budget is essentially a balance between five terms: along-shore mean heat advection, cross-shore mean heat advection, cross-shore eddy heat advection, surface air-sea heat flux, vertical mean heat advection and an unresolved term (unit: GW):

$$\begin{aligned} 0 = &- \sum_{i=1}^{max-1} \int_0^{h_c} \int_0^{w} \rho_0 C_p \Delta \bar{U}_i \bar{T}_i dydz - \sum_{i=1}^{max-1} \int_0^{h_c} \int_0^{l} \rho_0 C_p \Delta \bar{V}_i \bar{T}_i dxdz \\ &- \sum_{i=1}^{max-1} \int_0^{h_c} \int_0^{l} \rho_0 C_p \overline{V'T'} dxdz + \sum_{i=1}^{max-1} \int_0^{w} \int_0^{l} Q_a dxdy \\ &+ \sum_{i=1}^{max-1} \int_0^{w} \int_0^{l} \rho_0 C_p \Delta \bar{W}_{h_c} \bar{T} dxdy + D \end{aligned} \tag{4.3}$$

where dx, dy represent the integral widths in the x, y directions (l, w) of each box, and dz indicates the integral thickness of the full water column (h_c). The i denotes the locations of the transects with a total number of max, and a total number of boxes equaling $max-1$. ρ_0 is 1024 kg/m^3, C_p is heat capacity 4200 J/kg°C. The first term in rhs of Equation 4.2 denotes the along-shore mean heat advection. The second term denotes the cross-shore mean heat advection. The third term denotes the cross-shore eddy heat advection, taken across the 2800 m isobath ($j = max$), neglecting the small and noisy cross-shore eddy heat at the 1000 m isobath. The fourth term refers to integrated air-sea heat flux estimated from ERA5. The fifth term denotes vertical mean heat advection based on the rigid-lid assumption, which has been assessed through the vertical volume transport estimated in Chapter 3. The sixth (unresolved) term in rhs includes the along-shore and vertical eddy advection, and turbulent diffusion (gray terms in Equation 4.1 and 4.2). The total value of each term in the SPG boundary is computed by summing up the value of each small box. A Monte Carlo method is used to compute uncertainties from 1000 bootstrap estimates obtained by perturbing the ANDRO-derived velocity and OI-derived temperature fields with their respective error estimates. Using the two times standard deviation of 1000 iterations, the resulting heat flux errors are then generated.

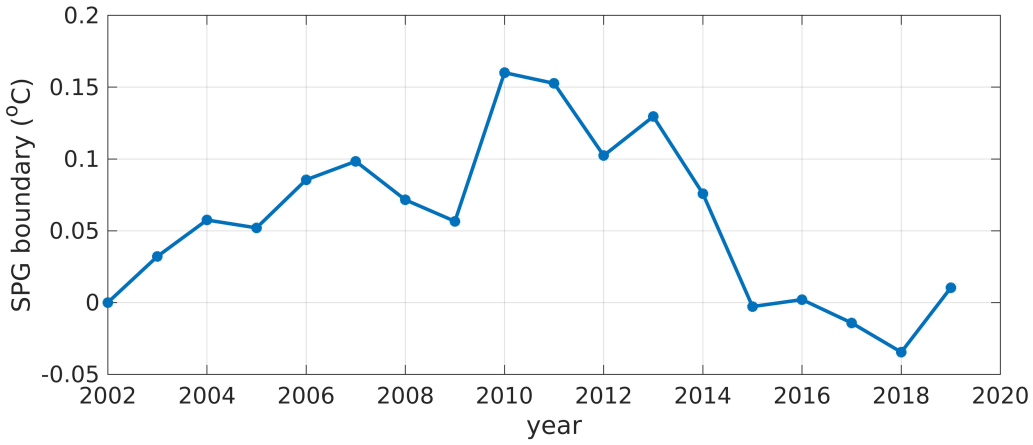

Fig. 4.4 The full-depth annual mean temperature change (relative to the 2002 mean) from 2002 to 2019 derived from the ISAS dataset in the SPG boundary defined in Figure 4.3. The heat tendency over the length of the times series is equivalent to 13 GW.

4.3 The mean and eddy temperature fluxes in the SPG boundary

4.3.1 Large-scale distributions of surface and 1000-m depth mean and eddy temperature fluxes

The mean temperature fluxes in the SPG at the sea surface and 1000 m are depicted in Figure 4.5(ab) and Figure 4.5(cd), respectively, with the along-shore terms in Figure 4.5(ac) and cross-shore terms in Figure 4.5(bd). While the patterns at the two levels are similar, the magnitude of the mean temperature flux at the surface is almost one order of magnitude higher than that at 1000 m due to the surface intensified boundary current. Due to the fact that the sign of the mean temperature flux is defined entirely by the mean velocity, the direction of the mean temperature flux corresponds to the direction of the mean flow. The along-shore boundary current is easily recognizable as a positive mean temperature flux parallel to the isobaths ($\bar{U}\bar{T}$). Strong positive values of the cross-shore mean temperature flux ($\bar{V}\bar{T}$) are found around the southern tip of Greenland, where the mean circulation transports heat from the boundary into the interior due to the deflection of the boundary current in the vicinity of Erik ridge over the sharply changing topography (Holliday et al., 2009). In the rest of the SPG boundary, the cross-shore mean temperature flux along the isobath 3000 m is mostly negative (and thus onshore).

The eddy temperature fluxes in the SPG at the sea surface and 1000 m are depicted in Figure 4.6(ab) and Figure 4.6(cd), respectively, with the along-shore terms in Figure 6(ac) and cross-shore terms in Figure 4.6(bd). The fluxes in both along- and cross-shore directions have similar magnitudes ($\sim 1\ ^{o}\mathrm{C}\cdot\mathrm{cm/s}$). The surface eddy temperature flux parallel to the isobaths ($\overline{U'T'}$) has a coherent, strong positive signature along western Greenland and a negative signature along eastern Greenland and the western Labrador Sea onshore of 1000 m isobath, while it shows opposite signs further offshore. Similar to the symmetric temperature fluxes of a coherent meandering jet in the Gulf Stream modelled by Treguier et al., (2017), the symmetric positive and negative patterns of the along-shore sea-surface eddy temperature flux

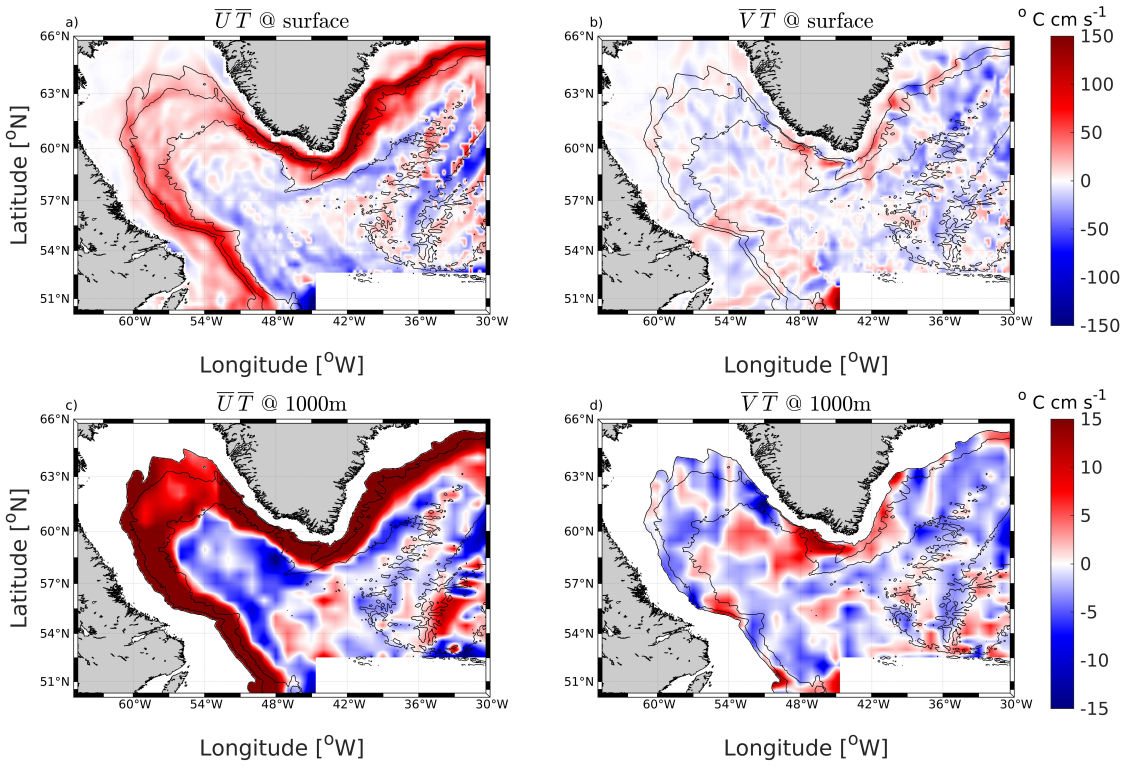

Fig. 4.5 Map of mean temperature flux parallel and perpendicular to the isobaths at sea surface derived from CMEMS dataset (a,b) and at 1000 m derived from ANDRO dataset (c,d). The positive (negative) values in b) and d) indicate offshore (onshore) fluxes. Note that the colorbar scale for the sea surface is one order of magnitude greater than that of 1000 m.

might be associated with the barotropic instability of the boundary current. The along-shore eddy temperature flux at 1000 m is generally positive along the Greenland boundary (Figure 4.6c). In line with previous studies (e.g., Palter et al., 2008; Georgiou et al., 2019) and with OSNAP mooring observations (Figure 4.2a), the cross-shore eddy temperature flux ($\overline{V'T'}$) at l000 m along the boundary is primarily positive between DKS and the northern Labrador Sea. Given that the mean temperature field suggests a cross-shore temperature gradient pointing outward from the interior (Figure 3.2 of chapter 3), the positive eddy temperature flux at 1000 m implies either a net transport of warm water into the interior or a net transport of cold water into the boundary. However, the sea surface cross-shore eddy temperature flux is mostly of opposite sign (negative) around Greenland, a pattern which was also observed on the OSNAP-based reconstruction of a typical vertical structure of the cross-shore eddy

temperature flux (Figure 4.2a), likely due to the opposite sign of the temperature anomaly (proved in Chapter 5).

We further extract the 1000-m depth $\overline{V'T'}$ along 2800 m isobath and compare it to the cross-shore temperature gradient (temperature difference divided by the width of the boundary) at the same depth in Figure 4.7. This result consistently demonstrates a negative correlation between cross-shore eddy temperature fluxes and the cross-shore temperature gradient (as already shown by Palter et al., 2008 for the Labrador Sea). When the cross-shore temperature difference is greater, with cooler water offshore and warmer water onshore in most regions, baroclinic instability of the boundary current increases. This directly affects the eddy generation and the amount of heat transported by eddies from the boundary to the interior. The smaller negative interior-boundary temperature gradient in the downstream direction (as intersect number increases) reflects the barotropization process of the boundary current due to the boundary cooling.

4.3.2 Reconstruction of the full-depth cross-shore eddy temperature flux

The along-boundary distribution of the surface and 1000m cross-shore eddy temperature fluxes along the 2800m isobath are shown in Figure 4.8. There is an approximate anticorrelation between the cross-shore temperature fluxes at the sea surface and at 1000 m depth from DKS to DVS, with the surface temperature fluxes being directed onshore and the 1000m temperature fluxes displaying an offshore pattern. Both fluxes at the sea surface and 1000 m depth increase from CF and peak in the strong EKE region of western Greenland. Along the western boundary of the Labrador Sea, both layers show onshore fluxes of a rather small magnitude.

To estimate the full-depth cross-shore eddy temperature flux, we combine the discrete values at the surface and 1000m with the typical vertical structure $f(z)$ deduced from the OSNAP dataset (Figure 4.2a). The water column can be divided into two layers depending on the vertical distribution of the cross-shore eddy temperature flux: the surface layer above

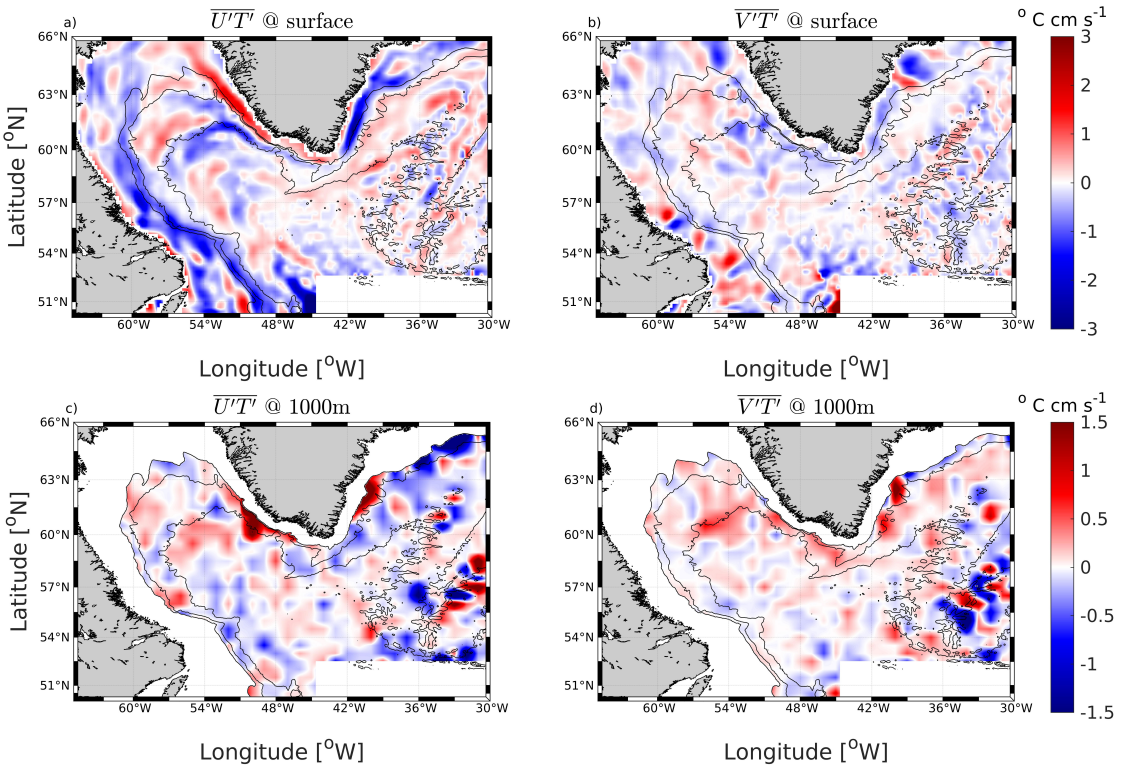

Fig. 4.6 Map of eddy temperature flux parallel and perpendicular to the isobaths at sea surface derived from CMEMS dataset (a,b) and 1000 m derived from ANDRO dataset (c,d). The positive (negative) values in b) and d) indicate offshore (onshore) fluxes.

100 m, where the maximum eddy temperature flux at the sea surface decreases dramatically and reaches a minimum around 100 m depth; and the main water column layer below 100 m with a relatively small but uniformly negative eddy temperature flux. We estimate the flux in the main water column by using a set of multiplicators $\alpha(z) = |(f(z))/(f(1000m))|$ defined by the typical OSNAP profile, i.e., the absolute values of the ratios of the eddy fluxes at depths below 100 m to the values at 1000 m. The magnitude of fluxes below 100 m is then obtained by multiplying the ANDRO-based value at 1000 m by the multiplicators. The fluxes above 100 m are then linearly interpolated towards the sea surface altimetry-based values. The 67 vertical profiles of cross-shore eddy temperature flux at the 2800 m isobath are shown in Figure 4.9a. In line with the eddy temperature flux derived from the OSNAP mooring, the ANDRO-based cross-shore eddy temperature flux averaged along the 2800 m isobath indicates that eddy exchange generally acts to cool the SPG boundary below the

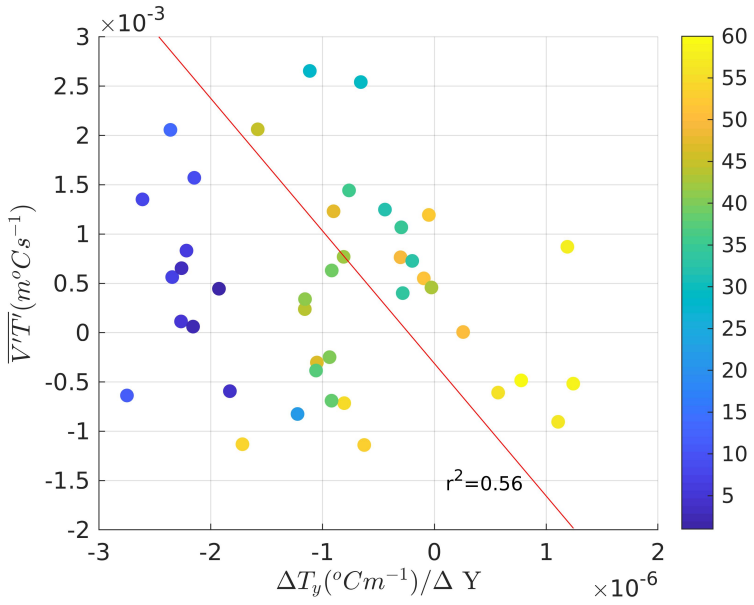

Fig. 4.7 Eddy temperature flux perpendicular to 2800 m isobath vs the cross-shore temperature gradient between 1000 m isobath and 2800 m, colored by the transect number. Note that some outliers have been deleted.

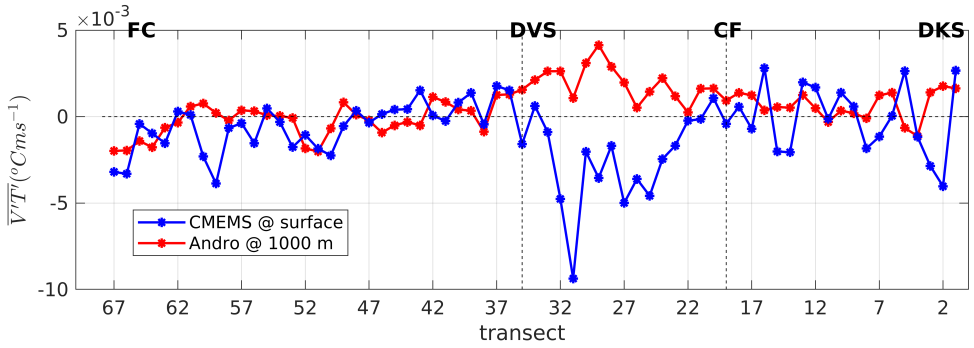

Fig. 4.8 The cross-shore eddy temperature flux along the 2800 m isobath at the sea surface (blue curve, derived from CMEMS dataset) and at 1000 m depth (red curve, derived from ANDRO dataset). The positive (negative) values indicate offshore (onshore) fluxes.

near-surface layer (Figure 4.9b). Note that if instead of assuming a non-uniform shape, we assume that the cross-shore eddy temperature flux below 100 m is uniform and equals the value at 1000 m, the total cross-shore eddy temperature flux does not change significantly and does fall within the range of uncertainty estimates indicated in Figure 4.12.

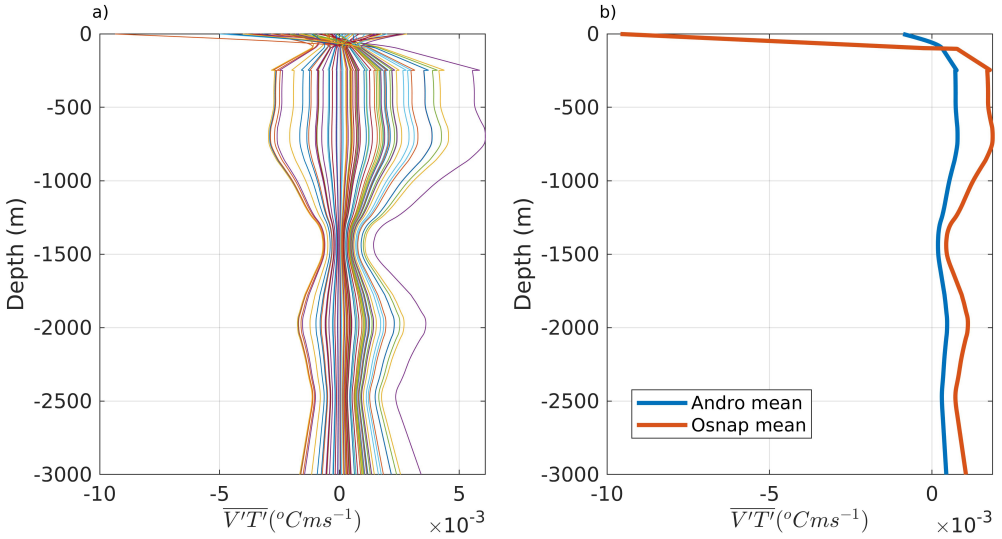

Fig. 4.9 Vertical profiles of the cross-shore eddy temperature flux at the points of 2800 m isobath (a). The corresponding averaged vertical profile (blue curve), and the 'typical' profile derived from OSNAP moorings (red curve) (b). The positive (negative) values indicate offshore (onshore) fluxes.

4.4 Heat budget of SPG boundary

Figure 4.10 illustrates the along-shore distributions of the four terms in Equation 4.3 (vertically-integrated with W_{in}=0), i.e., the along-shore mean heat advection, cross-shore mean heat advection, cross-shore eddy heat advection, and air-sea heat flux. We also show the horizontal mean advection (sum of the along-shore and cross-shore mean advection). The along- and cross-shore mean heat advection (Figure 4.10ab) follow the similar pattern as the volume transports (Figure 3.5a in Chapter 3), as they mostly depend on velocity variations rather than temperature variations. The mean circulation appears to predominantly warm the boundary (Figure 4.10c). Figure 4.10d illustrates that the cross-shore eddy heat advection primarily cools the boundary (between DKS and DVS), with significant heat advection between CF and DVS due to the most intense eddy field found in this particular region. The air-sea transport primarily cools the boundary current, and reaches its maximum magnitude around DVS because of both the maximum air-sea heat flux and the co-located maximum surface area of the boxes ($dxdy$). The heat advected by the mean circulation ($\sim 10^4$ GW) can be locally one or two orders of magnitude greater than the heat advected by the eddy

activity and air-sea flux ($\sim 10^2$ to $\sim 10^3$ GW), but, importantly, these three terms have the same order of magnitude when integrated along the whole boundary or within large-scale subregions ($\sim 10^4$ GW, see Figure 4.12).

By integrating horizontal heat advection, cross-shore eddy heat advection, and air-sea heat transport horizontally, we then evaluate the closure of the full-depth SPG boundary-mean heat budget. The total heat convergence due to the horizontal mean circulation ($7.3 \pm 0.5 \times 10^4$ GW) in Figure 4.11a indicates that mean currents warm the boundary, whereas cross-shore eddy heat advection ($2.08 \pm 0.3 \times^4$ GW) and air-sea heat transport ($2.5 \pm 0.5 \times 10^4$ GW) cool the boundary. In the WL region (Figure 4.11b), the heat convergence due to the mean circulation ($2.3 \pm 0.5 \times 10^4$ GW) is mainly balanced by air-sea heat transport (1.5 ± 10^4 GW). In the WG region (Figure 4.11c), the heat convergence due to the mean circulation ($1.7 \pm 0.9 \times 10^4$ GW) is mostly balanced by the cross-shore eddy heat advection ($-1.30 \pm 0.3 \times 10^4$ GW). Consistent with Chanut et al., 2008 and Saenko et al., 2014, the WG region has the most extreme values of the eddy heat advection along the SPG. In the EG region (Figure 4.11d), the mean heat advection ($4.26 \pm 0.7 \times 10^4$ GW) is compensated for both cross-shore eddy heat advection ($-0.89 \pm 0.2 \times 10^4$ GW) and air-sea heat transport (-1.03×10^4 GW). The consistent regional pattern of the three terms indicates that, in most regions, the mean circulation warms the boundary, while cross-shore eddy heat advection and surface heat flux cool the boundary.

The mean horizontal heat advection term in the SPG heat budget is then decomposed into along-shore and cross-shore components (Figure 4.12). The significant positive along-shore mean advection term (red bar), with a rate of $8.5 \pm 0.07 \times 10^4$ GW, is contributed by both the mass loss ($U_{FC} < U_{DKS}$, see Chapter 3) and the cooling ($T_{FC} < T_{DKS}$) in the along-shore direction. The former is primarily contributed by cross-shore volume transport (which is also implied in cross-shore mean heat advection), whereas the latter is contributed by cross-shore mean advection (yellow bar), cross-shore eddy advection (purple bar) and air-sea heat transport (green bar). Since we are interested in the along-shore temperature change which ultimately drives the BC downwelling, we then compare the along-shore mean advection term with the sum of the three other terms (light blue bar). We found the along-shore mean

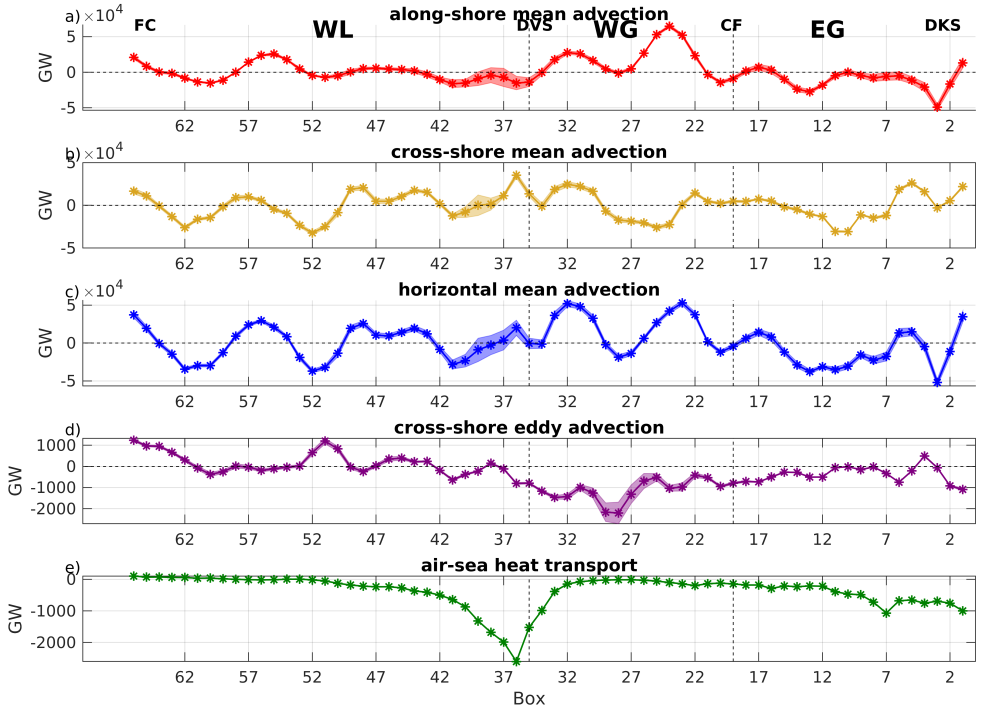

Fig. 4.10 The four terms of the small boxes with sign in the heat budget equation 4.2: the along-shore mean heat advection (a), the cross-shore mean heat advection (b), the horizontal mean heat advection (c), the cross-shore eddy heat advection (d) the air-sea heat transport (e). The errors in patch are two times the standard deviation derived from the bootstrap simulations. Positive (negative) values indicate heat convergence (divergence). WL, WG, and EG indicate the western Labrador Sea region, western Greenland region and Eastern Greenland region (defined in Chapter 3).

advection term is mostly balanced by the other three terms within uncertainties, keeping in mind that the averaged tendency term over the study period is relatively negligible (13 GW). Each of the three terms contributes significantly to balance the along-shore mean heat advection, with cross-shore mean heat advection contributing to about 26% ($2.2 \pm 0.9 \times 10^4$ GW), cross-shore eddy heat advection contributing to about 25% ($2.1 \pm 0.2 \times 10^4$ GW), and air-sea fluxes contributing to about 30% (2.5×10^4 GW). The remaining $\sim$19% of the boundary heat loss might be explained by the unresolved term D, which includes along-

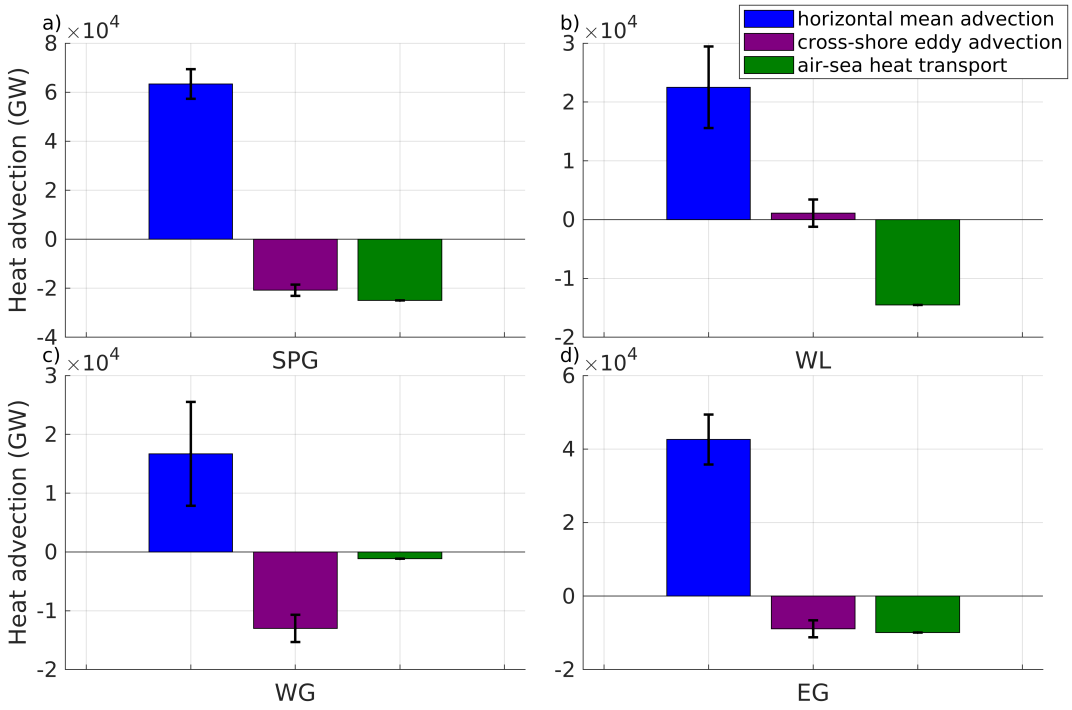

Fig. 4.11 The mean heat budget of the SPG boundary and the three regions, i.e., the regional integration of the mean advection, cross-shore eddy advection and air-sea heat transport terms in Figure 4.10. The error bars are the standard deviation derived from the bootstrap simulations. Positive (negative) values mean heat convergence (divergence).

shore eddy heat flux and horizontal diffusion, but also by the uncertainties inherent to our calculation (as discussed in Section 4.5).

To further investigate the vertical structure of the heat budget, we compute the convergence of the heat budget (the along-shore mean advection, on lhs of Equation 4.3, minus the first three on rhs) accumulated from the sea surface to the bottom (2800 m) with a 100-m interval (red line in Figure 4.13a). As indicated by Equation 4.3, the convergence term includes not only the unresolved term D (which includes the along-shore and vertical eddy heat fluxes and turbulent diffusion) but also the vertical mean heat transport (the fourth term on rhs of Equation 4.3). The convergence rises from the surface, reaching a maximum at 1300 m of $-8.2 \pm 2.0 \times 10^4$ GW, which indicates that the convergence term contributes to the upper boundary cooling. The vertical heat transport is then evaluated based on the vertical

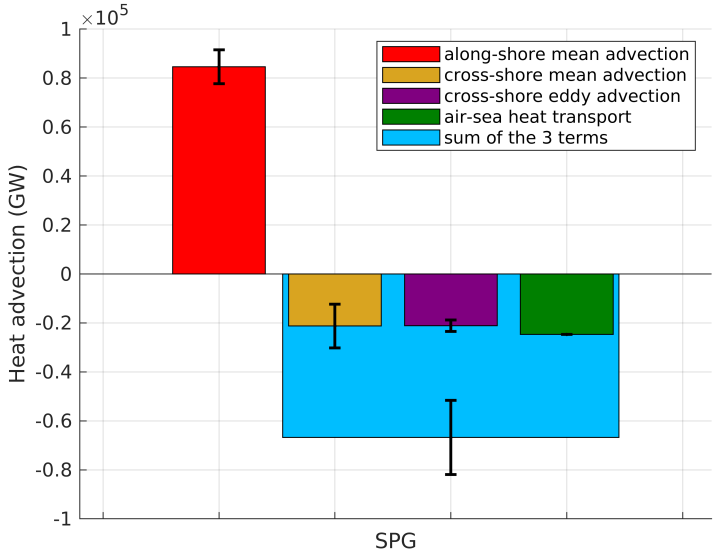

Fig. 4.12 The contribution of different terms in balancing along-shore mean heat advection assessed from the horizontal integration of the four terms in Figure 4.10. The light blue bar indicates the sum of the three terms. The error bars are the standard deviation derived from the bootstrap simulations. Positive (negative) values mean heat convergence (divergence). Since the contribution due to the temperature tendency is relatively small (13 GW, see text), the convergence between the along-shore mean advection (red bar) and the sum of the three terms (light blue) is mostly explained by the unresolved term, including along-shore eddy heat flux and horizontal diffusion.

volume transport at the SPG boundary with the offshore limit at 2800 m isobath. Figure 4.13b indicates that the total downwelling is 3.2±0.7 Sv at 1300 m, which is consistently smaller than what was estimated in Chapter 3 (4.0±0.9 Sv, with the offshore limit at 2400 m) due to the reduced baroclinic cross-shore transport at 2800 m isobath. We then obtain the vertical mean heat transport accumulated vertically (the black line in Figure 4.13a) by combining this vertical volume transport with the OI-based temperature field. The negative vertical mean heat transport, which reaches a maximum of $5.0 \pm 2.0 \times 10^4$ GW at 1300 m, indicates that the upper boundary current layer is subject to cooling as a result of heat convergence of the boundary downwelling. The vertical advection of the mean stratification, which draws warm water downward, further contributes to the cooling of the upper layer (above 1300 m) of the boundary current, and to the warming of the lower layer. The difference between the

convergence term and vertical heat transport (blue dashed line in Figure 4.13) indicates that the unresolved term D (and calculation uncertainties) contributes to the boundary warming above 100 m and the boundary cooling below. Interestingly, this is identical to the vertical structure of the cross-shore eddy heat flux (Figure 4.9b), which contributes to warming in the surface layer (above 100 m) and cooling below the SPG boundary.

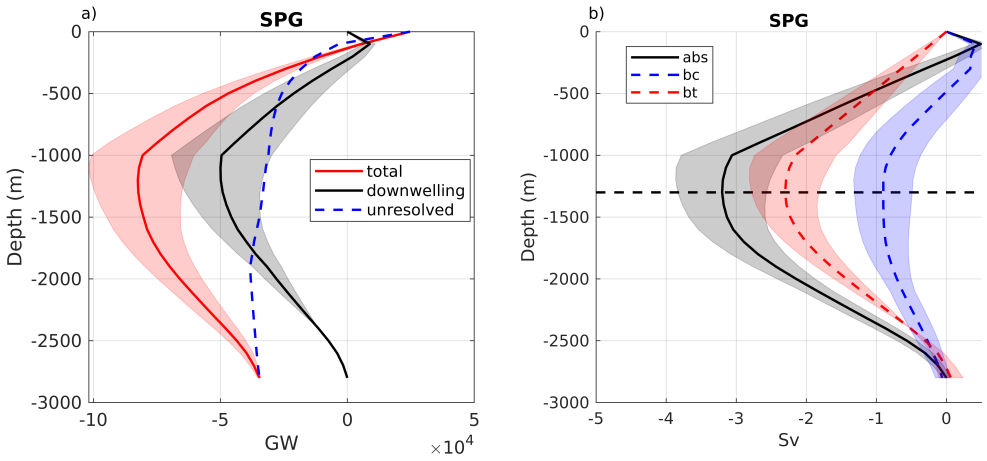

Fig. 4.13 (a) The convergence of the heat budget (the along-shore mean advection, on lhs of Equation 4.3, minus the first three on rhs, red line) and vertical mean heat transport (the fourth term on rhs of Equation 4.3, black line) accumulated from the surface to 2800 m with a 100 m interval. The patch errors are two times standard deviations derived from bootstrap simulations by perturbing velocity and temperature fields. A negative value indicates that the convergence of the heat budget (or the vertical heat transport) contributes to cooling the boundary above a given depth. The difference between the two lines (blue dashed line) indicates the contribution of the unresolved term D. (b) The vertical transport at 100m-spaced depths ranging from 0 m to 2800 m in SPG boundary. The total geostrophic transports are indicated by the black curves, along with the baroclinic (red) and barotropic (blue) components. Positive indicates upwelling transport, and negative indicates downwelling transport. The patches indicate the errors (two times the standard deviation) determined from the bootstrap simulations.

4.5 Summary and discussion

In this chapter, we carried out an observation-based time-mean (2002-2019) heat budget analysis of the SPG boundary current (from DKS to FC) to reveal the dominant mecha-

nisms driving its along-shore cooling, a key ingredient for boundary-focused baroclinic downwelling (see Chapter 3). The full-depth geostrophic velocities and OI-based full-depth temperature field were used to quantify cross-shore and along-shore advective mean heat fluxes. We further computed the full-depth cross-shore eddy heat fluxes using a combination of the ANDRO deep displacement database, satellite altimetry data, and OSNAP mooring observations. In general agreement with previous studies (Spall, 2004; Palter et al., 2008), it is found that cross-shore mean advection, cross-shore eddy heat advection, and atmospheric cooling all significantly contribute to removing heat from the boundary current. We provide a novel comprehensive description of the spatial variations of these processes through a direct calculation of the heat budget over the full-depth SPG boundary, and further describe the heat budget vertical structure to show that the SPG boundary's net downwelling drives heat from the upper layer (above approximately 1300 m) into the deeper layer.

The interior-boundary heat advection by the mean cross-shore flow is a significant mechanism for boundary heat loss. Following Chapter 3, offshore mean heat flux is observed at the southern tip of Greenland due to the offshore mean flow, whereas it is oriented onshore along the convergence of the SPG boundary. This indicates that barotropic volume flux not only contributes directly to boundary downwelling via horizontal divergence above the sloping bottom (Chapter 3) but also indirectly to boundary downwelling by removing heat from the boundary and therefore contributing to driving the baroclinic cross-shore transport. The total yearly heat loss in the Labrador Sea boundary by the full-depth cross-shore mean advective flux is 2.4 ± 0.8 GJ$/$m^2, which is similar to the rough estimate (0.2-1 GJ$/$m^2) within the layer 250-1000 m deduced by Palter et al. (2008). Note that Palter et al. (2008) only calculated the mean heat advection across the 3000 m isobath, which is not identical to the mean cross-shore advection (between 2800 m and 1000 m isobaths) that we calculate here as the offshore mean heat transport at 1000 m isobath (2.0×10^4 GW) is not negligible in comparison to that of 2800 m isobath (2.5×10^4 GW).

Eddies are also important for the SPG boundary heat loss, especially around Greenland. Prior observations have quantified local and punctual eddy heat advection in the Labrador Sea. Here, we provided a comprehensive quantification of the full-depth eddy heat flux

along the whole SPG boundary and a description ofits spatial variations. This study focuses on estimating the heat transport supplied by surface and subsurface ($\sim$1000 m) intensified coherent eddies. This eddy heat transport also incorporates the anomalies of noncoherent mesoscale structures, including fronts, filaments, and waves. The highest eddy heat flux is observed at Irminger rings production sites in western Greenland high-EKE region, where the boundary current is strongest, narrowest, and most unstable. Along the western Labrador Sea, there is no discernible pattern in the cross-shore eddy heat flux. More than 60% of the eddy-induced boundary heat loss in Labrador sea is accounted for by that in the eastern Labrador Sea, which is approximately 3.2×10^{11} GJ/yr. Considering that the Labrador Sea basin loses 3.6-6.1 $\times 10^{11}$ GJ/yr heat to the atmosphere (Lilly et al., 1999), cross-shore eddies can compensate for 52%-89% of this heat loss. This is consistent with the findings of Katsman et al. (2004), which concluded that boundary current eddies can compensate for 55%–92% of the heat loss to the atmosphere in the Labrador Sea basin. Therefore, eddies also play a significant role in the restratification of the convective region.

Our heat budget for the boundary region of the SPG does not close perfectly, with the combined effect of cross-shore mean heat advection, cross-shore eddy heat advection and air-sea heat flux, which does not fully compensate for the along-boundary mean heat advection (Figure 4.12). This residual may include the unresolved terms (such as along-shore eddy heat transport and horizontal diffusion), uncertainties associated with estimations such as the full-depth cross-shore eddy heat flux, ECMWF surface heat fluxes, and sampling errors of Argo floats. The source of uncertainty in the eddy heat fluxes across 2800 m isobath can be twofold. First, the resolution of Argo float displacements in each grid is between 10 and 30 km, which is larger than the first-baroclinic Rossby radius of deformation in SPG (around 5-10km, Chelton et al., 1998; Gelderloos et al., 2011). Therefore, the observations at certain SPG boundary sites cannot resolve small eddies. For instance, relatively small (15 km radius) eddies produced by the Irminger Current (Lilly and Rhines, 2002) as well as the Denmark Strait overflow cyclones (10 km radius, Pacini et al., 2021) were captured by OSNAP moorings around the tip of Greenland. These eddies may contribute to the overall impact of eddy heat fluxes and to an additional cooling of the boundary, which could explain

why the OSNAP-averaged eddy temperature flux is slightly greater than our estimation (Figure 4.9b). Second, there is still some uncertainty in the estimations of eddy heat flux below 1000 m. At certain locations of the SPG boundary not covered by OSNAP moorings, eddy activity can reach the deep overflow water layer (below 1800 dbar) (Zou et al., 2021). In addition, it has been demonstrated that turbulent diffusion due to unresolved eddy activity contributes significantly to the SPG boundary heat budget. Spall (2004) demonstrated through a heat budget of the convective region that horizontal diffusion contributes to the spreading of boundary currents by cooling the warmest waters near the outer boundary and warming the seaward region of the boundary current. Desbruyères et al. (2020) investigated the heat budget of the intermediate depth (700–2000 m) SPG and found that boundary-focused vertical mixing likely played a significant role in the recent warming trend observed in the SPG between 1996 and 2013. In addition, ageostrophic processes, such as viscosity, bottom Ekman flows, and nonlinear factors as discussed in Chapter 3, may also contribute to the heat budget but cannot be resolved by our analysis.

This work has underlined the importance of lateral mean and eddy heat transport, as well as atmospheric cooling, for cooling the SPG boundary current and partly governing the net baroclinic downwelling occurring within the region. Although the contribution of each mechanism has been previously explored in the Labrador Sea using both modelling and observations (e.g., Chanut et al., 2008; Palter et al., 2008; Saenko et a., 2014; Georgiou et al., 2019), the present analysis provides a novel comprehensive description of the mean heat budget within the entire western SPG by making extensive use of the most recent available observations. Understanding the dynamics and thermodynamics of the western SPG boundary is a crucial step in the study of boundary downwelling and interior water mass transformation and, thus, for the AMOC in general. A next step is to carefully evaluate the response of such boundary current dynamics in climate models to changing forcing conditions.

Chapter 5

Role of mesoscale eddies in the heat budget of the SPG boundary: a semi-Lagrangian perspective

In the previous chapter, we analyzed the heat budget of the SPG boundary and evidenced the crucial role of mesoscale eddies in maintaining an along-boundary density (temperature) gradient. We quantified the contribution of eddies from an Eulerian viewpoint by estimating the local anomaly fluxes caused by the correlation between velocity and temperature anomalies. In this chapter, we further investigate this role from a semi-Lagrangian perspective, i.e., we evaluate the heat transport across isobath 2800 m caused by the propagation of temperature anomalies by distinct coherent eddy structures, a component often referred to as the "trapping" eddy heat flux.

5.1 Introduction

Previous studies have identified four main kinds of coherent eddies that form and propagate in the SPG following distinct formation mechanisms: Irminger rings (IRs), Boundary current eddies (BCEs), Convective Eddies (CEs) and Denmark Strait Overflow Water Cyclones (DSOWC). Figure 5.1 shows locations where these several types of eddies form and propagate. The propagation of these eddies may contribute to the lateral heat exchange of physical properties between the boundary and the interior, thereby contributing to both maintaining

the along-boundary temperature gradient responsible for (part of) the Eulerian-mean boundary downwelling and for restratifying the basin interior where deep convection takes place.

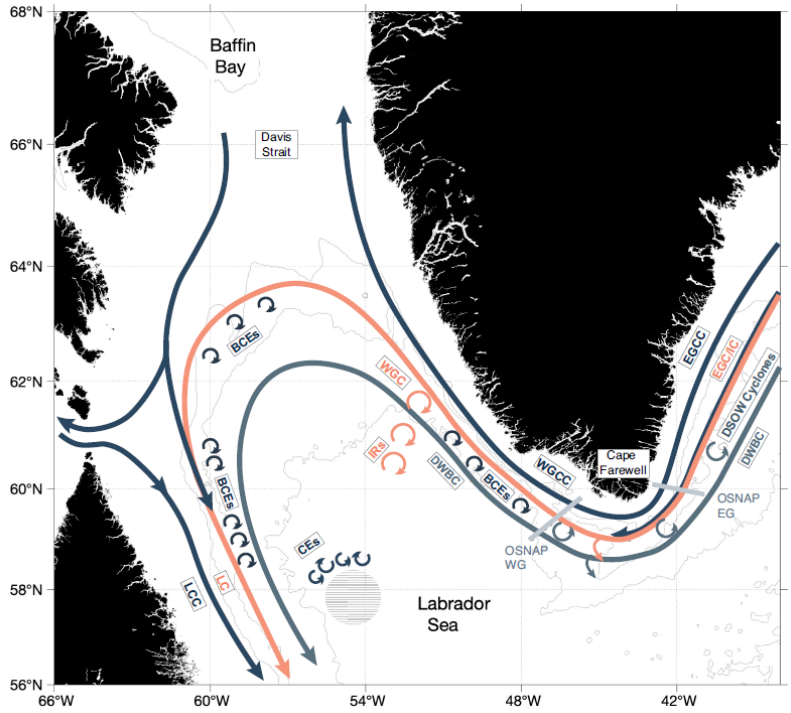

Fig. 5.1 Schematic circulation of the Labrador Sea. EGCC is the East Greenland Coastal Current; EGC/IC is the East Greenland Current/Irminger Current; DWBC is the Deep Western Boundary Current; WGCC is the West Greenland Coastal Current; WGC is the West Greenland Current; LCC is the Labrador Coastal Current; LC is the Labrador Current; DSOW Cyclones are Denmark Strait Overflow Water Cyclones; IRs are Irminger Rings; CEs are Convective Eddies, and BCEs are Boundary Current Eddies. The hatched area in the western/central Labrador Sea represents the area of the deepest convection. Grey lines across the boundary current with OSNAP EG and WG labels indicate the locations of the OSNAP East and West Greenland mooring arrays, respectively. Source: Pacini et al., (2022)

IRs form downstream of Cape Farewell (CF) as a result of the instability of the West Greenland/Irminger Current system caused by the steep topography (Heywood et al., 1994; Prater et al., 2002; Brandt et al., 2004). Studies have shown that the barotropic instability of boundary current drives the formation of IRs (Chanut et al., 2008). They are also generated by baroclinic instabilities near the bottom, which depend on the horizontal gradient of density (Katsman et al., 2004; Zhu et al., 2014). Most of these energetic eddies are anticyclones with

a radius between 10 and 45 km and are characterized by a thick and prominent layer of warm, salty Irminger Current Water (Lilly, 2003; Hátún et al., 2007). Importantly, the IRs have a fresh and cold surface layer (above about 200 m) derived from western Greenland shelf water (Hátún et al., 2007; Rykova et al., 2009). The IRs may trap warm and saline Irminger Current Water at depth and propagate to the west and southwest, thereby preventing deep convection and facilitating restratification in the northern Labrador Sea (Chanut et al., 2008; Rieck et al., 2019).

BCEs are less energetic eddies formed by the baroclinic instability at the boundary between the Western Greenland Current or Labrador Current and the interior along the boundary of the Labrador Sea (Chanut et al. 2008). Along the eastern boundary, BCEs are generated between the southern tip of Greenland and Cape Desolation. Along the western boundary, BCEs are generated between 56°N and 60°N (Eden and Böning, 2002; Brandt et al., 2004). The BCEs are smaller (10 km), shallower, and less influenced by the local topography than the IRs, and show a pronounced maximum number in winter when baroclinic instability of the boundary current increases as the boundary-interior density gradient sharpens (Chanut et al. 2008). The accompanying lateral eddy fluxes due to the propagation of BCEs, explored, for instance, by Spall (2004) and Saenko et al., (2014), can also be effective in compensating for the loss of buoyancy in the interior of the Labrador Sea, especially in the vicinity of the convective area in the western portion of the basin. The BCEs (both anticyclones and cyclones) were observed for the first time recently in the meanders of the West Greenland current with continuous mooring observations (Pacini et al., 2022).

CEs form in the vicinity of the deepest mixed layers in Labrador Sea convection regions, preferentially in early spring through baroclinic instability of the convective patch (Gascard and Clarke 1983; Marshall and Schott 1999; Luo et al. 2011). Theoretical and modelling studies indicate that CEs can be either anticyclonic or cyclonic (Send and Marshall, 1995; Jones and Marshall, 1997; Chanut et al., 2008), although the few observed CEs were exclusively anticyclonic (Lilly et al., 2003; Rykova et al., 2009). These eddies have a 10 to 15 km radius and mainly trap Labrador Sea water, which is vertically mixed cold and fresh mid-depth (200-1000 m) water (Lilly et al., 2003, Rykova et al., 2009). It is hypothesized

that the interannual variations in CE generation are related to the intensity of deep convection (Lilly et al., 2003; Brandt et al., 2004). CEs and the related baroclinic instabilities are thought to play a role in the rapid (few months) spring post-convective restratification due to the lateral buoyancy flux they cause (e.g., Jones and Marshall, 1997; Gelderloos et al., 2011; Saenko et al., 2014).

DSOWC are cyclonic eddies formed by the descent of overflowing water over the Denmark Strait sill (Bruce, 1995; Spall and Price, 1998; von Appen et al., 2014). According to numerical simulations, these cyclones develop due to the vortex stretching caused by the descent of dense overflow (Krauss and Kase 1998; Spall and Price 1998), bottom friction effects (Hill 1996), or the baroclinic instability in the hydrographic front (Spall et al., 2019). DSOWC have a 10-20 km radius and are intensified at mid-depth (700-1000 dbar). They contain warm and saline waters in the layer lighter than 27.65 $\mathrm{kg/m^3}$ and cold and fresh overflow waters in the 27.74–27.85 $\mathrm{kg/m^3}$ layer (Zou et al., 2021). Recent observations have revealed that the DSOWC can be found along the western Greenland boundary (Pacini et al., 2021, Zou et al., 2021). Water captured by DSOWC will propagate along Greenland coasts, contributing significantly to the export of overflow water. However, the role of these cyclones in boundary-interior interchange and the resulting interior restratification is largely unknown.

Table 5.1 summarizes the common properties of the four aforementioned types of eddies found along the SPG boundary, which can all transport heat between the boundary and the interior. There are primarily two mechanisms for coherent eddy-induced heat transport: a local effect, known as the stirring component, associated with the impact of rotational eddy motions on the stirring of local background isotherms; and a non-local effect, known as the trapping component, associated with the potential of coherent eddies to trap water masses without dispersion and release them in a very different environment, when their rotation speed is larger than the propagation speed (Chelton et al., 2011). Current eddy parameterizations in coarse-resolution models attempt to account for stirring components, while the trapping component is not accounted for in any existing coarse-resolution model parameterizations (Frenger et al., 2015). For example, the stirring component dominates the total eddy fluxes in the Southern Ocean because of the much larger swirl speed than the eddy propagation

speed (Frenger et al., 2015). However, for the eddies with long-distance propagation, such as for the Agulhas ring studied by Lehahn et al., (2011), the trapping component may be significant, as eddies can trap fluid properties inside their core and transport them over considerable distances. In addition, Dong et al., (2014) highlighted the importance of global meridional eddy "trapping" heat transport, as it accounts for about 20%-30% of the total oceanic meridional heat transport.

Table 5.1 A summary of characteristics of the four types of eddies from previous numerical/observational studies. N/A indicates not available or unknown. C/A indicates Cyclones/ Anticyclones. BTI indicates barotropic instability, and BCI indicates baroclinic instability.

Eddy type	**Location (Forming mechanism)**	**Radius (km)**	**Temperature structure**	**Propagation direction**
IRs (A)	Western Greenland (BTI/BCI)	10-45km	Cold at the surface (200 m) and warm below	Cross shore, mostly offshore
BCEs (C/A)	Coasts of Labrador Sea (BCI)	10 km	N/A	Cross shore
CEs (N/A)	Convection regions of the Labrador Sea (BCI)	10-15 km	Cold at mid-depth (200-1000 m)	Inshore
DSOW (C)	Southern Greenland (N/A)	10-20 km	Warm in the upper layer (lighter than 27.65 kg m-3) and cold below	Along shore

In Chapter 4, the lateral eddy heat transport has been estimated by calculating the correlation between temperature and velocity anomalies ($\overline{V'T'}$) in an Eulerian framework. These lateral heat transport relative to the mean current ($\overline{VT}$) can be driven by coherent eddies (the stirring and trapping effects, presented by rotation speed and propagation speed) but also by noncoherent mesoscale features (such as waves, meandering, front, and filament). This eddy heat transport is therefore referred to as the 'total eddy heat transport' in our study. To determine the impact of the coherent eddy trapping component on this total eddy heat transport, this chapter aims to estimate the boundary-interior eddy trapping heat transport in a semi-Lagrangian framework, i.e., by estimating the local heat transport from a set

of eddy trajectories. Single eddies crossing the 2800 m isobath are detected and tracked on altimetry-derived maps of sea surface height using an automated tracking technique, and their vertical thermal structure is obtained using collocated Argo profiles. This study provides a complementary explanation for the Eulerian framework-based calculation of boundary-to-interior eddy heat fluxes (see Chapter 4).

The structure of this chapter is as follows. In section 5.2, the eddy detection and the eddy heat transport calculation will be described. Then, using an anticyclonic eddy (Irminger ring) as an example, we describe in section 5.3 how the cross-shore heat transport of a single eddy is computed. Section 5.4 then presents the distribution of cross-shore eddy heat transport along the isobath 2800 m, and the characteristics (including temperature structure and propagation direction) of the eddies. The comparison between total eddy heat transport and eddy trapping heat transport is then presented in section 5.5. Some limitations in the heat transport estimations are discussed in section 5.6, while Section 5.7 summarizes this study.

5.2 Methodology

5.2.1 Eddy selection in SPG boundary

As described in Chapter 2, we use the daily sea-level anomaly (SLA) dataset to detect and track eddies with a radius larger than 20 km. Even though the inability to detect smaller eddies is a restriction in our study, we will nevertheless be able to draw conclusions related to the thermal structure and propagation characteristics of cross-shore eddies at the SPG boundary (see Section 5.4). The distribution of eddies in the subpolar North Atlantic from 2002 to 2019 is depicted in Figure 5.2 using a grid size of $1° \times 0.5°$ ($\sim$55 km). It should be noted that the number of eddies shown in the figure is the number of eddies found in daily snapshots (hereinafter referred to as 'single eddy'), which means the same propagating eddy will be detected and counted several times. If the coordinates of an eddy center fall within the grid cell, the eddy is considered to have appeared in this grid cell. Between 2002 and 2019, 51786 eddies were detected in the SPG, including 25613 anticyclones (493015 single eddies) and 26173 cyclones (462714 single eddies). Consistent with sea surface EKE, which

provides an integrated measure of eddy variability (Figure 1.6 in Chapter 1), the northwest Labrador Sea and the western side of Reykjanes Ridge exhibit significantly larger eddy populations.

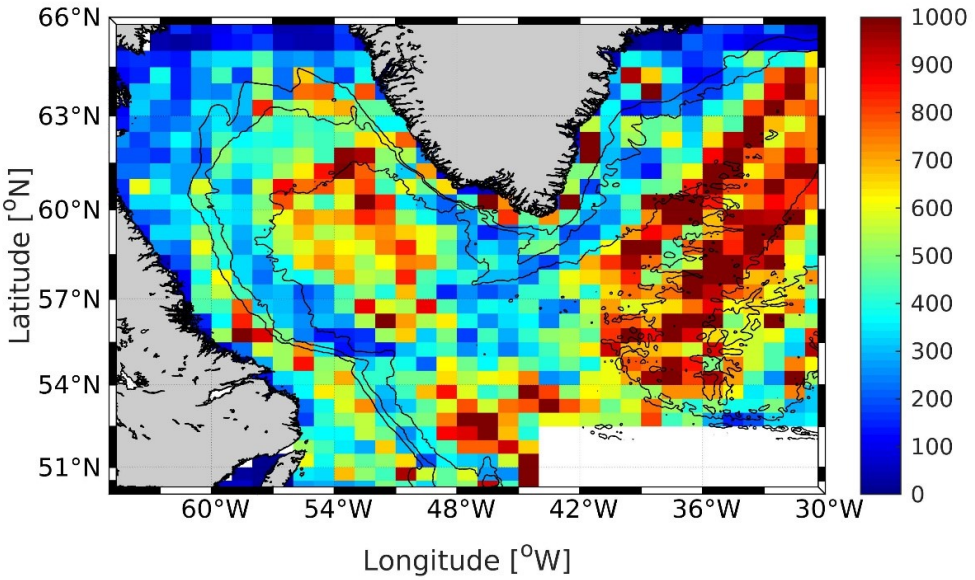

Fig. 5.2 The distribution of eddy number in $1^o0.5^o$ boxes. Contour lines indicate bathymetry of 0, 1000, 2000, and 3000 m.

To examine the eddy-trapping component of the eddy cross-shore heat transport, we select eddies that lie inside 66 circle-shaped bins with a radius of 55 km and centered on the 2800m isobath. The centers of these circles correspond to the centers of the volume/heat budget boxes in Chapter 3 and Chapter 4. We select all eddies with a distance to the isobath less than 55 km. Only eddies inside those circles that cross the 2800m isobath will be included in the calculation. The spatial distribution of the single eddies (or "snapshots") along the 2800m isobath is depicted in Figure 5.3. 167 anticyclones (3785 single eddies) and 170 cyclones (3033 single eddies) have been found to cross the isobath 2800 m between 2002 and 2019. Most eddies crossing the isobath have a lifetime greater than a week but less than four weeks. In accordance with Figure 5.1, there are more single eddies crossing isobath 2800 m in western Greenland due to the instability of the boundary current, as well as to

the north of Flemish Cap, where the northward subtropical flow meets the southeastward Labrador Current just off the continental slope. At the northernmost tip of the Labrador Sea, a large number of anticyclones are also detected.

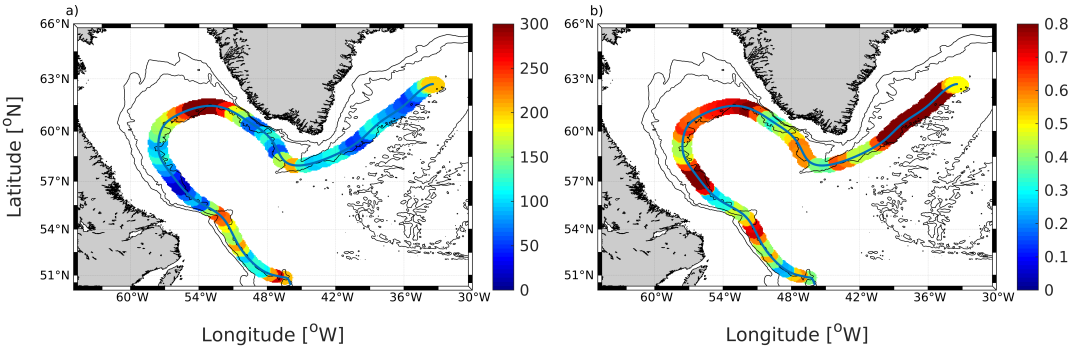

Fig. 5.3 The circle-shaped bins used to estimate heat transport crossing the isobath 2800m (continuous blue line), with a radius of 55 km. (a) The total number of single eddies detected in each bin. (b) The ratio of eddies with co-located Argo float (number of eddies with Argo floats/total number) in each bin.

5.2.2 Eddy trapping heat transport calculation

5.2.2.1 Heat transport by a single eddy

Following Dong et al., (2014), the cross-isobath heat transport Q_{eh} (unit: W) of a given eddy snapshot is calculated as

$$Q_{eh} = -\rho_0 C_{po}(2r_e)s \int v'_e T'_e dz \tag{5.1}$$

ρ_0=1025 kg/m^3 and C_{Po}=4200 J/(Kg $\cdot^{o}$ C) are the mean upper-ocean density and heat capacity, respectively. r_e is the eddy radius, and s is the "shape coefficient", which is set to 0.5 as a conservative value as most eddies are cone-shaped (Dong et al., 2014; Zhang et al., 2014). v'_e is the propagation speed, which is calculated from the displacements of the centers of the single eddies$((\mathrm{lon}_{\mathrm{eddy}}, \mathrm{lat}_{\mathrm{eddy}})^{\mathrm{t}+1} - (\mathrm{lon}_{\mathrm{eddy}}, \mathrm{lat}_{\mathrm{eddy}})^{\mathrm{t}-1})/2\mathrm{t}$ and then projected perpendicular to the isobath 2800 m. A sign convention is utilized, with a positive speed representing eddy entering the interior and a negative speed representing eddy entering the boundary region. T'_e denotes the temperature anomaly of the eddy calculated from Argo

profiles as follows. All temperature profiles available within 1.5 times the radius of a single eddy snapshot for the preceding or subsequent three days are gathered. For some single eddies along the trajectory with no collocated Argo profiles, temperature anomalies are taken as those of the single eddies in the closest snapshots. Half of the eddies detected in most of those circle-shaped bins have co-located Argo profiles (Figure 5.3b). Profiles of temperature anomaly are calculated by subtracting the OI-derived climatological seasonal temperature field (see Chapter 2) from the Argo temperature profiles. The trapping depth is set to 1000 m since the eddy loses its ability to trap water in deeper layers (Zhang et al., 2014). Negative Q_{eh} implies that eddies cool the boundary, either by transporting warm water towards the interior or cold water towards the boundary, whereas positive Q_{eh} suggests the opposite.

5.2.2.2 Eddy trapping heat transport across the SPG boundary

After calculating the heat transport associated with each single eddy, the total trapping heat transport by all the eddies across the isobath 2800 m will be evaluated. We evaluate the cross-shore eddy heat transport independently for anticyclones and cyclones, as the two types of eddies typically have different temperature structures. Because we are focusing on the heat flux across isobath 2800 m, the transport of each single eddy will be weighted depending on the distance of the eddy center to the isobath 2800 m (d_{2800}) and the radius of the eddy (r_e). The weight is defined by $w = 1 - d_{2800}/r_e$ (if $d_{2800} \leqslant r_e$), and $w = 0$ (if $d_{2800} > r_e$). Within each bin, following Dong et al., (2014), we average the heat transport of all the anticyclones (or cyclones) that were sampled by an Argo float (i.e., $<wQ_{eh}>$ in equation 5.2). The remaining anticyclones (or cyclones) intersecting the isobath 2800 m within the bin without any Argo profile are assumed to have the same heat transport as the average $<wQ_{eh}>$. The total time-mean transport in each bin is eventually estimated by multiplying the average with the detected population density Ne within each bin:

$$T = < wQ_{eh} > N_e = \frac{< wQ_{eh} > nt_i}{t_a} \tag{5.2}$$

where n is the total number of single anticyclonic (cyclonic) eddies in one bin, t_i is the time of sampling interval (1 day in our study), t_a is the analysis period (6573 days). The total heat transport across the isobath 2800 m will then be evaluated by summing up the heat transport of each bin. Since some of the eddies will overlap in two adjacent bins, the heat transport contributed by the overlapping eddies in the second bin will not be considered in the calculation of total heat transport.

The uncertainty of the heat transport in each bin is then evaluated by: $\varepsilon_{bin} = (1/ra_a)\sigma$, where ra_a indicates the ratio of eddies (anticyclones/cyclones) with co-located Argo float (number of eddies with Argo floats/total number) as shown in Figure 5.3b, and σ is the standard deviation of the eddy transports in one bin. The error estimates for total heat transport in the SPG boundary ε_{spg} are then equal to $\varepsilon_{spg} = \sqrt{(\sum \varepsilon_{bin}^2)}$.

5.3 Cross-shore eddy-trapping heat transport: an Irminger ring example

To illustrate the calculation of the eddy-trapping component of the cross-shore heat transport, we use an anticyclonic eddy with a 25-day lifetime (20021115-20021209) as an example. Figure 5.4(a) depicts this anticyclone trajectory (or all single eddy detections) as it moves from the western Greenland boundary to the Labrador Sea interior. This eddy is generated in the inshore region of northwestern Greenland, likely in response to the instability of the Irminger current. The intensity of the eddy shows that this anticyclone initially intensifies, then stabilizes, and then grows again until crossing the isobath at 2800 m (Figure 5.4b). It should be mentioned that the radius of the single eddy is determined using the variable 'area' from the algorithm, which assumes that the eddy has a circle shape. The 24^{th} day of this anticyclone life is then selected to illustrate local SLA, geostrophic velocity anomaly, and SSTA in Figure 5.5. The SSTA is calculated here by subtracting the monthly mean SST from the daily SST snapshot on the 24th day. The anticyclone shows enhanced geostrophic velocity anomalies rotating clockwise around a core of positive SLA maxima. This anticyclone has a negative SSTA value, indicating a cold core at the surface, which seemingly originates from

the Greenland shelf. The snapshot shows two additional negative SLA contours (cyclones) to the northwest and east of the anticyclone. The northwest cyclone traps the surface warm boundary current water (positive SSTA).

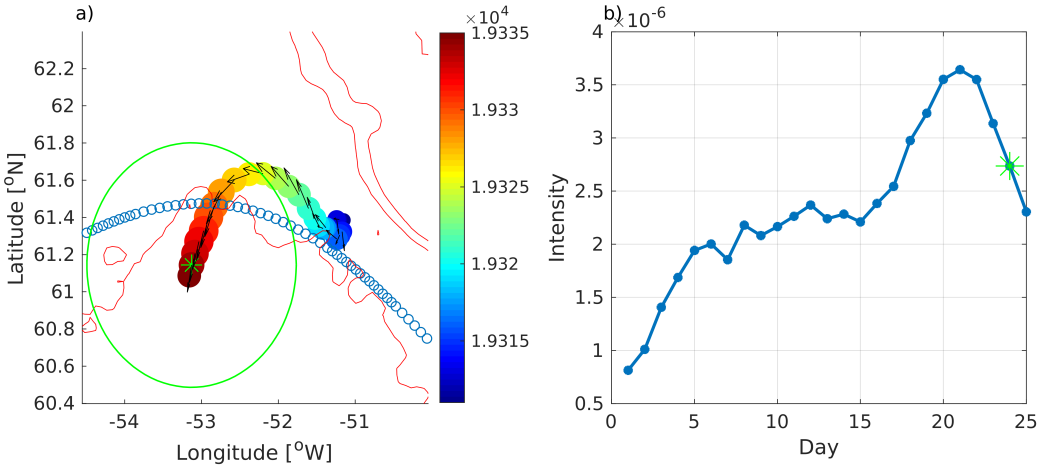

Fig. 5.4 The trajectory of an anticyclone intersecting isobath 2800 m from the western Greenland boundary into the Labrador Sea interior with a lifetime of 25 days. In panel (a), the color represents the Julian days associated with the single eddies. The black vectors denote the propagation velocity. The green star denotes the 24^{th} day of the eddy depicted in Figures 5.5 and 5.6, with the eddy boundary (1 radius) denoted in solid green circle. The blue dots denote the smoothed isobath 2800 m which is crossed by the eddy. Panel (b) depicts the evolution of intensity throughout the eddy lifetime.

We compute the temperature anomaly profile of the eddy using co-located Argo data. We look for T profiles available within 1.5 times the radius of a single eddy for the preceding or subsequent three days. As indicated by the green dot in Figure 5.5(b), one Argo profile is located near the 24^{th}-day eddy position (61°N, 53°W). The red line in Figure 5.6a represents the Argo temperature profile. The average SST within the eddy is close to the surface temperature measured by the Argo profile. The OI climatological temperature field at the corresponding season is averaged along the isobath 2800 m inside the eddy as the background temperature (black dotted line in Figure 5.6a), which is then subtracted from the Argo profile to calculate the temperature anomaly (T_e') (red line in Figure 5.6b). This anticyclone has a nonnegligible temperature anomaly in the uppermost 1000 m. It contains anomalously cold

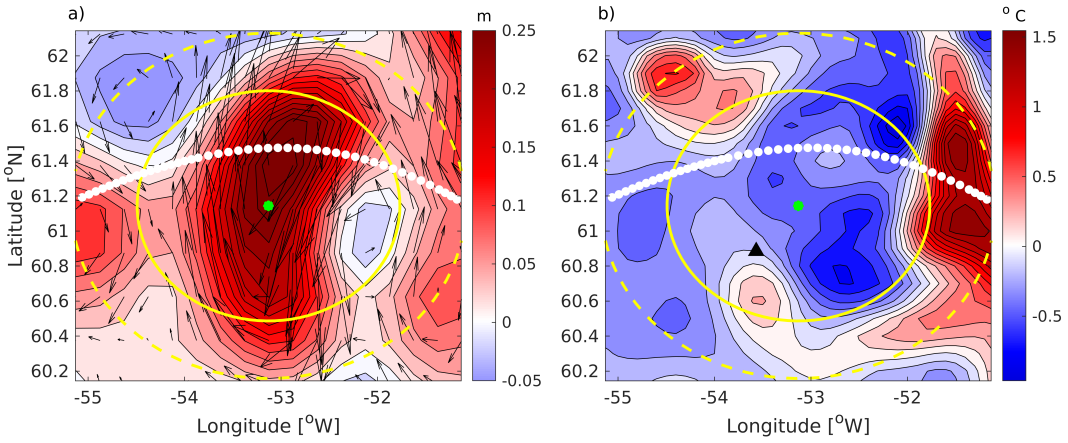

Fig. 5.5 The 24^{th}-day snapshot of SLA (a) and SSTA (b) for a single anticyclone (green star in Figure 4a). In (a), the black vectors represent the geostrophic velocity anomaly. The green dot denotes the center of the eddy on this day. The solid circle denotes the anticyclone boundary (1 radius), whereas the dashed circle denotes 1.5 times the radius. The white dots in the two panels indicate the isobath 2800 m. In (b), the black triangle indicates the location of the Argo float.

water in the uppermost 100 m (with an anomaly of -1.8°C at the sea surface) and warmer water in the deeper 100-1000 m layer (with a maximum anomaly of 1.3°C at 100-m depth).

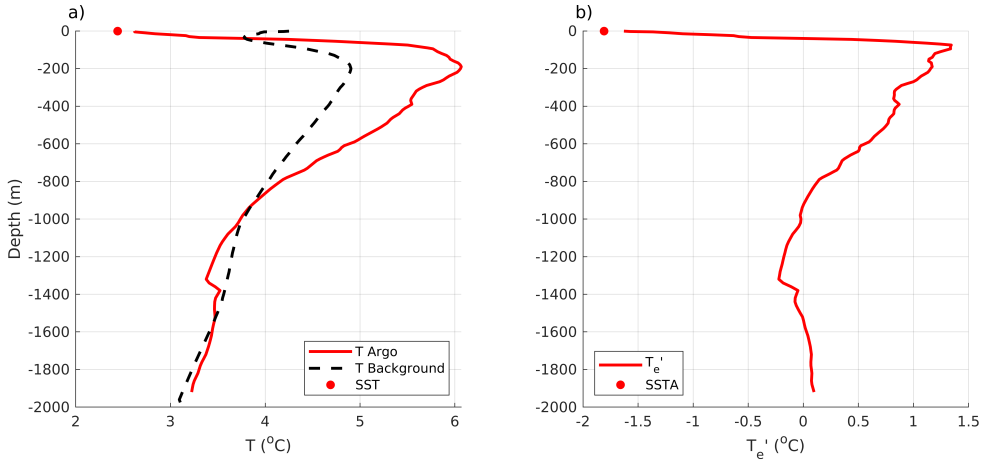

Fig. 5.6 (a) Vertical temperature profile (red curve) derived from an Argo float within the eddy interior (located in black triangle in Figure 5.5b). The background temperature profile (black dashes) averaged from the OI climatological seasonal field interpolated in the isobath 2800 m inside the eddy (i.e., white dots inside the solid yellow circle of Figure 5.5). The red dot indicates the satellite-measured SST value at the Argo float position. (b) The associated temperature anomaly profile (red curve), with the red dot indicating the averaged SST anomaly of the eddy.

After obtaining temperature anomaly profiles for all detections of this anticyclone, we use Equation 5.1 to compute its associated cross-shore heat transport. The T'_e profile is interpolated linearly onto 5 m evenly spaced depth levels ranging from 1 to 2000 m. By vertically integrating the $v'_e T'_e$ with a 1000 m depth, the heat transport of single eddies is derived, as illustrated in Figure 5.7a. Before reaching isobath 2800 m ($\sim 17^{th}$ day), the small negative heat transport of the offshore-flowing eddy ($v'_e > 0$, Figure 5.7b) indicates that the trapped shelf cold water ($T'_e < 0$, Figure 5.7c) would move into the interior. When the eddy is closest to the isobath 2800 m ($\sim 19^{th}$ day), its heat transport becomes strongly negative, implying that a vertically-integrated positive heat content anomaly is advected into the interior ($T'_e > 0$, Figure 5.7c). Here, the eddy also propagates more rapidly as its intensity rises (Figure 5.7b). The additional comparison of temperature anomaly profiles for single eddies on the 18^{th} and 24^{th} days (Figure 5.7d) reveals that, during the intensification phase, the isotherm of the anticyclone becomes deeper between 100 and 1000 m depth, where the trapped water gets warmer. The average heat transport over the lifespan of this eddy is oriented offshore and leads to a warming of the interior and a cooling of the boundary at a rate of -3.3×10^{12} W.

5.4 Cross-shore heat transport along the SPG boundary

5.4.1 The spatial pattern

The distribution of the eddy-trapping cross-shore heat transport along the isobaths 2800 m is depicted in Figure 5.8, with blue (red) colors indicating offshore (onshore) heat transport. The local magnitude of the heat transport (i.e., for each bin) is estimated between 10 and 100 GW. Along western Greenland, where eddy activity is most significant, a coherent cooling pattern is observed due to offshore eddy propagation. Elsewhere, the eddy trapping heat transport is relatively small and random, although an overall predominance of boundary cooling is seen. The total boundary-to-interior heat transport is 314 ± 115 GW, of which $\sim$60% (188 ± 36 GW) is contributed by the western Greenland eddies. Anticyclones and cyclones provide 166 ± 63 GW and 148 ± 83 GW, respectively, to the total heat transport.

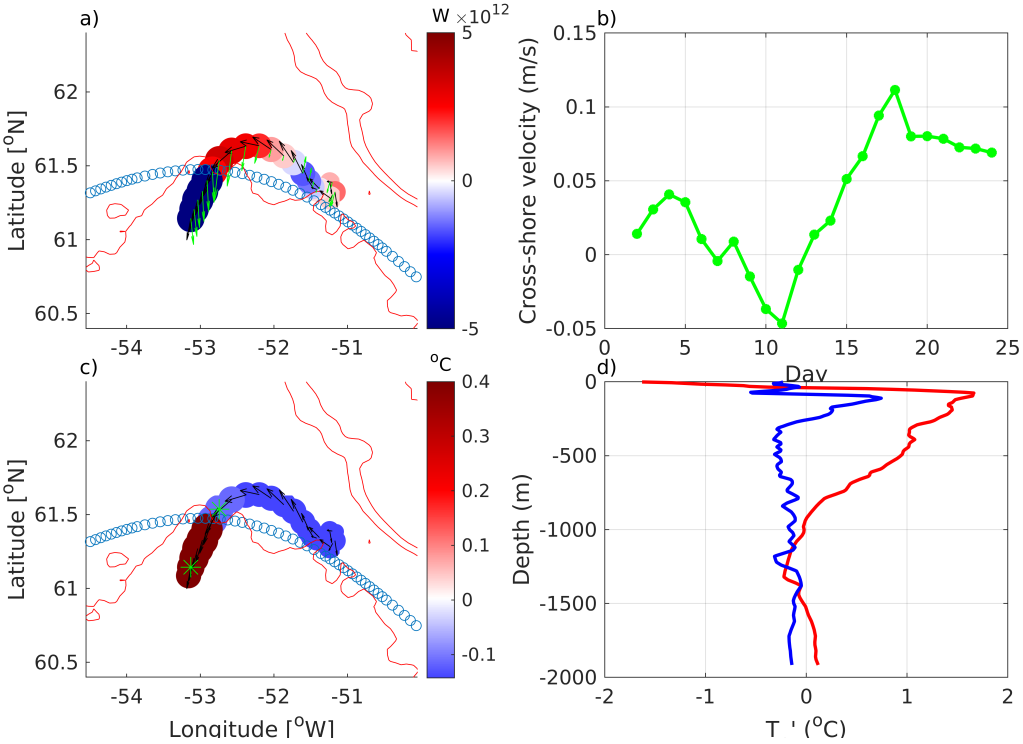

Fig. 5.7 (a) The trajectory of the anticyclone, where the color indicates the trapping heat transport of each single eddy snapshot as determined by Equation 5.1, with a positive (negative) value corresponding to an onshore (offshore) heat transport. The projected propagation velocity perpendicular to isobath 2800 m is indicated by the green vectors. (b) The cross-shore velocity of each single eddy, with a positive (negative) value corresponding to the offshore (onshore) propagation. (c) The depth-averaged temperature anomaly for each single eddy snapshot. (d) The temperature anomaly profiles of the single eddy on 18^{th} day and 24^{th} day (green stars in panel(c)).

5.4.2 The eddy propagation and thermal characteristics

5.4.2.1 The four scenarios

Figure 5.9 depicts four 'scenarios' associated with temperature anomalies and propagation direction from DKS to CF: warm-core (cold-core) eddies leaving (entering) the boundary contributes to boundary heat loss, whereas warm-core (cold-core) eddies entering (leaving) the boundary contributes to boundary heat gain. According to Figure 5.9(a), three distinct regions can be identified from the distribution of the four 'scenarios': along the boundary of east Greenland (EG), the cooling of the boundary is primarily due to cold-core eddies

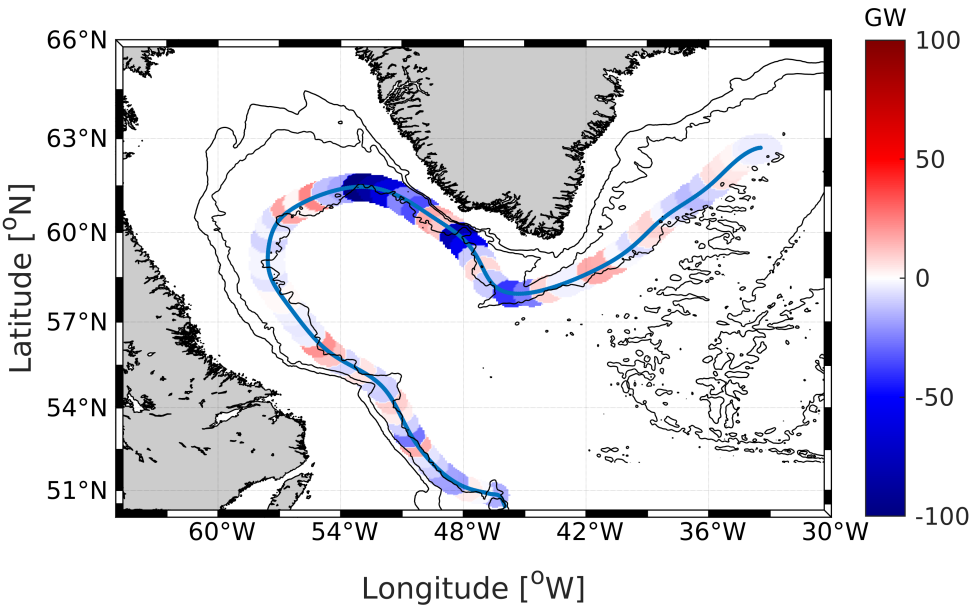

Fig. 5.8 The cross-shore eddy trapping heat transport along the isobath 2800 m. Positive (negative) value means the eddies warm (cool) the boundary region inshore of the isobath 2800 m.

advected into the boundary (orange bars); along the boundary of west Greenland (WG) until the west of DVS, warm-core/cold-core eddies leaving the boundary dominates the boundary cooling/warming (blue bars/yellow bars); the west Labrador (WL) exhibits a similar pattern as the EG. The eddy trajectories reveal that the majority of eddies propagate westward. As indicated by the first and last observed position of the eddies (Figure 5.10a), along the eastern coasts (EG and WL), most eddies form in the interior and propagate westward into the boundary. In contrast, along the western coast (WG), most eddies form in the boundary and propagate westward into the interior. The displacement of the eddies between the last-observed and first-observed locations indicates that more than 65% of the eddies (219 eddies) move westward, and that anticyclones usually propagate farther (to the southwest) than cyclones (Figure 5.10b). This is consistent with the westward eddy propagation caused by westward-propagating baroclinic Rossby waves as observed, e.g., by Chelton et al., (2007).

The 'scenarios' along WG compare favorably to previous simulations of the WG mesoscale circulation (e.g., Kawasaki and Hasumi, 2014; Georgiou et al., 2019) and provide additional evidence that eddies (typically warm-core) shed from the unstable boundary current along WG play a critical role in extracting buoyancy from the boundary and depositing it in the Labrador Sea interior. The cooling effects due to cold-core eddies entering the boundary from the interior, however, have not been reported yet.

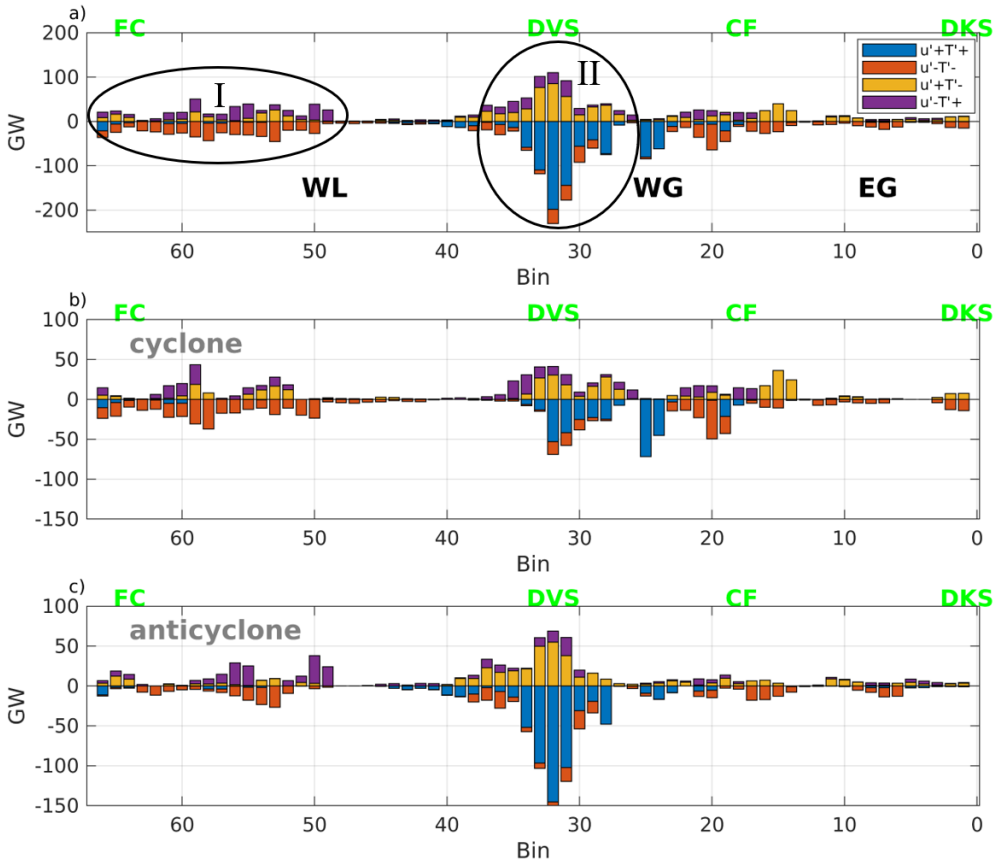

Fig. 5.9 The distribution of the cross-shore eddy trapping heat transport classified into four scenarios (a). u'+ (u'-) indicates offshore (inshore) transport, and T'+ (T'-) indicates depth-averaged positive (negative) temperature anomaly of the eddy. The cyclone and anticyclone decompositions are depicted in panels b) and c), respectively. A positive (negative) value means the eddies warm (cool) the boundary.

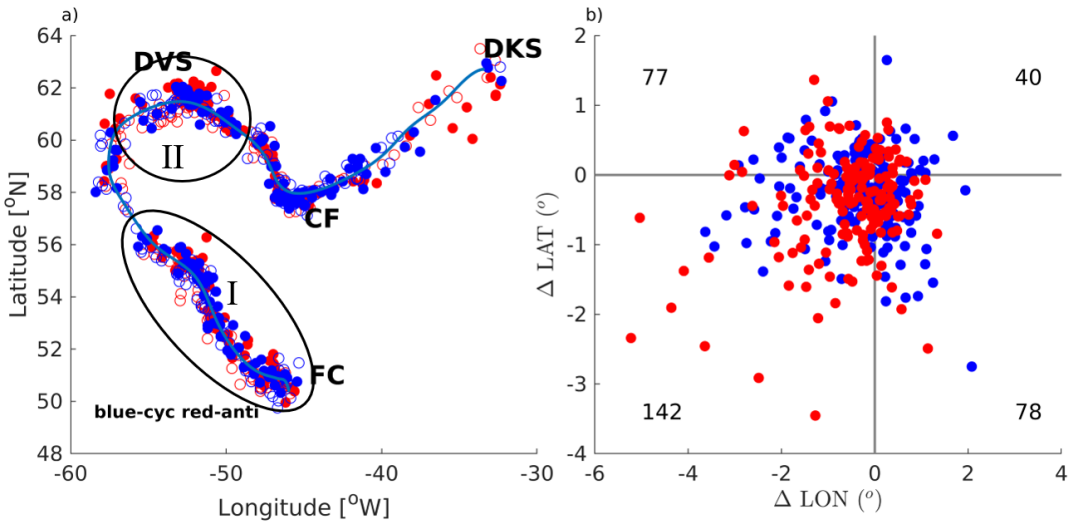

Fig. 5.10 The cross-shore eddy trapping heat transport along the isobath 2800 m. Positive (negative) value means the eddies warm (cool) the boundary region inshore of the isobath 2800 m.

The four scenarios are then shown for cyclones and anticyclones separately (Figure 5.9bc). The along-shore distribution and numbers appear similar for cyclones and anticyclones, although the southern Greenland region and the eastern DVS region (IRs formation region) have, respectively, more cyclones and anticyclones (Figure 5.9). The cyclones and anticyclones in the EG, WG, and WL regions demonstrate a consistent pattern of the four 'scenarios'. Cyclones and anticyclones with warm-core are shed from the boundary of WG, with anticyclones contributing more to boundary cooling than cyclones. Here, anticyclones most often present a longer lifetime, and they transport more heat than cyclones. Large mesoscale cyclones may be less stable than anticyclones, causing them to separate into smaller sub-mesoscale structures which cannot be detected by satellite altimetry (Stegner et al., 2021). Along the WL boundary, anticyclones and cyclones form outside the boundary and transport cold water inshore, with cyclones contributing more to heat transport. Note that the warm or cold anomalies shown by the four 'scenarios' are the vertically integrated anomalies within the eddies. Therefore, it is of interest to examine further the vertical thermal structure of the eddies in specific places with substantial cross-shore eddy heat transport.

5.4.2.2 T/S properties of eddies

Here, we select the WL region and the northern WG region (the regions enveloped by the circles shown in Figure 5.9 and Figure 5.10) to explore the hydrographic features of eddies originating from both interior and boundary regions. The typical cyclone and anticyclone temperature and salinity profiles in each region are determined by averaging the collocated Argo profiles in each section. To compare the T/S properties of eddies with those of the boundary current waters, the boundary current T/S profiles are averaged from the OI-based fields along the isobath 2800 m for each region.

The offshore heat transport in section I (WL region) is due to cold-core eddies advected from the interior (Figure 5.9). Figure 5.11(ac) displays the mean T/S profiles of the eddies, which exhibit consistent vertical structures with those of the boundary current. Both cyclones and anticyclones contain relatively light (warm and fresh) water above 100 m, whereas the cold and salty water below is relatively vertically homogenous. Figure 5.11(d) depicts a cold-core signature of the cyclones based on the mean vertical structure of temperature anomalies from the surface to 2000 m. The coldest water anomalies occur at 200 m (-0.3°C). Below 200 m, the mean temperature anomalies decrease linearly until shifting positive below about 1000 m. Note that the mean profile of the temperature anomalies is averaged from the anomalies of each single eddy (gray lines in Figure 5.11d), not the differences between the mean eddy and mean background temperature (red solid and dashed line in Figure 5.11c). Figure 5.11(b) shows that anticyclones exhibit the greatest cold anomalies at the 50 m level (-0.1°C); below this level, the cold anomalies are comparatively insignificant. The temperature anomalies of single anticyclones (Figure 5.11b) reveal a quasi-symmetry distribution of cold-core and warm-core eddies, indicating a partial compensation between their cooling effect (orange bars in Figure 5.9) and their warming effect (purple bars in Figure 5.9). Since the typical profile of the temperature anomalies indicates that the water trapped by cyclones is colder than that trapped by anticyclones, the cyclones cool the boundary region of WL significantly more than anticyclones.

In section II (northern WG region), where IRs usually originate, warm-core anticyclones and cyclones propagating offshore contribute to offshore heat transport and, consequently

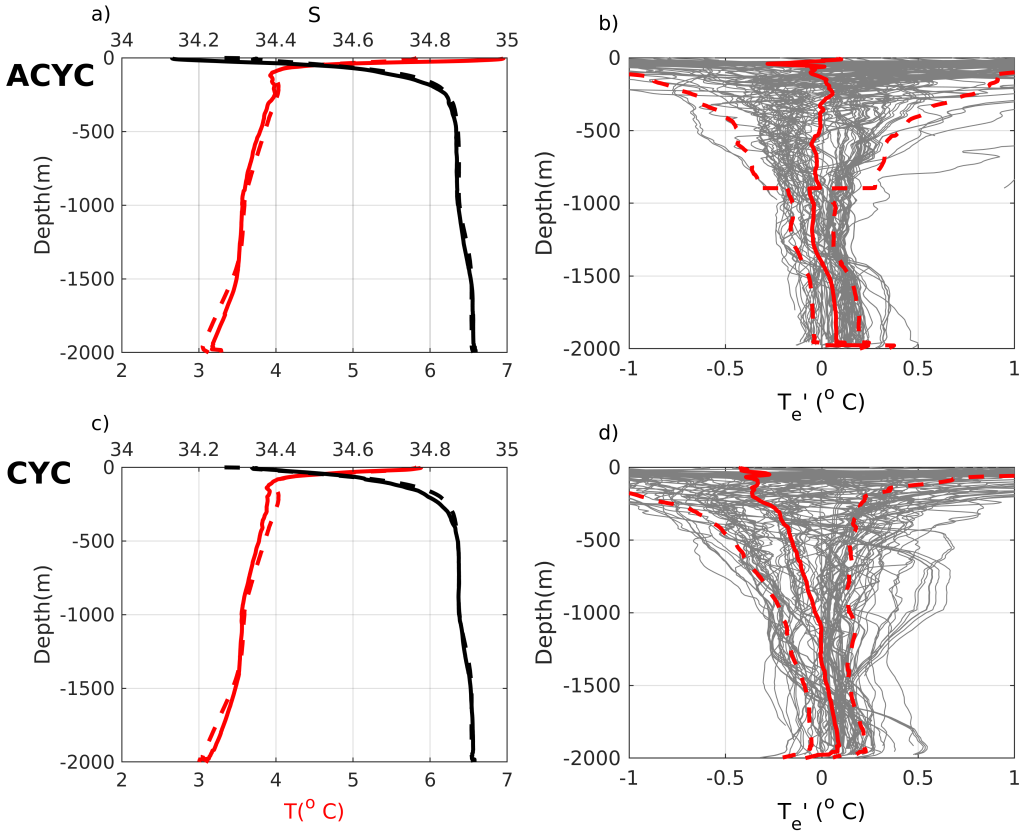

Fig. 5.11 (ac) The averaged temperature (red curve) and salinity (black curve) profiles of anticyclones (panel a) and cyclones (panel c) which have collocated Argo profiles observed in the western Labrador Sea (section I, indicated in Figure 5.9 and Figure 5.10). The averaged temperature and salinity profiles of the boundary current (dashed curves) averaged from the OI-based fields at the isobath 2800 m within each of the two sections. (bd) The temperature anomalies for anticyclones (panel b) and cyclones (panel d) observed in section I relative to a seasonal climatology, with average anomaly shown in solid red line and the associated standard deviation shown in dashed red line.

boundary cooling, with anticyclones transporting two times more heat than cyclones. The presence of some cold-core offshore eddies partially compensates for this offshore heat transport in this area (Figure 5.9). As shown by the mean temperature profiles in Figure 5.12(ac), eddy cores are generally warmer and saltier than the boundary current waters. Both of them reveal a relatively cold and fresh layer near the surface (200m), a warm and saline layer at mid-depths (200-800 m), and a cold and saline layer in the lower layer. The cold and fresh surface waters are Western Greenland Coastal Water. Below this surface

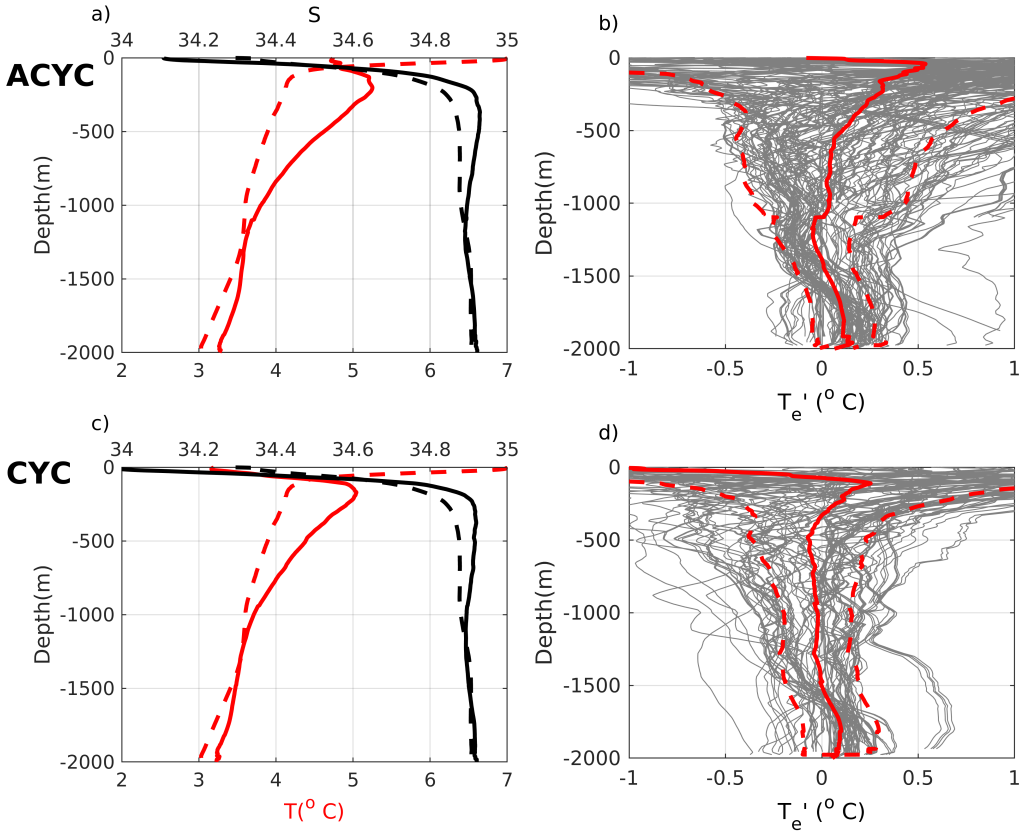

Fig. 5.12 Same as Figure 5.11, but for the eddies observed in northwestern Greenland (section II, indicated in Figure 5.9 and Figure 5.10).

layer, a distinguishing feature of the eddies and the boundary current is that the eddies have two salinity maxima: one at approximately 300 m can be recognized as Irminger Water transported by the relatively warm and salty Irminger Current, and another saline water below 1000 m is the cold and salty Iceland-Scotland Overflow Water from Nordic seas. In between these two layers, the cold and fresh Labrador Sea water can be seen. Figure 5.12(bd) shows that near the surface (above 200m), the temperature anomalies of a single eddy are considerably greater than those in the deeper layer. The mean profiles of the temperature anomalies demonstrate that both cyclones and anticyclones have warm anomalies that respectively reach an average maximum of 0.25°C (at 100 m) and 0.7°C (at 50 m). The cyclones have a cold anomaly at the surface. This indicates that Irminger warm water trapped in offshore eddies contributes to the cooling of the boundary layer.

We conclude that eddies (mainly cyclones) in the WL region contribute to boundary cooling by carrying cold interior water inshore from the interior. In contrast, eddies (both anticyclones and cyclones) in the WG region contribute to boundary cooling by transporting subsurface warm Irminger Water from the boundary into the interior. Anticyclones and cyclones generated within the boundary share similar boundary current-like characteristics but contain relatively colder or warmer waters than the 2800-m isobath background water, which induced cross-shore heat transport.

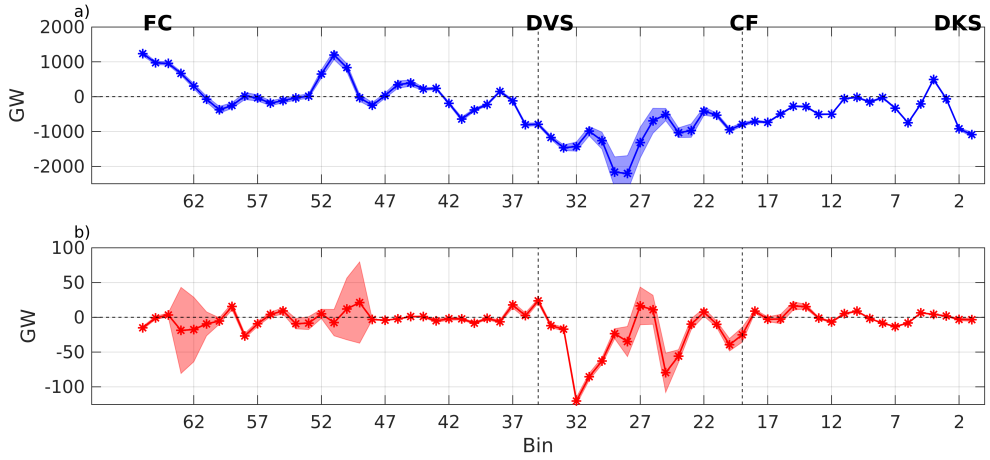

Fig. 5.13 The spatial pattern of the total cross-shore eddy heat transport (derived from Chapter 4, a) and eddy trapping heat transport (b) in each bin of the SPG boundary. A positive (negative) value means the eddies warm (cool) the boundary.

5.5 Implications for the total cross-shore eddy heat transport

Figure 5.13 depicts the spatial patterns of the total eddy heat transport (derived from Chapter 4) and of the eddy trapping heat transport (derived in the present chapter). They look relatively similar, with small offshore heat fluxes along the EG boundary and significant offshore heat fluxes along the WG boundary. Maximal total heat transport occurs at the southern WG boundary, where the continental slope steepens, while maximum trapping transport occurs downstream of this steepening in the northern WG. Locally, the trapping component can be

one to two orders of magnitude smaller than the total cross-shore eddy heat transport, with an estimated total cross-shore eddy heat transport for the whole SPG boundary (1.8×10^4 GW) that is two orders of magnitude larger than that of the trapping component (0.03×10^4 GW). The explanation is twofold. First, the total heat transport includes stirring effects notably due to coherent eddies, which should be much more effective than the trapping component due to the substantially larger eddy rotational velocity (on the order of 10-1 m s-1) than eddy propagation velocity (order of $10^{-2} \sim 10^{-3}$ m/s). Second, the float-based eddy heat transport includes the contributions of both small coherent eddies ($\sim$10 km) and noncoherent mesoscale features such as meandering, front, and filament, which contribute significantly to heat convergence in the Labrador Sea according to a simulation (de Jong et al., 2016).

Nonetheless, stirring and trapping processes are not entirely independent, as the trapping process of the cross-shore eddies is a prerequisite for the stirring process to come into play in lateral heat exchange. The continuous exchange may take place by stirring the surrounding waters the eddy propagates through. For instance, along the WG boundary, a large number of eddies that form onshore of the boundary transport warm Irminger water to the offshore region. These eddies may stir the ambient water and contribute to offshore heat transport as they reach the basin periphery (such as isobath 2800 m) and interior. If the eddies are unable to trap warm boundary current water when they propagate offshore, the water inside the eddies will be identical to the ambient interior water, and there will be no significant heat exchange by the stirring process. In addition, the combined evaluation of the two mechanisms can answer the question of which types of eddies are responsible for the boundary-interior heat exchange at various locations. For instance, the satellite-observed inshore sea surface heat fluxes at the WG boundary (Figure 4.8 of Chapter 4) can be explained by the fact that the offshore eddies trap cold shelf water at the surface layer.

5.6 Uncertainties and limitations

The present estimations of the cross-shore eddy trapping heat transports are associated with several sources of uncertainties, with an overall uncertainty estimate that accounts for 37%

(115 GW) of the total signal (314 GW). Most of these estimations are derived from the sample of single eddies detected from the satellite altimetry with collocated Argo profiles, and this uncertainty estimate is mostly determined by the scarcity of in situ observational data, i.e., the lack of sufficient spatial and temporal sampling of eddy structures by Argo floats. The choice of parameters in the heat transport calculation of Equation 5.1 may also introduce additional uncertainties associated with eddy heat transport (such as the shape coefficient, integral depth, and background temperature). However, taking these uncertainties into account will not alter the overall cooling/warming pattern due to the eddy trapping effect along the SPG boundary as a couple of tests have been conducted.

Additional limitations underlying the present calculation may result from the inability to detect some eddies at the SPG boundary. Indeed, not all eddies can be successfully tracked on satellite-derived SSH maps. First, even though we have observed numerous boundary current eddies (IRs and maybe BCEs) with radii equal to or greater than 20 km, some boundary current rings with small radii of approximately 10-20 km (Lilly and Rhines, 2002; Hátún et al., 2007; Rykova et al., 2009; de Jong et al., 2014) are still difficult to track using altimetry. In addition, two more significant causes of mesoscale eddies may not have been observed in our study. One source corresponds to convective eddies (10–15 km) that emerge rapidly in the Interior of the Labrador Sea in early spring (Jones and Marshall, 1997; Lilly et al., 2002; Rieck et al., 2019). If these eddies propagate westward, they will transport cold water from the interior of the Labrador Sea to the boundary current. Another source relates to the mid-depth-intensified overflow eddies, which generate a negligible signal on sea surface height (von Appen et al., 2014). The leakage of these eddies into the basin interior may also contribute to the boundary-interior heat exchange (de Jong et al., 2014; Zou et al., 2021; Pacini et al., 2021).

Due to the inability of satellites to detect all eddies, our study likely underestimates the local heat transport resulting from eddy trapping and, consequently, the overall cooling effect on the SPG boundary. Nevertheless, even when the heat transport of undetected eddies is considered, the overall eddy trapping heat transport at the SPG boundary is still supposed to be 10 to 100 times less than that of the total heat transport. Therefore, rather than

precisely quantifying the eddy trapping heat transport, it remains beneficial to investigate its cooling/warming pattern and the associated eddy properties (such as thermal structure and propagation direction), which can provide insight into the stirring component.

5.7 Summary and discussion

Based on satellite and Argo float measurements during the last two decades, we provide here a first regional investigation of the heat transport induced by mesoscale eddy propagation across the whole western boundary of the subpolar gyre in a semi-Lagrangian approach. From 2002 to 2019, we find 170 cyclones and 167 anticyclones with a radius greater than 20 km crossing the isobath at 2800 m. Using collocated Argo profiles within daily snapshots of detected eddies as they cross this particular isobath, we estimate an overall cross-shore heat transport for the whole SPG boundary. We further investigated the spatial patterns of eddy coverage and characteristics, as well as the distinctive roles of anticyclones and cyclones.

As anticipated from maps of eddy kinetic energy, the spatial coverage of the subpolar gyre by mesoscale eddies is very heterogeneous. Eddies (33 anticyclones and 22 cyclones) densely populate in the western Greenland area north of 58°N, where Irminger rings usually originate. In the remainder of the SPG, eddies are observed frequently around CF and the southwestern Labrador Sea. By estimating the temperature anomalies and propagation speed of eddies, we estimated the cross-shore heat transport by eddy trapping to be approximately 314±115 GW, with 166±63 GW attributable to anticyclones and 148±83 GW attributable to cyclones.

The trapping component of the eddy heat transport (on the order of 10^2 GW) has an insignificant contribution to the total eddy heat transport, which remains dominated by its stirring component of coherent eddies and noncoherent features (on the order of 10^4 GW). This is consistent with estimates of the coherent eddy stirring-trapping heat transport in the Southern Ocean, where the stirring heat transport is 1-3 orders of magnitude more than the trapping component due to the greater swirl velocity (Frenger et al., 2014). However, assessing the eddy trapping effect may help us to understand better which types of coherent

eddies contribute to the boundary-interior heat exchange in different marginal seas of SPG. In the eastern Greenland and western Labrador Sea, where the coast is on the west side, the boundary is cooled by the cold-interior water trapped by inshore eddies, a result that has not been reported yet. In contrast, in western Greenland, where the coast is on the east side, the boundary is cooled by westward-propagating eddies carrying anomalously warm waters. Contrary to the conventional views that anticyclones and cyclones exhibit opposing temperature anomalies (warm for anticyclones and cold for cyclones, Chelton et al., 2011), the anticyclones and cyclones along the SPG boundary exhibit identical temperature anomaly characteristics at sites. These eddies enhance the boundary-interior heat exchange by transporting trapped water across the boundary over certain distances, stirring it with very different ambient waters due to their rotation.

In particular, in line with previous observations or modelling analyses (Lilly et al., 2003; Hátún et al., 2007; Rykova et al., 2009; de Jong et al., 2014; Rieck et al., 2019) and the ANDRO-based observations (Chapter 4), western Greenland is the largest source of heat to the interior due to eddy cross-shore propagation, where Irminger rings form and then separate from the boundary region. As indicated by the heat transport estimates and the vertical shape of the temperature and salinity, the Irminger rings are believed to be the expression of boundary current instabilities that result in the advection of warm, salty, subtropical-origin Irminger Water into the Labrador Sea Interior from the boundary currents. It is also observed that these eddies may contribute to the offshore advection of Arctic-origin surface freshwater carried by the West Greenland Current. This result has significant implications for the role of eddies in preconditioning the Labrador Sea convection area, as they discharge anomalous heat and freshwater from the boundary to the interior.

This work provides a better understanding of the contribution of eddies to the boundary-to-interior transport of heat along the SPG margins. While there are still limitations on the availability of high-quality, well-resolved observations in space and time, this study confirms that mesoscale activities (by coherent eddies and incoherent features) are essential for boundary-interior heat exchanges. More efforts should be made to examine the relative contribution of coherent eddies and incoherent features to cross-shore heat transport, as well

as their seasonal to interannual variability. The evaluation of the involvement of mesoscale eddies in the buoyancy budget of the SPG boundary is also of interest. These will improve our understanding of boundary vertical transport and associated changes in the Atlantic meridional overturning circulation.

Chapter 6

Conclusions and perspective

Significant vertical transport occurs along the boundary of the North Atlantic subpolar gyre (SPG) to connect the upper and the lower limbs of the (depth-space) Atlantic Meridional Overturning Circulation (AMOC). Complex interactions between the atmosphere, the mean ocean circulation, and the turbulent mesoscale field drive this downwelling. Theoretical and numerical studies have thus far shed light on the spatiotemporal variability of downwelling and the physical processes underlying those interactions (e.g., Spall and Pickart, 2001; Straneo, 2006; Cenedese, 2012; Katsman et al., 2018). This dissertation aimed to pursue this effort with an observational and comprehensive approach, and quantify the long-term mean vertical boundary downwelling, investigate the associated heat budget of the boundary current system, and evaluate the specific cross-shore eddy trapping heat transport. Several global and regional ocean observational networks (including Argo, GO-SHIP, altimetry, mooring, and atmospheric reanalysis) from 2002 to 2019 were used. Here, I first outline the major findings described in this dissertation, and then I propose a set of key forward-looking and related research questions.

6.1 Conclusions

In Chapter 3, we quantified for the first time the long-term mean vertical volume transport confined to the SPG boundary from Denmark Strait (DKS) to Flemish Cap (FC) based on

observations. According to a full-depth volume budget of the SPG boundary, this vertical transport is estimated to reach -4.00±0.96 Sv across 1100 m depth. This vertical transport consists of a barotropic component (BT) of -2.00±0.61 Sv and a baroclinic component (BC) of -2.00±0.43 Sv. The BT downwelling is primarily controlled by the interaction of offshore barotropic flows with the bottom slope, whereas the BC downwelling is primarily controlled by the along-shore cooling, i.e., the inshore baroclinic transport. A distinct regional pattern of downwelling is observed, with downwelling occurring in the western Labrador Sea (WL) and western Greenland (WG) and upwelling occurring in eastern Greenland (EG). The downwelling estimates at particular locations compare favorably to previous modeling estimates. In addition, the SPG boundary contributes to the diapycnal downwelling of the AMOC, with a boundary-focused water mass transformation that reaches -2.88±0.61 Sv across the isopycnal surface of 27.74 kg/m^3.

By attempting to close the long-term mean heat budget of the full-depth SPG boundary with observations, I investigate in Chapter 4 the physical processes that control the along-boundary cooling and, consequently, the BC downwelling. It is found that lateral mean and eddy-driven advection and air-sea heat fluxes all contribute significantly to the removal of heat from the boundary current. These processes are non-uniformly distributed over the SPG boundary. Similar to the cross-shore volume transport, the spatial distribution of the cross-shore mean heat flux reveals a strong offshore heat flux at the southern tip of Greenland, whereas it is mostly oriented onshore along the remainder of the SPG boundary. The cross-shore eddy heat flux from DKS to Davis Strait (DVS) is primarily offshore and reaches its maximum in regions of strong eddy activity along the western coast of Greenland, where eddies remove heat from the coast and supply it to the interior. The air-sea heat flux cools the entire SPG boundary and reaches its maximum in the northwest Labrador Sea. Furthermore, the vertical structure of the heat budget reveals that the boundary downwelling transports heat from the upper layer (above 1300 m) to the deeper layer.

The remainder of the dissertation focused on the importance of mesoscale activities for the along-boundary cooling. In Chapter 5, I quantified and discussed the eddy-trapping component of the total cross-shore heat transport in a semi-Lagrangian framework. Consistent

with previous modeling and observational studies, a large number of eddies (primarily Irminger rings) formed in the WG region trap warm Irminger water at mid-depth and propagate southwestward into the interior of the Labrador Sea. In the WL and EG regions, eddies tend to also propagate westward (inshore), but they here advect cold interior waters into the boundary region. These eddies that trap warm (cold) waters offshore (inshore) all contribute to cooling the boundary, and the most significant heat transport occurs in northwest Greenland. The eddy trapping transport in the SPG boundary is two orders of magnitude smaller than the total eddy heat transport estimated in Chapter 4, and thus plays a minor contribution to the SPG heat budget. This indicates that the majority of the eddy heat transport is contributed by the stirring component, a local effect caused by eddy rotation, as well as incoherent turbulent activities such as waves, filaments and meanders. However, it is still of great interest to investigate the trapping effect, as the along-boundary distributions of the total eddy heat transport and eddy trapping heat transport are comparable. This implies that the eddy trapping effect and the stirring effect are not independent, with water trapped by eddies crossing the boundary laterally over great distances and mixing with those significantly different water masses in the basin inteiror.

This dissertation evaluates the vertical transport in the SPG boundary and the underlying mechanism based on observations. The findings of this dissertation highlight the role of boundary current systems in the vertical transport and heat budget of SPG, which has potential effects on the restratification in the deep convection region as well as the AMOC variability. To better simulate AMOC changes, it is imperative that models accurately represent the water mass properties and physical processes of boundary current systems.

6.2 Perspective: Interannual to decadal variability of Eulerian mean downwelling in the subpolar North Atlantic in realistic numerical model

This dissertation has highlighted the role of western boundary region in the sinking of dense waters that constitute the downwelling limb of the AMOC in a climatological framework. There remain many open questions regarding the dynamic of boundary vertical transport. Since the AMOC has experienced significant interannual/decadal variability since the 1990s, in this section, I outline a future research plan that aims to investigate how the boundary vertical transport adapts and evolves in response to such variability. Here, I propose two novel modeling outputs to answer two main questions: (1) What is the interannual/decadal variability of the boundary-confined downwelling in several semi-closed basins of the SPG? and (2) What are the principal drivers of such variability, including the local fluxes (e.g. eddy heat flux or atmospheric forcing), wind-stress curl variations, and the intensity of the gyre-circulation related to AMOC change? I seek to improve our comprehension of the dynamics governing the variability of boundary downwelling and its response to varying forcing conditions.

6.2.1 Background

The Atlantic Meridional Overturning Circulation (AMOC) is responsible for 90% of the northward oceanic heat transport at 26°N in the subtropical North Atlantic (Johns et al., 2011). Particularly, AMOC variations are linked to multidecadal fluctuations in North Atlantic sea surface temperature – usually referred to as the Atlantic Multidecadal Variability (AMV) – that are known to influence weather and climate (including air temperature, summer precipitation, drought conditions, and hurricane activity) of the Northern Hemisphere (Knight et al. 2006; Zhang and Delworth 2006; Sutton et al., 2018). Recent observations of what appears to be a decadal change in the AMOC have generated much interest. Direct observations from the RAPID mooring array at 26°N, as well as reconstruction from hydrographic and satellite

data at 45°N, indicate that the AMOC declined from the mid-1990s (and 2004 for RAPID) to 2010 before starting to recover (Smeed et al., 2018; Desbruyères et al., 2019; Moat et al., 2020, also see Figure 6.1). This decrease in the horizontal circulation in the subpolar gyre is also captured by float-derived estimates of the subsurface circulation (Palter et al., 2016) and altimetry-derived estimates of the upper subpolar gyre strength (Hakkinen and Rhines, 2004; Hakkinen and Rhines, 2009).

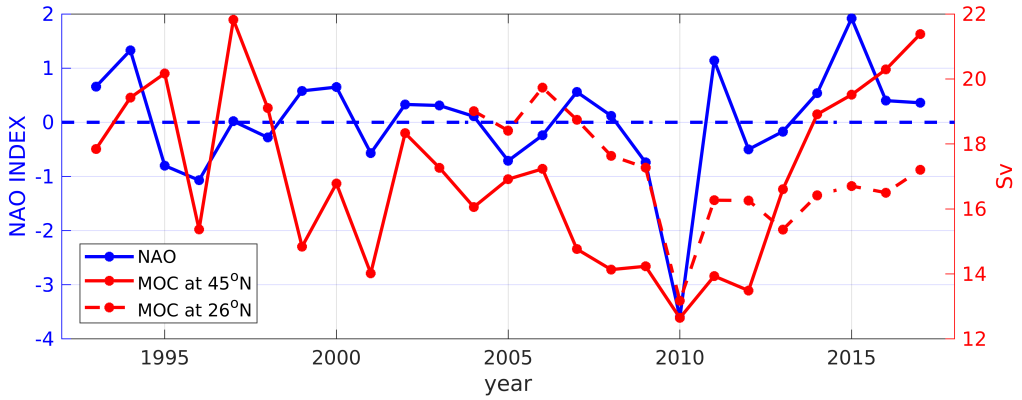

Fig. 6.1 The normalized NAO index calculated as the first principal component of sea-level pressure in the North Atlantic from 1993 to 2017 (blue curve, data source: NCAR). The annual mean meridional transport (in σ_1 space) derived from the hydrographic line at 45°N between 1993 and 2017 (red curve, data source: Desbruyères et al., 2019) and the RAPID array at 26°N between 2004 and 2017 (dashed red curve, data source: RAPID AMOC monitoring project).

A key yet vulnerable component of this global circulation is the net downwelling (in depth space) of North Atlantic surface waters within the lower limb of the AMOC. Such a net downwelling partially occurs along the perimeter of the marginal seas due to intense heat loss (Spall and Pickart, 2001; Spall, 2003; Straneo, 2006; Katsman et al., 2018; Georgie et al., 2019; Liu et al., 2022) and the interaction of boundary meandering with the bottom topography. The remaining contribution to AMOC-related sinking occurs as dense overflow plumes from the Nordic Seas (Katsman et al., 2018; Yanovsky and Legg et al., 2019). The climatological mean and seasonal variability of the boundary downwelling have been described via the analysis of realistic numerical models (Katsman et al., 2018; Sayol et al.,2019) and observations (Liu et al., 2022). However, the description of the interannual/decadal

Previous studies have recently concentrated on the diapycnal downwelling (in σ space) in the northern North Atlantic that underlies the interannual and decadal changes of the density-spaced AMOC, which has been recognized for a long time as a key determinant of the strength of the overturning circulation. This diapycnal downwelling is caused by winter buoyancy loss at various sites in the subpolar gyre (SPG) and in the Nordic Seas, producing North Atlantic Deep Water (NADW) that is transported southward by the Deep Western Boundary Current (DWBC) and interior pathways (e.g., Mauritzen, 1996; Schmitz and McCartney, 1993; Bower et al., 2009; Roberts et al., 2013; Lozier et al., 2019). The light-to-dense transformation, which forms the upper portion of NADW, is primarily driven by episodes of winter buoyancy loss and thus occurs in the winter mixed layer. The associated water mass conversion in the subpolar gyre, takes place particularly in the Irminger and Iceland basins and the Nordic Seas, rather than the Labrador Sea, where the Labrador Sea Water (LSW) forms (Zou and Lozier 2016; Desbruyères et al., 2019; Lozier et al., 2019; Chafik and Rossby, 2019). Petit et al., (2020) also found that most of the AMOC's lower branch comprises waters originating from the Nordic Seas and the Irminger and Iceland Basins.

The North Atlantic Oscillation (NAO), one of the main modes of atmospheric variability in the Northern Hemisphere, partially explains the variability in NADW production rate (Hurrell et al., 2001; Dickson et al., 2002; Lazier et al.,2002). The positive (negative) NAO phase indicates a greater (lower) heat loss from the ocean as a result of the stronger (weaker) westerly winds. Interannual and interdecadal variability in the properties of upper NADW has been linked to the NAO, with positive (negative) phases of the NAO corresponding to periods of stronger (weaker) DWBC (Curry et al., 1998; Stramma et al., 2004; Kieke and Yashayaev, 2015). For example, during repeated positive winter NAO phases from 2012 to 2016, the LSW class was one of the deepest and most persistent ever observed (Yashayaev and Loder, 2017). The substantial decrease in AMOC strength of 4.1 Sv recorded at 26°N between 2009 and 2010 (in σ_1 space) is associated with the 2010 high negative NAO index (Figure 6.1).

The change in AMOC intensity has recently resulted in decadal reversals in ocean heat content (OHC) trends in the SPG. Following a gradual cooling from 2006 to 2016 as a result of the decrease in AMOC intensity from the mid-1990s to 2010 (Robson et al., 2016), the SPG has experienced a shift from cooling to warming since 2016 as a result of an AMOC increase and an associated increase in the northward inflow of warm subtropical water toward subpolar latitudes (Desbruyères et al., 2019; Desbruyères et al., 2021). During the cooling years (2006-2016), for example, the SPG reduction in heat content is largely driven by a reduction in the transport of northward subtropical waters due to the slower ocean circulation (Dong et al., 2005; Hermanson et al., 2014; Desbruyères et al., 2015; Foukal and Lozier, 2017). Simultaneously, density anomalies in the deep Labrador Sea decreased significantly (Robson et al., 2016). Figure 6.2 summarizes the cross-correlation of deep Labrador Sea density with AMOC intensity and upper-ocean OHC using 15-year moving trends at the cooling phase (Robson et al. 2016): after five to ten years of negative NAO, a decrease in deep Labrador Sea density was concurrent with a weakening of the AMOC; this decreases meridional heat transport, and results in the cooling of the upper Labrador Sea and eastern SPG with a five- to ten-year lag. The SPG cooling could result in a negative phase of the SST and, consequently, the AWV, which could have significant climate effects (Hermanson et al., 2014).

The aforementioned chain events associated with the interannual or decadal variability of the AMOC demonstrates the complexity of the SPG dynamical system. How and where the Eulerian-mean vertical transport adapts and evolves within this dynamical system has not yet been investigated. Here, we propose examining the SPG downwelling's interannual and decadal variability in realistic numerical models. We will investigate the regional contributions to the variability of the SPG downwelling. Specifically, we seek a deeper understanding of the dynamics that govern the variability of boundary downwelling and its response to changing forcing and oceanic conditions.

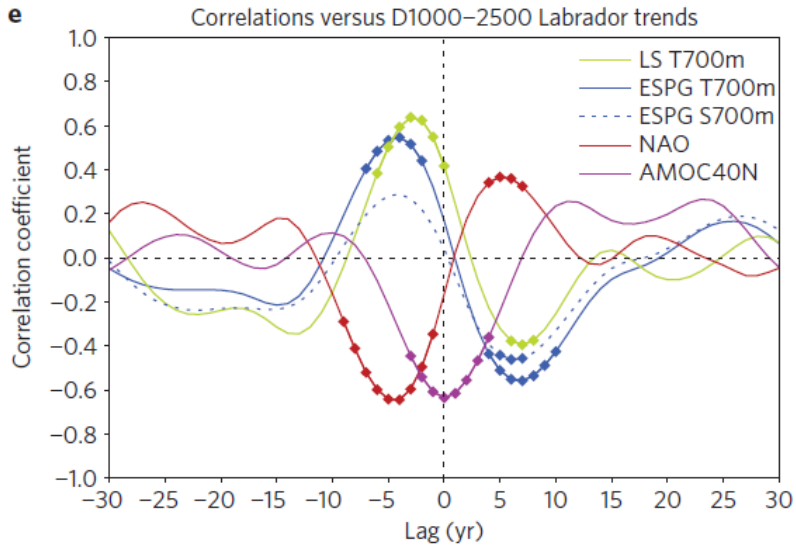

Fig. 6.2 Lead/lag relationships between 15-year rolling mean time series in deep (1000-2500 m) Labrador Sea density, and the 15-year rolling mean time series in AMOC at 40°N (with Ekman component removed, in purple), NAO index (in red), Labrador Sea 0–700m temperature (LS T700, in green), and the eastern SPG (ESPG) for 0–700m temperature (T700, in blue solid) and 0–700m salinity (S700, in blue dash). Positive lags show where the deep Labrador Sea density is leading the other variables (source: Robson et al., 2016).

6.2.2 Methodology

Here, we describe two numerical models that may effectively help us achieve our research objectives.

6.2.2.1 The ASTE model

The Arctic Subpolar gyre sTate Estimate (ASTE) project developed a data-constrained state estimate for ocean circulation and sea ice (Nguyen et al., 2021). ASTE is an adjoint-based state estimate based on the Estimating the Circulation and Climate of the Ocean (ECCO) framework in which the MITgcm serves as a dynamical interpolator. ASTE has a nominal resolution of 1/3° (22 km in the North Atlantic) and 50 unequal vertical layers. The ASTE domain encompasses the Atlantic north of 32.5°S, the Arctic and its nearby seas (Labrador, Nordic, Barents, Bering) north of 47.5°N, and the Canadian Archipelago from 2002 to 2017. The model was fitted to a vast ($O(10^9)$) collection of satellite and in situ measurements to

capture the large-scale dynamics of the Arctic ocean-sea ice system. Importantly, complete compliance with conservation rules guarantees that all inputs and outputs are accounted for, allowing for relevant budget analyses such as heat, salt, and momentum budgets. In addition, it permits linear sensitivity analyses to be conducted using ASTE to investigate the causal mechanisms driving the variability in key climate quantities (e.g., Pillar et al., 2016; Bigdeli et al., 2020; Nguyen et al., 2020). The lower resolution ECCOv4 releases have been utilized extensively in the North Atlantic, with applications such as the investigation of heat budgets in the North Atlantic (Buckley et al., 2014, 2015; Foukal and Lozier, 2018; Piecuch et al., 2017) and the Nordic Seas (Asbjrnsen et al., 2019), and the decadal to multidecadal temperature variability of SPG (Desbruyères et al., 2020). As the ASTE release is dedicated to the Arctic and North Atlantic with higher resolution than ECCOv4, it will be favorable for assessing the large-scale dynamics of the SPG.

To gain insight into the intensity of downwelling and variability on interannual to decadal scales, we provide the first overview of outputs of ASTE from 2002 to 2017. Figure 6.3 illustrates the annual mean meridional transport at 45°N computed from hydrographic data and ASTE model outputs from 2002 to 2017. The ASTE meridional transport in density space (σ_1, Figure 6.3a) correlates favorably with the observed transport on a decadal time scale. The observed AMOC decrease from 2003 to 2012 and subsequent recovery are reproduced in the model, although the latter is smaller than the observational estimate. The comparison of meridional transports in depth space is also consistent on a decadal time scale (Figure 6.3b), with a decrease from 2005 to 2014 and an increase subsequently. The ASTE vertical transport accumulated over SPG (45°N-65°N) at a depth of its maximum ($\sim$900 m) is consistent with the meridional transport as expected from the volume conservation. In addition to the applications mentioned above relying on ECCO simulations, these comparisons indicate that the ASTE simulation should be well suited for examining the variability of SPG downwelling and related heat budget on a decadal time scale.

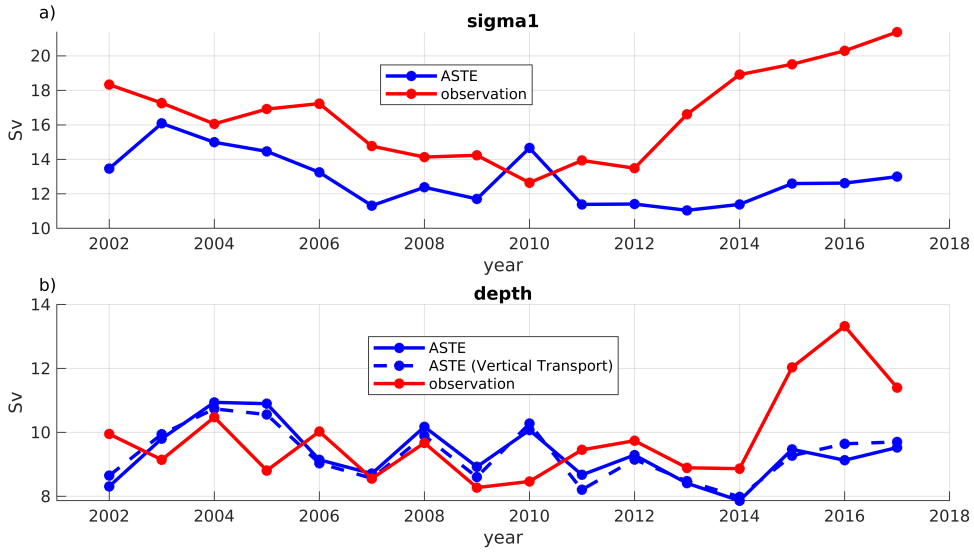

Fig. 6.3 a) The times series of meridional transport (in σ_1 space) at 45°N calculated from the ASTE model output (blue curve) and observations (red curve). b) Same for the meridional transports in depth space, as well as the modelled vertical transport accumulated over SPG (45°N to 65°N) at 900 m.

6.2.2.2 The VIKING20X model

The VIKING20X model is an eddy-resolving model configuration based on the configuration NEMO v3.6 (Madec, 2008) and the sea-ice model LIM2 (Fichefet and Maqueda, 1997; Goosse and Fichefet, 1999), which was developed by Biastoch et al. (2021). This configuration is based on a local grid refinement approach (Debreu et al., 2008), allowing the embedding of a high-resolution "nest" into a coarser (global) model domain and allowing interactions between the two models. The objective of VIKING20 is to depict the North Atlantic's oceanic conditions as realistically as possible. It comprises a global ORCA025 host grid and a nest covering the Atlantic Ocean from 33.5°S to 65°N with a nominal horizontal resolution of 0.05°, resulting in grid sizes around Greenland of approximately 3 km. In the vertical direction, the VIKING20X model utilizes 46 geopotential vertical levels with layer thicknesses ranging from 6 m at the surface to 250 m in the deepest layers. The fine mesh ensures an explicit description of mesoscale processes.

It has been demonstrated that the output of the VIKING20X-JRA model hindcast effectively represents the SPG circulation (Biastoch et al., 2021). The run is driven by JRA55-do atmospheric forcing and runoff from 1980 to the present (Tsujino et al., 2018). This eddy-rich design replicates the large-scale horizontal circulation, the overflow route, the distribution and role of mesoscale eddies, and the convection processes based on hindcasts over the previous 50 to 60 years in SPG (see more details in Biastoch et al., 2021). The interannual variability of the AMOC is highly correlated between model experiments and observations, notably the 2010 minimum at 26.5°N seen by RAPID. Therefore, the VIKING20X is deemed highly suitable for studying the mechanisms that drive the interannual to decadal variability of the SPG downwelling.

The above-mentioned model data will be used to diagnose the distribution of the Eulerian downwelling and its interannual and interdecadal variability since the 1990s, as well as the dynamical mechanisms, so as to provide a theoretical basis for the North Atlantic ocean circulation and the related model design. We intend to answer some key research questions listed below.

6.2.3 Key forward-looking research questions

- **How does the Eulerian-mean vertical transport vary on interannual/decadal timescales in the SPG?**

The model outputs allow for direct estimations of the interannual/decadal and regional changes in the vertical mass transport. Due to mass conservation, the total vertical transport in the SPG is expected to vary in phase with AMOC changes. While the majority of current studies are diagnosing the AMOC variability in the SPG in density-space to emphasize the spatial and temporal characteristics of water mass transformation (Zou and Lozier 2016; Lozier et al. 2019; Chafik and Rossby 2019; Petit et al. 2020), no study has examined the depth-space downwelling patterns and their variability on relatively "low-frequency" timescales. The spatial and temporal variability of the Eulerian-mean downwelling in several semi-closed basins of the SPG (such as the Labrador Sea and the Irminger Sea) as well as

across the Greenland-Iceland-Scotland sills will be explored. The correlation between the vertical transport along the SPG boundary and the total basin-wide meridional transport will be further described on a range of timescales.

- **What are the underlying drivers of boundary downwelling variability?**

After assessing the regional distribution of the interannual/decadal variability of the net vertical transport in the SPG, the mechanisms that drive such variability will be investigated. As discussed in this dissertation, the intensity of the boundary vertical transport is associated with both the baroclinic and barotropic flows of the boundary current. The former results from the along-shore densification of the boundary current and the development of a cross-shore geostrophic flow into the solid boundary. The physical processes responsible for this boundary heat loss include air-sea heat fluxes and mean and eddy-driven lateral heat fluxes. The latter is the result of the interaction between cross-shore barotropic flows associated with the meandering of the boundary current and the sloping bottom.

The impact of the changing SPG hydrography and dynamics on the boundary downwelling will be studied by focusing on two decadal phases characterized by large-scale OHC variations (2006-2016 cooling and 2016-2019 warming) and the transitions between those phases. During the warming phases, for instance, the warming signal starts in the eastern SPG and expands westward to the Irminger and Labrador Seas (Desbruyères et al., 2019), and the density gradient between the eastern and western SPG will hence change following this propagation. In addition, the weaker convection caused by the warming signal should reduce the lateral density gradient between the boundary and the interior, resulting in fewer baroclinic instabilities of the boundary current and, subsequently, a decrease in eddy activity and lateral eddy heat fluxes. It is therefore anticipated that the BC boundary downwelling will change due to the interplay of large-scale OHC variations and local eddy and air-sea heat flux variations. In addition, we expect that the BT boundary downwelling will vary periodically in response to changes in wind stress and associated intensity of the boundary currents. On the basis of these potential mechanisms, the BC/BT downwelling variability and their link to the concomitant changes of large-scale OHC/gyre circulation and local heat fluxes will be examined.

Appendix A

The publication in Geophysical Research Letters

A.1 Observation-based Eulerian mean downwelling in the western Subpolar North Atlantic

Geophysical Research Letters

RESEARCH LETTER
10.1029/2021GL097243

Key Points:

- The long-term mean full-depth density field of the subpolar North Atlantic's boundary is reconstructed from hydrography data
- The along-boundary densification results in a 2.12 ± 0.43 Sv Eulerian-mean downwelling between Denmark Strait and Flemish Cap
- A first observation-based regional and seasonal distribution of near-boundary Eulerian-mean downwelling is provided

Supporting Information:

Supporting Information may be found in the online version of this article.

Correspondence to:

Y. Liu,
yingjie.liu@ifremer.fr

Citation:

Liu, Y., Desbruyères, D. G., Mercier, H., & Spall, M. A. (2022). Observation-based estimates of Eulerian-mean boundary downwelling in the western subpolar North Atlantic. *Geophysical Research Letters*, *49*, e2021GL097243. https://doi.org/10.1029/2021GL097243

Received 3 DEC 2021
Accepted 4 APR 2022

Observation-Based Estimates of Eulerian-Mean Boundary Downwelling in the Western Subpolar North Atlantic

Yingjie Liu[1], Damien G. Desbruyères[1], Herlé Mercier[1], and Michael A. Spall[2]

[1]University of Brest, CNRS, Ifremer, IRD, Laboratoire d'Océanographie Physique et Spatiale, IUEM, Ifremer centre de Brest, Plouzané, France, [2]Woods Hole Oceanographic Institution, Woods Hole, MA, USA

Abstract A significant fraction of the Eulerian-mean downwelling feeding the lower limb of the Atlantic Meridional Overturning Circulation (AMOC) occurs along the subpolar North Atlantic continental slopes and is maintained by along-boundary densification and large-scale geostrophic balance. We here use Argo and shipboard hydrography data to map the 2002–2015 long-term mean density field along the boundary via a dedicated optimal interpolation tool. The overall downstream densification implies an Eulerian-mean downwelling of 2.12 ± 0.43 Sv at 1100 m depth between Denmark Strait and Flemish Cap. A clear regional pattern emerges with downwelling in the Irminger Sea and western Labrador Sea and upwelling along Greenland western continental slope. Comparisons with independent cross-basin estimates confirm that vertical overturning transport across the marginal seas of the subpolar North Atlantic mainly occurs along the continental slopes, and suggest the usefulness of hydrographic data in providing quantitative information about the sinking branch of the AMOC.

Plain Language Summary The Atlantic Meridional Overturning Circulation (AMOC), a critical component of the Earth's climate system due to its role in redistributing heat and freshwater between low and high latitudes, is anticipated to decline over the next century. The downwelling of surface waters in the subpolar North Atlantic that feeds the lower limb of AMOC is a vital yet vulnerable process. As revealed by previous theoretical and modeling work, the overall downstream densification along the boundary results in a significant boundary downwelling. Here, the density along the western boundary between Denmark Strait and Flemish Cap is reconstructed to provide a first observation-based description of the regional and seasonal distribution of this boundary-focused downwelling in the subpolar North Atlantic. This study not only provides valuable insights into how to improve existing ocean circulation theories of overturning but also contributes to a solid benchmark for evaluating how climate models simulate the sinking branch of the AMOC.

1. Introduction

Through its role in redistributing heat, freshwater, and chemical properties between low and high latitudes, the Atlantic Meridional Overturning Circulation (AMOC) is a critical component of Earth's climate system. Warm and saline waters flow from low latitudes toward the poles within the AMOC upper limb. Following significant mixing-driven and surface-forced water mass transformation, colder and fresher waters are returned southward as intermediate and deep-water masses within the AMOC lower limb. Climate model studies indicate that the AMOC could weaken significantly over the next century (IPCC, 2021), and significant efforts have been consequently made over the last decades to understand the processes maintaining the AMOC and the drivers of its variability (e.g., Buckley & Marshall, 2016; Johnson et al., 2019; Lozier, 2012).

The vertical connection between the upper and lower limb of the AMOC, as well as the underlying mechanism, are still under investigation (e.g., Brüggemann & Katsman, 2019; Pedlosky, 2003; Spall & Pickart, 2001; Spall, 2010; Straneo, 2006). The location of this downwelling has long been associated with regions of intense open-ocean convection, such as the Labrador and Irminger seas, where dense and deep waters form because of convective mixing. However, deep convection regions have large vertical heat and salt transports (in density space) but a negligible vertical mass transport (in depth space) (Marshall & Schott, 1999; Send & Marshall, 1995; Spall, 2003, 2004). Instead, the Eulerian-mean downwelling connecting the AMOC upper and lower limbs should occur near continental boundaries, where geostrophy breaks down and a new balance between vertical stretching of planetary vorticity and dissipation of relative vorticity in a thin boundary layer emerges (Spall, 2010). Previous research has established that such downwelling through modification of the boundary current properties

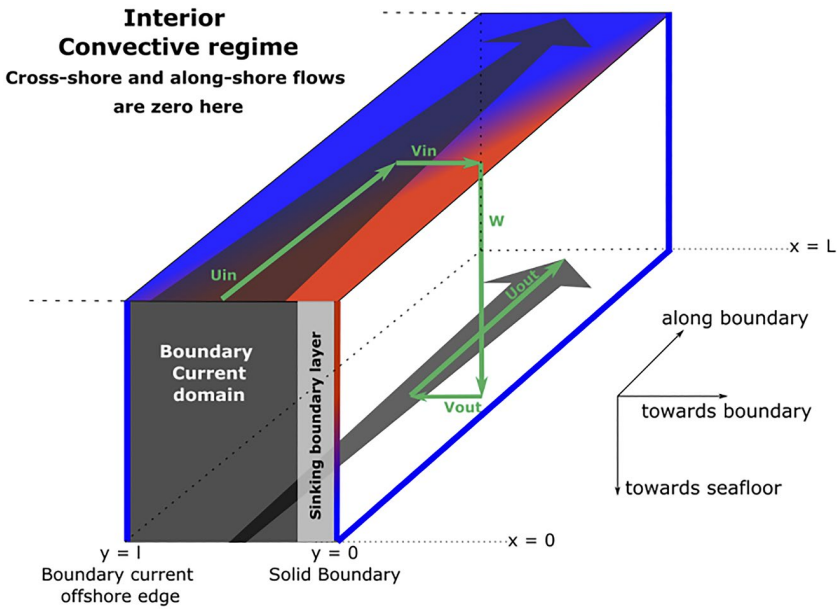

Figure 1. The cooling spiral and associated boundary downwelling. Gray arrows represent the background boundary current. The blue-red shading depicts the horizontal density fields, with the distribution of light waters in red and dense waters in blue giving rise to a cross-shore baroclinic flow in thermal wind balance (V_{in}) fed by the boundary current (U_{in}). Local mass conservation leads to a downward flow at the wall (W), a deep entrainment in the boundary current (V_{out}), and a rapid along-boundary export (U_{out}). The overall effect is a net downwelling within and a barotropization of the boundary current.

in a region is undergoing buoyancy loss (e.g., Cenedese, 2012; Katsman et al., 2018; Spall & Pickart, 2001; Spall, 2010; Straneo, 2006). Notably, the dynamics of Eulerian-mean downwelling are primarily governed by the large-scale geostrophic flow, so that the details of the thin boundary layer where vorticity is ultimately dissipated do not need to be resolved for capturing the overall impact of downwelling (Spall, 2008).

Several studies have focused on the location and underlying mechanism of boundary downwelling. Spall and Pickart (2001) investigated the boundary sinking using a thermodynamic balance. During winter, the boundary current loses heat and buoyancy. As shown schematically in Figure 1, the resulting along-boundary density increase requires a vertically sheared cross-shore baroclinic flow in thermal wind balance (V_{in}) fed by the boundary current itself (U_{in}; there is no exchange with the basin interior). Therefore, the flow rotates counterclockwise with depth along the boundary within a so-called "cooling spiral" To maintain local mass conservation, a net downwelling (W) is required to balance the mass flux toward the boundary. This causes a barotropization of the boundary current, with the upper part decelerating and the lower part accelerating (Spall, 2004, 2008; Straneo, 2006). Without any mean mass flux between the boundary region and the basin interior, the sinking water joins the lower part of the boundary current (V_{out}) and is rapidly exported within the lower limb of AMOC (U_{out}). Thus, the along-boundary pressure (or density) gradient and associated cross-shore geostrophic flow are vital for sinking to occur.

Several processes, including surface buoyancy flux or mean and eddy-driven heat advection, likely contribute to maintaining an along-boundary density gradient. While the respective contribution of these processes is regionally unknown, lateral eddy-driven heat exchanges—generated by the lateral density gradients and baroclinic instability—are widely acknowledged as important in densifying the boundary region, as seen for instance in the Labrador Sea (Katsman et al., 2004; Lilly et al., 2003). Lateral eddy-induced heat fluxes are required to balance the heat loss to the atmosphere and restratify open-ocean water columns following deep convection events (Chanut et al., 2008; Hátún et al., 2007; Katsman et al., 2004; Kawasaki & Hasumi, 2014; Tagklis et al., 2020). Additionally, eddies contribute to interior downwelling and boundary current barotropization through along-isopycnal water masses stirring and exchange between the boundary current and the interior (Brüggemann & Katsman, 2019; Khatiwala & Visbeck, 2000).

Recent studies have used realistic and high-resolution model simulations to investigate the net downwelling in the entire Subpolar Gyre (SPG) (Katsman et al., 2018; Sayol et al., 2019) or in marginal seas characterized by high convective activity, such as the Labrador Sea (Brüggemann & Katsman, 2019; Georgiou et al., 2019). Katsman et al. (2018) and Sayol et al. (2019) confirmed that the bulk of the vertical volume flux occurs along the boundary and that its spatial integral in the SPG is close to the magnitude of the AMOC—the zonally integrated meridional flow—at the southern exit of the SPG (i.e., near 45°N). Katsman et al. (2018) further demonstrated that the amount of boundary sinking is largely determined by density change, except in the region where eddy-driven processes or hydraulic controls may become significant. The role of eddy-driven processes was particularly studied by Brüggemann and Katsman (2019) and Georgiou et al. (2019), who showed the importance of eddies in balancing heat loss over the Labrador Sea and in triggering boundary downwelling along steepened isopycnal surfaces.

Estimates of boundary-focused sinking and its associated mechanisms from in situ observations are still lacking. Here, we use hydrography data from global ocean monitoring programs (e.g., Argo, go-ship) to estimate for the first time the long-term Eulerian-mean along-boundary downwelling and its spatial and seasonal distribution within the western SPG, from Denmark Strait (DKS) to Flemish Cap (FC). While such observations cannot resolve the intricate and small-scale dynamics of downwelling within the thin boundary layer where it is most likely to occur, they can be used to infer the large-scale geostrophic balance governing it.

We begin by introducing a specific optimal interpolation method to map temperature and salinity along the boundary, and then describe the method used for calculating cross-shore velocities and resulting vertical transport (Section 2). Section 3 describes the reconstruction of the along-boundary density field, as well as the subsequent calculation of geostrophic velocity and associated downwelling. A summary and a discussion conclude this study (Section 4).

2. Data and Methodology

2.1. Data

We use three datasets of temperature and salinity profiles to map the long-term mean (2002–2015) and seasonal cycle of hydrographic properties in the SPG (52–66°N; 30°W–66°W): the In Situ Analysis System-ISAS15 (Gaillard et al., 2016; Kolodziejczyk et al., 2021), the Coriolis data set for ReAnalysis-CORA (Cabanes et al., 2013; Szekely et al., 2019), and EN4.4.2.2 (Good et al., 2013). Whereas ISAS15 only contains Argo profiles, EN4 and CORA include profiles from fixed moorings and shipboard full-depth CTD profiles. These profiles have undergone quality control checks in delayed mode, and we only use *good* profiles (i.e., fully acceptable). Because most Argo floats drift at 1000 m depth, ISAS15 exhibits an uneven distribution across the domain with decreasing near the shelf (see Figure S1 in Supporting Information S1). The EN4 and CORA provide adequate coverage of profiles near the shelf. The temperature and salinity fields are then used to derive the in situ (ρ) and potential (σ_0) density fields. Bathymetry is derived from ETOPO2.

2.2. Optimal Interpolation

Optimal interpolation (OI) is a frequently used technique for generating gridded property fields from sparse and irregular data (Bretherton et al., 1976; Kaplan et al., 1997). The conventional OI algorithms for climatological mapping use circle-shaped Gaussian correlation functions (see Gaillard et al., 2016 for additional details), but we herein employ an elliptic Gaussian correlation function parallel to isobaths, with length scales of 67 km (cross-shore axis) and 145 km (along-shore axis) to account for the larger (smaller) correlation length scales in the along-shore (cross-shore) directions. In other words, this provides data along the boundary current's primary path with larger weights in the estimation. Based on convergence sensitivity tests, the horizontal resolution is set as 4 km, which enables us to refine the properties along boundaries and topographic features (such as the sharpest portions of the continental slope). Interpolation is conducted at 152 levels independently between 0 and 2000 m; the vertical spacing is 5 m down to 100 m, 10 m down to 800 m, and 20 m below. The configuration of the OI is explained in more detail in Gaillard et al. (2016). The overall mapping methodology was eventually validated by good performance in estimating properties along the OVIDE and AR7W hydrographic lines (see Figure S2–S5 in Supporting Information S1). To estimate the vertical transport, the final multiproduct mappings of temperature and salinity for the four seasons (Winter (January–March), Spring (April–June), Summer (July–September),

Autumn (October–December)) is the average of the fields derived independently from the three datasets. The density below 2000 m is obtained by linear extrapolation from the above 2000 m. The three-dimensional density field is eventually interpolated onto the locations of 100 m-spaced isobaths spanning 700 to 3000 m from DKS to FC.

2.3. Computing Cross-Shore Geostrophic Velocity and the Vertical Transport

To calculate the absolute geostrophic cross-shore velocity, a local mass balance assumes equal inshore and offshore transport. Any horizontal recirculations between the boundary current and the interior are assumed to be mostly barotropic, with no effect on the cross-shore baroclinic density field. These assumptions are supported by laboratory experiments showing that water downwelling along a vertical wall returns offshore in the opposite direction (Cenedese, 2012), and by observations of the strong barotropic nature of inner gyres and lateral entrainments (Våge et al., 2011). The baroclinic component of the cross-shore velocity relative to the sea surface ($v_{baroclinic}$) is first derived from the along-boundary density gradient and the thermal wind balance:

$$\frac{\partial v_{baroclinic}(x,y,z)}{\partial z} = -\frac{g}{\rho_0 f}\frac{\partial \rho(x,y,z)}{\partial x} \tag{1}$$

where x, y, and z represent the along-shore, cross-shore, and vertical directions, respectively. g is 9.8 m/s^2, ρ is the *in-situ* density field derived from OI, ρ_0 is 1024 kg/m^3, and f is 1.26×10^{-4} s^{-1}.

The reference velocity $v_{reference}$ is then obtained by applying the local *zero-mass transport constraint*:

$$v_{reference}(x,y) = \frac{-\int_{H(x,y)}^{0}\left(v_{baroclinic}(x,y,z)\right)dz}{\Delta z} \tag{2}$$

where H (x,y) denotes the bottom depth and Δz the water depth.

We calculate vertical transport along the SPG at isobaths ranging from 700 to 3,000 m with a 100 m interval. The analysis focuses offshore of the 700 m isobath because of poorer sampling inshore. This has little effect on the maximum transport estimate, however, which is found across much deeper slope. For a given isobath (y_0), the vertical transport stream function $\psi(z)$ is estimated as follows:

$$\psi\left(y_0,z\right) = \int_{x_u}^{x_d}\int_{z}^{0}\left(v_{baroclinic}\left(x,y_0,z'\right) + v_{reference}\left(x,y_0\right)\right)dz'dx \tag{3}$$

where x_u and x_d are the upstream and downstream locations along a given isobath y_0. The maximum of ψ (y_0, z) represents the net shoreward transport integrated along an isobath between x_u and x_d. The maximum vertical transport is thus defined as the maximum of the net shoreward transport ψ_{max} across the 100-m spaced isobaths between 700 and 3,000 m.

A Monte Carlo approach is used to add an uncertainty estimate to our mean vertical transport calculation. We use the errors estimated from the OI calculation, which depend on the distribution density and variability of adjacent profiles, to perturb the temperature and salinity fields randomly and re-compute overturning stream functions. 12,000 bootstrap estimates of the stream functions in four seasons are calculated using 3,000 iterations on the three datasets. The errors of the transport are considered as two times the standard deviation of the 12,000 estimates (see Figure S6 in Supporting Information S1).

3. Results

Figure 2 shows the multiproduct long-term mean temperature field averaged over the upper 300 m depth. It depicts the cooling of the warm boundary current in the upper layer as it flows from DKS to FC. The full-depth surface-referenced in situ (ρ) and potential (σ_0) fields are determined along 100 m-spaced isobaths ranging from 700 to 3000 m. The 2400 m isobath is shown here (for the reason that will become obvious later) and labeled using the distance relative to the isobath's total length (4,032 km), starting at s = 0 near the DKS at −30°W and ending at s = 1 near FC at −48°W.

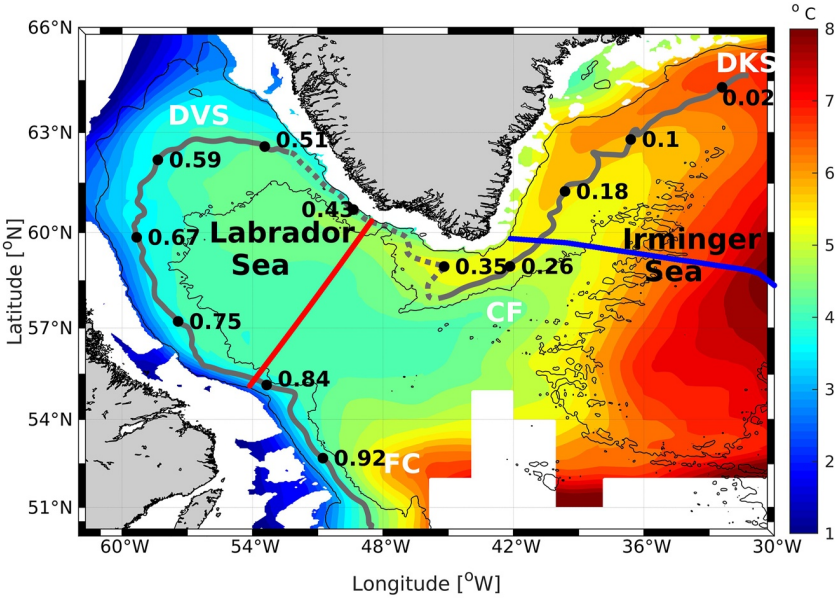

Figure 2. Observed multiproduct time-mean (2002–2015) temperature field averaged in upper 300 m as obtained from an optimal interpolation tool specifically designed for the boundary region (see Section 2.2). The isobaths 700 and 3,000 m are shown as thin black contours, and the isobath 2400 m (thick black line) is used in Figure 3 to show along-boundary density and velocity fields, from s = 0 at Denmark Strait (DKS) until s = 1 at Flemish Cap. Solid and dashed portions of this contour refer to (Eulerian) downwelling and upwelling regions. Key locations noted in the plot are DKS, Cape Farewell (CF), Davis Strait (DVS), and Flemish Cape (FC). Red line indicates the AR7W section, whereas the blue line indicates the OVIDE section.

Figures 3a and 3b depicts the density and associated cross-shore geostrophic velocity sections following isobath 2400 m from DKS to FC (the along-isobath baroclinic and reference velocities in Equation 2 are shown in Figure S8 in Supporting Information S1). The density generally increases downstream (Figures 3a and 3c) and is primarily determined by the change in along-shore temperature (see Figure S7 in Supporting Information S1). The density of the upper (above 300 m) and intermediate layer (300–1500 m) gradually increases from s = 0 to s = 0.3, while it decreases from s = 0.3 until the east of Davis Strait (DVS) (s = 0.5) (Figure 3c). Downstream of DVS, the density in the intermediate layer increases again but remains constant in the upper layer. Overall, even though the density in the upper layer remains constant, the increase in density in the intermediate layer along isobath 2400 m from 27.71 kg m^{-3} to 27.74 kg m^{-3} should expectedly drive an overall downwelling. The resulting cross-shore absolute geostrophic velocity (Figure 3b) shows the water flows inshore (offshore) and offshore (inshore) in the upper and lower layers, driving downwelling (upwelling). There are two levels of no motion at some boundary locations due to more complex changes of stratification (induced by the freshwater inflow near DVS, for instance). The level of no motion is deeper in the Irminger Sea than in the Labrador Sea and ranges from 500 to 1500 m depth.

A vertical section of the DKS-FC along-shore average of the cross-shore velocity crossing different isobaths is shown in Figure 4a. It reveals a cell-like structure in the upper and lower layers, with a cell center in the isobath 2400 m at 100 m depth. In line with theory and experimental works (Cenedese, 2012; Spall, 2008), the cross-shore velocity increases from the coast offshore to a maximum near the 2400 m isobath and then decreases offshore until the along-shore density gradient becomes insignificant at circa the 3,000 m isobath. The mean maximum vertical transport along the SPG boundary is 2.12 Sv at 1088 m, with an uncertainty of 0.43 Sv (2 times STD) estimated from 12,000 bootstrap estimates. The transport in density space is 2.11 ± 0.28 Sv by crossing the nearly horizontal 27.73 kg m^{-3} isopycnal surface. Note that this does not fully account for water mass formation near the boundary since the diapycnal flux is also carried out by the along-stream densification in the upper layer and cross-stream eddy circulation in the deeper layer (Brüggemann & Katsman, 2019).

The cumulative transport (Figure 3c) along the 2400 m isobath reveals that the entire DKS-FC boundary can be divided into three distinct areas: a downwelling region in the Irminger Sea (ID, s = 0 to s = 0.33), an upwelling

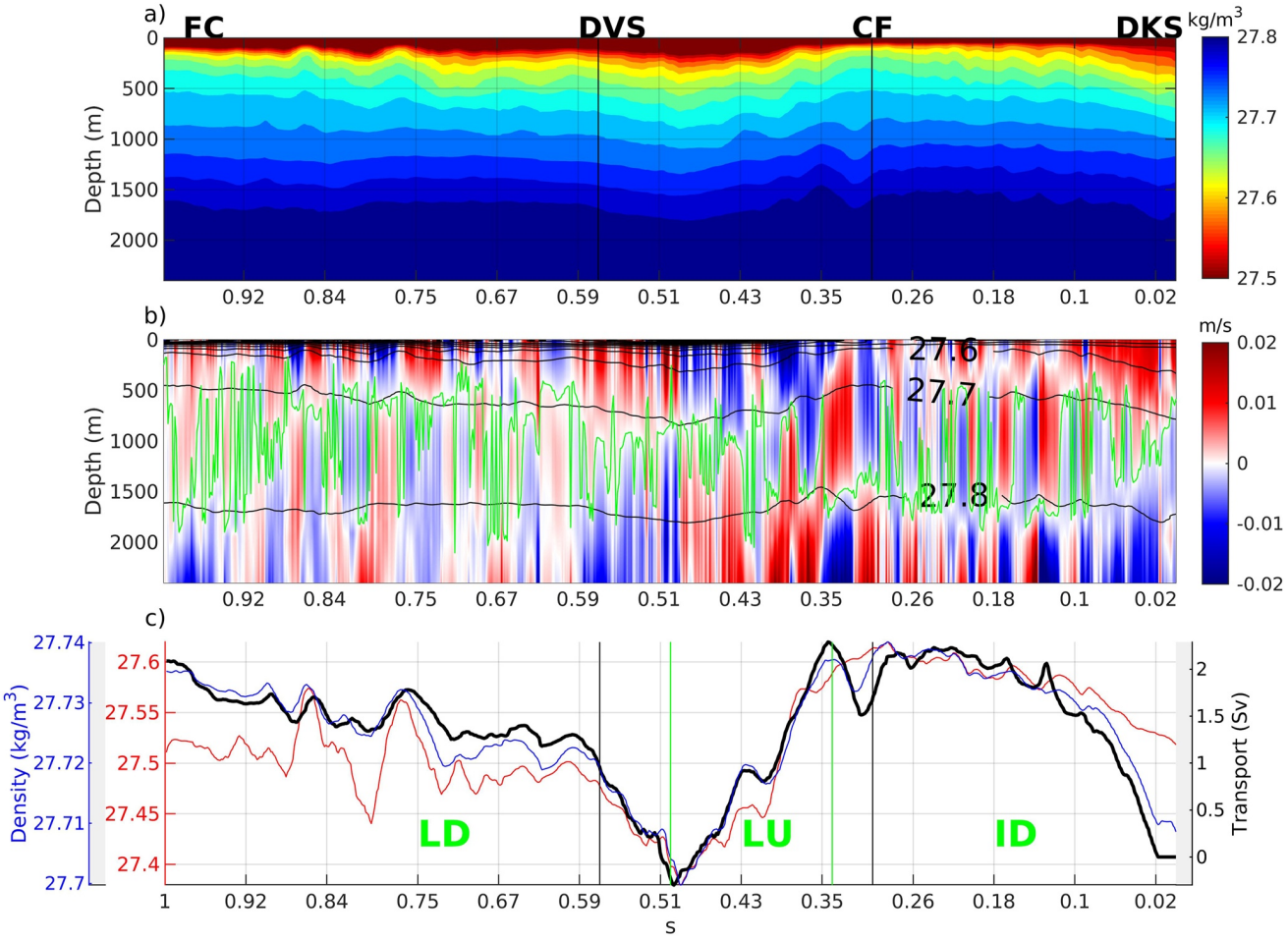

Figure 3. (a) Optimal interpolation-derived multiproduct density (σ_0) field along isobath 2400 m. (b) The cross-shore geostrophic velocity field along isobath 2400 m. The positive (negative) values indicate inshore (offshore) flows. The green line indicates the depth at which the maximum (accumulated) vertical transport is found (i.e., levels of no motion). The σ_o = 27.6, 27.7, 27.8 kg m^{-3} isopycnals are contoured in black. (c) The density along the boundary from s = 0 to s = 1 averaged in the upper layer (1–300 m, red curve) and the intermediate layer (301–1500 m, blue curve). The maximum vertical transport (black curve) accumulated along the boundary from s = 0 to s = 1. The upward slopes indicate the downwelling (LD-Labrador Downwelling, s = 0.5–1, ID-Irminger Downwelling, s = 0–0.33), and the downward slope indicates upwelling (LU-Labrador Upwelling, s = 0.33–0.5).

region in the eastern Labrador Sea (LU, s = 0.33 to s = 0.5), and a downwelling region in the western Labrador Sea (LD, s = 0.5 to s = 1). These downwelling/upwelling patterns result from the downstream density increase/decrease along the boundary (Figure 3c). The cross-shore velocities averaged along the isobaths in these three regions are shown in Figures 4d, 4g and 4j. They also capture cell-like structures within the boundary current system, with waters flowing inshore (offshore) in the upper layer and offshore (inshore) in the lower layer of the downwelling (upwelling) region. Maximum cross-shore transports, which are consistently observed at the 2400 m isobath, are of comparable magnitude in each of the three regions, with upwelling (2.17 Sv) along the western slope of Greenland balancing half of the total downwelling (4.28 Sv) (Figure 4e, 4h and 4k).

Water sinks (upwells) all year in the downwelling (upwelling) regions. The Eulerian-mean transport in the LD region is 2.23 ± 0.71 Sv (Figures 4e and Table 1) at a depth of 986 m. The transport in the LU region (Figures 4h and Table 1) is 2.17 ± 0.74 Sv at a depth of 1182 m. The ID has similar downwelling of 2.05 ± 0.79 Sv to the LD (Figures 4k and Table 1) at a depth of 1304 m. The regional density-space transport follows a very similar pattern to that in depth-space, and the density level of maximum transport remains nearly constant at around 27.71–27.76 kg/m^{-3}. The uncertainty estimates in Table 1 show the standard deviations calculated from 3,000 iterations using the three datasets. Seasonal and regional errors are all between 0.3 and 0.8 Sv. The seasonal variations are of the same magnitude as the uncertainties derived from the bootstrap estimates based on the three datasets, and

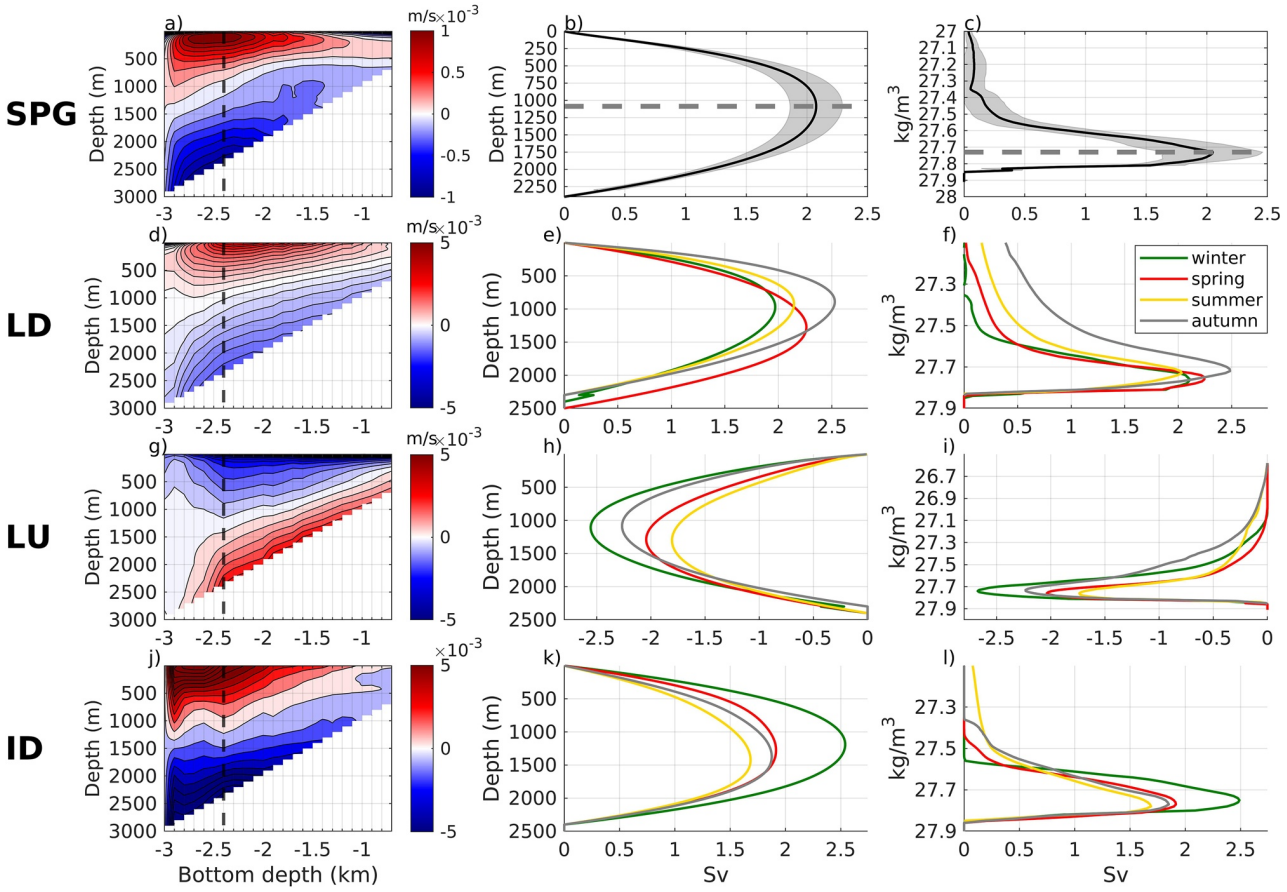

Figure 4. (a) The along-shore average of the cross-shore velocity along the Subpolar Gyre averaged at the 100 m-spaced isobaths between 700 and 3,000 m. The x-axis represents distinct isobaths rather than the cross-shore distance. The dashed line indicates the isobath (2400 m) where the maximum vertical transport is found. (b and c) The corresponding geostrophic stream functions obtained by accumulating the vertical transport from the surface in depth space and density space. The errors in gray patch are one standard deviation derived from the bootstrap simulations. The dashed lines indicate the depth (density) of maximum overturning. Panels (d–l) are the same as (a–c), but for the three regions defined in Figures 1 and 2c and for the four seasons: Winter (January–March), Spring (April–June), Summer (July–September), Autumn (October–December). The uncertainty estimates and maximum overturning depths for each region are represented in Table 1.

the present estimates of seasonal changes of the Eulerian-mean downwelling are not statistically significant for the whole SPG or individual basins. This is in line with Li et al. (2021), who did not detect a statistically significant signal cycle when estimating the composite monthly mean MOC transport using the OSNAP program's 46-month records. Furthermore, Sayol et al. (2019) used a high-resolution model to find that seasonal variability

Table 1
The Maximum Vertical Transport (Sv) Derived From the Multiproduct Mean in the Labrador Downwelling (LD), Labrador Upwelling (LU) and Irminger Downwelling (ID) Regions (Defined in Figure 2) and Whole Subpolar Gyre (SPG)

Season	LD	LU	ID	SPG
Winter	1.97 ± 0.30 (970)	−2.56 ± 0.44 (1108)	2.57 ± 0.31 (1190)	**1.99 ± 0.58** (975)
Spring	2.27 ± 0.31 (1274)	−2.04 ± 0.31 (1288)	1.92 ± 0.61 (1278)	**2.14 ± 0.81** (1253)
Summer	2.16 ± 0.28 (923)	−1.81 ± 0.34 (1301)	1.84 ± 0.84 (1425)	**2.19 ± 0.82** (903)
Autumn	2.54 ± 0.51 (891)	−2.27 ± 0.60 (1084)	1.88 ± 0.45 (1372)	**2.14 ± 0.47** (1044)
Annual	**2.23 ± 0.71 (986)**	**−2.17 ± 0.74** (1182)	**2.05 ± 0.79** (1304)	**2.12 ± 0.43** (1088)

Note. The errors are two times of standard deviation derived from the bootstrap simulations. The depths (m) of the maximum transport are displayed in parentheses.

in boundary sinking is rather insignificant in comparison to interior sinking, and that the variability is thought to be driven by ageostrophic dynamics that our large-scale geostrophic balance cannot capture. Nevertheless, based on our observations, a potential upper bound on the seasonal cycle amplitude has been established.

4. Discussion and Conclusion

We have provided here a first observation-based estimate of the Eulerian-mean downwelling along the boundary of the SPG. Using in situ temperature and salinity profiles from sustained global ocean observational networks, we mapped the long-term mean density along the continental slope from the Denmark Strait to Flemish Cap. The cooling and resulting densification along the boundary region result in a geostrophic cross-shore flow and a downwelling above the continental slope, with a maximum value of 2.12 ± 0.43 Sv at 1,100 m depth. The transport in density space, which is here representative of the cross-shore diapycnal flux, is very similar to the transport in depth space. Cross-shore velocity is found to increase offshore and peak near the 2,400 m isobath, before eventually disappearing near the 3,000 m isobath, in good agreement with observation-based descriptions of the distinct circulation of the interior and the boundary current (Pacini et al., 2020), and with theoretical or modeling works suggesting limited mean advective exchanges between those two regimes (Brüggemann & Katsman, 2019; Cenedese, 2012). Our analysis further reveals no strong or statistically significant seasonality in the magnitude of downwelling across the entire SPG.

Interestingly, the total Eulerian-mean downwelling from CF to FC is estimated as only 0.1 ± 0.03 Sv due to compensation between upwelling along the western slope of Greenland and downwelling in the remaining portion of the Labrador Sea. Downwelling was estimated to be 1.4 Sv in that region by Katsman et al. (2018) in high-resolution simulations. Western Greenland is in fact generally described as a region with strong along-shore densification due notably to eddy-driven heat flux, as described in several modeling works (Georgiou et al., 2019; Katsman et al., 2004). This apparent discrepancy could arise for several reasons. Warming in the intermediate layer might be overly represented due to an uneven distribution of profiles along western Greenland's narrowing boundary, which may be insufficient to represent the boundary current's features. It is also possible that the subsurface warming along western Greenland (also observed in other estimates, see, e.g., Palter et al., 2008) indicates a signal of restratification following baroclinic instability. The tilted isopycnals on the offshore side of an unstable current should deepen downstream and drive a warming signal in this portion of the water column. Additionally, the cross-shore transport along the narrowing boundary might represent the deflection of upper layer water into the interior. An offshore mass flux, resulting from either a flux of less dense water off the shelf or a broadening of the boundary current due to baroclinic instability, would be diagnosed as upwelling because of the assumption of no net flow across the isobaths. Future work may focus on describing the properties in shallower depths further inshore when sampling is denser. Nevertheless, the net downwelling in SPG is not sensitive to the distribution of boundary downwelling or upwelling, as demonstrated by the fact that the strong downstream warming and subsequent upwelling in the eastern Labrador Sea are compensated by the significant downstream cooling and subsequent downwelling in the western Labrador Sea. Indeed, the full-basin integrated downwelling only depends on the density variation between the DKS and FC and thus remains a robust estimate.

Further comparison with independent overturning estimates from cross-basin arrays or realistic modeling provides insights and confidence in the values reported herein. The Irminger Sea downwelling is estimated to be 2.05 ± 0.79 Sv at 1200 m depth, in line with the high-resolution modeling estimates of 1.4 Sv from Katsman et al. (2018) and 1.13 Sv from Sayol et al. (2019) within uncertainty estimates. Summer downwelling in the Labrador Sea is estimated to be 0.85 ± 0.15 Sv at depth 685 m by integrating the transport between the two ends of the AR7W line (Figure 2), which agrees quantitatively with Pickart and Spall (2007) observation-based meridional transports of about 1 Sv at depth 800 m. The annual mean downwelling rate in the Labrador Sea is estimated here as 0.72 ± 0.07 Sv, similar to Holte and Straneo's (2017) and Lozier et al. (2019) observations, which amount to 0.9 and 0.8 Sv, respectively. This also confirms that the majority of sinking occurs near the Labrador Sea's boundary, with little vertical mass transport occurring in the convective interior.

Furthermore, we quantify here only the western boundary downwelling downstream of DKS, omitting potential upstream contributions around Reykjanes Ridge (RR) or the Rockall Plateau, for instance. The zero-mass constraint used herein to estimate cross-shore overturning is likely inadequate in such regions where the vertical integral of the cross-shore geostrophic flow is not zero (consider for instance the net westward flow above the crest of RR). Addi-

tionally, overflows across the DKS or the Iceland-Scotland Ridge contribute significantly to the overall net sinking in the SPG—about 7 Sv (Hansen & Østerhus, 2000)—via hydraulically controlled dynamics not captured by our geostrophic estimate. A refinement of the boundary sinking calculation is being investigated for these specific areas.

Ekman transport was estimated from the long-term mean (2002–2015) along-shore wind stress averaged from the NCEP/NCAR Reanalysis 1 and ERA5 data set. It carries 0.7–0.9 Sv of water inshore of the DKS-FC boundary. Two-dimensional models require that this onshore flow returns to the basin interior (e.g., Choboter et al., 2011; Lentz & Chapman, 2004), but three-dimensional models with spatially variable winds (or coastlines) demonstrate that some of this water flows along the shelf (e.g., Allen, 1976; Suginohara, 1982). It is difficult to determine a priori the partition of this downwelled water between along-shelf and interior pathways as it will depend on various factors such as stratification, topography, nonlinearity, wind pattern, etc. However, any of the Ekman transport that does flow back into the interior will remain relatively shallow and have a negligible effect on the deep overturning circulation, and so is not included in our estimate.

We finally emphasize that novel descriptions of the Eulerian-mean downwelling rooted in observations are critical for understanding AMOC variability in the current context of anthropogenic climate change (IPCC, 2021). Both upper-ocean warming and increased ice melting may significantly affect along-boundary density gradients and result in the reduced sinking and a consequent weakening of the AMOC. A better observation-based understanding of boundary-focused vertical transport may also help us to properly represent or parameterize the details of the underlying boundary dynamics in climate models. It can assist in not only describing the circulation and diagnosing its controls, but also in providing valuable insights into how to improve existing ocean circulation theories of overturning.

Data Availability Statement

The In Situ Analysis System-ISAS15 data set (2002–2015) is available from the SEANOE repository (https://www.seanoe.org/data/00412/52367/, last access: July 2021) and described in Gaillard et al. (2016). The Coriolis data set for ReAnalysis-CORA V5.2 (1950-to present) is available from the SEANOE repository (https://www.seanoe.org/data/00351/46219/, last access: September 2019) and described in Szekely et al. (2019). The EN4.4.2.2 data set for years 1990 to present is provided by Met Office Hadley Centre and available at https://www.metoffice.gov.uk/hadobs/en4/ (last access: November 2021) and described in Good et al. (2013). The A25-Ovide and AR7W hydrography sections are available via the CLIVAR and Carbon Hydrographic Data Office (CCHDO) platform (https://cchdo.ucsd.edu/). The NCEP/NCAR Reanalysis 1 (1948/01/01 to present) is provided in National Centers for Environmental Prediction (/data/gridded/data.ncep.reanalysis.html) and described in Kalnay et al., (1996). The ERA5 data set (1950-to present) is available in Copernicus Climate Change Service Climate Data Store (CDS), https://cds.climate.copernicus.eu/cdsapp#!/home. The present analysis does not use new unpublished data.

Acknowledgments
We greatly appreciate the reviewers for their constructive comments. Yingjie Liu and Damien G. Desbruyères are funded by IFREMER (Institut Français de Recherche pour l'Exploitation de le Mer), Herlé Mercier is funded by CNRS (the French Centre National de la Recherche Scientifique), and Michael A. Spall is funded by NSF (National Science Foundation) Grant OCE-1947290 and NSF Grant OCE-1922538. This work was carried out within the framework of the NAOS and ARGO-2030 projects. The two projects received the support of the French government within the framework of the "Investissements d'avenir" program managed by the Agence Nationale de la Recherche (ANR) under the references ANR-10-EQPX-40 and ANR-21-ESRE-0019. The authors thank all colleagues and ship crews involved in the OVIDE cruises during which the hydrography data were obtained. The OVIDE project was supported by CNRS, Ifremer, the national program LEFE (Les Enveloppes Fluides et l'Environnement) and the Spanish Ministry of Sciences and Innovation co-funded by the Fondo Europeo de Desarrollo Regional 2007–2012 (FEDER) through the CATARINA project (CTM2010-17141).

References

Allen, J. S. (1976). Some aspects of the forced wave response of stratified coastal regions. *Journal of Physical Oceanography*, *6*, 113–119. https://doi.org/10.1175/1520-0485(1976)006<0113:saotfw>2.0.co;2

Bretherton, F. P., Davis, R. E., & Fandry, C. B. (1976). A technique for objective analysis and design of oceanographic experiments applied to MODE-73. *DeepSea Res*, *23*, 559–582. https://doi.org/10.1016/0011-7471(76)90001-2

Brüggemann, N., & Katsman, C. A. (2019). Dynamics of downwelling in an eddying marginal sea: Contrasting the eulerian and the isopycnal perspective. *Journal of Physical Oceanography*, *49*(11), 3017–3035. https://doi.org/10.1175/JPO-D-19-0090.1

Buckley, M. W., & Marshall, J. (2016). Observations, inferences, and mechanisms of Atlantic meridional overturning circulation variability: A review. *Reviews of Geophysics*, *54*, 5–63. https://doi.org/10.1002/2015RG000493

Cabanes, C., Grouazel, A., Von Schuckmann, K., Hamon, M., Turpin, V., & Coatanoan, C. (2013). The CORA dataset: Validation and diagnostics of in-situ ocean temperature and salinity measurements. *Ocean Science*, *9*(1), 1–18. https://doi.org/10.5194/os-9-1-2013

Cenedese, C. (2012). Downwelling in basins subject to buoyancy loss. *Journal of Physical Oceanography*, *42*(11), 1817–1833. https://doi.org/10.1175/JPO-D-11-0114.1

Chanut, J., Barńier, B., Large, W., Debreu, L., Penduff, T., Molines, J. M., & Mathiot, P. (2008). Mesoscale eddies in the Labrador Sea and their contribution to convection and restratification. *Journal of Physical Oceanography*, *38*(8), 1617–1643. https://doi.org/10.1175/2008JPO3485.1

Choboter, P. F., Duke, D., Horton, J. P., & Sinz, P. (2011). Exact solutions of wind-driven coastal upwelling and downwelling over sloping topography. *Journal of Physical Oceanography*, *41*(7), 1277–1296. https://doi.org/10.1175/2011JPO4527.1

Gaillard, F., Reynaud, T., Thierry, V., Kolodziejczyk, N., & Von Schuckmann, K. (2016). In situ-based reanalysis of the global ocean temperature and salinity with ISAS: Variability of the heat content and steric height. *Journal of Climate*, *29*(4), 1305–1323. https://doi.org/10.1175/JCLI-D-15-0028.1

Georgiou, S., van der Boog, C. G., Brüggemann, N., Ypma, S. L., Pietrzak, J. D., & Katsman, C. A. (2019). On the interplay between downwelling, deep convection and mesoscale eddies in the Labrador Sea. *Ocean Modelling*, *135*, 56–70. https://doi.org/10.1016/j.ocemod.2019.02.004

Good, S. A., Martin, M. J., & Rayner, N. A. (2013). EN4: Quality controlled ocean temperature and salinity profiles and monthly objective analyses with uncertainty estimates. *Journal of Geophysical Research: Oceans*. https://doi.org/10.1002/2013JC009067

Hansen, B., & Østerhus, S. (2000). North Atlantic-Nordic Seas exchanges. *Progress in Oceanography*, *45*(2), 109–208. https://doi.org/10.1016/S0079-6611(99)00052-X

Hátún, H., Eriksen, C. C., & Rhines, P. B. (2007). Buoyant eddies entering the Labrador Sea observed with gliders and altimetry. *Journal of Physical Oceanography*, *37*(12), 2838–2854. https://doi.org/10.1175/2007JPO3567.1

Holte, J., & Straneo, F. (2017). Seasonal overturning of the Labrador Sea as observed by Argo floats. *Journal of Physical Oceanography*, *47*(10), 2531–2543. https://doi.org/10.1175/JPO-D-17-0051.1

IPCC. (2021). In V. P. Zhai, A. Pirani, S. L. Connors, C. Péan, S. Berger, N. Caud, et al. (Eds.), *Climate change 2021: The physical science basis. Contribution of working group I to the sixth assessment report of the intergovernmental panel on climate change [Masson-Delmotte]*. Cambridge University Press.

Johnson, H. L., Cessi, P., Marshall, D. P., Schloesser, F., & Spall, M. A. (2019). Recent contributions of theory to our understanding of the Atlantic meridional overturning circulation. *Journal of Geophysical Research: Oceans*, *124*(8), 5376–5399. https://doi.org/10.1029/2019JC015330

Kalnay, E., Kanamitsu, M., Kistler, R., Collins, W., Deaven, D., Gandin, L., et al. (1996). The NCEP/NCAR 40-year reanalysis project. *Bulletin of the American Meteorological Society*, *77*(3), 437–471. https://doi.org/10.1175/1520-0477(1996)077<0437:tnyrp>2.0.co;2

Kaplan, A., Kushnir, Y., Cane, M., & Blumenthal, B. (1997). Reduced space optimal analysis for historical data sets: 136 years of Atlantic sea surface temperature. *Journal of Geophysical Research*, *102*, 27853–27860. https://doi.org/10.1029/97jc01734

Katsman, C. A., Drijfhout, S. S., Dijkstra, H. A., & Spall, M. A. (2018). Sinking of dense North Atlantic waters in a global ocean model: Location and controls. *Journal of Geophysical Research: Oceans*, *123*(5), 3563–3576. https://doi.org/10.1029/2017JC013329

Katsman, C. A., Spall, M. A., & Pickart, R. S. (2004). Boundary current eddies and their role in the restratification of the Labrador Sea. *Journal of Physical Oceanography*, *34*(9), 1967–1983. https://doi.org/10.1175/1520-0485(2004)034<1967:bceatr>2.0.co;2

Kawasaki, T., & Hasumi, H. (2014). Effect of freshwater from the West Greenland current on the winter deep convection in the Labrador Sea. *Ocean Modelling*, *75*, 51–64. https://doi.org/10.1016/j.ocemod.2014.01.003

Khatiwala, S., & Visbeck, M. (2000). An estimate of the eddy-induced circulation in the Labrador Sea. *Geophysical Research Letters*, *27*(15), 2277–2280. https://doi.org/10.1029/1999GL011073

Kolodziejczyk, N., Prigent-Mazella, A., & Gaillard, F. (2021). ISAS temperature and salinity gridded fields. *SEANOE*. https://doi.org/10.17882/52367

Lentz, S. J., & Chapman, D. C. (2004). The importance of nonlinear cross-shelf momentum flux during wind-driven coastal upwelling. *Journal of Physical Oceanography*, *34*(11), 2444–2457. https://doi.org/10.1175/jpo2644.1

Li, F., Lozier, M. S., Bacon, S., Bower, A. S., Cunningham, S. A., de Jong, M. F., et al. (2021). Subpolar North Atlantic western boundary density anomalies and the meridional overturning circulation. *Nature Communications*, *12*(1). https://doi.org/10.1038/s41467-021-23350-2

Lilly, J. M., Rhines, P. B., Schott, F., Lavender, K., Lazier, J., Send, U., & D'Asaro, E. (2003). Observations of the Labrador Sea eddy field. *Progress in Oceanography*, *59*(1), 75–176. https://doi.org/10.1016/j.pocean.2003.08.013

Lozier, M. S. (2012). Overturning in the North Atlantic. *Annual Review of Marine Science*, *4*, 291–315. https://doi.org/10.1146/annurev-marine-120710-100740

Lozier, M. S., Li, F., Bacon, S., Bahr, F., Bower, A. S., Cunningham, S. A., et al. (2019). A sea change in our view of overturning in the subpolar North Atlantic. *Science*, *363*, 516–521. https://doi.org/10.1126/science.aau6592

Marshall, J., & Schott, F. (1999). Open-ocean convection: Observations, theory, and models. *Reviews of Geophysics*, *37*(1), 1–64. https://doi.org/10.1029/98RG02739

Pacini, A., Pickart, R. S., Bahr, F., Torres, D. J., Ramsey, A. L., Holte, J., et al. (2020). Mean conditions and seasonality of the West Greenland boundary current system near cape farewell. *Journal of Physical Oceanography*, *50*(10), 2849–2871. https://doi.org/10.1175/JPO-D-20-0086.1

Palter, J. B., Lozier, M. S., & Lavender, K. L. (2008). How does Labrador Sea water enter the deep western boundary current? *Journal of Physical Oceanography*, *38*(5), 968–983. https://doi.org/10.1175/2007JPO3807.1

Pedlosky, J. (2003). Thermally driven circulations in small oceanic basins. *Journal of Physical Oceanography*, *33*(11), 2333–2340. https://doi.org/10.1175/1520-0485(2003)033<2333:tdciso>2.0.co;2

Pickart, R. S., & Spall, M. A. (2007). Impact of Labrador Sea convection on the North Atlantic meridional overturning circulation. *Journal of Physical Oceanography*, *37*(9), 2207–2227. https://doi.org/10.1175/JPO3178.1

Sayol, J. M., Dijkstra, H., & Katsman, C. (2019). Seasonal and regional variations of sinking in the subpolar North Atlantic from a high-resolution ocean model. *Ocean Science*, *15*(4), 1033–1053. https://doi.org/10.5194/os-15-1033-2019

Send, U., & Marshall, J. (1995). Integral effects of deep convection. *Journal of Physical Oceanography*, *25*, 855–872. https://doi.org/10.1175/1520-0485(1995)025<0855:ieodc>2.0.co;2

Spall, M. A. (2003). On the thermohaline circulation in at bottom marginal seas. *Number 1 Journal of Marine Research*, *61*. https://doi.org/10.1357/002224003321586390

Spall, M. A. (2004). Boundary currents and watermass transformation in marginal seas. *Journal of Physical Oceanography*, *34*(5), 1197–1213. https://doi.org/10.1175/1520-0485(2004)034<1197:bcawti>2.0.co;2

Spall, M. A. (2008). Buoyancy-forced downwelling in boundary currents. *Journal of Physical Oceanography*, *38*(12), 2704–2721. https://doi.org/10.1175/2008JPO3993.1

Spall, M. A. (2010). Dynamics of down welling in an eddy-resolving convective basin. *Journal of Physical Oceanography*, *40*(10), 2341–2347. https://doi.org/10.1175/2010JPO4465.1

Spall, M. A., & Pickart, R. S. (2001). Where does dense water sink? A subpolar gyre example. *Journal of Physical Oceanography*, *31*(3), 810–826. https://doi.org/10.1175/1520-0485(2001)031<0810:wddwsa>2.0.co;2

Straneo, F. (2006). On the connection between dense Water formation, overturning, and Poleward heat transport in a convective basin. *Journal of Physical Oceanography*, *36*, 1822–1840. https://doi.org/10.1175/JPO2932.1

Suginohara, N. (1982). Coastal upwelling: Onshore–offshore circulation, Equatorward coastal jet and Poleward undercurrent over a continental shelf-slope. *Journal of Physical Oceanography*, *12*, 272–284. https://doi.org/10.1175/1520-0485(1982)012<0272:cuocec>2.0.co;2

Szekely, T., Gourrion, J., Pouliquen, S., & Reverdin, G. (2019). CORA, Coriolis ocean dataset for reanalysis. *SEANOE*. https://doi.org/10.17882/46219

Tagklis, F., Bracco, A., Ito, T., & Castelao, R. M. (2020). Submesoscale modulation of deep water formation in the Labrador Sea. *Scientific Reports*, *10*(1), 1–13. https://doi.org/10.1038/s41598-020-74345-w

Våge, K., Pickart, R. S., Sarafanov, A., Knutsen, Ø., Mercier, H., Lherminier, P., et al. (2011). The Irminger Gyre: Circulation, convection, and interannual variability. *Deep-Sea Research Part I Oceanographic Research Papers*, *58*(5), 590–614. https://doi.org/10.1016/j.dsr.2011.03.001

A.2 Supporting information

Geophysical Research Letters

Supporting Information for

Observation-based estimates of Eulerian-mean boundary downwelling in the western subpolar North Atlantic

Y. J. Liu[1*], D. G. Desbruyères[1], H. Mercier[1] and M. A. Spall[2]

[1]University of Brest, CNRS, Ifremer, IRD, Laboratoire d'Océanographie Physique et Spatiale, UMR6523, IUEM, Ifremer centre de Brest, 29280 PLOUZANE, France

[2]Woods Hole Oceanographic Institution, Woods Hole, MA, USA

Contents of this file

Introduction

The supporting information provides the spatial distribution of the three datasets (ISAS, EN4 and CORA, in Text S1), an evaluation of our specifically-designed OI product (in Text S2), additional details of the transport estimations derived from the three datasets (in Text S3) and the relative importance of temperature and salinity in along-boundary density change (Text S4).

Text S1. Spatial distribution of the data

Figure S1 illustrates the number of profiles in the research domain.

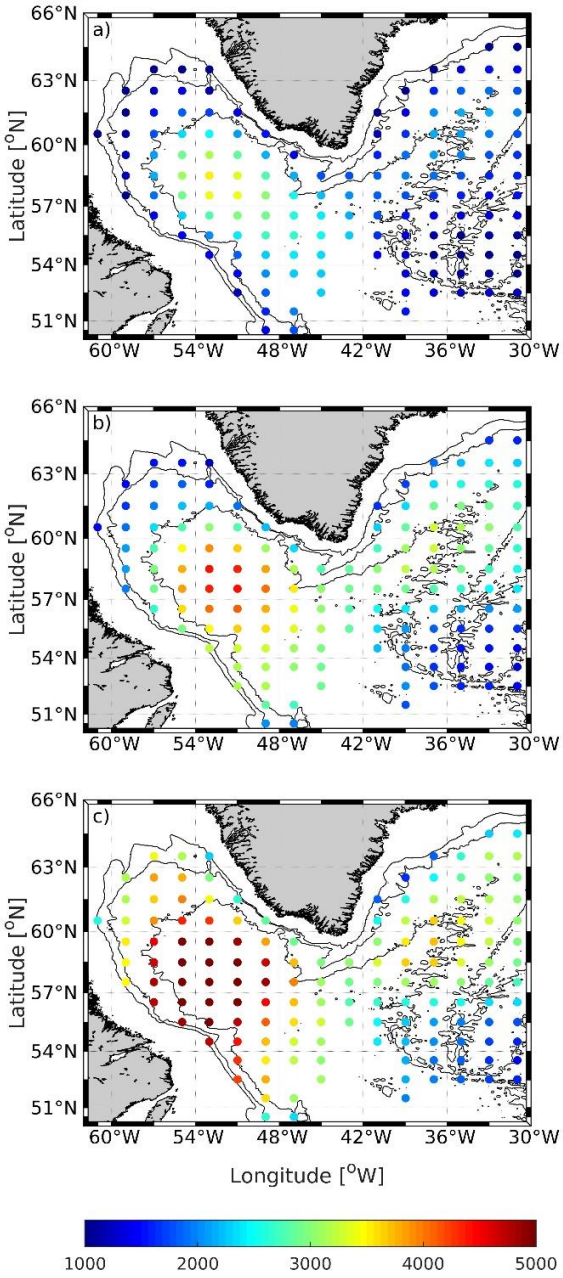

Figure S1. The number of profiles in each computational box (7.2°× 3.6°) derived from ISAS/CORA/EN4 (a/b/c) datasets between 2002 and 2015. Contours indicate isobaths 1000 m, 2000 m and 3000 m. All three datasets have an irregular and uneven distribution of profiles: the density distribution is largest in the region with a depth of more than 3000 m and decreases toward the shelf. The ISAS dataset contains 600-3000 profiles in each bin. The CORA dataset contains 1000–4000 profiles and the EN4 dataset contains 1000–6000 profiles in each bin.

Text S2. Comparison between OI and hydrographic sections

To assess the robustness of our specifically-designed OI product, we compare our estimation to two hydrographic sections, A25-OVIDE and AR7W (see Figure 2 in the paper for the position of the sections). Figures S2 and S3 show summer mean temperature and salinity fields along the OVIDE and AR7W sections. We examine the temperature and salinity profiles of stations along the slope shallower than 3000 m of the OVIDE section (Figure S4(a)(b)(c)) and the AR7W section (Figure S4(d)(e)(f)/Figure S4(g)(h)(i)), respectively. The OI error matrix (used for bootstrap) is compared to the errors between OVIDE/AR7W and OI, at the stations with water depth of 2400 m in Figure S5. Figure S6 shows the overall streamfunctions derived from the three datasets. These intercomparison and error analysis demonstrate that OI-derived fields can be used to describe ocean circulation in both boundary and open-ocean interior basins with satisfactory accuracy.

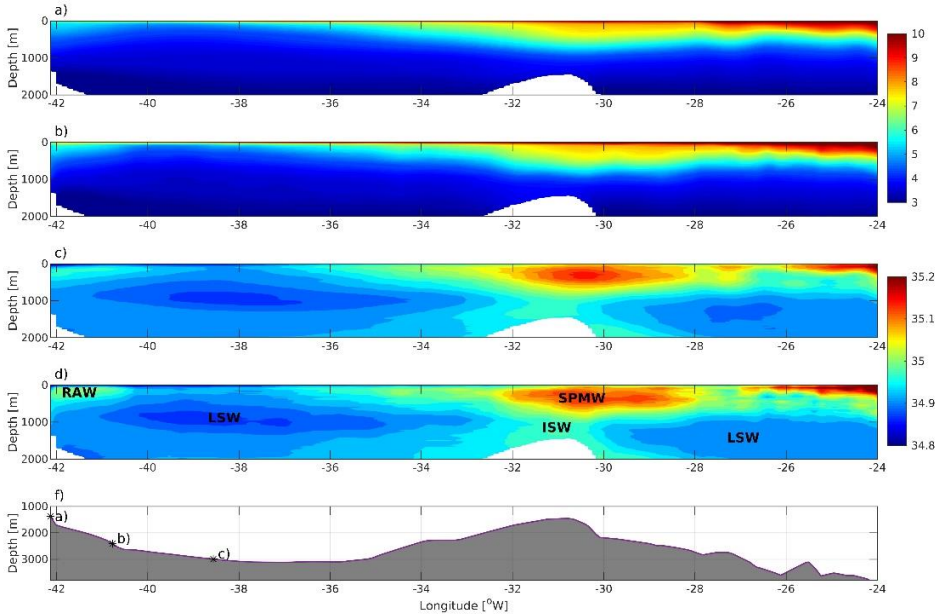

Figure S2. The summer mean potential temperature (°C) and salinity derived from the OI method based on ISAS dataset (a,c) and OVIDE hydrographic data (b,d) along the OVIDE section (see Figure 1). The corresponding bathymetry is shown in (f). The symbol stars in (f) indicate the stations of the profiles in Figure S4. The estimated properties at the OVIDE section based on OI exhibit remarkable consistency with those derived from the shipboard database, such as the slope of isopycnals and the main water masses (such as Recirculating Atlantic Water, Labrador Sea Water, Subpolar Mode Water, and Icelandic Slope Water). The smoother contours and fewer small structures suggest that the data processed by OI tends to filter out undesired high-frequency variability.

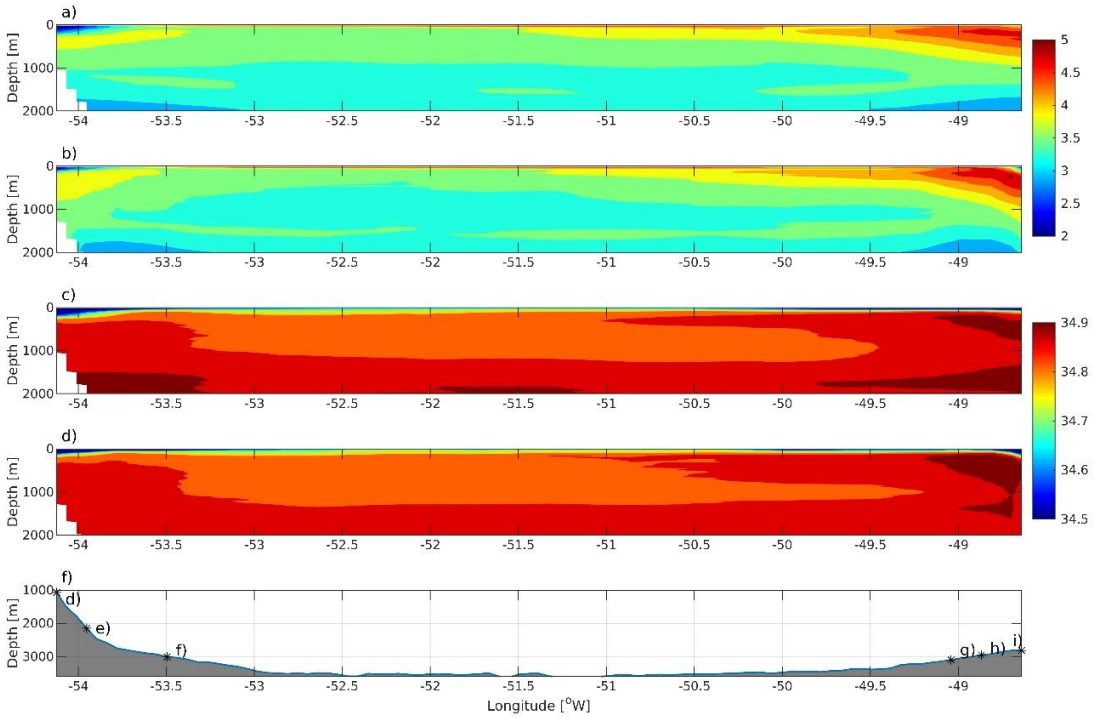

Figure S3. The summer mean potential temperature (°C) and salinity derived from the OI method based on ISAS dataset (a,c) and AR7W hydrographic data (b,d) along the AR7W section (see Figure 1.). The corresponding bathymetry is shown in (f). The symbol stars in (f) indicate the stations of the profiles in Figure S4. The temperature and salinity derived from OI are consistent with the AR7W section profiles. The Labrador Sea Water is evident in the basin's interior as a body of cold, fresh water in the water column's middle (relative to the boundaries). The warm and salty Irminger current transports Irminger water onto the basin's eastern continental slope.

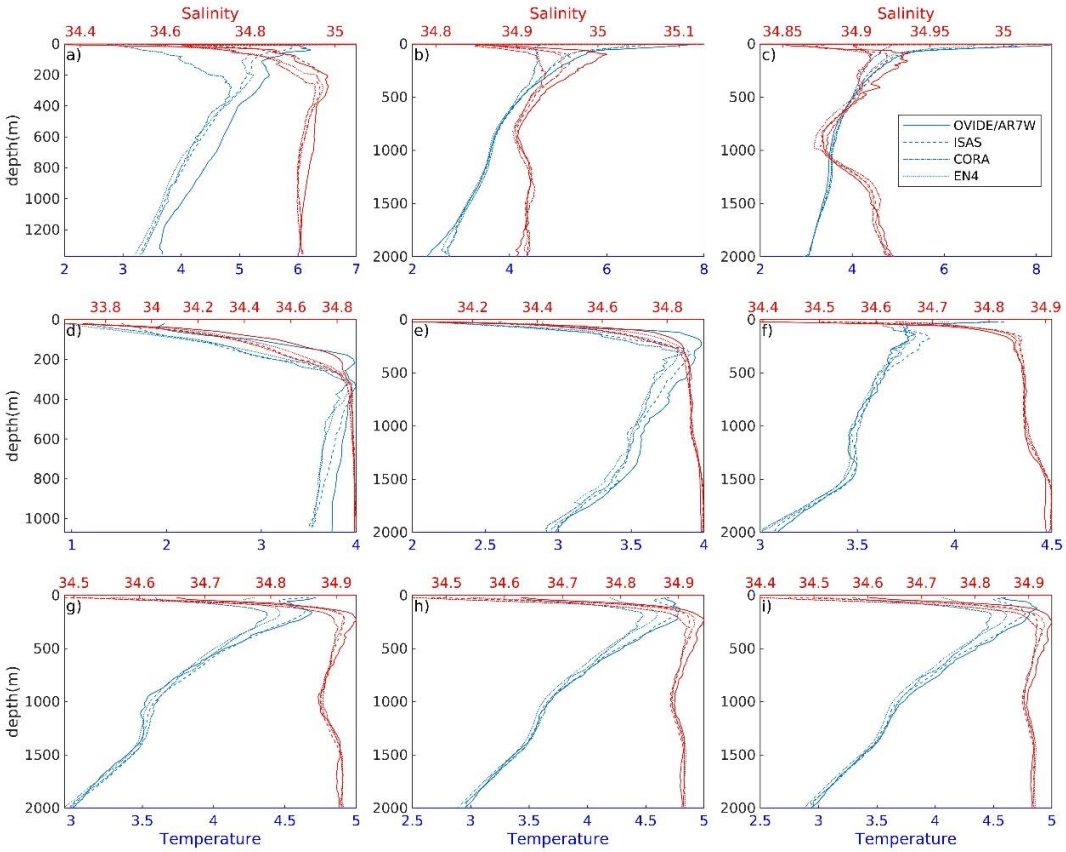

Figure S4. The temperature (blue curves, in ^{o}C) and salinity (red curves) profiles from the estimations of OI (dashed lines: dashed-ISAS, dotted dashed-CORA, dotted-EN4) and hydrographic lines OVIDE/AR7W (solid lines) at the stations shown in Figure S2 and Figure S3. The temperature and salinity estimations from the OI agree well with the hydrographic sections. Commonly, significant deviations occur near the sea surface (150 m) due to higher-frequency variations in properties such as freshwater flux and air-sea flux. Nonetheless, the significant surface errors, which account for less than 10% of the water column, will have a negligible effect on the subsequent calculation of the large-scale overturning transport.

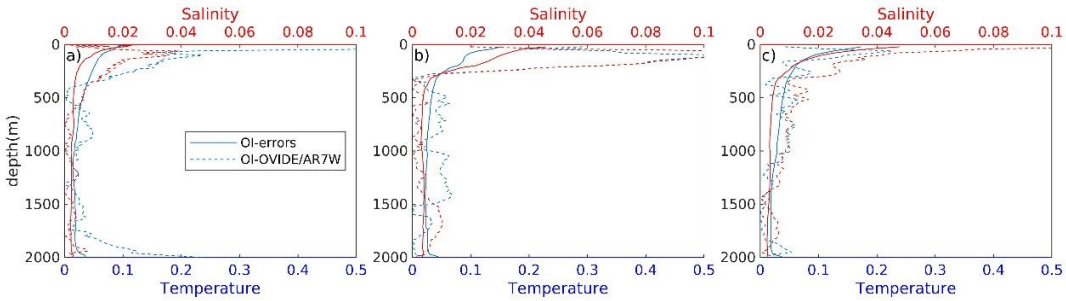

Figure S5. The multi-product mean errors of temperature (blue curves, in ^{o}C) and salinity (red curves) from the error matrix of OI used for bootstrap (OI-errors, solid lines) and the errors between OVIDE/AR7W and OI (dashed lines, OI-OVIDE/AR7W) at the stations

with water depth of 2400 m (stations b), e), i) in Figure S2 and Figure S3). The OI-OVIDE/AR7W errors are of similar magnitude than the OI-errors, which provides confidence in the bootstrap-based estimations of transport uncertainties along isobath 2400 m.

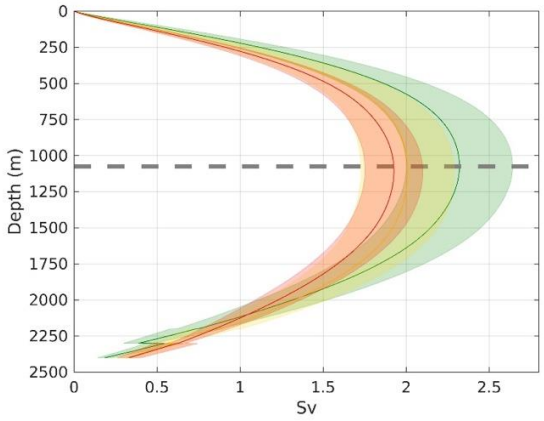

Figure S6. The geostrophic streamfunctions from each product (green-ISAS, gold-CORA, red-EN4) for the whole SPG, as obtained by accumulating the vertical transport from the surface in depth space. The errors in patches are two times of standard deviation derived (STD) from the bootstrap simulations of each product. The dashed line indicates the depth of maximum overturning.

Text S3. The vertical transport in SPG from different datasets and the multiproduct mean

The first three classified rows of Table S1 provide additional information about the Eulerian-mean vertical transport in various regions and seasons as derived from the three individual datasets. Depending on the considered datasets, transport varies slightly and exhibits distinct seasonality in each region. The most notable difference between CORA and ISAS/EN4 is the relatively substantial winter transport in the Labrador Sea in CORA (both downwelling and upwelling regions). The explanation for this substantial downwelling/upwelling is the presence of anomalously light waters (warm and salty) along Greenland's west coast (between s~0.48 and s~0.54 in Figure 2), where the CORA dataset contains more warm and salty profiles. Therefore, the winter transport derived from the CORA dataset is not considered in the transport calculation shown in Figure 4 and Table 1. Our estimations do not yield a conclusive seasonal signature (both along the whole SPG and within individual basins), as no consistent seasonal patterns are observed amongst individual product estimates.

Table S1. The maximum vertical transport (Sv) derived from each product in the three regions (defined in Figure 2) and whole SPG. The errors are two times of standard deviation derived from the bootstrap simulations.

Dataset	Season	LD	LU	ID	SPG

ISAS	Winter	2.06±0.21	-2.54±0.24	2.54±0.29	2.06±0.38
	Spring	2.38±0.28	-1.92±0.22	2.15±0.28	2.61±0.41
	Summer	2.32±0.14	-1.84±0.21	2.11±0.28	2.58±0.35
	Autumn	2.86±0.13	-2.62±0.18	2.07±0.28	2.31±0.35
	Annual	2.40±0.75	-2.23±0.88	2.22±0.48	2.39±0.32
CORA	Winter	**3.35±0.17**	**-3.33±0.20**	2.51±0.32	2.53±0.38
	Spring	2.22±0.26	-2.00±0.19	1.52±0.22	1.74±0.36
	Summer	2.10±0.15	-1.84±0.17	1.63±0.18	1.89±0.26
	Autumn	2.25±0.13	-1.94±0.16	1.83±0.26	2.15±0.33
	Annual	2.48±1.15	-2.27±1.36	1.87±0.81	2.08±0.28
EN4	Winter	1.88±0.11	-2.57±0.12	2.67±0.24	1.98±0.26
	Spring	2.21±0.20	-2.21±0.12	2.10±0.13	2.09±0.24
	Summer	2.06±0.09	-1.73±0.10	1.77±0.08	2.10±0.13
	Autumn	2.50±0.08	-2.26±0.13	1.72±0.21	1.96±0.24
	Annual	2.16±0.56	-2.19±0.69	2.07±0.93	2.03±0.18

Text S4. The relative importance of temperature and salinity in boundary downwelling

We simply decompose the density change using a linear equation of state:

$$\frac{\rho - \rho_0}{\rho_0} = -\alpha(T - T_0) + \beta(S - S_0) \qquad (S1)$$

The α and β are the thermal expansion and saline contraction coefficients, respectively, which are determined by temperature and salinity. To investigate the downstream density variation starts from DKS (s=0), ρ_0, T_0 and S_0 are assumed to be the values at s=0 of isobath 2400 m. The terms in the rhs of the equation $-\alpha(T - T_0)$, $\beta(S - S_0)$ then indicate their relative importance in determining the density change $(\rho - \rho_0)/\rho_0$ along the boundary. The three components along the SPG in the upper layer (above 300m) and in the intermediate layer (300-1500m) are presented in Figure S7.

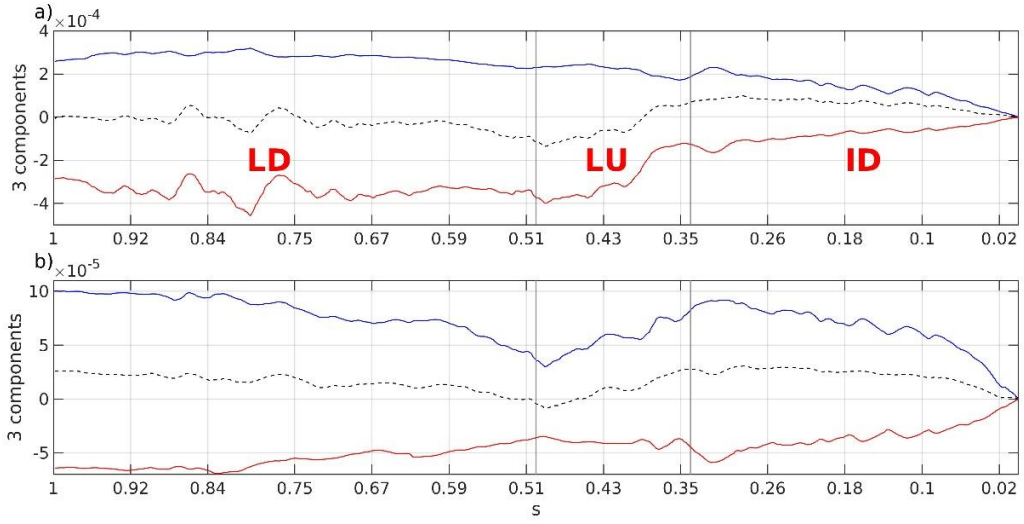

Figure S7. The three terms in equation S1, i.e., density component (dashed black curve), temperature component (solid blue curve), and salinity component (solid red curve) along the boundary from s=0 to s=1 averaged in the upper layer (1-300 m, panel a) and in the intermediate layer (301-1500 m, panel b), for the three distinct regions defined in Figure 1. Temperature and salinity play opposing roles in the along-boundary density variation. In the upper layer, the along-boundary density change is significantly contributed by temperature in the Irminger Sea (ID) and by salinity in the Labrador Sea (LD and LU); in the intermediate layer, the density change is overly determined by temperature. As the overall density change in the upper layer is negligible and the significant along-boundary density gradient occurs in the depth of around 1000 m, the Eulerian boundary transport is mostly a result of boundary cooling in the intermediate layers.

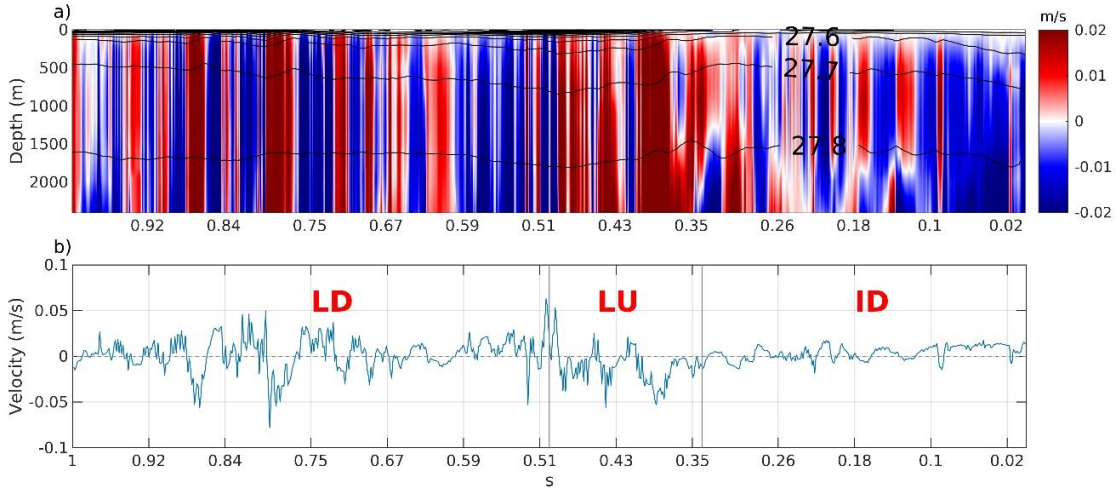

Figure S8. The baroclinic (panel(a)) and reference (panel(b)) velocities fields in equation 2 along isobath 2400 m. The positive (negative) values indicate inshore (offshore) flows.

References

Barcilon, V., and Joseph P., (1967). A unified theory of homogeneous and stratified rotating fluids. *Journal of Fluid Mechanics*, 29, 609–621.

Biastoch, A., Schwarzkopf, F.U., Getzlaff, K., Rühs, S., Martin, T., Scheinert, M., Schulzki, T., Handmann, P., Hummels, R. and Böning, C.W.(2021). Regional imprints of changes in the Atlantic meridional overturning circulation in the eddy-rich ocean model VIKING20X, *Ocean Sci. Discuss.*, 1-52, 2021.

Bigdeli, A., Nguyen, A. T., Pillar, H. R., Ocana, V., and Heimbach, P. (2020). Atmospheric warming drives growth in Arctic sea-ice: A key role for snow. *Geophysical Research Letters*, 47(20), e2020GL090236. https://doi.org/10.1029/2020GL090236 Böning, C. W., Behrens, E., Biastoch, A., Getzlaff, K., and Bamber, J. L. (2016). Emerging impact of Greenland meltwater on deepwater formation in the North Atlantic Ocean. *Nature Geoscience*, 9(7), 523–527. https://doi.org/10.1038/ngeo2740

Bower, A. S., and W.-J. von Appen (2007). Interannual variability in the Pathways of the North Atlantic Current over the Mid-Atlantic Ridge and the Impact of Topography, *Journal of Physical Oceanography*, 38, 104–120, doi:10.1175/2007JPO3686.1

Bower, A., Lozier, M., Gary, S. and Böning, C., (2009). Interior pathways of the North Atlantic meridional overturning circulation. *Nature*,Volume 459, pp. 243-247.

Brandt, P., F. A. Schott, A. Funk, and C. S. Martins, (2004). Seasonal to interannual variability of the eddy field in the Labrador Sea from satellite altimetry. *J. Geophys. Res.*, 109, C02028, https:// doi.org/10.1029/2002JC001551.

Brayshaw, D. J., Hoskins, B., and Blackburn, M. (2011). The basic ingredients of the north atlantic storm track. Part II: Sea surface temperatures. *Journal of the Atmospheric Sciences*, 68(8), 1784–1805. https://doi.org/10.1175/2011JAS3674.1

Bretherton, F. P., Davis, R. E., and Fandry, C. B. (1976). A technique for objective analysis and design of oceanographic experiments applied to MODE-73. *Deep Sea Res*, 23, 559–582. https://doi.org/10.1016/0011-7471(76)90001-2

Broecker, W. S. 1987. The Biggest Chill. Natural History, 96, 74–82.

Bruce, J. G., (1995). Eddies southwest of the Denmark Strait. *Deep Sea Res.*, 42, 13–29,

https://doi.org/10.1016/0967-0637(94)00040-Y.

Brüggemann, N., and Katsman, C. A. (2019). Dynamics of downwelling in an eddying marginal sea: Contrasting the eulerian and the isopycnal perspective. *Journal of Physical Oceanography*, 49(11), 3017–3035. https://doi.org/10.1175/JPO-D-19-0090.1

Buckley, M. W., and Marshall, J. (2016). Observations, inferences, and mechanisms of Atlantic meridional overturning circulation variability: A review. *Reviews of Geophysics*, 54, 5–63. https://doi.org/10.1002/2015RG000493

Cabanes, C., Grouazel, A., Von Schuckmann, K., Hamon, M., Turpin, V., Coatanoan, C., Paris, F., Guinehut, S., Boone, C., Ferry, N., De Boyer Montégut, C., Carval, T., Reverdin, G., Pouliquen, S., and Le Traon, P. Y. (2013). The CORA dataset: Validation and diagnostics of in-situ ocean temperature and salinity measurements. *Ocean Science*, 9(1), 1–18. https://doi.org/10.5194/os-9-1-2013

Caesar, L., Rahmstorf, S., Robinson, A., Feulner, G., and Saba, V. (2018). Observed fingerprint of a weakening Atlantic Ocean overturning circulation. *Nature*, 556(7700):191–196.

Cenedese, C. (2012). Downwelling in basins subject to buoyancy loss. *Journal of Physical Oceanography*, 42(11), 1817–1833. https://doi.org/10.1175/JPO-D-11-0114.1

Chen, X., and Tung, K. K. (2016). Correspondence: Variations in ocean heat uptake during the surface warming hiatus. *Nature Communications*, 7, 2012–2014. https://doi.org/10.1038/ncomms12541

Chelton, D. B., R. A. deSzoeke, M. G. Schlax, K. El Naggar and N. Siwertz, (1998). Geographical variability of the first-baroclinic Rossby radius of deformation. *J. Phys. Oceanogr.*, 28, 433-460.

Chelton, D. B., Schlax, M. G., Samelson, R. M., and de Szoeke, R. A. (2007). Global observations of large oceanic eddies. Geophysical Research Letters, 34(15), 1–5. https://doi.org/10.1029/2007GL030812

Chelton, D. B., M. G. Schlax, and R. M. Samelson (2011), Global observations of nonlinear mesoscale eddies, *Prog. Oceanogr.*, 91, 167–216, doi:10.1016/j.pocean.2011.01.002.

Cunningham, S. A., Kanzow, T., Rayner, D., Baringer, M. O., Johns, W. E., Marotzke, J., Longworth, H. R., Grant, E. M., Hirschi, J. J., Beal, L. M., Meinen, C. S., and Bryden, H. L. (2007). Temporal variability of the Atlantic Meridional Overturning Circulation at 26.5 *N. Science*, 317(5840):935–938.

Chafik, L., and Rossby, T. (2019). Volume, heat, and freshwater divergences in the subpolar North Atlantic suggest the Nordic Seas as key to the state of the meridional overturning circulation. *Geophysical Research Letters*, 46, 4799–4808. https://doi.org/10.1029/2019GL082110

Chanut, J., Barńier, B., Large, W., Debreu, L., Penduff, T., Molines, J. M., and Mathiot, P. (2008). Mesoscale eddies in the Labrador Sea and their contribution to convection and restrati-

fication. *Journal of Physical Oceanography*, 38(8), 1617–1643. https://doi.org/10.1175/2008JPO3485.1

Cuny J., Rhines, P., Niiler P., Bacon S. (2002). Labrador Sea boundary currents and fate of Irminger Water, *Journal of Physical Oceanography*,32, pp. 627-647.

Curry, R., McCartney, M. and Joyce, T., (1998). Oceanic transport of subpolar climate signals to mid-depth subtropical waters. *Nature*, Volume 391, pp. 575-577.

Curry, R. G., and M. S. McCartney (2001), Ocean Gyre Circulation Change Associated with the North Atlantic Oscillation, *Journal of Physical Oceanography*, 31, 3374–3400, doi: 10.1175/1520-0485(2001)031¡3374:OGCCAW¿2.0.

Daniault, N., Mercier, H., Lherminier, P., Sarafanov, A., Falina, A., Zunino, P., et al. (2016). The northern North Atlantic Ocean mean circulation in the early 21st century. *Progress in Oceanography*, 146(June), 142–158. https://doi.org/10.1016/j.pocean.2016.06.007

Debreu, L., C. Vouland, and E. Blayo, (2008). AGRIF: Adaptive grid renement in Fortran. *Computers and Geosciences*, 34 (1), 813, doi:10.1016/j.cageo.2007.01.009. 8, 12, 126

de Jong, M. F., Oltmanns, M., Karstensen, J., and de Steur, L. (2018). Deep Convection in the Irminger Sea Observed with a Dense Mooring Array. *Oceanography*, 31(1), 50–59. https://doi.org/10.5670/oceanog.2018.109

Delworth, T., Manabe, S. and Stouffer, R., (1993). Interdecadal variations of the thermohaline circulation in a coupled ocean-atmosphere model. *Journal of Climate*,, 6(11), pp. 1993-2011.

Damien Desbruyères. (2013). The meridional overturning circulation variability and heat content changes in the North Atlantic subpolar gyre. Earth Sciences. Université de Bretagne occidentale - Brest, 2013. English.NNT : 2013BRES0074. tel-01362211

Desbruyères, D. G., Maze, G., Daniault, M., and Daniault, N. (2019). Surface predictor of overturning circulation and heat content change in the subpolar North Atlantic. *Ocean Science*, 15, 809–817. https://doi.org/10.5194/os-15-809-2019

Desbruyères, D., Chafik, L., and Maze, G. (2021). A shift in the ocean circulation has warmed the subpolar North Atlantic Ocean since 2016. *Communications Earth and Environment*, 2(1). https://doi.org/10.1038/s43247-021-00120-y

Dickson R., Yashayaev I., Meincke J., Turrell B., Dye S., Holfort J. (2002). "Rapid freshening of the deep North Atlantic over the past four decades.", *Nature*, 416, pp. 832-837.

Dong, B. and Sutton, R. T. (2005). Mechanism of interdecadal thermohaline circulation variability in a coupled ocean-atmosphere GCM. *J. Clim.* 18, 1117 1135 (2005)

Dong, C., McWilliams, J. C., Liu, Y., and Chen, D. (2014). Global heat and salt transports by eddy movement. *Nature Communications*, 5, 1–6. https://doi.org/10.1038/ncomms4294

Drijfhout, S. S., Blaker, A. T., Josey, S. A., Nurser, A. J. G., Sinha, B., and Balmaseda, M. A. (2014). Surface warming hiatus caused by increased heat uptake across multiple ocean basins. *Geophysical Research Letters*, 41(22), 7868–7874. https://doi.org/10.1002/2014GL061456

Eden, C., and C. Böning, (2002). Sources of eddy kinetic energy in the Labrador Sea. *J. Phys. Oceanogr.*, 32, 3346–3363, https:// doi.org/10.1175/1520 0485(2002)032,3346:SOEKEI. 2.0.CO;2.

Eldevik, T. et al., (2009). Observed sources and variability of Nordic seas overflow. *Nature Geoscience*, Volume 2, pp. 406-410.

Enfield, D.B, Mestas Nuñez, A.M., and Trimble, P.J.(2001). The Atlantic multidecadal oscillation and its relation to rainfall and river flows in the continental US. *Geophysical Research Letters*, 28(10), 2077–2080. https://doi.org/10.1029/2000GL012745

Faghmous, J. H., Frenger, I., Yao, Y., Warmka, R., Lindell, A., and Kumar, V. (2015). A daily global mesoscale ocean eddy dataset from satellite altimetry. *Scientific Data*, 2, 1–16. https://doi.org/10.1038/sdata.2015.28

Falina, A., Sarafanov, A., Mercier, H., Lherminier, P., Sokov, A., Daniault, N., (2012). On the cascading of dense shelf waters in the Irminger Sea. Journal of Physical Oceanography 42, 2254–2267. http://dx.doi.org/10.1175/JPO-D-12012.1

Ferrari, R., Mashayek, A., McDougall, T. J., Nikurashin, M., and Campin, J. M. (2016). Turning ocean mixing upside down. *Journal of Physical Oceanography*, 46(7), 2239–2261. https://doi.org/10.1175/JPO-D-15-0244.1

Fichefet, T. and M. A. M. Maqueda, (1997). Sensitivity of a global sea ice model to the treatment of ice thermodynamics and dynamics. *Journal of Geophysical Research*, 102 (C6), 12 60912 646, doi:10.1029/97JC00480. 9, 126

Fischer, J., Karstensen, J., Oltmanns, M., and Schmidtko, S. (2018). Mean circulation and EKE distribution in the Labrador Sea Water level of the subpolar North Atlantic. *Ocean Science*, 14(5), 1167–1183. https://doi.org/10.5194/os-14-1167-2018

Flatau, M.K., Talley, L., Niiler, P.P., (2003). The North Atlantic Oscillation, surface current velocities, and SST changes in the subpolar North Atlantic. *Journal of Climate* 16, 2355–2369. http://dx.doi.org/10.1175/2787.1.

Foukal, N. P., and M. Susan Lozier (2017), Assessing variability in the size and strength of the North Atlantic subpolar gyre, *J. Geophys. Res. Oceans*,122, 6295–6308, doi:10.1002/2017JC 012798.

Frenger, I., Münnich, M., Gruber, N., and Knutti, R. (2015). Southern Ocean eddy phenomenology. *Journal of Geophysical Research: Oceans*, 120, 7413–7449. https://doi.org/10.1 002/2015JC011047

Gaillard, F., Autret, E., Thierry, V., Galaup, P., Coatanoan, C., and Loubrieu, T. (2009). Quality control of large argo datasets. *Journal of Atmospheric and Oceanic Technology*, 26(2), 337–351. https://doi.org/10.1175/2008JTECHO552.1

Gaillard, F., Reynaud, T., Thierry, V., Kolodziejczyk, N., and Von Schuckmann, K. (2016). In situ-based reanalysis of the global ocean temperature and salinity with ISAS: Variability of the heat content and steric height. *Journal of Climate*, 29(4), 1305–1323. https://doi.org/10.1175/JCLI-D-15-0028.1

Gascard, J., and R. A. Clarke, (1983). The formation of Labrador Sea Water. Part II: Mesoscale and smaller-scale processes. *J. Phys. Oceanogr.*, 13, 1779–1797.

Gelderloos, R., Katsman, C. A., and Drijfhout, S. S. (2011). Assessing the roles of three eddy types in restratifying the Labrador Sea after deep convection. *Journal of Physical Oceanography*, 41(11):2102–2119.

Good, S. A., Martin, M. J., and Rayner, N. A. (2013). EN4: Quality controlled ocean temperature and salinity profiles and monthly objective analyses with uncertainty estimates. *Journal of Geophysical Research: Oceans.* https://doi.org/10.1002/2013JC009067

Georgiou, S., van der Boog, C. G., Brüggemann, N., Ypma, S. L., Pietrzak, J. D., and Katsman, C. A. (2019). On the interplay between downwelling, deep convection and mesoscale eddies in the Labrador Sea. *Ocean Modelling*, 135, 56–70. https://doi.org/10.1016/j.ocemod.2019.02.004

Goosse, H. and T. Fichefet, (1999). Importance of ice-ocean interactions for the global ocean circulation: A model study. *Journal of Geophysical Research*, 104 (C10), 23 33723 355. 126

Gregory, J. M., et al. (2005), A model intercomparison of changes in the Atlantic thermohaline circulation in response to increasing atmospheric CO2 concentration, *Geophys. Res. Lett.*, 32, L12703, doi:10.1029/2005GL023209.

Hansen, B., and .sterhus, S. (2000). North Atlantic-Nordic Seas exchanges. *Progress in Oceanography*, 45(2), 109–208. https://doi.org/10.1016/ S0079-6611(99)00052-X

Hakkinen S, Rhines PB (2009) Shifting surface currents in the northern North Atlantic Ocean. *J Geophys Res* 114:C04005 Hakkinen S (2002) Freshening of the Labrador Sea surface waters in the 1990s: another great salinity anomaly? Geophys Res Lett 29:2232. doi:10.1029/2002GL015243

Hátún, H., Eriksen, C. C., and Rhines, P. B. (2007). Buoyant eddies entering the Labrador Sea observed with gliders and altimetry. *Journal of Physical Oceanography*, 37(12), 2838–2854. https://doi.org/10.1175/2007JPO3567.1

Hermanson, L., R. Eade, N. H. Robinson,N. J. Dunstone, M. B. Andrews, J. R. Knight,A. A. Scaife, and D. M. Smith (2014),Forecast cooling of the Atlantic subpolargyre and associated impacts, *Geophys.Res. Lett.*,41, 5167–5174, doi:10.1002/2014GL060420.

Heywood, K. J., E. L. McDonagh, and M. A. White, (1994). Eddy kinetic energy of the North Atlantic subpolar gyre from satellite altimetry. *J. Geophys. Res.*, 99, 22 525–22 539, https:// doi.org/10.1029/94JC01740.

Hill, A. E., (1996). Spin-down and the dynamics of dense pool gyres in shallow seas. *J. Mar. Res.*, 54, 471–486, https://doi.org/ 10.1357/0022240963213538.

Hodson DLR, Sutton RT. (2012). The impact of resolution on the adjustment and decadal variability of the Atlantic meridional overturning circulation in a coupled climate model. *Clim Dyn* 39:3057–3073. doi:10.1007/s00382-012-1309-0

Holliday, N. P., Bacon, S., Allen, J., and McDonagh, E. L. (2009). Circulation and transport in the western boundary currents at Cape Farewell, Greenland. *Journal of Physical Oceanography*, 39(8), 1854–1870. https://doi.org/10.1175/2009JPO4160.1

Holte, J., and Straneo, F. (2017). Seasonal overturning of the Labrador sea as observed by Argo floats. *Journal of Physical Oceanography*, 47(10), 2531–2543 https://doi.org/10.1175/JPO-D-17-0051.1

Hurrell, J. W. (1995), Decadal trends in the North Atlantic Oscillation: Regional temperatures and precipitation, *Science*, 269, 676–679, doi:10.1126/science.269.5224.676.

Hurrell, J. W., Y. Kushnir, M. Visbeck (2001). "Climate. The North Atlantic oscillation." *Science*, 26, pp. 603-605.

IPCC (2021). Climate Change 2021: The Physical Science Basis. Contribution of Working Group I to the Sixth Assessment Report of the Intergovernmental Panel on Climate Change. *Technical report*, Cambridge University Press.

Iudicone, D., Mades, G., Blanke, B., and Speich, S. (2008). The role of Southern Ocean surface forcings and mixing in the global conveyor. *Journal of Physical Oceanography*, 38(7), 1377–1400. https://doi.org/10.1175/2008JPO3519.1

Jochumsen, K., D. Quadfasel, H. Valdimarsson, and S. Jonsson (2012), variability of the Denmark Strait overflow: Moored time series from1996-2011, *J. Geophys. Res.*,117, C12003, doi:10.1029/2012JC008244.

Jones, H., and Marshall, J. (1997). Restratification after deep convection. *Journal of Physical Oceanography*, 27(10), 2276–2287. https://doi.org/10.1175/1520-0485(1997)027<2276:RADC>2.0.CO;2

Johns,W., et al. (2011), Continuous array-based estimates of Atlantic ocean heat transport at 26.5°N, *J. Clim.*, 24, 2429–2448.

Johnson, H. L., Cessi, P., Marshall, D. P., Schloesser, F., and Spall, M. A. (2019). Recent contributions of theory to our understanding of the Atlantic meridional overturning circulation. *Journal of Geophysical Research: Oceans*, 124(8), 5376–5399. https://doi.org/10.1029/2019J

Kanzow, T., and Zenk, W. (2014). Structure and transport of the Iceland Scotland Overflow plume along the Reykjanes Ridge in the Iceland Basin. *Deep-Sea Research Part I: Oceanographic Research Papers*, 86, 82–93. https://doi.org/10.1016/j.dsr.2013.11.003

Katsman, Caroline A, Spall, M. A., and Pickart, R. S.(2004). Boundary Current Eddies and Their Role in the Restratification of the Labrador Sea. *Journal of Physical Oceanography*, 34, 1967-1983, https://doi.org/10.1175/1520-0485(2004)034<1967:BCEATR>2.0.CO;2

Katsman, C. A., Drijfhout, S. S., Dijkstra, H. A., and Spall, M. A. (2018). Sinking of dense north atlantic waters in a global ocean model: Location and controls. *Journal of Geophysical Research: Oceans*, 123(5), 3563–3576. https://doi.org/10.1029/2017JC013329

Khatiwala, S., and Visbeck, M. (2000). An estimate of the eddy-induced circulation in the Labrador Sea. *Geophysical Research Letters*, 27(15), 2277–2280. https://doi.org/10.1029/1999GL011073

Kieke, D., M. Rhein, L. Stramma, W. M. Smethie, D. A. LeBel, and W. Zenk (2006), Changes in the CFC Inventories and Formation Rates of Upper Labrador Sea Water, 1977-2001, *Journal of Physical Oceanography*, 36, 64–86, doi:10.1175/JPO2814.1. Kieke, D., M. Rhein, L. Stramma, W. M. Smethie, J. L. Bullister, and D. A. LeBel (2007), Changes in the pool of Labrador Sea Water in the subpolar North Atlantic, *Geophysical Research Letters*, 34 (L06605), doi:10.1029/2006GL028959.

Knight, J. R., C. K. Folland, and A. A. Scaife (2006), Climate impacts of the Atlantic Multidecadal Oscillation, *Geophys. Res. Lett.*, 33, L17706, doi:10.1029/2006GL026242.

Kolodziejczyk, N., Prigent-Mazella, A., and Gaillard, F. (2021). ISAS temperature and salinity gridded fields. SEANOE. https://doi. org/10.17882/52367

Krauss, W., and R. H. Käse, (1998). Eddy formation in the Denmark Strait overflow. *J. Geophys. Res. Oceans*, 103, 15 525–15 538, https:// doi.org/10.1029/98JC00785.

Le Bras, I. A.-A., F. Straneo, J. Holte, M. F. de Jong, and N. P. Holliday, 2020: Rapid export of waters formed by convection near the Irminger Sea's western boundary. *Geophys. Res. Lett.*, 47, e2019GL085989, https://doi.org/10.1029/ 2019GL085989.

Lehahn, Y., D'Ovidio, F., Lévy, M., Amitai, Y., and Heifetz, E. (2011). Long range transport of a quasi isolated chlorophyll patch by an Agulhas ring. *Geophysical Research Letters*, 38(16). https://doi.org/10.1029/2011GL048588

Lherminier, P., Mercier, H., Gourcuff, C., Alvarez, M., Bacon, S., and Kermabon, C. (2007). Transports across the 2002 Greenland-Portugal Ovide section and comparison with 1997. *Journal of Geophysical Research: Oceans*, 112(7), C07003. https://doi.org/10.1029/2006JC003716

Li, F., Lozier, M. S., Bacon, S., Bower, A. S., Cunningham, S. A., de Jong, M. F., et

al. (2021). Subpolar North Atlantic western boundary density anomalies and the meridional overturning circulation. *Nature Communications*, 12(1). https://doi.org/10.1038/s41467-021-23350-2

Lilly J. M., Rhines P.B., Visbeck M., Davis R., Lazier J.R.n., F Schott, D Send, U., and Marshall, J. (1995). Integral effects of deep convection. *Journal of Physical Oceanography*, 25, 855–872.

Lilly, J. M., Rhines, P. B., Visbeck, M., Davis, R., Lazier, J. R. N., Schott, F., and Farmer, D. (1999). Observing deep convection in the labrador sea during winter 1994/95. *Journal of Physical Oceanography*, 29(8 PART 2), 2065–2098. https://doi.org/10.1175/1520-0485(1999)029<2065:odcitl>2.0.co;2

Lilly, J. M., and Rhines, P. B. (2002). Coherent eddies in the Labrador Sea observed from a mooring. *Journal of Physical Oceanography*, 32(2), 585–598. https://doi.org/10.1175/1520-0485(2002)032<0585:CEITLS>2.0.CO;2

Lilly, J. M., Rhines, P. B., Schott, F., Lavender, K., Lazier, J., Send, U., and D'Asaro, E. (2003). Observations of the Labrador Sea eddy field. *Progress in Oceanography* (Vol. 59, Issue 1, pp. 75–176). Elsevier Ltd. https://doi.org/10.1016/j.pocean.2003.08.013

Liu, Y. J., Desbruyères, D. G., Mercier, H., and Spall, M. A. (2022). Observation-based estimates of Eulerian-mean boundary downwelling in the western subpolar North Atlantic. *Geophysical Research Letters*, 1–10. https://doi.org/10.1029/2021gl097243

Lazier J. R. N., A. Clarke, I. Yashayaev, and P. B. Rhines (2002). "Convection and restratification in the Labrador Sea, 1990-2000". *Deep-Sea Res.*, 49, pp. 1819-1835.

Lozier, M. S., (2012). Overturning in the North Atlantic. *Annual review of marine science*, Volume 4, pp. 291-315.

Lozier, M. S., Bacon, S., Bower, A. S., Cunningham, S. A., De Jong, M. F., De Steur, L., De Young, B., Fischer, J., Gary, S. F., Greenan, B. J., Heimbmbach, P., Holliday, N. P., Houpert, L., Inall, M. E., Johns, W. E., Johnson, H. L., Karstensen, J., Li, F., Lin, X., Mackay, N., Marshall, D. P., Mercier, H., Myers, P. G., Pickart, R. S., Pillar, H. R., Straneo, F., Thierry, V., Weller, R. A., Williams, R. G., Wilson, C., Yang, J., Zhao, J., and Zika, J. D. (2017). Overturning in the Subpolar North Atlantic Program: A new international ocean observing system. *Bulletin of the American Meteorological Society*, 98(4):737–752.

Lozier, M. S., Li, F., Bacon, S., Bahr, F., Bower, A. S., Cunningham, S. A., et al. (2019). A sea change in our view of overturning in the subpolar North Atlantic. *Science*, 363, 516–521. https://doi.org/10.1126/science.aau6592

Lumpkin, R., and Speer, K. (2007). Global ocean meridional overturning. *Journal of Physical Oceanography*, 37(10), 2550–2562. https://doi.org/10.1175/JPO3130.1

Luo, H., A. Bracco, and E. Di Lorenzo, (2011). The interannual variability of the surface eddy kinetic energy in the Labrador Sea. *Prog. Oceanogr.*, 91, 295–311, https://doi.org/

10.1016/j.pocean.2011.01.006.

Lumpkin, R., and Speer, K. (2007). Global ocean meridional overturning. *Journal of Physical Oceanography*, 37(10), 2550–2562. https://doi.org/10.1175/JPO3130.1

Luo, H., A. Bracco, and E. Di Lorenzo, (2011). The interannual variability of the surface eddy kinetic energy in the Labrador Sea. *Prog. Oceanogr.*, 91, 295–311, https://doi.org/10.1016/j.pocean.2011.01.006.

Madec, G., (2008). NEMO the Ocean Engine. *Tech. Rep.*, Notes de l IPSL, 27 (1288-1619), 193. 8,126

Marotzke, J., and Scott, J. R. (1999). Convective mixing and the thermohaline circulation. *Journal of Physical Oceanography*, 29(11), 2962–2970. https://doi.org/10.1175/1520-0485(1999)029<2962:CMATTC>2.0.CO;2

Marshall, J., and F. Schott (1999), Open-ocean convection: Observations, theory, and models, *Rev. Geophys.*, 37(1), 1–64, doi:10.1029/98RG02739.

Marshall, J., and Speer, K. (2012). Closure of the meridional overturning circulation through Southern Ocean upwelling, *Nat. Geosci.*, 5(3), 171–180, doi:10.1038/ngeo1391

Marshall, J., J. R. Scott, K. C. Armour, J. M. Campin, M. Kelley, and A. Romanou (2014), The ocean's role in the transient response of climate to abrupt greenhouse gas forcing, *Clim. Dyn.*, 44, 2287–2299, doi:10.1007/s00382-014-2308-0.

Mauritzen, C. (1996). Production of dense overflow waters feeding the North Atlantic across the Greenland-Scotland Ridge. Part 1: Evidence for a revised circulation scheme. *Deep-Sea Research Part I Oceanographic Research Papers,* 43, 769–806. https://doi. org/10.1016/0967-0637(96)00037-4

McGeehan, T., and Maslowski, W. (2012). Evaluation and control mechanisms of volume and freshwater export through the Canadian Arctic Archipelago in a high-resolution pan-Arctic ice-ocean model. *Journal of Geophysical Research: Oceans*, 117(3), 1–25. https://doi.org/10.1029/2011JC007261

Moat, B. I., Smeed, D. A., Frajka-Williams, E., Desbruyeres, D. G., Beaulieu, C., Johns, W. E., et al. (2020). Pending recovery in the strength of the meridional overturning circulation at 26°N. *Ocean Science*, 16(4), 863–874. https://doi.org/10.5194/os-16-863-2020

Nguyen, A. T., Woodgate, R. A., and Heimbach, P. (2020). Elucidating large-scale atmospheric controls on bering strait throughflow variability using a data-constrained ocean model and its adjoint. *J. Geophys. Res. Oceans*, 125. https://doi.org/10.1029/2020JC016213

Nguyen, A. T., Pillar, H., Ocana, V., Bigdeli, A., Smith, T. A., and Heimbach, P. (2021). The Arctic Subpolar gyre sTate Estimate: Description and assessment of a data-constrained, dynamically consistent ocean-sea ice estimate for 2002–2017. *Journal of Advances in Modeling Earth Systems*, 13, e2020MS002398. https://doi. org/10.1029/2020MS002398

Ollitrault Michel, Rannou Philippe, Brion Emilie, Cabanes Cecile, Piron Anne, Reverdin Gilles, Kolodziejczyk Nicolas (2021). ANDRO: An Argo-based deep displacement dataset. SEANOE. https://doi.org/10.17882/47077

Pacini, A., Pickart, R. S., Bahr, F., Torres, D. J., Ramsey, A. L., Holte, J., Karstensen, J., Oltmanns, M., Straneo, F., Le Bras, I. A., Moore, G. W. K., and Femke de Jong, M. (2020). Mean conditions and seasonality of the west Greenland boundary current system near cape farewell. *Journal of Physical Oceanography*, 50(10), 2849–2871. https://doi.org/10.1175/JPO-D-20-0086.1

Pacini, A., Pickart, R. S., Le Bras, I. A., Straneo, F., Penny Holliday, N., and Spall, M. A. (2021). Cyclonic eddies in the west greenland boundary current system. *Journal of Physical Oceanography*, 51(7), 2087–2102. https://doi.org/10.1175/JPO-D-20-0255.1

Pacini, A., and Pickart, R. S. (2022). Meanders of the West Greenland Current near Cape Farewell. *Deep-Sea Research Part I: Oceanographic Research Papers*, 179(August 2021), 103664. https://doi.org/10.1016/j.dsr.2021.103664

Palter, J. B., Lozier, M. S., and Lavender, K. L. (2008). How does Labrador sea water enter the deep western boundary current? *Journal of Physical Oceanography*, 38(5), 968–983. https://doi.org/10.1175/2007JPO3807.1

Palter JB, Caron C, Law KL et al (2016) Variability of the directly observed, middepth subpolar North Atlantic circulation. *Geophys Res Lett* 43:2700–2708. doi:10.1002/2015GL067235

Pedlosky, J. (2003). Thermally Driven Circulations in Small Oceanic Basins. *Journal of Physical Oceanography*. 2333–2340. https://doi.org/10.1175/1520-0485(2003)033<2333:TDCISO>2.0.CO;2

Petit, T., Lozier, M. S., Josey, S. A., and Cunningham, S. A. (2020). *Geophysical Research Letters*, 47, e2020GL091028. https://doi.org/10.1029/2020GL091028

Pickart, R. S. (1992). Water mass components of the North Atlantic deep western boundary current. *Deep-Sea Res. Part I: Oceanogr. Res. P.*, 39(9):1553–1572.

Pickart, R. S., Torres, D. J., and Clarke, R. A. (2002). Hydrography of the Labrador Sea during active convection. *Journal of Physical Oceanography,* 32(2):428–457.

Pickart, R. S., and Spall, M. A. (2007). Impact of Labrador Sea convection on the North Atlantic meridional overturning circulation. *Journal of Physical Oceanography*, 37(9), 2207–2227. https://doi.org/10.1175/JPO3178.1

Pillar, H. R., Heimbach, P., Johnson, H. L., and Marshall, D. P. (2016). Dynamical attribution of recent variability in Atlantic overturning. *Journal of Climate*, 29, 3339–3352. https://doi.org/10.1175/JCLI-D-15-0727.1

Piron, A., Thierry, V., Mercier, H., and Caniaux, G. (2016). Argo float observations of basin-

scale deep convection in the Irminger sea during winter 2011–2012. *Deep-Sea Research Part I: Oceanographic Research Papers*, 109(October 2018), 76–90. https://doi.org/10.1016/j.dsr.2015.12.012

Prater M. (2002). Eddies in the Labrador Sea as observed by profiling RAFOS floats and remote sensing., *Journal of Physical Oceanography*, 32, pp. 411-427.

Rahmstorf, S. (1999), Decadal variability of the thermohaline ocean circulation, in Beyond El Niño, edited by A. Navarra, pp. 309–331, Springer, Berlin.

Rahmstorf, S. (2002). Ocean circulation and climate during the past 120,000 years. *Nature*, 419(6903):207–214.

Rhein, M., D. Kieke, and R. Steinfeldt (2007), Ventilation of the Upper Labrador Sea Water, 2003-2005., *Geophysical Research Letters*, 34 (L06603), doi:10.1029/2006GL028540.

Rieck, J. K., Böning, C. W., and Getzlaff, K. (2019). The nature of eddy kinetic energy in the labrador sea: Different types of mesoscale eddies, their temporal variability, and impact on deep convection. *Journal of Physical Oceanography*, 49(8), 2075–2094. https://doi.org/10.1175/JPO-D-18-0243.1

Riser, S. C., Freeland, H. J., Roemmich, D., Wijffels, S., Troisi, A., Belbéoch, M., Gilbert, D., Xu, J., Pouliquen, S., Thresher, A., Le Traon, P. Y., Maze, G., Klein, B., Ravichandran, M., Grant, F., Poulain, P. M., Suga, T., Lim, B., Sterl, A., … Jayne, S. R. (2016). Fifteen years of ocean observations with the global Argo array. *Nature Climate Change*, 6(2), 145–153. https://doi.org/10.1038/nclimate2872

Roberts, C. D., Waters, J., Peterson, K. A., Palmer, M. D., McCarthy, G. D., Frajka-Williams, E., et al. (2013). Atmosphere drives recent interannual variability of the Atlantic meridional overturning circulation at 26.5°N. *Geophysical Research Letters*, 40, 5164–5170. https://doi.org/10.1002/grl.50930

Robson, J., Ortega, P., and Sutton, R. (2016). A reversal of climatic trends in the North Atlantic since 2005. *Nature Geoscience,* 9, 513–517. https://doi.org/10.1038/ngeo2727

Robson, J., Polo, I., Hodson, D. L. R., Stevens, D. P., and Shaffrey, L. C. (2018). Decadal prediction of the North Atlantic subpolar gyre in the HiGEM high-resolution climate model. *Climate Dynamics*, 50(3–4), 921–937. https://doi.org/10.1007/s00382-017-3649-2

Roessler, A., Rhein, M., Kieke, D., Mertens, C., (2015). Long-term observations of North Atlantic Current transport at the gateway between western and eastern Atlantic: NAC transport observations at MAR. *Journal of Geophysical Research: Oceans* 120, 4003–4027. http://dx.doi.org/10.1002/2014JC010662.

Rossby, T. (1996). The North Atlantic Current and surrounding waters: At the crossroads, Rev. Geophys., 34(4), 463–481, doi:10.1029/96RG02214.

Rossby, T. (1999). On gyre interactions, *Deep-Sea Res., Part II*, 46(1–2), 139–164, doi:10.1016

/S0967-0645(98)00095-2.

Rudels, B., Friedrich, H. J., and Quadfasel, D.(1999). The Arctic Circumpolar Boundary Current, *Deep-Sea Res. II*, 46, 1023–1062, 1999.

Rykova, T., Straneo, F., Lilly, J. M., and Yashayaev, I. (2009). Irminger current anticyclones in the Labrador Sea observed in the hydrographic record, 1990-2004. *Journal of Marine Research*, 67(3), 361–384. https://doi.org/10.1357/002224009789954739

Saenko, O. A., Dupont, F., Yang, D., Myers, P. G., Yashayaev, I., and Smith, G. C. (2014). Role of resolved and parameterized eddies in the labrador sea balance of heat and buoyancy. *Journal of Physical Oceanography*, 44(12), 3008–3032. https://doi.org/10.1175/JPO-D-14-0041.1

Sarafanov, A., Falina, A., Mercier, H., Sokov, A., Lherminier, P., Gourcuff, C., Gladyshev, S., Gaillard, F., and Daniault, N. (2012). Mean full-depth summer circulation and transports at the northern periphery of the Atlantic Ocean in the 2000s. *Journal of Geophysical Research: Oceans*, 117(1). https://doi.org/10.1029/2011JC007572

Saunders, P. M., (1996). The Flux of Dense Cold Overflow Water Southeast of Iceland. *Journal of Physical Oceanography*, Volume 26, pp. 85-95.

Sayol, J. M., Dijkstra, H., and Katsman, C. (2019). Seasonal and regional variations of sinking in the subpolar North Atlantic from a high-resolution ocean model. *Ocean Science*, 15(4), 1033–1053. https://doi.org/10.5194/os-15-1033-2019

Schaeffer, A., M. Roughan, and J. E. Wood (2014), Observed bottom boundary layer transport and uplift on the continental shelf adjacent to a western boundary current, *J. Geophys. Res. Oceans*, 119, 4922–4939, doi:10.1002/2013JC009735.

Send, U. and J. C. Marshall. (1995). Integral effects of deep convection. *J. Phys. Oceanogr.*, 25, 855-872.

Schott, F., Fischer, J., Reppin, J., and Send, U. (1993). On mean and seasonal currents and transports at the western boundary of the equatorial Atlantic. *Journal of Geophysical Research*, 98(C8). https://doi.org/10.1029/93jc01287

Shapiro G.I., Hill A.E.(1997).Dynamics of dense water cascades at the shelf edge *Journal of Physical Oceanography* 27 (11), 2381-2394

Smethie Jr W.M., Swift J.H. (1989).The tritium: krypton-85 age of Denmark Strait overflow water and Gibbs Fracture Zone water just south of Denmark Strait. *Journal of Geophysical Research: Oceans* 94 (C6), 8265-8275

Smethie, W., Fine, R., Putzka, A. and Jones, E., (2000). Tracing the flow of North Atlantic Deep Water using chlorofluorocarbons. *Journal of Geophysical Research: Oceans*, 105(C6), pp. 14297-14323.

Spall, M. A.,and J. F. Price, (1998:) Mesoscale variability in Denmark Strait: The PV outflow hypothesis. *J. Phys. Oceanogr.*, 28, 1598–1623, https://doi.org/10.1175/1520-0485(1998)028,1598:MVIDST. 2.0.CO;2.

Spall, M. A., and Pickart, R. S. (2001). Where does dense water sink? a subpolar gyre example. *Journal of Physical Oceanography*, 31(3), 810–826. https://doi.org/10.1175/1520-0485(2001)031<0810:WDDWSA>2.0.CO;2

Spall, Michael A. (2003). On the thermohaline circulation in at bottom marginal seas. *Journal of Marine Research* (Vol. 61).

Spall, M. A., (2004): Boundary currents and water mass transformation in marginal seas. *J. Phys. Oceanogr.*, 34, 1197–1213, https://doi.org/10.1175/1520-0485(2004)034,1197:BCAWT I.2.0.CO;2.

Spall, M. A. (2008). Low-frequency interaction between horizontal and overturning gyres in the ocean. *Geophysical Research Letters,* 35(18), 1–5. https://doi.org/10.1029/2008GL035206

Spall, M. A. (2010). Dynamics of downwelling in an eddy-resolving convective basin. *Journal of Physical Oceanography*, 40(10), 2341–2347. https://doi.org/10.1175/2010JPO4465.1

Spall, M. A., R. S. Pickart, P. Lin, W. J. von Appen, D. Mastropole, H. Valdimarsson, T. W. Haine, and M. Almansi, (2019): Frontogenesis and variability in Denmark Strait and its influence on overflow water. *J. Phys. Oceanogr.*, 49, 1889–1904, https://doi.org/10.1175/JPO-D-19-0053.1.

Stegner, A., Le Vu, B., Dumas, F., Ghannami, M. A., Nicolle, A., Durand, C., and Faugere, Y. (2021). Cyclone-Anticyclone Asymmetry of Eddy Detection on Gridded Altimetry Product in the Mediterranean Sea. *Journal of Geophysical Research: Oceans*, 126(9). https://doi.org/10.1029/2021JC017475

Stramma, L. et al., (2004). Deep water changes at the western boundary of the subpolar North Atlantic during 1996 to 2001. *Deep-Sea Research I*, Volume 51, pp. 1033-1056.

Straneo, F. (2006). On the Connection between Dense Water Formation, Overturning, and Poleward Heat Transport in a Convective Basin. *Journal of Physical Oceanography*, 36, 1822–1840. https://doi.org/10.1175/JPO2932.1

Szekely, T., Gourrion, J., Pouliquen, S., and Reverdin, G. (2019). CORA, Coriolis ocean dataset for reanalysis. SEANOE. https://doi. org/10.17882/46219

Talley, L. and McCartney, M., (1982). Distribution and circulation of Labrador Sea water. *Journal of Physical Oceanography*, 12(11), pp. 1189-1205.

Talley, Lynne D. (2013).Closure of the global overturning circulation through the Indian, Pacific, and Southern Oceans: Schematics and transports. *Oceanography* 26.1 (2013): 80–97

Talley, L. D., Feely, R. A., Sloyan, B. M., Wanninkhof, R., Baringer, M. O., Bullister,

J. L., Carlson, C. A., Doney, S. C., Fine, R. A., Firing, E., Gruber, N., Hansell, D. A., Ishii, M., Johnson, G. C., Katsumata, K., Key, R. M., Kramp, M., Langdon, C., MacDonald, A. M., ... Zhang, J. Z. (2016). Changes in Ocean Heat, Carbon Content, and Ventilation: A Review of the First Decade of GO-SHIP Global Repeat Hydrography. *Annual Review of Marine Science*, 8, 185–215. https://doi.org/10.1146/annurev-marine-052915-100829

Toole, J. et al., (2017). Moored observations of the Deep Western Boundary Current in the NW Atlantic: 2004–2014. *Journal of Geophysical Research: Oceans*, 122(9), pp. 7488-7505.

Tsujino, H., Urakawa, L. S., Griffies, S. M., Danabasoglu, G., Adcroft, A. J., Amaral, A. E., Arsouze, T., Bentsen, M., Bernardello, R., Böning, C. W., Bozec, A., Chassignet, E. P., Danilov, S., Dussin, R., Exarchou, E., Fogli, P. G., Fox-Kemper, B., Guo, C., Ilicak, M., Iovino, D., Kim, W. M., Koldunov, N., Lapin, V., Li, Y., Lin, P., Lindsay, K., Liu, H., Long, M. C., Komuro, Y., Marsland, S. J., Masina, S., Nummelin, A., Rieck, J. K., Ruprich-Robert, Y., Scheinert, M., Sicardi, V., Sidorenko, D.,Suzuki, T., Tatebe, H., Wang, Q., Yeager, S. G., and Yu, Z.(2020). Evaluation of global ocean–sea-ice model simulations based on the experimental protocols of the Ocean Model Intercomparison Project phase 2 (OMIP-2), *Geosci. Model Dev.*, 13, 3643–3708, https://doi.org/10.5194/gmd-13-3643-2020, 2020.

Treguier, A. M., Lique, C., Deshayes, J., and Molines, J. M. (2017). The North Atlantic eddy heat transport and its relation with the vertical tilting of the Gulf Stream axis. *Journal of Physical Oceanography*, 47(6), 1281–1289. https://doi.org/10.1175/JPO-D-16-0172.1

Våge, K., Pickart, R. S., Moore, G. W., and Ribergaard, M. H. (2008). Winter mixed layer development in the central Irminger Sea: The effect of strong, intermittent wind events. *Journal of Physical Oceanography*, 38(3):541–565.

Våge, K., Pickart, R. S., Sarafanov, A., Knutsen, Ø., Mercier, H., Lherminier, P., et al. (2011). The Irminger Gyre: Circulation, convection, and interannual variability. *Deep-Sea Research Part I: Oceanographic Research Papers*, 58(5), 590–614. https://doi.org/10.1016/j.dsr.2011.03.001

Vellinga, M., and Wood, R. (2002). Global climatic impacts of a collapse of the Atlantic hermohaline circulation, *Clim. Change*, 54(3), 251–267, doi:10.1023/A:1016168827653.

Visbeck M., Marshall J., Jones H. (1996) Dynamics of isolated convective regions in the ocean. *Journal of Physical Oceanography* 26 (9), 1721-1734

von Appen, W., R. S. Pickart, K. Brink, and T. Haine, (2014). Water column structure and statistics of Denmark Strait Overflow Water cyclones. *Deep-Sea Res. I*, 84, 110–126, https://doi.org/ 10.1016/j.dsr.2013.10.007.

Wåhlin, A. K., Muench, R. D., Arneborg, L., Björk, G., Ha, H. K., Lee, S. H., and Alsén, H. (2012). Some implications of ekman layer dynamics for cross-shelf exchange in the Amundsen sea. *Journal of Physical Oceanography*, 42(9), 1461–1474. https://doi.org/10.1175/JPO-D-11-041.1

Weaver, A. J., M. Eby, M. Kienast, and O. A. Saenko (2007), Response of the Atlantic

meridional overturning circulation to increasing atmospheric CO2: Sensitivity to mean climate state, *Geophys. Res. Lett.*, 34, L05708, doi:10.1029/2006GL028756.

Xu, X., Bower, A., Furey, H., and Chassignet,E. P. (2018). Variability of the Iceland-Scotland overflow water transport through the Charlie-Gibbs fracture zone: Results from an eddying simulation and observations. *Journal of Geophysical Research: Oceans*,123,5808–5823. https://doi.org/10.1029/2018JC01389

Yankovsky, E. and Legg, S.(2019). Symmetric and Baroclinic Instability in Dense Shelf Overflows, *J. Phys. Oceanogr.*, 49, 39–61, https://doi.org/10.1175/JPO-D-18-0072.1, 2019.

Yashayaev, I., (2007). Hydrographic changes in the Labrador Sea, 1960–2005. *Progress in Oceanography*, Volume 73, pp. 242-276.

Yeager, S. and Danabasoglu, G., (2014). The origins of late-twentieth-century variations in the large-scale North Atlantic circulation. *Journal of Climate*, 27(9), pp. 3222-3247.

Zantopp, R., Fischer, J., Visbeck, M., and Karstensen, J. (2017). From interannual to decadal: 17 years of boundary current transports at the exit of the Labrador Sea. *Journal of Geophysical Research: Oceans*, 122(3), 1724–1748. https://doi.org/10.1002/2016JC012271

Zhang, R., and T. L. Delworth (2006), Impact of Atlantic multidecadal oscillations on India/Sahel rainfall and Atlantic hurricanes, *Geophys. Res. Lett.*, 33, L17712, doi:10.1029/2006 GL026267.

Zhang, R. (2010), Latitudinal dependence of Atlantic Meridional Overturning Circulation (AMOC) variations, *Geophys. Res. Lett.*, 37, L16703, doi:10.1029/2010GL044474.

Zhang, R. (2017). On the persistence and coherence of subpolar sea surface temperature and salinity anomalies associated with the Atlantic multidecadal variability. *Geophysical Research Letters*, 44, 7865–7875. https://doi.org/10.1002/2017GL074342

Zhang, Z., Wang, W., and Qiu, B. (2014). Oceanic mass transport by mesoscale eddies. *Science*, 345(6194), 322–324. https://doi.org/10.1126/science.1252418

Zhu, J. S., E. Demirov, Y. Zhang, and A. Polomska-Harlick, (2014). Model simulations of mesoscale eddies and deep convection in the Labrador Sea. *Adv. Atmos. Sci.*, 31, 743–754, https:// doi.org/10.1007/s00376-013-3107-y.

Zou, S., and Lozier, M. S. (2016). Breaking the linkage between Labrador Sea Water production and its export to the subtropical gyre. *Journal of Physical Oceanography*, 46, 2169–2182. https://doi.org/10.1175/jpo-d-15-0210.1

Zou, S., Bower, A. S., Furey, H., Pickart, R. S., Houpert, L., and Penny Holliday, N. (2021). Observed Deep Cyclonic Eddies around Southern Greenland. *Journal of Physical Oceanography*, 51(10), 3235–3252. https://doi.org/10.1175/JPO-D-20-0288.1

DOCTORAT SCIENCES BRETAGNE DE LA MER LOIRE ET DU LITTORAL

UBO Université de Bretagne Occidentale

Titre : Dynamique de bord ouest et circulation méridienne verticale dans le Gyre Subpolaire de l'Atlantique Nord

Mots clés : AMOC - Gyre subpolaire - Transport vertical -Observations

Résumé : La circulation méridienne de retournement de l'Atlantique (AMOC) est une composante essentielle du système climatique en raison de son rôle vital dans la distribution globale de la chaleur, du carbone et des masses d'eau. La descente des eaux de surface de l'Atlantique Nord reliant les branches supérieure et inférieure de l'AMOC est une composante essentielle mais vulnérable de cette circulation globale. Le transport vertical associé se produit en partie le long des frontières continentales. Cette thèse présente une étude observationnelle étendue sur la quantification du « downwelling » moyen eulérien le long des pentes continentales du gyre subpolaire de l'Atlantique Nord (SPG) et un examen des mécanismes sous-jacents, en mettant l'accent sur le rôle des tourbillons de méso-échelle. Un bilan de volume révèle un « downwelling » total moyen (2002-2019) de 4.41±0.96 Sv à 1300 m de profondeur entre le détroit du Danemark et le Cap de Flemish, le transport barotrope (BT) contribuant pour 2.66±0.40 Sv et le transport barocline (BC) pour 1.84±0.44 Sv. Afin d'étudier les processus à l'origine de la plongée BC le long des bords du gyre SPG, i.e. la perte de chaleur et le gradient de densité associé, le bilan de chaleur moyen du courant de bords est étudié. A la fois les flux de chaleur latéraux, induits par les courants de bord et les tourbillons à méso-échelle, et les flux de chaleur air-mer jouent un rôle important dans la perte de chaleur du courant de bord. Dans un cadre lagrangien basé, on constate que la propagation des tourbillons contribue à refroidir la région de bord du gyre SPG.

Title : Western boundary dynamics and overturning circulation in the subpolar North Atlantic

Keywords : AMOC – Subpolar Gyre – Vertical Transport –Observations

Abstract : The Atlantic Meridional Overturning Circulation (AMOC) is an essential component of the climate system due to its vital role in the global distribution of heat, carbon, and water masses. The downwelling of North Atlantic surface waters connecting the upper and lower AMOC limbs is an essential yet vulnerable part of this global circulation. This downwelling partly occurs along continental boundaries. This dissertation presents an extended observational investigation on the quantification of Eulerian-mean downwelling along the continental slopes of the North Atlantic subpolar gyre (SPG) and an examination of the underlying mechanisms, with an emphasis on the role of mesoscale eddies. A volume budget of the SPG boundary reveals a total Eulerian-mean (2002-2019) downwelling of -4.41±0.96 Sv at 1300 m depth between Denmark Strait and Flemish Cap, with the barotropic transport (BT) contributing 2.66±0.40 Sv and the baroclinic transport (BC) contributing 1.75±0.43 Sv. To investigate the processes that cause the BC boundary downwelling, i.e., the boundary heat loss and associate along-boundary density gradient, the long-term mean heat budget of the boundary current system is studied. Both lateral heat fluxes, driven by the boundary current/mesoscale eddies, and air-sea heat flux play significant roles in the boundary heat loss. In a Lagrangian framework, it is found that cross-shore eddy propagation generally cools the SPG boundary.